CORRELATIONS IN MOIRÉ HETEROSTRUCTURES

A DISSERTATION
SUBMITTED TO THE DEPARTMENT OF APPLIED PHYSICS
AND THE COMMITTEE ON GRADUATE STUDIES
OF STANFORD UNIVERSITY
IN PARTIAL FULFILLMENT OF THE REQUIREMENTS
FOR THE DEGREE OF
DOCTOR OF PHILOSOPHY

Aaron Sharpe
December 2020

© 2020 by Aaron Layne Sharpe. All Rights Reserved.
Re-distributed by Stanford University under license with the author.

This work is licensed under a Creative Commons Attribution-Share Alike 3.0 United States License.
http://creativecommons.org/licenses/by-sa/3.0/us/

This dissertation is online at: http://purl.stanford.edu/cs071hw8313

I certify that I have read this dissertation and that, in my opinion, it is fully adequate in scope and quality as a dissertation for the degree of Doctor of Philosophy.

David Goldhaber-Gordon, Primary Adviser

I certify that I have read this dissertation and that, in my opinion, it is fully adequate in scope and quality as a dissertation for the degree of Doctor of Philosophy.

Marc Kastner

I certify that I have read this dissertation and that, in my opinion, it is fully adequate in scope and quality as a dissertation for the degree of Doctor of Philosophy.

Steven Kivelson

Approved for the Stanford University Committee on Graduate Studies.

Stacey F. Bent, Vice Provost for Graduate Education

This signature page was generated electronically upon submission of this dissertation in electronic format. An original signed hard copy of the signature page is on file in University Archives.

Abstract

Moiré patterns in van der Waals heterostructures are a readily realizable class of 2D superlattices with electronic properties distinct from those of the parent materials that can be controlled by the composition and relative orientations of layers. The large artificial superlattice generates minibands that disperse on a finer energy scale in a significantly smaller mini Brillouin zone. I begin with transport measurements in highly aligned graphene/hexagonal boron nitride (hBN) heterostructures, a high electron mobility superlattice with miniband edges and Van Hove singularities that are accessible via electrostatic gating. By using recently developed absorptive pinhole collimators, consisting of absorptive sidewalls between a pair of collinear slits, it is possible to populate and detect a narrow window of k-states. Low-field transport measurements yield results consistent with ballistic Monte Carlo simulations based on numerical bandstructure calculations when the superlattice has been tuned to exhibit non-circular Fermi surfaces. Subsequent scanning gate measurements spatially image the non-circular Fermi surface, raising the possibility of using absorptive pinhole collimators as geometric valley filters.

A number of moiré superlattices have recently emerged that exhibit flat electronic bands, making them ideal for exploring strongly correlated physics. The flat bands in magic-angle twisted bilayer graphene (tBLG) and ABC-trilayer graphene aligned with hBN (ABC-TLG/hBN) have been shown to give rise to correlated insulators [1,2]. An amazing recent discovery is that tBLG becomes superconducting when doped slightly away from two holes per site, reminiscent of high temperature superconductors [3]. Understanding the mechanism of high-transition-temperature (high-T_c) superconductivity is a central problem in condensed matter physics. It is highly desirable to study a tunable Hubbard system, in which systematic investigations of the unconventional superconductivity and its evolution with the Hubbard parameters can deepen our understanding of high-T_c superconductivity.

I begin with a report of signatures of tunable superconductivity in ABC-TLG/hBN. Unlike in tBLG, theoretical calculations show that under a vertical displacement field, the ABC-TLG/hBN heterostructure features an isolated flat valence miniband associated with a Hubbard model on a triangular superlattice [2,4]. Signatures of superconductivity emerge below 1 kelvin for the electron- and hole-doped sides of the one-quarter-filling correlated state. The electronic behaviour in the ABC-TLG/hBN superlattice is expected to depend sensitively on the interplay between electron–electron interactions and the miniband bandwidth. By varying the vertical displacement field, transitions from the candidate superconductor to correlated insulator

and metallic phases are observed.

Superconductivity is one of many possible ground states in flat band systems when electron-electron interactions dominate. I present evidence of an incipient Chern insulating state at integer filling of the flat band in both tBLG and ABC-TLG/hBN. Notably, in tBLG, the magnetization of the sample can be reversed by applying a small direct current. Additionally, when tilting a tBLG sample in an external magnetic field, the ferromagnetism is highly anisotropic. Because spin-orbit coupling is negligible in graphene [5], such behavior is unlikely to come from spin, but rather favors theories in which the ferromagnetism is orbital. For an in-plane field larger than 5 T, the out-of-plane magnetization is destroyed, suggesting a transition to a new phase.

At integer filling of these strongly correlated moiré systems, it is natural to expect the possibility of spontaneous spin/valley polarization. However, there is the possibility of fractional quantum anomalous Hall insulators at fractional filling if interactions are strong enough. I report evidence of ferromagnetism at fractional filling in both tBLG and ABC-TLG/hBN. These states depend very sensitively on the control parameters in the moiré system, to the point where the results in tBLG were not repeatable between cooldowns of the same device. However, the state in ABC-TLG/hBN is much more robust, exhibiting prominent ferromagnetic hysteresis behavior with large anomalous Hall resistivity in a broad region of density. In ABC-TLG/hBN, not only the magnitude of the anomalous Hall signal, but also the sign of the hysteretic ferromagnetic response can be modulated by tuning the carrier density and displacement field. The plethora of interesting ground states found thus far highlights the exciting opportunities for exploring strongly correlated physics enabled in moiré superlattices.

Acknowledgments

Throughout the path to my PhD, I have been lucky to have a life filled with people who have continually supported, mentored, and believed in me. I would not be where I am today without them. I am indebted to too many people to list, but I will single out as many as I reasonably can here.

During the past six years as a member of his group, David Goldhaber-Gordon has offered tireless and endlessly caring mentorship. He truly dedicates himself to all of his students. David has helped me become a much more thoughtful and prudent scientist. His impact on my life is immeasurable. Given the chance, there is no question that I would work with him again.

Marc Kastner's (David's advisor) decision to retire to the Bay Area was one of the greatest things to happen during my PhD studies. Not only did Marc agree to serve as one of my committee members, he also functioned as an auxiliary advisor and mentor. Marc's enthusiasm for science is infectious. His proclivity for asking challenging questions helped me grow as a scientist. I cannot thank Marc enough for his help and mentorship.

I would also like to thank the remaining members of my committee. I relished every opportunity I had to meet with Steven Kivelson. His mastery of physics is truly inspiring. When I questioned which experiments to pursue in my final few years of graduate school, Kathryn Moler encouraged me to strive for experiments that I found exciting, advice that led me to making some of the best decisions I made during graduate school. Finally, Felipe da Jornada, the chair of my committee, helped to reset my perspective. It is easy to become too narrowly focused while studying for a PhD. Through our discussions, Felipe helped me to rekindle a broader scientific perspective.

Throughout my academic career, other teachers laid the foundation for my graduate studies. While in middle school at Westminster School in Oklahoma City, Dave Evans was the first teacher to really encourage me to pursue math and science. During high school at Casady School, Joe Miano, my physics teacher, started my passion for physics. Then while at Rice University, discussions with several of my professors led me to purse a career in Physics. This list includes Randall Hulet, Stanley Dodds, James Hannon, and Douglas Natelson. During my undergraduate years, I was fortunate enough to work in a number of labs and learned much from my advisors Sidney Nagel, Deborah Jin, Ryan Briggs, and Daniel Mittleman. I sincerely thank each of you for your contributions to my life.

In David's group, I was fortunate to have a number of students serve as mentors. Andrew Bestwick taught me the basics of transport measurements. Menyoung Lee taught me how to fabricate devices. Patrick Gallagher patiently answered all my simple questions. Arthur Barnard and I shared an office for several years, through the course of which we had a number of stimulating discussions. Thank you all.

I also had the pleasure of working with a number of fellow students. Eli Fox and I worked together tirelessly for over a year. I learned a lot from Eli and made a great friend throughout our long nights working together. Derrick Boone and I spent a number of weeks at the Los Alamos National High Magnetic Field Lab. While we unfortunately do not have much to show for our work there, only strong friendships can survive repeated scientific failures. Finally, I am leaving the graphene subgroup in the capable hands of Joe Finney. Through Joe's experience in the cooperate realm, I learned a lot on prioritization and, with the additional help of my friend Zack Gomez, to vastly improve my coding skills.

During my time in David's group, I also had the chance to interact with a number of great fellow students. This list of peers includes Monica Allen, Evgeny Mikheev, Trevor Petach, John Bartel, Sam Stanwyck, Lucase Peeters, Alex Houghes, Ilan Rosen, Winston Pouse, Connie Hsueh, Linsey Rodenbach, Molley Andersen, Rupini Kamat, Praveen Sriram, and Steven Tran. Thank you all for all the fun times and good discussions.

I have also had the opportunity to collaborate with a number of people outside of David's group. This list includes Wenmin Yang, a champion of device fabrication; Maja Bachmann, Andy Mackenzie, and Phillp Moll who all trusted me to do theoretical calculations; Guorui Chen and Feng Wang who trusted me to do measurements on extremely precious devices. Thank you for the invaluable collaborations.

All research at Stanford would cease to function without the hard work and dedication of our staff. In the Applied Physics Department, Paula Perron, Patrice O'Dwyer, and Claire Nicholas; in GLAM, Cynthia Sanchez, Deborah Woodward, Larry Candido, Tim Omi, Mark Gibson, Laraine Lietz Lucas, Alice Lee, Sybille Katz, Diana Kulic, and Clora Yeung; in SNSF, Tobi Beetz, Tom Carver, Juliet Jamtgaard, Stanley Lin, Grant Shao, Rich Tiberio, Marcin Walkiewicz, Shiva Bhaskaran, and Cliff Knollenberg; in SIMES, Mia Sibug, Jackie Chin, Margo Holley, Chris MacIntosh, Corrina Peng, and Marta Vitale. Thank you all for all of the support.

My friends have continually supported me throughout the course of graduate school. Graduate school is a grind — having friends who are always around for the occasional break are the reason I made it through. I am thankful to have you all in my life.

Finally, I must thank my family. It says a lot when a family offers truly unconditional support. My family continually provided every opportunity they could conceivably muster and wholeheartedly backed me, despite not really understanding what it is I do. They are all lawyers, after all. I love you and will never be able to thank you enough.

Contents

Abstract iv

Acknowledgments vi

1 Introduction 1

1.1 Designer van der Waals heterostructures . . . 1

1.2 Moiré superlattice basics . . . 3

2 Collimating graphene/hBN moiré superlattice Hall bar 6

2.1 Introduction . . . 6

2.2 Basic characterizations . . . 10

2.3 Magnetic field response . . . 10

2.4 Comparing with ballistic Monte Carlo simulations . . . 11

2.5 Temperature dependence . . . 15

2.6 Scanning gate microscopy measurements . . . 16

3 Flat bands in moiré systems 21

3.1 Magic-angle twisted bilayer graphene (tBLG) . . . 21

3.1.1 Introduction . . . 21

3.1.2 Band Structure . . . 21

3.1.3 Fabrication . . . 25

3.1.4 Prior experimental work . . . 27

3.2 ABC-trilayer graphene/hexagonal boron nitride moiré superlattices . . . 33

3.2.1 Introduction . . . 33

3.2.2 Fabrication . . . 34

3.2.3 Band structure . . . 37

3.2.4 Prior experimental work . . . 41

4 Superconductivity in ABC-TLG/hBN 46

4.1 Introduction 46
4.2 Basic characterization 46
4.3 Signatures of superconductivity. 49
4.4 Searching for coherent oscillations 50
4.5 Mapping the phase diagram 52
4.6 Discussion 54

5 Magnetism at integer filling in moiré systems 56

5.1 Ferromagnetism in Twisted Bilayer Graphene 56
  5.1.1 Introduction 56
  5.1.2 Fabrication and basic device characterization 57
  5.1.3 Comparison to a superconducting tBLG device with misaligned hBN 60
  5.1.4 Magnetic field response 61
  5.1.5 Nonlocal transport 68
  5.1.6 Response to DC bias current 71
  5.1.7 Evidence for orbital Chern insulator 73
  5.1.8 Discussion 75
5.2 Angular dependence of magnetisation in tBLG 80
  5.2.1 Introduction 80
  5.2.2 Measuring magnetic anisotropy 81
  5.2.3 Affects of large in-plane field 82
  5.2.4 Discussion 85
5.3 Chern insulating state in ABC-TLG/hBN moiré superlattice 86
  5.3.1 Introduction 86
  5.3.2 Basic characterization 86
  5.3.3 Magnetic field response 87
  5.3.4 Hartree-Fock calculations 94
  5.3.5 Discussion 95

6 Magnetism at non-integer filling in moiré systems 96

6.1 Magnetism at non-integer filling in ABC-TLG/hBN 96
  6.1.1 Introduction 96
  6.1.2 Basic and magneto-transport characterization 97
  6.1.3 Characterizing the magnetic state 100
  6.1.4 Behavior of the conductivity tensor 104
  6.1.5 Discussion 105
6.2 Evidence for magnetism at non-integer filling in tBLG 106

7 Outlook **108**
7.1 Superconductivity in ABC-TLG/hBN 108
7.2 Ferromagnetism at integer filling 109
7.3 Ferromagnetism at non-integer filling 110

A Designing a vdWs transfer station **112**

B Gate voltages to charge density and displacement field **115**

C Simulating ballistic electrons **117**

D Additional tBLG data **119**
D.1 Quantum oscillations 119
D.2 Longitudinal resistance data 120
D.3 Antisymmetric components and dependence on magnitude of in-plane field 123
D.4 Effect of out-of-plane at small tilt angles 124
D.5 Effect of in-plane field on longitudinal resistivity 125

Bibliography **127**

List of Figures

1.1 **Angular dependence of the superlattice density.** Four times the moiré superlattice density n_s corresponding to four electrons (holes) per moiré unit cell as a function of the relative twist angle between the two constituent crystal lattices forming the moiré superlattice. The two cases of graphene on hBN and on graphene are shown in red and blue, respectively. . . . 5

2.1 **Transverse electron focusing.** (**A**) Schematic of the experiment overlaid on a photo of the device. The hBN/graphene/hBN/few layer graphene heterostructure is shown in green, the $\mathrm{SiO_2}$ substrate is purple, and the dashed line denotes the upper edge of the graphene flake. In the electrical measurement configuration applied to obtain the data in Fig. 2.2B, the two leftmost contacts were grounded to act as absorbers. Current was injected into the left local contact L and the voltage difference between local contacts, M and R, was measured. Arrows depict skipping orbits a hole would take if injected at normal incidence with $B = B_1 \equiv 2\hbar k_e/eL$ (red) or $B_2 \equiv 4\hbar k_f/eL$ (blue). (**B**) Ensemble of simulated skipping orbits emanating from an emitter (red star). Electron trajectories bunch along caustics (red dashed curves) and focus onto an equidistant array of points at the boundary. Scale markers show the cyclotron diameters $2R_c = 2\hbar k_f/eB$. (**C**) Transverse electron focusing (TEF) spectra collected at a single voltage probe M (lower trace) and differentially between voltage probes M and R (upper trace), with $n = -1.1 \times 10^{12}\ \mathrm{cm}^{-2}$ and $T = 1.55$ K. The first, third and sixth focusing peaks are labeled. Taking the differential measurement of the spectrum does not shift the peak positions, because the device geometry partially shields R from being reached by skipping orbits from L, such that oscillations of the voltage at R are much weaker. Figure from Ref. 6. 7

2.2 **TEF spectra at base temperature.** (**A**) Miniband structure of the graphene/hBN superlattice, calculated as in Refs. 6, 7. Each miniband for which TEF was observed is labeled. This dispersion results from a symmetric moiré perturbation: $\varepsilon^{+} = 17\ \mathrm{meV}$ and $\varepsilon^{-} = 0\ \mathrm{meV}$; this choice gives the best match between (B) experiment and (C) theory [6]. Equipotential contours are shown; the dashed contours are at the energy levels of saddle-point Van Hove singularities (VHS). (**B**) TEF spectra as a function of gate voltage V_g. $T = 1.55$ K. The plotted ratio $(V_M - V_R)/I_L$ is measured as depicted in Fig. 2.1A. Black dashed curves indicate B_1, B_3, and B_6, which are some of the peak positions where the Fermi level is close to the Dirac point. Green dashed lines indicate the abrupt termination of TEF caused by the breakdown of cyclotron motion at each VHS. Dashed arrows from (B) to (A) point to the energy levels (dashed contours) of the corresponding VHS; Voltage values are labeled by the miniband in which the breakdown occurs (e.g., V_{C1} for the breakdown of cyclotron motion in C1). Dotted lines show selected densities (I, II, III, and IV) that place the Fermi level in minibands C2, C1, V1, and V2, respectively. (**C**) TEF spectra as a function of V_g, calculated from the dispersion in (A) according to Ref. 6. Figure from Ref. 6. 8

2.3 **Absorptive pinhole collimator.** (**A**) Schematic of a double pinhole collimator. Current is sourced from the bottom contact (red), passes through the bottom aperture and is either absorbed by the intermediate contact (black) or passes into the bulk of the device. Only trajectories that pass through both apertures reach the bulk, producing a collimated beam. The collimated beam is steered by an external magnetic field. (**B**) Optical micrograph of the device with four collimators in a Hall-bar-like geometry. Scale bar is 2 μm. (**C**) Measuring angular distribution. Non-local resistance at $n = 1.65\times10^{12}\ \mathrm{cm}^{-2}$ (Fermi wavelength: $\lambda_F = 27.6$ nm) is plotted with V_{S3F3} measured relative to V_{F1} when current is sourced from both S4 and F4 (blue), and only from S4, whereas F4 is grounded (green). The narrowness of the central peak for the F4-grounded data results from collimation. (**D**) Theoretical collimation behavior versus experiment. Left: diagram of effective collimator width $w(\theta)$ at a fixed angle for classical ballistic trajectories. Middle: polar plot of theoretical angular dependence for a 300 nm-wide point contact (blue) and a $w_0 = 300$ nm, $L_0 = 850$ nm collimator (green). Right: experimental data from (C) mapped to angle. Figure from Ref. 8. 9

2.4 **Collimating graphene/hBN moiré superlattice Hall bar.** (**A**) Schematic of the collimating graphene/hBN moiré superlattice Hall bar. Sourcing contacts are labeled with the prefix S. Focusing contacts are labeled with the prefix F. Side contacts used to drain stray carriers are labeled with the prefix O. (**B**) Laser micrograph of the fabricated device. Scale bar is 1 μm. (**C**) Longitudinal resistance R_{xx} as a function of gate voltage V_g. The peak near 0 V corresponds to the charge neutrality point. The peak near 8 V corresponds to the secondary Dirac point, confirming that the sample is a moiré superlattice. 10

2.5 **Magnetic field dependence for different contacts.** Resistance (**A**) R_{S4} and (**B**) R_{S2} as a function of gate voltage V_g and magnetic field B when injecting current from S1 in a collimating configuration (F1 is grounded). Contacts O1 and O2 are also grounded. Dashed black lines in (B) are guides of the form $V_g \propto B^2/j^2$ for $j = 1$ and 2 as one would expect for TEF with a circular Fermi surface corresponding to zero and one bounce(s) along the sidewall of the device, respectively. 11

2.6 **Transport at $\boldsymbol{E_F = -188\ \mathrm{meV}}$.** (**A**) Fermi surface at $E_F = -188\ \mathrm{meV}$ in the K valley, which corresponds to a gate voltage of -9.89 V. The Fermi surface of the K' valley is the time-reversed pair of the K valley. (**B**) Normalized heat map of the position of charge carriers, simulated using a ballistic Monte Carlo for the Fermi surface shown in (A) at a magnetic field of 0.053 T. Trajectories are color coded red or blue if they belong to the K or K' valley, respectively. A count for each plaquette is incremented when an electron's trajectory passes through that plaquette. This count is reflected in the intensity of either color, with higher intensity corresponding to a higher count (where the count has been cut off at a high number to provide contrast in the bulk of the device). Carriers are injected at the source (teal contact) and propagated until hitting a contact. Carriers hitting the source are absorbed and reinjected into the bulk of the device. All contacts colored gold are virtual grounds that perfectly absorb any incoming charge carrier. The device is oriented relative to the crystal axis such that the Fermi surface is oriented as shown in (A). (**C**) Fraction of injected current $I_{\mathrm{injected}} = I_{\mathrm{S1}} + I_{\mathrm{F1}}$ making it to S4 (upper panel) and F4 (lower panel) as a function of magnetic field. Simulation results, a frame of which are shown in (B), are color coded according to their valley index $K^{(')}$ in red or blue, respectively. Experimental results are shown in black. 13

2.7 **Transport at $\boldsymbol{E_F = -135}$ meV.** (**A**) Fermi surface at $E_F = -135$ meV in the K valley, which corresponds to a gate voltage of -7.05 V. The color coding corresponds to two different hole-like pockets in the Fermi surface. The Fermi surface of the K' valley is the time-reversed pair of the K valley. (**B**) Normalized heat map of the position of charge carriers, simulated using a ballistic Monte Carlo for the Fermi surface shown in (A) at a magnetic field of -0.011 T. Trajectories are color coded red or blue according to the different hole-like pockets in the Fermi surface shown in (A). A count for each plaquette is incremented when an electron's trajectory passes through that plaquette. This count is reflected in the intensity of either color, with higher intensity corresponding to a higher count (where the count has been cut off at a high number to provide contrast in the bulk of the device). Carriers are injected at the source (teal contact) and propagated until hitting a contact. Carriers hitting the source are absorbed and reinjected into the bulk of the device. All contacts colored gold are virtual grounds that perfectly absorb any incoming charge carrier. The device is oriented relative to the crystal axis such that the Fermi surface is oriented as shown in (A). (**C**) Fraction of injected current $I_{\text{injected}} = I_{\text{S1}} + I_{\text{F1}}$ making it to S4 (upper panel) and F4 (lower panel) as a function of magnetic field. Simulation results, a frame of which are shown in (B), are color coded according red or blue according to which hole like-pocket of the Fermi surface was simulated. Experimental results are shown in black. 14

2.8 **Temperature dependence of collimatated beam.** (**A**) Temperature dependence of the fractional current to reach S4, $I_{\text{S4}}/I_{\text{injected}}$, as a function of field for $E_F = -135$ meV ($V_g = -7.05$ V). A smooth background has been subtracted from each curve, followed by Gaussian smoothing of each curve. (**B**) Orange filled circles correspond to scattering rates extracted from the amplitude of the zero-field peak shown in (A). Circles and triangles denote effective scattering rates $\tau(T)^{-1}$ extracted from the amplitude of TEF oscillations in Ref. 6. The heavy green curve shows the theoretical scattering rate τ_{e-e}^{-1} related to the electron-electron interaction. Square and diamond symbols denote the rate of scattering by phonons τ_{ph}^{-1} inferred from temperature-dependent sheet resistivity reported in Refs. 9 and 10. The detection limit set by noise is shaded. This panel is modified from Ref. 6. 16

2.9 **Scanning gate microscopy measurements of a circular Fermi surface.** (**A**) Fermi surface at $E_F = 80$ meV which corresponds to a gate voltage of 1.20 V. (**B**) Current drained by F2 as a function of magnetic field. The red dot indicates the field at which S1 is connected to F2 via a single cyclotron orbit. Inset: Schematic of the device showing the trajectories of carriers that connect S1 and F2 when the field is tuned to the value of the red dot. (**C**) Differential current between the source (blue) and a virtual ground (green) measured as a function of the scanning gate tip position for a constant tip potential. All contacts besides the source function as virtual grounds, the currents through which are measured simultaneously and plotted individually. The field has been tuned to the value indicated by the red dot in (B). 18

2.10 **Scanning gate microscopy of a triangular Fermi surface.** Differential current between the source (blue) and a virtual ground (green) measured as a function of the scanning gate tip position for a constant tip potential and $E_F = -135$ meV ($V_g = -7.05$ V). All contacts besides the source function as virtual grounds, the currents through which are measured simultaneously and plotted individually. The white trace is a guide showing a trajectory of the appropriate shape and size for the given E_F and B that would connect S1 to F2. 19

2.11 **High resolution scanning gate microscopy measurement of a triangular Fermi surface.** Differential current of $I_{\mathrm{F2}} + I_{\mathrm{S2}}$ (contacts colored green) when current is injected from the source (blue), measured as a function of the scanning gate tip position for a constant tip potential and $E_F = -135$ meV ($V_g = -7.05$ V). All other contacts are also grounded. the white trace is a guide showing a trajectory of the appropriate shape and size for the given E_F and B. 20

3.1 **Interlayer hopping parameters in tBLG.** (**A**) The blue dashed hexagon marks the Brillouin zone for an unrotated graphene sheet. The black (red) circles are the three equivalent K points for layer 1 (2) that are rotated by $(-)\theta/2$. Crystal momentum is conserved when $\mathbf{p}' - \mathbf{k} = \mathbf{q}_0$, $\mathbf{q}_1$, or $\mathbf{q}_2$. In the chosen reference frame, these momentum transfers have modulus $|\mathbf{q}_j| = 2|\mathbf{K}|\sin(\theta/2)$ and direction $(0,\, 1)$, $(-\sqrt{3}/2,\, -1/2)$, or $(\sqrt{3}/2,\, -1/2)$. Equivalent Dirac points are connected by the reciprocal lattice vectors $\mathbf{G}^{(2)}$ and $\mathbf{G}^{(3)}$, shown as solid blue lines. (**B**) A separate representation of the hopping parameters. When we account for repeated hopping, we generate this honeycomb lattice in reciprocal space. In a repeated zone scheme, the dots correspond to the Dirac points of the two layers. The dashed blue line marks the moiré band Wigner-Seitz cell. Figure adapted from Refs. 11 and 12. . . 22

3.2 **Calculated band structure of tBLG.** (**A**) Band structure of tBLG in the K valley calculated using a continuum model Hamiltonian for $\theta = 1.05°$, $w = 117$ meV, and $w_{AA}/w_{AB} = 0.7$. The band structure for K' is the time reversed partner of the K band structure (**B**) Panel (A) replotted to more clearly show the dispersion of the nearly-flat valence and conduction bands. 25

3.3 **Stacking tBLG heterostructures.** "Tear-and-stack" dry transfer technique used to create tBLG heterostructures. (1) We first pick up a hBN flake using a PC/PDMS stamp. (2) Position the hBN crystal over an exfoliated graphene flake and press the hBN down partially onto the graphene. (3) Once the hBN has been pressed down partially onto the graphene, retract the hBN, hopefully ripping the graphene cleanly in half. (4) Fully retract the stamp. (5) Rotate the remaining portion of the graphene flake to the desired twist angle. (6) Pick up the remaining portion of graphene using the ripped portion. (7) Finish the heterostructure. In this case, this includes fully encapsulating the heterostructure. Figure adapted from Ref. 13. 26

3.4 **Half-filling insulating states in tBLG.** (**A**) Measured conductance G of a tBLG device with twist angle $\theta = 1.08°$ and $T = 0.3$ K. The lighter-shaded regions are superlattice gaps at carrier density $n = \pm 4n_s = \pm 2.7 \times 10^{12}\ \mathrm{cm}^{-2}$. The darker-shaded regions denote half-filling states at $\pm 2n_s$. The inset shows the densities at which half-filling states in four different devices were measured in Ref. 1. (**B**) Minimum conductance values in the p-side (red) and n-side (blue) half-filling states in the $1.08°$ device. The dashed lines are fits of the form $\exp[-\Delta/(2kT)]$, where $\Delta \approx 0.31$ meV is the thermal activation gap. (**C, D**) Temperature-dependent conductance of the $1.08°$ device for temperatures from 0.3 K (black) to 1.7 K (orange) near the (C) p-side and (D) n-side half-filling states. Figure from Ref. 1. Note that Ref. 1 defines n_s as four carriers per moiré unit cell. 28

3.5 **Superconductivity in tBLG.** (**A**) Four-terminal resistance $R_{xx} = V_{xx}/I$ measured in two devices M1 and M2, that have twist angles of $\theta = 1.16°$ and $\theta = 1.05°$, respectively. The inset shows an optical image of device M1, including the main Hall bar (dark brown), electrical contacts (gold), back gate (light green), and $\mathrm{SiO_2/Si}$ substrate (dark grey). (**B**) Current-voltage ($V_{xx} - I$) curves for device M2 measured at $n = -1.44 \times 10^{12}\ \mathrm{cm}^{-2}$ and various temperatures. At the lowest temperature of 70 mK, the curves indicate a critical current of approximately 50 nA. The inset shows the same data on a logarithmic scale, which is typically used to extract the Berezinskii-Kosterlitz-Thouless transition temperature ($T_{\mathrm{BKT}} = 1.0$ K in this case), by fitting to a $V_{xx} \propto I^3$ power law (blue dashed line). Figure adapted from Ref. 3. 29

3.6 **Gate-tunability of superconductivity in tBLG.** (**A**) Two-terminal conductance $G_2 = I/V_{\mathrm{bias}}$ of device M1 ($\theta = 1.16°$) measured in zero magnetic field (red) and with a perpendicular field of $B_\perp = 0.4$ T (blue). The curves exhibit the typical V-shaped conductance near charge neutrality ($n = 0$, vertical purple dotted line) and insulating states at the superlattice bandgaps ($n = \pm 4n_s$, the blue and red bars). They also exhibit reduced conductance at intermediate integer fillings of the superlattice owing to Coulomb interactions (other colored bars). Near a filling of -2 electrons per unit cell, there is considerable conductance enhancement at zero field that is suppressed with $B_\perp = 0.4$ T. This enhancement signals the onset of superconductivity. Measurements were performed at 70 mK with $V_{\mathrm{bias}} = 10\ \mu$V. (**B**) Four-terminal resistance R_{xx}, measured at densities corresponding to the region bounded by the pink dashed lines in (A) as a function of temperature. Two superconducting domes are observed next to the half-filling state, which is labelled 'Mott' and centered around $-2n_s = -1.58 \times 10^{12}\ \mathrm{cm}^{-2}$. The remaining regions in the diagram are labeled as 'metal' owing to the observed metallic temperature dependence. The highest critical temperature observed in device M1 is $T_c = 0.5$ K (as determined by 50% normal-state resistance). (**C**) Similar phase diagram for device M2, showing two asymmetric and overlapping superconducting domes. The highest critical temperature in device M2 is $T_c = 1.7$ K. Figure from Ref. 3. Note that Ref. 3 defines n_s as four carriers per moiré unit cell. 30

3.7 **Magnetic-field response of the superconducting state in tBLG.** (**A, B**) Four-terminal resistance as a function of density n and perpendicular magnetic field $B_\perp$ in devices (A) M1 and (B) M2. As well as the dome structures around half-filling, there are oscillatory features near the boundary between the superconducting phase and the correlated insulator phase. These oscillations are indicative of phase-coherent transport through inhomogeneous regions in the device. (**C**) Differential resistance dV_{xx}/dI as a function of DC bias current I for different $B_\perp$, measured for device M2. (**D**) $R_{xx} - T$ curves for different $B_\perp$, measured for device M1. (**E**) Perpendicular ($B_{c\perp}$) and parallel ($B_{c\|}$) critical magnetic field as a function of temperature for device M1. The fitting curves for $B_{c\perp}$ correspond to Ginzburg-Landau theory for a two-dimensional superconductor. $B_{c\|}$ is fitted to $B_{c\|}(0)(1 - T/T_c)^{1/2}$, where $B_{c\|}(0)$ is the parallel critical field at zero temperature. Measurements in (A-C) were conducted at $70\ \mathrm{mK}$. Figure adapted from Ref. 3. 31

3.8 **Evidence of phase-coherent transport in superconducting tBLG.** (**A, B**) Differential resistance dV/dI versus bias current I and perpendicular field $B_\perp$, at two different charge densities n, corresponding to those in Fig. 3.7A. Periodic oscillations are observed in the critical current (identified approximately as the position of the bright peaks in dV/dI). (**C, D**) Simulations intended to reproduce qualitatively the behavior observed in A and B. Figure adapted from Ref. 3. 32

3.9 **Superconductivity in a $1.14°$ device.** (**A**) Schematic of an all-van der Waals tBLG heterostructure. tBLG is encapsulate between flakes of hBN, with encapsulating flakes of few-layer graphite acting as gates. (**B**) Temperature dependence of the resistance of device D1 over the density range necessary to fill the moiré unit cell, $n \in [-4n_s, 4n_s]$ at $D = 0$. The resistance drops to zero over a finite range of n for electron ($n > 2n_s$) and hole ($n < -2n_s$) doping. (**C**) Resistance as a function of temperature at optimal doping of the hole- and electron-doped superconductors in blue and red, respectively. (**D**) Resistance (R) of device D1 as a function of displacement field. At $-2n_s$, an insulating phase develops at positive D, whereas a superconducting phase develops at negative D. (**E** to **G**) Fraunhofer-like quantum interferences of the critical current, arising from one or more Josephson weak links within the sample, measured at (E) $n = -2.03 \times 10^{12}\ \mathrm{cm}^{-2}$ and $D = 0.61\ \mathrm{V/nm}$, (F) $n = -1.76 \times 10^{12}\ \mathrm{cm}^{-2}$ and $D = -0.59\ \mathrm{V/nm}$, and (G) $n = -1.52 \times 10^{12}\ \mathrm{cm}^{-2}$ and $D = -0.17\ \mathrm{V/nm}$. An anomalous quantum interference pattern with a minimum in I_c at zero field is observed in (G). The measured temperature is $T \approx 10\ \mathrm{mK}$ for all datasets unless otherwise noted. Figure adapted from Ref. 14. Note that Ref. 14 defines n_s as four carriers per moiré unit cell. 33

3.10 **Identifying ABC stacked domains in exfoliated TLG.** (**A**) Atomic force microscope topography image of an exfoliated TLG flake on SiO_2/Si. (**B**) Near-field infrared image corresponding to (A) showing contrast between the ABA and ABC stacked regions. 34

3.11 **Schematic of dual gated device.** Schematic of a dual-gated encapsulated graphene heterostructure Hall bar device and the typical measurement configuration. 35

3.12 **ABC-TLG/hBN devices.** (**A**) Optical image of ABC-TLG/hBN device 1, the device that will be discussed in Ch. 4. Scale bar is 3 $\mu\mathrm{m}$. (**B**) Schematic cross-sectional view of device 1 shown in (A). The red atoms represent on unit cell of ABC-TLG. Note that the top hBN is aligned in device 1. (**C**) Optical image of ABC-TLG/hBN device 2, the device that will be discussed in Ch. 5 and 6. Scale bar is 5 $\mu\mathrm{m}$. (**D**) Schematic cross-sectional view of device 2 shown in (C). The red atoms represent on unit cell of ABC-TLG. Note that the bottom hBN is aligned in device 2. 36

3.13 **ABC vs. ABA stacked TLG.** (**A**) Schematic of the ABC-stacked trilayer lattice containing sic sites in the unit cell, A (white circles) and B (black circles) on each layer, showing the Slonczewski-Weiss-McClure parameterization [15] of relevant couplings γ_0 to γ_4. (**B**) Schematic of the hexagonal Brillouin zone with two inequivalent valleys $\mathrm{K}^{(\prime)}$ shwoing the momentum $\mathbf{p}$ measured from the center of the valley K. (**C**) Schematic of the unit cell of ABC-stacked trilayer graphene, (**D**) ABA-stacked trilayer graphene, and (**E**) bernal stacked bilayer graphene. In (C), γ_2 describes a vertical coupling between sites B3 and A1 in different unit cells. Figure from Ref. 16. 38

3.14 **Comparison of the bandstructure of ABA- and ABC-stacked TLG.** (**A**) The predicted bandstructure of ABC trilayer graphene with (red) and without (green) the presence of a perpendicular electric field, as calculated within the tight-binding model described in Ref. 17. Transitions 1 and 2 are the strongest optical transitions near the K-point for electron doping. (**B**) The predicted bandstructure of ABA trilayer graphene with (red) and without (green) a perpendicular electric field, as calculated within the tight-binding model described in Ref. 17. The arrow indicates the transition responsible for the main absorption peak at 0.5-0.6 eV observed in Ref. 17. Figure from Ref. 17. 39

3.15 **Single-particle bandstructure of ABC-TLG/hBN.** (**A, B, and C**) Calculated single-particle bandstructure of ABC-TLG/hBN in the K valley for displacement fields $D/\epsilon_0 = 0.5$, 0, and $-0.5\ \mathrm{V/nm}$. At $D/\epsilon_0 = 0.5\ \mathrm{V/nm}$, a finite bandgap separates the conduction and valence minibands. The highest energy valence miniband is topologically trivial with $C = 0$. The bandgap closes at $D/\epsilon_0 = 0\ \mathrm{V/nm}$. At $D/\epsilon_0 = -0.5\ \mathrm{V/nm}$, the miniband invert to generate a new bandgap. The highest energy valence miniband becomes topologically nontrivial with a finite Chern number. The minibands of the K' are time-reversed pairs of the K valley minibands and have opposite Chern numbers. 40

3.16 **Optical image of previously studied ABC-TLG/hBN moiré superlattice device.** Optical image of a dual-gated ABC-TLG/hBN moiré superlattice device. The bottom hBN crystal is aligned with the ABC-TLG in this device. Figure from Ref. 2. 42

3.17 **Gate-dependent resistivity of ABC- and ABA-TLG.** (**A**) Resistivity of ABC-TLG as a function of V_{tg} varying V_{bg} from -50 V to 50 V. (**B**) Resistivity of ABA-TLG as a function of V_{bg} varying V_{tg} from -3 V to 3 V. Data were obtained at $T = 50$ K. Figure from Ref. 2. 42

3.18 **Landau fan of ABC- and ABA-TLG/hBN moiré superlattices.** (**A**) Landau fan of ABC-TLG/hBN showing well-resolved quantum Hall states at filling factors $\nu = 6$, 10, 14, 18..., unambiguously confirming that the ABC-stacking has been retained in this device. (**B**) ABA-TLG is characterized by two sets of Landau levels, one from the bilayer-like subband and the other from the monolayer-like subband. The Landau levels of the bilayer-like and monolayer-like subbands are marked by solid and dashed lines, respectively. Figure from Ref. 2. 43

3.19 **Transport of gate-tunable Mott state.** (**A, B**) Top-gate-dependent resistivity of ABC-TLG/hBN moiré superlattice when (A) $V_{bg} = 0$ V and (B) 20 V. (**C**) Resistance as a function of V_{tg} and V_{bg}. The color scale is from 10 Ω to 100 kΩ in a logarithmic scale. The highlighted straight lines correspond to the charge-neutrality point (CNP), 1/4 filling, 1/2 filling, fully-filled point (FFP) and 3/2 filling resistance peaks. (**D**) Resistivity at the CNP (green), 1/4 filling on the hole side (red) and 1/2 filling on the hole side (blue) as a function of the displacement field D. The insulating behavior at 1/4 and 1/2 fillings, corresponding to one and two charges per lattice site, provide the defining signature of a Mott insulator. Figure from Ref. 2. 44

3.20 **Landau fan of ABC- and ABA-TLG/hBN moiré superlattices.** R_{xx} and R_{xy} as a function of n/n_s and fixed $D = 0.4\ \mathrm{V/nm}$ and $B = 1$ T. At fixed D, the band structure does not change while tuning the carrier density. There are resistance peaks at 1/4, 1/2, and full fillings in R_{xx} and zero R_{xy} corresponding to zero Hall density. n_s corresponds to one electron per unit cell. Figure from Ref. 2. 45

4.1 **Trilayer graphene/hBN moiré superlattice.** (**A**) Optical image of ABC-TLG/hBN device 1 with the top and bottom gates. Scale bar is 3 $\mu\mathrm{m}$. (**B**) A schematic of the triangular ABC-TLG/hBN moiré superlattice and the 1/4-filling correlated insulating state, which corresponds to one hole per superlattice unit cell. (**C**) The single-particle energy dispersion of the lowest electron and hole minibands in the ABC-TLG/hBN superlattice with an effective potential energy difference between the bottom and top graphene layers of $2\Delta = -20\ \mathrm{meV}$, which can be generated by a vertical displacement field of $-0.4\ \mathrm{V/nm}$. It features a narrow and isolated hole miniband, shown highlighted in red. The first electron miniband is highlighted in blue. 48

4.2 **Correlated insulators in trilayer graphene/hBN moiré superlattice.** (**A**) R_{xx} as a function of carrier density shows prominent correlated insulating states at 1/4 and 1/2 fillings with $D = -0.4\ \mathrm{V/nm}$ at $T = 5$ K. (**B**) R_{xx} as a function of V_{tg} and V_{bg} at $T = 5$ K. The resistance peaks at 1/4 and 1/2 fillings of the first hole miniband can be clearly identified for relatively large D. 49

4.3 **Signatures of superconductivity in ABC-TLG/hBN.** (**A**) The $R_{xx} - T$ curve at $D = -0.54\ \mathrm{V/nm}$ and $n = -5.4 \times 10^{11}\ \mathrm{cm}^{-2}$ shows characteristic behavior of a superconducting transition. An empirical fit to the Aslamazov-Larkin formula (red line) yields an estimated superconducting transition temperature of $0.65\ \mathrm{K}$. (**B**) $I - V$ curves at different temperatures show a plateau below the critical current at about $10\ \mathrm{nA}$ for temperatures below $0.3\ \mathrm{K}$. This plateau region tilts and becomes close to linear at higher temperature, characteristic of a superconducting transition. (**C**) $dV_{xx}/dI - I$ curves at different temperatures. A critical current of about $10\ \mathrm{nA}$ is observed at the lowest temperatures. 50

4.4 **Searching for coherent oscillations.** (**A**) The dV_{xx}/dI color plot as a function of direct current (DC) bias and perpendicular magnetic field at $T = 0.04\ \mathrm{K}$ (**B**) Line cuts of (A) at $B_\perp = 0$ T, 0.4 T, 0.7 T, and 2 T. (**C**) The dV_{xx}/dI color plot as a function of direct current (DC) bias and in-plane magnetic field at $T = 0.04\ \mathrm{K}$ (**D**) Line cuts of (C) at $B_\parallel = 0$ T, 0.4 T, 0.8 T, and 1.2 T. A symmetrized $V_{xx}(B) = [V_{xx}(B) + V_{xx}(-B)]/2$ is presented to removed any possible V_{xy} component in all panels 51

4.5 **Carrier-density-dependent phase diagram.** R_{xx} as a function of carrier density and temperature at (**A**) $D = -0.54\ \mathrm{V/nm}$ and (**B**) $D = -0.17\ \mathrm{V/nm}$. The superconducting phase emerges at low temperature near the 1/4-filling Mott state for $D = -0.54\ \mathrm{V/nm}$. Only the 1/2-filling Mott state exists for $D = -0.17\ \mathrm{V/nm}$, and no superconductivity exits at base temperature. Both the superconducting phase and the metallic phase show very small resistance values at base temperature, but they can be distinguished by the supercurent behaviour in the $I - V$ and $dI - dV$ curves and by the $R - T$ dependence (Fig. 4.6b vs. Fig. 4.6d). $R_0 = 380\ \Omega$. 52

4.6 **Tunable electronic phases with the displacement field.** (**A**) R_{xx} as a function of D and T at fixed doping $n = -5.2 \times 10^{12}\ \mathrm{cm}^{-2}$ relative to the CNP, corresponding to slight electron doping relative to 1/4-hole filling. D modifies the band structure of the minibands in ABC-TLG/hBN, and therefore the charge correlations. As a function of D, the system can be tuned across four different electronic states from left to right: superconducting, correlated resistive state, metal, and correlated insulating state. (**B-E**) Vertical line cuts of (A) at selected D values to illustrate the $R_{xx} - T$ behavior of different electronic states. (B) The metallic state at $D = 0\ \mathrm{V/nm}$ shows a low and constant resistance owing to the dominating impurity scattering. (C) The correlated insulating state at $D = 0.45\ \mathrm{V/nm}$ shows an increased resistance at lower temperature. (D) The superconducting state at $D = -0.59\ \mathrm{V/nm}$ shows a rapidly decreasing resistance to a constant residual value at lower temperature. (E) The transition region between $D = -0.28\ \mathrm{V/nm}$ and $D = -0.53\ \mathrm{V/nm}$ exhibits rather complex behavior, and we refer to it as a "correlated resistive state" because the overall resistance is relatively high compared with the metallic region. The state at $D = -0.32\ \mathrm{V/nm}$ shows a weak insulator-like behavior with increased reistance at the lowest temperatures, the state at $D = -0.4\ \mathrm{V/nm}$ show an almost constant but relatively large resistance value, and the state at $D = -0.45\ \mathrm{V/nm}$ displace a strange-metal-like behavior with an almost linear decrease of resistance at low temperature. 54

5.1 **Correlated states in near-magic-angle tBLG.** (Upper panel) Longitudinal resistance R_{xx} of the tBLG device (measured between contacts separated by 2.15 squares) as a function of carrier density n (shown on the top axis) and perpendicular displacement field D (left axis), which are tuned by the top- and back-gate voltages, at $2.1\ \mathrm{K}$. n is mapped to a filling factor relative to the superlattice density n_s, corresponding to one electrons per moiré unit cell, shown on the bottom axis. (Inset) Optical micrograph of the completed device. The scale bar is $5\ \mu\mathrm{m}$. (Lower panel) Line cut of R_{xx} with respect to n taken at $D/\epsilon_0 = -0.22\ \mathrm{V/nm}$ showing the resistance peaks at full filling of the superlattice, and additional peaks likely corresponding to correlated states emerging at intermediate fillings. Figure replicated from Ref. 18. 57

5.2 **Micrograph of the tBLG heterostructure.** A false color optical micrograph of the completed heterostructure (before lithography) demonstrates the rotational alignment of the top hBN layer and graphene. The arrow labeled 'G' indicates a crystallographic edge of the top graphene layer of the tBLG while the arrow labeled 'hBN' indicates a crystallographic edge of the top encapsulating hBN crystal. Based on this micrograph, the alignment of the crystallographic edge of the top hBN to that of top graphene of the tBLG is consistent with the experimentally measured angle of $\theta_{\mathrm{hBN}} = 0.83^\circ \pm 0.02^\circ$ (calculated based on the density corresponding to the peak we associate with the hBN moiré pattern; see Fig. 5.1). The bottom hBN is far from rotational alignment with the bottom graphene layer of the tBLG. 59

5.3 **Displacement field dependence from separate cooldown.** Longitudinal resistance R_{xx} of the tBLG device (measured between contacts separated by 2.15 squares at 40 mK) as a function of carrier density n (shown on the top axis), filling factor relative to the superlattice density n_s (bottom axis), and the applied perpendicular displacement field D (left axis). . . . 59

5.4 **Displacement field dependence of superconducting tBLG device with misaligned hBN.** (**A**) An optical micrograph of the completed device. The scale bar is 20 $\mu\mathrm{m}$. (**B**) Longitudinal resistance R_{xx} of the misaligned tBLG device (measured between contacts separated by 1.25 squares at 1.5 K) as a function of carrier density n (shown on the top axis, or as a filling factor relative to the superlattice density shown on the bottom axis) and perpendicular displacement field D. We do not observe zero resistance as we are above the superconducting transition temperature, for a better comparison with Fig. 5.1. 60

5.5 **Emergent ferromagnetism near three-quarters filling.** (**A**) Magnetic field dependence of the longitudinal resistance R_{xx} (upper panel) and Hall resistance R_{yx} (lower panel) with $n/n_s = 2.984$ and $D/\epsilon_0 = -0.62$ $\mathrm{V/nm}$ at 30 mK, demonstrating a hysteretic anomalous Hall effect resulting from emergent magnetic order. The solid and dashed lines correspond to measurements taken while sweeping the magnetic field B up and down, respectively. (**B**) Zero-field anomalous Hall resistance R_{yx}^{AH} (red) and ordinary Hall slope R_{H} (blue) as a function of n/n_s for $D/\epsilon_0 \approx -0.6$ $\mathrm{V/nm}$. R_{yx}^{AH} is peaked sharply with a maximum around $n/n_s = 3.032$, coincident with R_{H} changing sign. These parameters are extracted from line fits of R_{yx} versus B on the upward and downward sweeping traces in a region where the B-dependence appears dominated by the ordinary Hall effect. The error bars reflect fitting parameter uncertainty along with the effect of varying the fitting window, and are omitted when smaller than the marker. (**C**) Temperature dependence of R_{yx} versus B at $D/\epsilon_0 = -0.62$ $\mathrm{V/nm}$ and $n/n_s = 2.984$ between 46 mK and 5.0 K, showing the hysteresis loop closing with increasing temperature. Successive curves are offset vertically by 20 kΩ for clarity. (**D**) Coercive field and anomalous Hall resistance (extracted using the same fitting procedure as above) plotted as a function of temperature from the same data partially shown in (C). Data in Fig. 5.5 were taken during a separate cooldown from that of the data in the rest of the figures, but show representative behavior [18] 62

5.6 **Temporal stability of the magnetization.** (**A**) Hall resistance R_{yx} at $n/n_s = 2.984$ and $D/\epsilon_0 = -0.52$ $\mathrm{V/nm}$ as a function of time over the course of 6 hours in zero field, after first magnetizing the sample by applying -500 mT and then returning the field to 0 T. (**B**) A full hysteresis loop taken prior to the measurement shown in (A) is displayed in red. The blue trace shows the behavior of R_{yx} as the field is swept from 0 to 500 mT following the measurement in (A). A clear anomalous Hall jump in the blue trace is comparable to those in the continuous red loop, indicating that the magnetization was stable through the 6 hour pause. 63

5.7 **Repeated hysteresis loops.** Longitudinal resistance R_{xx} (top panel) and Hall resistance R_{yx} (bottom panel) are shown as a function of magnetic field for twelve consecutive loops of the field between ± 250 mT for $n/n_s = 3.032$ and $D/\epsilon_0 = 0$ V/nm (in the same cooldown as that of Fig. 5.3). The solid and dashed lines correspond to measurements taken while sweeping the magnetic field B up and down, respectively. 64

5.8 **Displacement field dependence of hysteresis loops.** Longitudinal resistance R_{xx} (upper panel) and Hall resistance R_{yx} (lower panel) at $n/n_s = 2.996$ for two different displacement fields as labeled in the figure. Although tuning the displacement field from a large negative field to near zero causes a slight change in the longitudinal resistance and the hysteresis loop structure, the tBLG magnetic field dependence remains hysteretic. 66

5.9 **Density dependence near $3/4$ with fixed displacement field at 2.1 K.** (**A**) Zero-field anomalous Hall resistance R_{yx}^{AH} (red) and ordinary Hall slope R_{H} (blue) as a function of n/n_s while maintaining a constant displacement field $D/\epsilon_0 = -0.22$ V/nm. R_{yx}^{AH} is peaked at $n/n_s = 3.096$, close to the position of the peak at 0.758 in Fig. 5.5B and again coincident with a sign change in R_{H}. The full width at half maximum is slightly increased, at 0.07 instead of 0.04. (**B**) Magnetic field dependence of the longitudinal resistance R_{xx} (upper panel) and Hall resistance R_{yx} (lower panel) at $n/n_s = 3.096$, the largest hysteresis loop of the series shown in (A), with $R_{yx}^{\mathrm{AH}} = 10.4\ \mathrm{k}\Omega$. 67

5.10 **Nonlocal resistances providing evidence of chiral edge states.** Three- and four- terminal nonlocal resistances $R_{54,14}$ and $R_{54,12}$, measured at 2.1 K with $D/\epsilon_0 = -0.22$ V/nm, are shown in the upper and lower panels, respectively. For $n/n_s = 2.9$ (blue) away from the peak in AH resistance R_{yx}^{AH}, the nonlocal resistances are consistent with diffusive bulk transport. However, with $n/n_s = 2.996$ (red) in the magnetic regime where R_{yx}^{AH} is maximal, large, hysteretic nonlocal resistances suggest chiral edge states are present. The inset schematics display the respective measurement configurations. Green arrows in the upper inset represent the apparent edge state chirality for positive magnetization, while in the lower inset they reflect negative magnetization. 69

5.11 **Current-driven switching of the magnetization.** Differential Hall resistance dV_{yx}/dI measured with a 5 nA AC bias as a function of an applied DC current I_{DC} at 2.1 K with $D/\epsilon_0 = -0.22$ V/nm and $n/n_s = 2.996$. Note that dV_{yx}/dI is plotted against $-I_{\mathrm{DC}}$ for better comparison with magnetic field hysteresis loops. After magnetizing the sample in a -500 mT field and returning to $B = 0$, I_{DC} was swept from 0 to -50 nA (black trace), resulting in dV_{yx}/dI changing sign. Successive loops in I_{DC} between ± 50 nA demonstrate reversible and repeatable switching of the differential Hall resistance (red and blue, with solid and dashed traces corresponding to opposite sweep directions). 72

5.12 **Current-driven switching in nonzero magnetic field, and characterization of the transition.** (**A**) Hysteresis loops of the differential Hall resistance dV_{yx}/dI with respect to DC current (plotted as $-I_{\text{DC}}$ as in Fig. 5.11) at three different static magnetic fields after the sample was magnetized at $500\ \text{mT}$. These data were taken at $35\ \text{mK}$ with $n/n_s = 2.996$ and $D/\epsilon_0 = -0.22\ \text{V/nm}$ during the same cooldown as for the data of Fig. 4. (**B**) Transition rate of the apparent magnetization switching at a fixed current I_{DC} after magnetizing the sample with a $-75\ \text{nA}$ current (at $T = 2.1\ \text{K}$ and zero field). The transition appears to be a memoryless process. 72

5.13 **Displacement field dependence near $n = 3n_s$.** (**A**) Longitudinal resistance R_{xx} as a function of both n and D. Panel is a zoomed in portion of Fig. 5.1 centered near $n = 3n_s$. (**B**) Line cuts of (A) showing R_{xx} as a function of n at three different displacement fields. . 74

5.14 **Hysteresis loops at large a positive displacement field.** Magnetic field dependence of R_{yx} for a displacement field of $D/\epsilon_0 = 0.59\ \text{V/nm}$ and charge densities of (**A**) $3.04n_s$, (**B**) $3.12n_s$, (**C**) $3.16n_s$, and (**D**) $3.24n_s$. Measurements are performed at 2.16 K. 74

5.15 **Behavior of the conductivity tensor.** (**A**) The longitudinal conductivity σ_{xx} is plotted parametrically against the Hall conductivity σ_{yx} for a series of measurements at different temperatures with the density fixed at $n/n_s = 2.984$ and $D/\epsilon_0 = -0.62\ \text{V/nm}$ (shown in Fig. 5.5C). All conductivity values in this figure have been extracted from resistance measurements taken at $50\ \text{mT}$ when sweeping the applied field downward from a value larger than the coercive field (so the sample has been magnetized by an upward field). The resistivity is derived from the measurements by assuming a homogeneous sample, and the conductivities are given by $\sigma_{xx} = \rho_{xx}/\left(\rho_{xx}^2 + \rho_{yx}^2\right)$ and $\sigma_{xy} = \rho_{yx}/\left(\rho_{xx}^2 + \rho_{yx}^2\right)$. The relationship between σ_{xy} and σ_{xx} is not consistent with an extrinsic AH effect resulting from skew scattering. (**B**). Arrhenius plot of σ_{xx} on a log scale versus $1/T$, with the same data shown in (A). The blue curve shows a fit of the data for $4.9\ \text{K} > T \geq 2.5\ \text{K}$ (the points shown in blue) to a model of activated conductivity with an additional, temperature-independent conduction channel (data points shown in red are excluded from the fit), yielding an estimated activation scale of $T_0 = 43\ \text{K}$. (Inset) σ_{xx} is plotted on a linear scale against temperature. (**C**) σ_{xx} is plotted parametrically against σ_{xy} for a series of measurements at different densities at $T = 2.1\ \text{K}$, with $D/\epsilon_0 = -0.22\ \text{V/nm}$. These data were obtained during the same cooldown as that of the data shown in Figs. 5.1, 5.10, and 5.11. Again, the behavior appears inconsistent with skew scattering. Moreover, it is qualitatively similar to the density dependence of the conductivity in a magnetic topological insulator approaching a QAH effect shown in Ref. 19. (**D**) σ_{xx} as a function of n/n_s, from the same data as in (C), showing the emergence of a dip in σ_{xx} around $n/n_s = 3$ consistent with the approach to a Chern insulator state. 78

5.16 **Angular dependence of magnetic hysteresis loops.** Magnetic field dependence of the Hall resistance R_{yx} with $n/n_s = 2.984$ and $D/\epsilon_0 = -0.30\ \mathrm{V/nm}$ at 29 mK as a function of the angle of the device relative to the field direction; $0°$ corresponds to field in the plane of the sample. The hysteresis loops are plotted as a function of (a) the applied field and (b) the component of the field perpendicular to the plane of the sample. The solid and dashed lines correspond to sweeping the magnetic field B up and down, respectively. 82

5.17 **Hysteresis loops for nearly in-plane fields.** Angular dependence of R_{yx} vs B with $n/n_s = 2.984$ and $D/\epsilon_0 = -30\ \mathrm{V/nm}$ for angles of the field relative to the plane of the sample: (a) $4.71° \pm 0.10°$, (b) $1.82° \pm 0.10°$, (c) $0.85° \pm 0.10°$, (d) $+0.223° \pm 0.049°$, and $-0.171° \pm 0.025°$. All traces were taken at $27\ \mathrm{mK}$ except for the trace with tilt angle $+0.223° \pm 0.049°$, which was taken at $1.35\ \mathrm{K}$. 83

5.18 **Erasing the initial magnetic state.** In-plane hysteresis loops of R_{yx} with $n/n_s = 2.984$ and $D/\epsilon_0 = -30\ \mathrm{V/nm}$ at $26\ \mathrm{mK}$. The sample is initially polarized with an out-of-plane field. The sample is then rotated to $-57 \pm 21\ \mathrm{mdeg}$ in zero magnetic field. The field $B_{\|}$ is then increased from zero (red trace) before completing a hysteresis loop (blue traces). 84

5.19 **Tunable Chern bands in ABC-TLG/hBN moiré superlattice.** Color plot of the longitudinal resistivity ρ_{xx} as a function of V_t and V_b at $T = 1.5$ K. The arrows show the direction of changing doping n and displacement field D, respectively. In addition to the band insulating states (characterized by the resistance peaks) at the charge neutral point (CNP) and fully filled point (FFP), tunable correlated insulator states also emerge at 1/4 and 1/2 filling of the hole minibands at large displacement field $|D|$. It has been predicted theoretically [4, 20] that the hole miniband is topical (that is, Chern number $C \neq 0$) for $D < 0$ and trivial ($C = 0$) for $D > 0$. The inset shows the optical image of the device. In this device, the graphene is aligned with the bottom hBN (this is opposite to the device discussed in Ch. 4, which leads to an overall flipping of the gate map with respect to the sign of D). The Hall bar is $1\ \mu\mathrm{m}$ wide. 87

5.20 **Landau fan at $D = 0\ \mathrm{V/nm}$.** Longitudinal resistivity ρ_{yx} as a function of carrier density and magnetic field at displacement field $D = 0\ \mathrm{V/nm}$. Clear Landau levels develop from the charge neutrality point and fully filled points, which is direct evidence of the high quality of the encapsulated ABC-TLG device. The first resolved quantum Hall state of the charge neutrality point is $\nu = 6$. This Landau fan diagram establishes conclusively that we have ABC trilayer graphene in the hBN encapsulated device; it is completely different from the Landau fan diagram of ABA trilayer graphene (see Ref. 2). 89

5.21 **Quantum Hall effect from the correlated $C = 2$ Chern insulator.** (**A, C**) Color plot of (A) ρ_{xx} and (C) ρ_{yx} as a function of carrier density and magnetic field for the topological hole miniband at $D = -0.5\ \mathrm{V/nm}$ and $T = 0.06\ \mathrm{K}$. The experimental data at $T = 1.5\ \mathrm{K}$ are qualitatively similar. (**B, D**) Corresponding (B) ρ_{xx} and (D) ρ_{yx} plots for the trivial hole miniband at $D = 0.4\ \mathrm{V/nm}$ and $T = 1.5\ \mathrm{K}$. n_s corresponds to the carrier density of the 1/4 filling of the first miniband. No quantum Hall signatures are present in the trivial hole miniband, whereas a $\nu = 2$ quantum Hall effect characterized by a minimum of ρ_{xx} and a quantized ρ_{yx} emerges from 1/4 filling of the topological hole miniband. (**E, F**) Horizontal line cuts of (A) and (C), respectively. (E) shows that ρ_{yx} is well quantized beyond $B = 0.4$ T. An offset of $2.5\ \mathrm{k\Omega}$ is applied for each trace in (F) (**G**) Line cut of ρ_{xx} and ρ_{yx} along the quantum Hall state (denoted by the dashed lines in (A) and (E)) shows that ρ_{yx} reaches a quantized value of $\nu = 2$ at 0.4 T, and a large ρ_{yx} persists down to zero magnetic field. It represents a quantum anomalous Hall state for the $C = 2$ correlated Chern insulator at $1/4$ filling. The inset shows a zoomed-in plot of ρ_{yx} at small magnetic field. 90

5.22 **Anomalous Hall effect and ferromagnetism.** (**A-C**) Arrhenius plot of the (A) longitudinal resistivity ρ_{xx}, (B) longitudinal conductivity σ_{xx}, and (C) the estimated gap at different magnetic field Δ. A manual offset of -0.15 is applied between each curve in (A) and (B). The gap size in (C) is extracted from the linear fit of $\sigma_{xx} \propto e^{-\Delta/2k_BT}$ (red line) in (B). We note that the Arrhenius plot is only valid for a limited temperature range, suggesting deviation from the thermal activated behavior at low temperatures. Therefore, the estimated gaps have relatively large uncertainty. However, the qualitative behavior is robust: insulating behavior is observed at all magnetic fields, and the quantized Hall insulator at finite magnetic field connects smoothly with the anomalous Hall insulator at zero magnetic field, supporting the identification of the state as a Chern insulator. 92

5.23 **Anomalous Hall effect and ferromagnetism.** (**A**) Magnetic-field-dependent ρ_{yx} at $1/4$ filling and $D = -0.5\ \mathrm{V/nm}$ at different temperatures. The Hall resistivity displace a clear anomalous Hall signal with strong ferromagnetic hysteresis. At the base temperature of $T = 0.06\ \mathrm{K}$, the anomalous Hall signal can be as large as $\rho_{yx}^{\mathrm{AH}} = 8\ \mathrm{k\Omega}$ and the coercive field is $B_c = 30\ \mathrm{mT}$. The inset shows the extracted coercive field B_c and anomalous Hall signal ρ_{yx}^{AH} as a function of temperature. (**B**) The evolution of ρ_{xx}, B_c, and ρ_{yx}^{AH} as a function of hole doping at $D = -0.5\ \mathrm{V/nm}$ and $T = 0.06\ \mathrm{K}$. The strongest anomalous Hall signal is observed close to $n = n_s$. (**C**) The evolution of ρ_{xx}, B_c, and ρ_{yx}^{AH} as a function of the displacement field D at $n = n_s$ and $T = 0.06\ \mathrm{K}$. The strongest anomalous Hall signal is observed when the device is most insulating (that is, largest ρ_{xx}). 93

5.24 **Calculated Chern number including the electron-electron interaction effects.** (**A, B**) Calculated single-particle band structure of the ABC-TLG/hBN moiré superlattice for $\Phi = -25\ \mathrm{meV}$ and $25\ \mathrm{meV}$, respectively. Here Φ is the energy difference between the top and bottom layers of the ABC-TLG, and $\Phi = -25\ \mathrm{meV}$ corresponds to the vertical displacement field around $D = -0.5\ \mathrm{V/nm}$. The red line highlights the topological hole miniband for $\Phi = -25\ \mathrm{meV}$. (**C**) Calculated Chern number of the hole miniband as a function of the energy difference Φ and the effective dielectric constant ϵ_{hBN} after including the electron-electron interaction effects using the Hartree-Fock approximation. The resulting band Chern number can be 2 for parameters close to the experimental device where $\Phi \approx -25\ \mathrm{meV}$ and $\epsilon_{\mathrm{hBN}} \approx 4$. 95

6.1 **Longitudinal resistance of ABC-TLG/hBN.** Longitudinal resistance $R_{xx} = V_{xx}/I$ as a function of band filling factor n/n_s and vertical displacement field D at $T = 1.5$ K. In addition to the band insulating states at the charge neutrality point ($n = 0$) and the fulling filled point ($n = -4n_s$), correlated insulator states emerge at $1/4$ filling ($n = -n_s$) and $1/2$ filling ($n = -2n_s$) at finite $|D|$. 97

6.2 **Longitudinal and Hall resistances at selected values of *D*.** (**A and B**) Longitudinal resistance R_{xx} as a function of band filling at $D = 0.4\ \mathrm{V/nm}$ and $-0.47\ \mathrm{V/nm}$, respectively. (**C and D**) Corresponding color plots of the Hall resistance as a function of band filling and perpendicular magnetic field. For (C) $D = 0.4\ \mathrm{V/nm}$, the Hall resistance tends to be small for all doping and no ferromagnetic signature is observed (the relatively large signals at $n = -n_s$ and $n = -2n_s$ in (C) are artifacts coming from crosstalk from the large R_{xx}, evinced by the observation that they do not change sign when the magnetic field is reversed). For (D) $D = -0.47\ \mathrm{V/nm}$, the Hall resistance is very large at weak magnetic fields and can persist down to zero magnetic field at $n = -n_s$ and $n = -2.3n_s$ (denoted by the two dashed vertical lines). The non-zero values of R_{yx} at $B = 0$ represents AH signals from ferromagnetic states at $n = -n_s$ and $n = -2.3n_s$. The state at $n = -n_s$ has been identified as a $C = 2$ Chern insulator state (two oblique solid lines) with orbital ferromagnetism [21]. The AH at $n = -2.3n_s$ results from a new magnetic state that emerges at non-integer filling of the topological hole miniband. 99

6.3 **Anomalous Hall effect at non-integer filling.** (**A and B**) R_{yx} and R_{xx} as functions of band filling and displacement field, respectively, for the valence miniband at $B = 0.2$ T and $T = 0.07$ K. The dashed oval outlines a region with large R_{yx} signals at very small field between $n = -2.1n_s$ and $2.6n_s$ and between $D = -0.4$ and -0.53 V/nm (more detail is given in Fig. 6.4). The oval region also shows enhanced R_{xx} in (B), suggesting that the ferromagnetic phase is insulating (**C and D**) Magnetic-field dependent antisymmetrized ρ_{yx} and symmetrized ρ_{xx} ad different temperatures for the ferromagnetic state with largest AH at the center of the oval region ($n = -2.3n_s$ and $D = -0.48$ V/nm). The AH signal shows clear ferromagnetic hysteresis in (C), reaching $\rho_{yx}^{\mathrm{AH}} = -4.8$ k$\Omega$and a coercive field of $B_c = 0.04$ T at $T = 0.07$ K. (**E and F**) The evolution of ρ_{yx}^{AH} and σ_{xx} as a function of temperature at $n = -2.3n_s$ and $D = -0.48$ V/nm. The amplitude of ρ_{yx}^{AH} decreases with increasing T, vanishing around 1.6 K, while σ_{xx} increases with increasing T. 100

6.4 **Tunable anomalous Hall effect at non-integer filling.** (**A**) The D-dependent ferromagnetism at $n = -2.5n_s$. The AH resistance is maximal at $D = -0.48$ V/nm, becomes zero at $D = -0.38$ V/nm, and then reappears with a sign change at $D = -0.37$ V/nm. The ρ_{yx} signals at $D = -0.49$, -0.48, and -0.43 V/nm are manually multiplied by a factor of 0.1 for clarity. (**B**) The n-dependent ferromagnetism at fixed $D = -0.39$ V/nm. The AH signal reaches a maximum at $n = -2.48n_s$, becomes nearly zero at $n = -2.38n_s$, and reappears with a sign change at $n = -2.31n_s$. Although the hysteresis is gone at $n = -2.2n_s$, the strongly nonlinear dependence indicates a large AH; AH vanishes at less negative n. Each curve in (A and B) is offset for clarity, and the dashed lines denote zero ρ_{yx}. (**C**) The individual squares represent measured AH resistance, with color scale shown in the lower left corner. The circles represent data with no measurable AH. 102

6.5 **Additional hysteresis loops.** R_{yx} as a function of magnetic field at (**A**) fixed $n = -2.3n_s$ for various D, (**B**) at fixed $n = -2.5n_s$ for various D, (**C**) at fixed $D = -0.39$ V/nm for various n, and (**D**) at fixed $D = -0.46$ V/nm for various n. Each curve is offset for clarity, with the dashed line of the same color denoting $R_{yx} = 0$ for that data set. The dashed line is often not located at the center of the corresponding AH loop due to cross-talk of R_{xx} because of inhomogeneity. The traces annotated with an adjacent 'x0.1' are manually multiplied by a factor of 0.1. 103

6.6 **Behavior of the conductivity tensor at $B = 0$ T.** (**A**) The longitudinal conductivity σ_{xx} is plotted parametrically against the Hall conductivity σ_{xy} for a series of measurements at different temperatures with the density and displacement field fixed at $n = -2.3n_s$ and $D = -0.48$ V/nm. (**B**) σ_{xx} is plotted parametrically against σ_{xy} for a series of measurements at different densities for fixed temperature $T = 0.07$ K and displacement field $D = -0.48$ V/nm. (**C**) Arrhenius plot of σ_{xx} on a log scale versus $1/T$. (**D**) σ_{xx} and σ_{xy} as functions of carrier density, from the same data as in (B), showing the emergence of a dip in σ_{xx} accompanied by the σ_{xy} maximum around $n = -2.3n_s$. 105

6.7 **Peak in anomalous Hall at non-integer filling.** Zero-field anomalous Hall resistance R_{yx}^{AH} (red) and ordinary Hall slope R_{H} (black) as a function of n/n_s for $D/\epsilon_0 = -0.22$ V/nm. R_{yx}^{AH} is peaked with a maximum around $n/n_s = 3.08$, coincident with R_{H} changing sign. Additionally, we observe a second peak in R_{yx}^{AH} at $n/n_s = 3.5$ that is approximately $1/3$ the height of the main peak. This secondary peak is coincident with a strong dip in R_{H}. 107

A.1 **vdWs transfer station.** Sample side (left) and stamp side (right) micromanipulator assembly that comprise the vdWs transfer station. The base is a 1 in optical breadboard. 113

A.2 **Isolating transfer station from pump vibrations.** Without any isolation, the vibrations of the diaphragm pump (shown on the left) would couple through the vacuum line to the transfer station, negatively impacting transfer quality. To mitigate this, the vacuum line is run through a 5 gallon bucket filled with sand (shown on the right). 114

C.1 **Simulating a two-terminal bar.** Electrons propagate along a bar of length L and width w. The injector (left) and ground (right) are assumed to be perfect ohmic contacts. A virtual line placed a distance several times thew width of the bar away from the injection point is used to calculate backward scattered electrons. 118

D.1 **Quantum oscillations of tBLG at fixed displacement field.** (**A**) Landau fan diagram of the longitudinal resistance R_{xx} taken at 2.1 K for a fixed displacement field $D/\epsilon_0 = 0$ V/nm. Emerging from the CNP, we observe the Landau levels $\nu = \pm 2, \pm 4$. We further observe Landau levels from $n/n_s = 1/2$ of $\nu = 2, 4$, from $n/n_s = 3/4$ of $\nu = 1, 4$, and the sequence from $n/n_s = -1$ of $\nu = -8, -12, -16, -20$. (**B**) Schematic of the Landau levels observed in (A). 119

D.2 **Angular dependence of longitudinal Resistance in magnetic hysteresis loops.** Magnetic field dependence of the longitudinal resistance R_{xx} corresponding to the data shown in Fig. 5.16, with $n/n_s = 2.984$ and $D/\epsilon_0 = -0.30\ \mathrm{V/nm}$ at $29\ \mathrm{mK}$ as a function of the angle of the device relative to the field direction; 0° corresponds to field in the plane of the sample. The hysteresis loops are plotted as a function of (a) the applied field and (b) the component of the field perpendicular to the plane of the sample. The solid and dashed lines correspond to sweeping the magnetic field B up and down, respectively. 121

D.3 **Hysteresis loops for nearly in-plane fields.** Angular dependence of the longitudinal resistance R_{xx} vs B corresponding to the data shown in Fig. 5.17 with $n/n_s = 2.984$ and $D/\epsilon_0 = -30\ \mathrm{V/nm}$ for angles of the field relative to the plane of the sample: (a) $4.71^\circ \pm 0.10^\circ$, (b) $1.82^\circ \pm 0.10^\circ$, (c) $0.85^\circ \pm 0.10^\circ$, (d) $+0.223^\circ \pm 0.049^\circ$, and $-0.171^\circ \pm 0.025^\circ$. All traces were taken at $27\ \mathrm{mK}$ except for the trace with tilt angle $+0.223^\circ \pm 0.049^\circ$, which was taken at 1.35 K. 121

D.4 **Erasing the initial magnetic state.** In-plane hysteresis loops of the longitudinal resistance R_{xx} corresponding to the data shown in Fig. 5.18 with $n/n_s = 2.984$ and $D/\epsilon_0 = -30\ \mathrm{V/nm}$ at $26\ \mathrm{mK}$. The sample is initially polarized with an out-of-plane field. The sample is then rotated to $-57 \pm 21\mathrm{mdeg}$ in zero magnetic field. The field $B_{||}$ is then increased from zero (red trace) before completing a hysteresis loop (blue traces). 122

D.5 **Antisymmetric component of in-plane hysteresis loop.** Antisymmetric component of the Hall resistance R_{yx}^{ASYM} corresponding to the Hall data shown in Fig. 5.18 with $n/n_s = 2.984$ and $D/\epsilon_0 = -30\ \mathrm{V/nm}$ at 26 mK. The initial up sweep has been omitted in this figure. . . 123

D.6 **Dependence on the magnitude of the in-plane field.** In-plane hysteresis loops of corresponding longitudinal resistance R_{xx} to the data shown in Fig. 5.18 with $n/n_s = 2.984$ and $D/\epsilon_0 = -30\ \mathrm{V/nm}$ at $26\ \mathrm{mK}$. The sample is initially polarized with an out-of-plane field. The sample is then rotated to $-57 \pm 21\mathrm{mdeg}$ in zero magnetic field. The field $B_{||}$ is then increased from zero (red trace) before completing a hysteresis loop (blue traces). The range of resistance shown in both panels is the same. 124

D.7 **Flipping a small out-of-plane field at small angles.** Magnetic field hysteresis loops where R_{yx} is measured at two small angles of opposite sign: $+172 \pm 29\ \mathrm{mdeg}$ in red and $-17 \pm 22\ \mathrm{mdeg}$ in blue. Both traces were taken at $28\ \mathrm{mK}$ with $n/n_s = 2.984$ and $D/\epsilon_0 = -30\ \mathrm{V/nm}$. The sample has been rotated in the plane by an angle of 20° relative the measurements performed in Fig. 5.17. 125

D.8 **In-plane field dependence of longitudinal resistivity.** Longitudinal resistivity ρ_{xx} as a function of carrier density n for several different in-plane magnetic fields at a fixed displacement field of $D/\epsilon_0 = -0.30\ \mathrm{V/nm}$ and 1.2 K for a tilt angle of $-62 \pm 23\mathrm{mdeg}$. 126

Chapter 1

Introduction

1.1 Designer van der Waals heterostructures

The electronic properties of many materials can be described by approximating electrons as non-interacting. However, in weakly dispersing electronic bands, electron-electron interactions can dominate the kinetic energy of the electrons, leading to a plethora of interesting strongly correlated ground states, such as magnetism and superconductivity, that attempt to minimize the mutual Coulomb repulsion between electrons. Theoretically modeling strongly correlated systems is quite challenging. Therefore, we often turn to experiments to guide theory. Until recently, the available strongly correlated systems have been predominantly grown materials such as the cuprates and iron pnictides. These materials can be grown as single crystals using flux or floating zone techniques or as thin films using molecular beam epitaxy. Significant effort has been made in searching for other strongly correlated systems, such as in heavy-fermion systems [22], Kagome lattices [23, 24], and Lieb lattices [25–27].

Recently developed techniques for fabricating heterostructures assembled of two-dimensional materials have enabled an entirely new class of strongly correlated materials, ushering in a new era for synthetic quantum materials. In this thesis, we will focus on heterostructures where the conductive material is graphene. With a particular thickness of $\mathrm{SiO_2}$ on Si as a substrate, it is quite easy to optically identify mechanically exfoliated monolayers of graphene deposited on the substrate [28]. At room temperature, graphene has the highest intrinsic electron mobility of any material. However, the first graphene devices that were fabricated directly on the $\mathrm{SiO_2}$/Si substrate were limited to mobilities of $\sim 25000\,\mathrm{cm^2/(V\,s)}$ at cryogenic temperatures due to the large density of charge disorder and significant surface roughness of $\mathrm{SiO_2}$ [29–32].

The development of first wet [33] then dry [34] transfer techniques for stacking van der Waals heterostructures assembled of exfoliated two-dimensional materials solves this issue, by encapsulating graphene in another layered material, hexagonal boron nitride (hBN), allowing for much higher mobility devices. hBN is an extremely clean and atomically flat insulator with a similar crystal lattice to graphene and with one to two orders of magnitude less charge disorder than $\mathrm{SiO_2}$ [29], allowing for dramatic improvements in the mobilities of graphene devices [33, 34]. hBN also has the added benefit of having a fairly high breakdown electric field [33]. We can then use hBN as a gate dielectric in encapsulated devices and deposit metallic gates directly on top of the heterostructure to tune the graphene's chemical potential. One can use graphite gates to produce even higher quality devices [35]. These high mobility sheets of graphene encapsulated in hBN have displayed unique and tunable electronic properties. For example, in a sheet of graphene at cryogenic temperatures, electrons can travel ballistically for tens of microns at 10^6 meters per second; the electrons effectively ignore each other.

Because we are physically stacking materials on top of each other when building a van der Waals heterostructure, we have two advantages over grown films: arbitrary materials can be stacked without worrying about lattice matching criteria and materials can be stacked with arbitrary relative orientations. The freedom to control orientation provides a new continuous experimental parameter we will explore in this thesis, namely the rotational alignment between to layers in a van der Waals heterostructure.

We begin by considering a graphene/hBN moiré superlattice: a sheet of graphene well aligned to a sheet of hBN. In such a system, one would reasonably expect the composite system to behave like any other sheet of monolayer graphene because the hBN is just acting as a dielectric. However, this is an oversimplification: hBN shares graphene's hexagonal lattice structure (with a slight lattice mismatch). If the two lattices are stacked with a slight twist, they can drift in and out of registry, forming a periodic pattern called a moiré superlattice, with a period much larger than the lattice constant of either layer. The size of the period depends inversely on the size of the twist between the lattices, which we will quantitatively describe in the next section. This new large artificial superlattice generates minibands that disperse at a finer energy scale over a mini Brillouin zone, that is significantly smaller than the original Brillouin zone of the graphene lattice. This results in the composite system having significantly different electronic properties than isolated monolayer graphene. Others have attempted to form superlattices by fabricating periodic patterns in the substrates of two-dimensional electron systems [36–38] or van der Waals heterostructures [39, 40]. While these systems have demonstrated evidence of Fermi surface reconstruction due to the superlattice potential, these techniques come at the cost of undermining the material quality. Fortunately, this is not the case in moiré superlattice.

Graphene/hBN moiré superlattice demonstrates the ability to tunably control the electronic properties of a heterostructure through the stacking orientation of different layers. Fascinating physics has been observed in graphene on hBN, particularly Hofstadter's butterfly which requires more than one magnetic flux quantum per superlattice unit cell (an experimental criterion that can only reasonably be achieved in moiré superlattices due to the large [but not too large] size of the unit cell) [35,41–44]. For a small enough twist angle, we can tune the chemical potential continuously through entire minibands without inducing extra disorder, something that is much more difficult in more conventional materials and often requires the use of chemical dopants. However, there are limitations to our ability to explore these minibands with conventional Hall bar devices. Previously, Ref. 6 used ballistic transport phenomena (in conjunction with theoretical modeling) in a graphene/hBN moiré superlattice two study the details of the miniband structure. Due to experimental limitations, this study was unable to extensively explore the region between the Van Hove singularities of the first and second valence bands. In Ch. 2, we will further expand on these ballistic transport measurements through the use of absorptive pinhole collimators [8]. These collimators, which consist of absorptive sidewalls between a pair of collinear slits, allow us to populate and detect a narrow window of k-states when transport is ballistic. This allows for clearer measurements at energies in-between these Van Hove singularities, where the Fermi surface is non-circular and would otherwise not result in clear transport signatures.

While graphene/hBN moiré superlattice have thus far shown no evidence of strongly correlated phenomena without the application of a magnetic field, there are a number of other avenues for creating superlattice systems that are good candidates for strongly correlated phenomena. In the remaining chapters of this thesis, we will focus on magic-angle twisted bilayer graphene (tBLG), a moiré superlattice formed between two sheets of monolayer graphene with a relative twist between the two layers of $\sim 1.05°$, and ABC-TLG/hBN moiré superlattice. Both systems exhibit flat electronic bands which are ideal playgrounds for exploring strongly correlated physics.

Pristine ABC-trilayer graphene has a cubic band structure ($\epsilon \propto |k|^3$ at low energy) and therefore has relatively flat dispersion at low energy. Signatures of strong correlations have already been observed in pristine ABC-trilayer [45]. In Chs. 3-6, we will discuss how using hBN to form a superlattice with ABC-trilayer graphene leads to minibands of very narrow bandwidth. We will see in Ch. 4 and Ch. 5 that at the appropriate integer number of carriers per moiré unit cell, the superlattice can become either what appears to be a superconductor or ferromagnetic. In Ch. 6, we will discuss an additional magnetic state at non-integer filling of the superlattice.

In Chs. 3-6, we will discuss tBLG, which was enabled by the development of recent fabrication techniques [46,47]. As both layers are now conductors, with the choice of a twist angle of $\sim 1.05°$ between the monolayer sheets, interlayer tunneling results in strongly hybridized minibands with a bandwidth that can be made small enough that electron correlations dominate [11,48]. In Ch. 5, I will show that a ferromagnetic ground state exists when the system is tuned to three electrons per moiré unit cell. In Ch. 6, we will discuss signatures of an additional magnetic state at non-integer filling of the moiré superlattice.

1.2 Moiré superlattice basics

Consider stacking two hexagonal lattices atop each other with a relative twist angle θ: one being graphene (which has a lattice constant $a \approx 0.2504\ \mathrm{nm}$) and the second being either another sheet of graphene or hBN (which has a lattice constant $a \approx 0.246\ \mathrm{nm}$ [49]). The primitive lattice vectors of the graphene lattice are typically written as [50]

$$\boldsymbol{a}_1^1 = \frac{a}{2}(3, \sqrt{3}), \quad \boldsymbol{a}_2^1 = \frac{a}{2}(3, -\sqrt{3}), \tag{1.1}$$

where the superscript is used to denote which of the two crystal lattices we are discussing. We position the second lattice at the B sites of the graphene lattice such that the A-B bonds are parallel. We then rotate the top lattice by θ. Its primitive lattice vectors are then [51]

$$\boldsymbol{a}_i^2 = \boldsymbol{MRa}_i^1 \quad (i = 1, 2), \tag{1.2}$$

where $\boldsymbol{R}$ is the matrix for rotation by θ and $\boldsymbol{M} = (1 + \delta)\mathbb{1}$ is to account for any difference in the lattice constants. For example, in the case of hBN atop graphene, $1 + \delta = a_{\mathrm{hBN}}/a \approx 1.018$.

We can now find the reciprocal lattice vectors of either lattice following the usual prescription that, for a given reciprocal lattice vector $\mathbf{b}_i$, $\mathbf{b}_i \cdot \mathbf{a}_j = 2\pi\delta_{ij}$. We obtain

$$\boldsymbol{b}_1^1 = \frac{2\pi}{3a}(1, \sqrt{3}), \quad \boldsymbol{b}_2^1 = \frac{2\pi}{3a}(1, -\sqrt{3}). \tag{1.3}$$

To study the moiré superlattice formed by the overlapping graphene lattices, we start by finding a single reciprocal lattice vector of the moiré superlattice, which is just the difference in the reciprocal lattice vectors of the two original lattices. Let's make our lives easier by applying a coordinate transformation such that our reciprocal lattice vectors are [52]

$$\tilde{\boldsymbol{b}}_1^1 = \frac{2\pi}{a}(1, 0), \quad \tilde{\boldsymbol{b}}_1^2 = \boldsymbol{MR}\tilde{\boldsymbol{b}}_1^1 = \frac{1}{1+\delta}\frac{2\pi}{a}(\cos\theta, \sin\theta). \tag{1.4}$$

Then a reciprocal lattice vector of the moiré superlattice is

$$\boldsymbol{k} = \tilde{\boldsymbol{b}}_1^1 - \tilde{\boldsymbol{b}}_1^2 = \frac{2\pi}{a}\left(1 - \frac{\cos\theta}{1+\delta}, \frac{-\sin\theta}{1+\delta}\right). \tag{1.5}$$

We now define the moiré lattice period,

$$\lambda = \frac{2\pi}{|\boldsymbol{k}|} = \frac{(1+\delta)a}{\sqrt{2(1+\delta)(1-\cos\theta)+\delta^2}}. \tag{1.6}$$

One important length scale to keep in mind is that for graphene atop hBN, the largest moiré lattice period we can obtain ($\theta = 0$) is 13.9 nm.

Experimentally, the typical signature we attribute to the existence of a moiré superlattice is an increase in longitudinal resistance at finite carrier density (relative to the charge neutrality point). Modeling our electrostatic gate as a parallel plate capacitor, then the density of such a feature is $n_s = C_g(V_s - V_0)/e$, where C_g is the geometric capacitance of the gate, V_s is the gate voltage at which the resistance feature occurs, V_0 is the gate voltage at which the charge neutrality point occurs, and e is the charge of an electron. In the absence of interactions, such a feature likely corresponds to a fully filled (empty) conduction (valence) band. Given the spin and valley degeneracy of these bands, each band can hold four electrons per moiré unit cell, $4n_s = 4/A$, where $A = \sqrt{3}\lambda^2/2$ is the area of the moiré unit cell. Then we find that

$$\lambda = \sqrt{\frac{2}{\sqrt{3}n_s}}. \tag{1.7}$$

Additionally, rearranging equation 1.6, we find

$$\theta = \pm\cos^{-1}\left(1+\frac{\delta^2}{2(1+\delta)}-\frac{(1+\delta)a^2}{2\lambda^2}\right) = \pm\cos^{-1}\left(1+\frac{\delta^2}{2(1+\delta)}-\frac{\sqrt{3}(1+\delta)n_s a^2}{4}\right). \tag{1.8}$$

These equations reduce significantly in the case of graphene on graphene because $\delta = 0$.

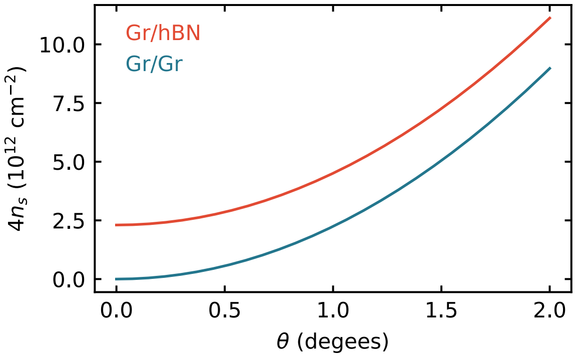

Figure 1.1: **Angular dependence of the superlattice density.** Four times the moiré superlattice density n_s corresponding to four electrons (holes) per moiré unit cell as a function of the relative twist angle between the two constituent crystal lattices forming the moiré superlattice. The two cases of graphene on hBN and on graphene are shown in red and blue, respectively.

We can use equation 1.8 to study quantitatively how n_s depends on θ (Fig. 1.1). For both graphene on graphene and graphene on hBN, the superlattice density is beginning to approach the upper limits of the range of densities achievable by electrostatic gating for a twist angle of 2°.

Chapter 2

Collimating graphene/hBN moiré superlattice Hall bar

2.1 Introduction

In ultraclean material systems at low temperature, electrons can travel ballistically for many microns. A small magnetic field can be treated semiclassically: the equations of motion for an electron in an out-of-plane magnetic field $\boldsymbol{B} = B\hat{z}$ are

$$\hbar v = \frac{\partial \varepsilon}{\partial k}, \quad \hbar \dot{\boldsymbol{k}} = -e\boldsymbol{E} + eB\hat{z} \times \boldsymbol{v}, \tag{2.1}$$

where e is the charge of an electron, $\boldsymbol{v}$ is the carrier velocity, and $\hbar\boldsymbol{k}$ is the carrier momentum. In the ballistic regime, there is negligible electric field in the bulk, therefore we assume that $\boldsymbol{E} = 0$. From these equations of motion, one can see that the shape of the cyclotron orbit in a two-dimensional metal is a 90° rotation of the shape of the Fermi surface. The size of this orbit scales inversely with the magnitude of the applied field. Electrons near the edge of the device may travel in skipping orbits drifting along the edge in a direction determined by the effective charge of the carrier [6]. It is somewhat surprising that these electron trajectories bunch along caustics, where they are focused onto equidistant points on the boundary (see Fig. 2.1B for an example of a circular Fermi surface). This effect is called transverse electron focusing (TEF) and has been used to study the Fermi surface in bulk materials [53, 54] and in two-dimensional systems [55, 56]. In our example of a circular Fermi surface, for a contact separated from a current injector by a distance L, TEF occurs for magnetic fields $B = 2jB_j\hbar k_F/ \pm eL$ (for $j = 1, 2, ...$) resulting in a series of peaks in the nonlocal resistance as a function of field (Fig. 2.1C). From such a trace, the Fermi momentum $\hbar k_F$ can be obtained if the shape of the Fermi surface is known and the sign of the effective charge $\pm e$ can be inferred.

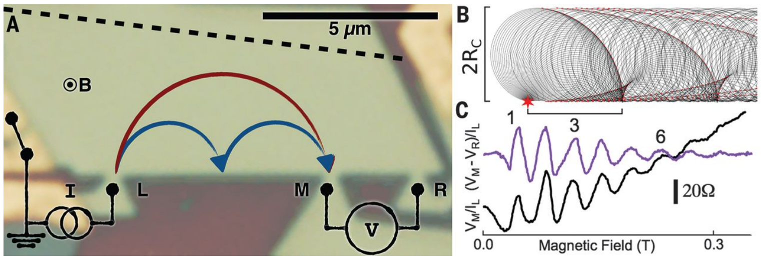

Figure 2.1: **Transverse electron focusing.** (**A**) Schematic of the experiment overlaid on a photo of the device. The hBN/graphene/hBN/few layer graphene heterostructure is shown in green, the $\mathrm{SiO_2}$ substrate is purple, and the dashed line denotes the upper edge of the graphene flake. In the electrical measurement configuration applied to obtain the data in Fig. 2.2B, the two leftmost contacts were grounded to act as absorbers. Current was injected into the left local contact L and the voltage difference between local contacts, M and R, was measured. Arrows depict skipping orbits a hole would take if injected at normal incidence with $B = B_1 \equiv 2\hbar k_e/eL$ (red) or $B_2 \equiv 4\hbar k_f/eL$ (blue). (**B**) Ensemble of simulated skipping orbits emanating from an emitter (red star). Electron trajectories bunch along caustics (red dashed curves) and focus onto an equidistant array of points at the boundary. Scale markers show the cyclotron diameters $2R_c = 2\hbar k_f/eB$. (**C**) Transverse electron focusing (TEF) spectra collected at a single voltage probe M (lower trace) and differentially between voltage probes M and R (upper trace), with $n = -1.1 \times 10^{12}\ \mathrm{cm}^{-2}$ and $T = 1.55$ K. The first, third and sixth focusing peaks are labeled. Taking the differential measurement of the spectrum does not shift the peak positions, because the device geometry partially shields R from being reached by skipping orbits from L, such that oscillations of the voltage at R are much weaker. Figure from Ref. 6.

It is possible to fabricate ultra-high quality graphene/hBN moiré superlattices (Fig. 2.1A), where transport at low temperatures is ballistic [6]. TEF electron focusing can then be measured as a function of carrier density and magnetic field (Fig. 2.2B). For carrier densities bounded by V_v^1 and V_c^1, the dispersion should be well approximated the Dirac cone of unperturbed graphene, where $k_F = \sqrt{\pi|n|}$. This appears to be the case as the data is consistent with the dashed curves which are are plotted according to $B_j = (2j\hbar/ \pm eL)\sqrt{\pi|n|}$ [56]. As many as eight focusing peaks are observed, confirming that transport is ballistic and carrier reflection at the boundary of the sample is quite specular (each peak should be lower than the last by a factor of the probability of diffuse scattering [53]).

The voltages V_v^1 and V_c^1 correspond to Van Hove singularities (VHS) in the first valence and conduction bands, respectively. Similarly, there are two additional VHSs, V_v^2 and V_c^2, beyond which TEF is recovered (Fig. 2.2B). The locations of these VHSs can be used fit the strength of the moiré perturbation and calculate the miniband structure (Fig. 2.2A). The TEF spectra for this bandstructure can then be shown to be consistent with the experimental data in regions were clear TEF is observed (Fig. 2.2C). However, in the regions bounded by the VHSs of the conduction or valence miniband, no clear TEF is measured. In fact, right at the VHS, the Fermi surface is open such that carriers follow a runaway trajectory, not skipping orbits, and TEF cannot be observed in a phenomena termed orbital switching [57].

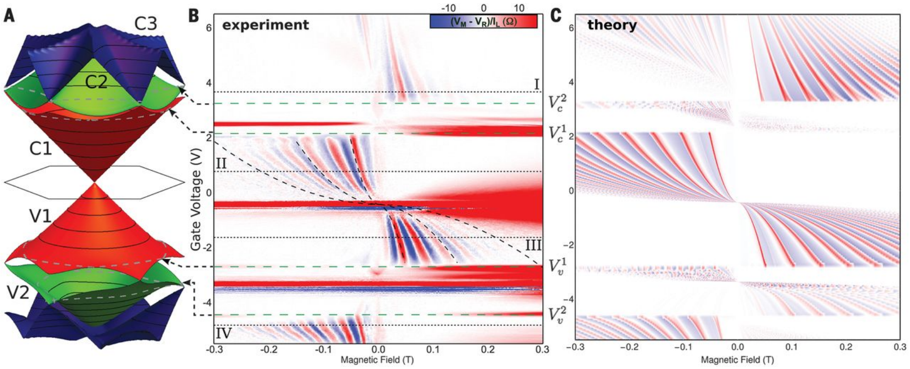

Figure 2.2: **TEF spectra at base temperature.** (**A**) Miniband structure of the graphene/hBN superlattice, calculated as in Refs. 6, 7. Each miniband for which TEF was observed is labeled. This dispersion results from a symmetric moiré perturbation: $\varepsilon^+ = 17\ \mathrm{meV}$ and $\varepsilon^- = 0\ \mathrm{meV}$; this choice gives the best match between (B) experiment and (C) theory [6]. Equipotential contours are shown; the dashed contours are at the energy levels of saddle-point Van Hove singularities (VHS). (**B**) TEF spectra as a function of gate voltage V_g. $T = 1.55$ K. The plotted ratio $(V_M - V_R)/I_L$ is measured as depicted in Fig. 2.1A. Black dashed curves indicate B_1, B_3, and B_6, which are some of the peak positions where the Fermi level is close to the Dirac point. Green dashed lines indicate the abrupt termination of TEF caused by the breakdown of cyclotron motion at each VHS. Dashed arrows from (B) to (A) point to the energy levels (dashed contours) of the corresponding VHS; Voltage values are labeled by the miniband in which the breakdown occurs (e.g., V_{C1} for the breakdown of cyclotron motion in C1). Dotted lines show selected densities (I, II, III, and IV) that place the Fermi level in minibands C2, C1, V1, and V2, respectively. (**C**) TEF spectra as a function of V_g, calculated from the dispersion in (A) according to Ref. 6. Figure from Ref. 6.

As we will discuss more in this chapter, the Fermi surfaces are hole like and non-circular in the energy range bounded by the VHSs of the first two conduction minibands or valence minibands. Either the presence of multiple hole pockets or a single valley asymmetric hole pocket may be to blame for the lack of a clear TEF signal in Fig. 2.2B. We may be able to rectify this issue through the use of absorptive pinhole collimators (displayed schematically in Fig. 2.3). The contact to the bottom chamber (source contact [S] shown in red) serves as a source of charge carriers, while the contact to the intermediate chamber (filter contact [F] shown in black) serves as an absorptive filter. When the filter is grounded, only the trajectories that travel from the source and through both pinhole apertures pass through to the bulk of the device. This produces a highly collimated beam of carriers injected into the bulk of the device: the angular full width at half maximum is 70° when injecting in the uncollimated configuration (electrically shorting the source to the focusing contact) and 18° when injecting in the collimated configuration. Using collimators may allow us to populate and/or detect a narrow window of k-states for a given field, perhaps allowing for clear TEF in these regions between VHSs.

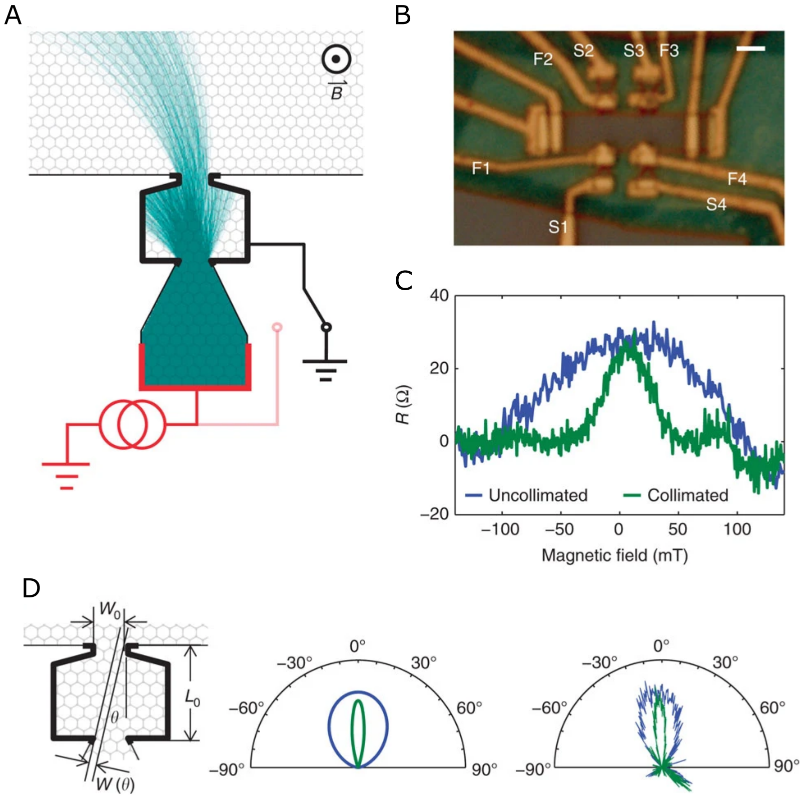

Figure 2.3: **Absorptive pinhole collimator.** (**A**) Schematic of a double pinhole collimator. Current is sourced from the bottom contact (red), passes through the bottom aperture and is either absorbed by the intermediate contact (black) or passes into the bulk of the device. Only trajectories that pass through both apertures reach the bulk, producing a collimated beam. The collimated beam is steered by an external magnetic field. (**B**) Optical micrograph of the device with four collimators in a Hall-bar-like geometry. Scale bar is 2 μm. (**C**) Measuring angular distribution. Non-local resistance at $n = 1.65 \times 10^{12}\ \mathrm{cm}^{-2}$ (Fermi wavelength: $\lambda_F = 27.6\ \mathrm{nm}$) is plotted with V_{S3F3} measured relative to V_{F1} when current is sourced from both S4 and F4 (blue), and only from S4, whereas F4 is grounded (green). The narrowness of the central peak for the F4-grounded data results from collimation. (**D**) Theoretical collimation behavior versus experiment. Left: diagram of effective collimator width $w(\theta)$ at a fixed angle for classical ballistic trajectories. Middle: polar plot of theoretical angular dependence for a 300 nm-wide point contact (blue) and a $w_0 = 300\ \mathrm{nm}$, $L_0 = 850\ \mathrm{nm}$ collimator (green). Right: experimental data from (C) mapped to angle. Figure from Ref. 8.

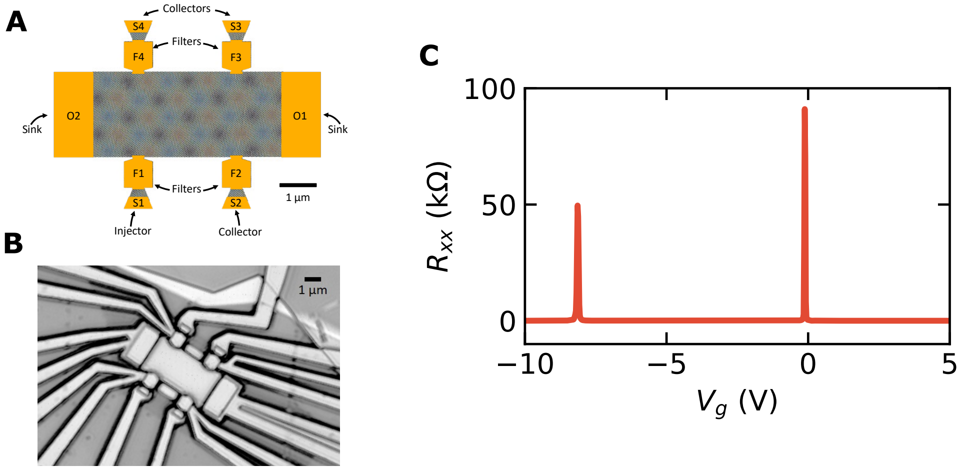

Figure 2.4: **Collimating graphene/hBN moiré superlattice Hall bar.** (**A**) Schematic of the collimating graphene/hBN moiré superlattice Hall bar. Sourcing contacts are labeled with the prefix S. Focusing contacts are labeled with the prefix F. Side contacts used to drain stray carriers are labeled with the prefix O. (**B**) Laser micrograph of the fabricated device. Scale bar is $1\ \mu\mathrm{m}$. (**C**) Longitudinal resistance R_{xx} as a function of gate voltage V_g. The peak near 0 V corresponds to the charge neutrality point. The peak near 8 V corresponds to the secondary Dirac point, confirming that the sample is a moiré superlattice.

2.2 Basic characterizations

Such a device is shown schematically in Fig. 2.4. The device consists of two large side ohmics (labeled O1 and O2) and four collimating injectors arranged in a Hall bar configuration. The heterostructure consists of monolayer graphene encapsulated with hBN and a graphite back gate. During the stacking procedure, the top hBN was intended to be rotationally aligned with the sheet of monolayer graphene. Using the graphite gate to tune the carrier density, we see peaks in the longitudinal resistance R_{xx} near 0 V and -8 V, which correspond to the charge neutrality point and secondary Dirac point, respectively, confirming that the sample is indeed a highly aligned moiré superlattice (Fig. 2.4C). This location of the secondary Dirac peak corresponds to a superlattice density $4n_s = 0.70 \times 10^{12}\ \mathrm{cm}^{-2}$ and a twist angle $\theta = 0.43°$. Fig. 2.4C shows the accessible range of gate voltages that can be safely used without potentially damaging the gate dielectric (as seen by the onset of an exponential rise in the leakage current). For some reason, this range is quite asymmetric, as has been seen in other graphite gated devices.

2.3 Magnetic field response

By injecting current into the device through S1 with F1 grounded, we inject a well collimated beam of charge carriers into the bulk of the device. With contacts O1 and O2 grounded and all other contacts floating, we can measure the resistance $R_i = V_i/I_{\mathrm{S1}}$ at each contact as a function of gate voltage and magnetic field (Fig. 2.5). R_{S2} is the collimating analog of a traditional TEF measurement. For gate voltages in the range $-6.5 < V_g < 0$, there are two TEF peaks that are consistent with the expectation for a circular Fermi surface: $V_g \propto B^2/j^2$ for $j = 1$ and 2 which corresponding to zero and one bounce(s) along the sidewall of the device, respectively. Based on the geometry of the device, higher order bounces should not be possible as the field is too high for carriers to make it through the filter contacts. For voltages beyond this range there are several reversals of the sign of the charge carriers: A gate voltage of -6.5 V corresponds to the VHS in the first valence band, -8.1 V corresponds to the secondary Dirac point, and -11 V corresponds to the VHS in the second valence band. Beyond -11 V, there is a resistance peak that may correspond to the recovery of TEF, however the gate cannot be lowered far enough to study the peak's field dependence.

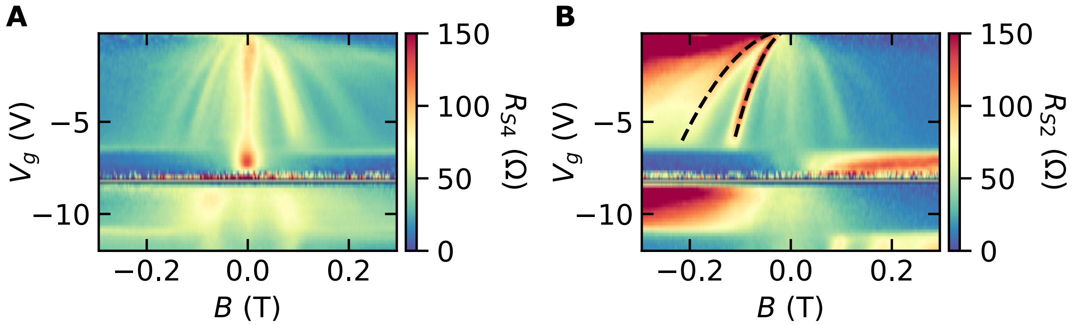

Figure 2.5: **Magnetic field dependence for different contacts.** Resistance (**A**) R_{S4} and (**B**) R_{S2} as a function of gate voltage V_g and magnetic field B when injecting current from S1 in a collimating configuration (F1 is grounded). Contacts O1 and O2 are also grounded. Dashed black lines in (B) are guides of the form $V_g \propto B^2/j^2$ for $j = 1$ and 2 as one would expect for TEF with a circular Fermi surface corresponding to zero and one bounce(s) along the sidewall of the device, respectively.

The resistance of contact S4, which is directly across from the injecting contact S1, shows a prominent zero field peak. Below the VHS of the first valence band, the zero field peak becomes more pronounced. After crossing the secondary Dirac point, two bulbous side peaks emerge near $75\ \mathrm{mT}$. Line cuts in both these regions will be presented in the next section.

2.4 Comparing with ballistic Monte Carlo simulations

First, consider a line cut at a gate voltage $V_g = -9.89\ \mathrm{V}$. The Fermi surface at this gate voltage consists of hole pockets that link together to form a single real space trajectory (Fig. 2.6A shows the Fermi surface in the K valley, the K' valley is the time reversed partner). The fraction of the injected current $I_{\mathrm{injected}} = I_{\mathrm{S1}} + I_{\mathrm{F1}}$ that makes it to contacts S4 and F4 as a function of magnetic field shows a peak at zero field and two side peaks at finite field (black traces in Fig. 2.6C). Although the device was attempted to be fabricated to be rotationally aligned with the crystal axis (such that the relative orientation between the device and crystal axis would yield a Fermi surface as oriented in Fig. 2.6A relative to the device as shown in Fig. 2.6B), both panels show a slight asymmetry in field that may be due to slight misalignment between the two. This relative angle does not matter when the Fermi surface is circular, but now must be considered.

We can compare the experimental results to those of a ballistic Monte Carlo simulation for this Fermi surface (described in Appx. C). When looking at a heat map of simulated carrier trajectories color coded by valley at 0.053 T (Fig. 2.6B), the K' valley (blue) is entirely absorbed by the filter F1 while the K valley (red) has a large number of carriers making their way to S4. Results of the simulated charge transport as a function of magnetic field are also reported in Fig. 2.6C, color coded according to valley. The simulations show that transport is dominated by the K valley. Additionally, there is qualitative agreement between the experiment and simulations: there are peaks in both in the fractional current at S4 and F4 at nearly the same fields in the experiment and theory. Getting good quantitative agreement is quite challenging as there are a number of parameters to consider: Is the correct Fermi surface being simulated? How specular is reflection at the edges of the device? How likely is a carrier to reflect off of an ohmic contact? What is the true orientation of the device relative to the crystal axis? All of these parameters can be controlled in the simulation but fitting to the experimental data is difficult. Given that significant current is still making its way into the device at $\pm 200\ \mathrm{mT}$, it is likely that the experimental ohmic contacts are far more reflective than the simulated contacts. Additionally, although transport should be ballistic on the length scale of the device, the simulation does not consider bulk scattering.

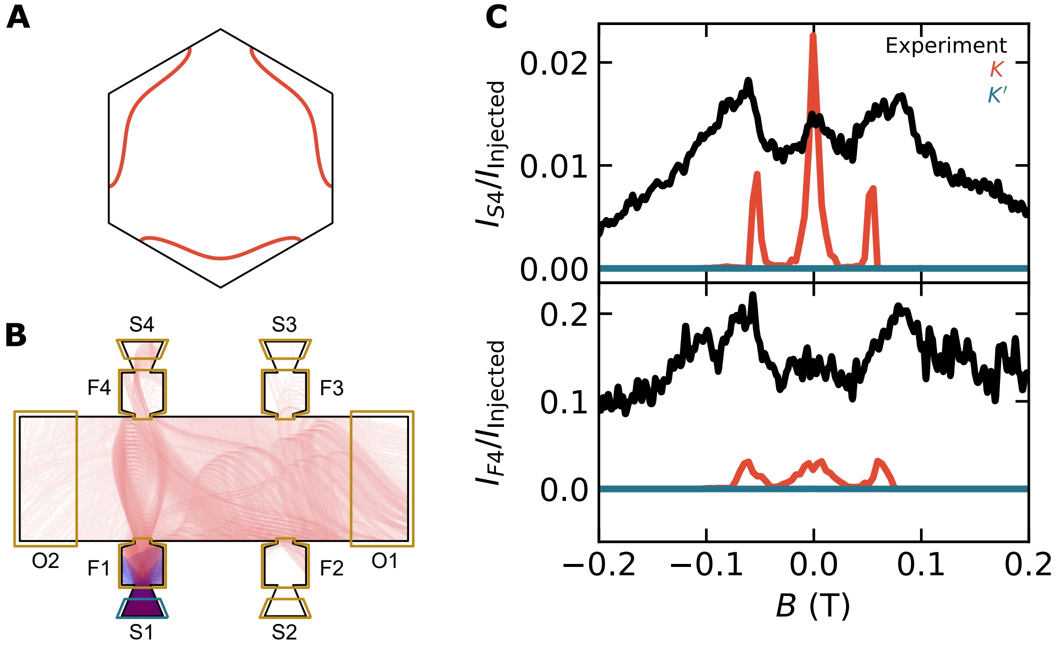

Figure 2.6: **Transport at $E_F = -188$ meV.** (**A**) Fermi surface at $E_F = -188$ meV in the K valley, which corresponds to a gate voltage of -9.89 V. The Fermi surface of the K' valley is the time-reversed pair of the K valley. (**B**) Normalized heat map of the position of charge carriers, simulated using a ballistic Monte Carlo for the Fermi surface shown in (A) at a magnetic field of 0.053 T. Trajectories are color coded red or blue if they belong to the K or K' valley, respectively. A count for each plaquette is incremented when an electron's trajectory passes through that plaquette. This count is reflected in the intensity of either color, with higher intensity corresponding to a higher count (where the count has been cut off at a high number to provide contrast in the bulk of the device). Carriers are injected at the source (teal contact) and propagated until hitting a contact. Carriers hitting the source are absorbed and reinjected into the bulk of the device. All contacts colored gold are virtual grounds that perfectly absorb any incoming charge carrier. The device is oriented relative to the crystal axis such that the Fermi surface is oriented as shown in (A). (**C**) Fraction of injected current $I_{\mathrm{injected}} = I_{\mathrm{S1}} + I_{\mathrm{F1}}$ making it to S4 (upper panel) and F4 (lower panel) as a function of magnetic field. Simulation results, a frame of which are shown in (B), are color coded according to their valley index $K^{(\prime)}$ in red or blue, respectively. Experimental results are shown in black.

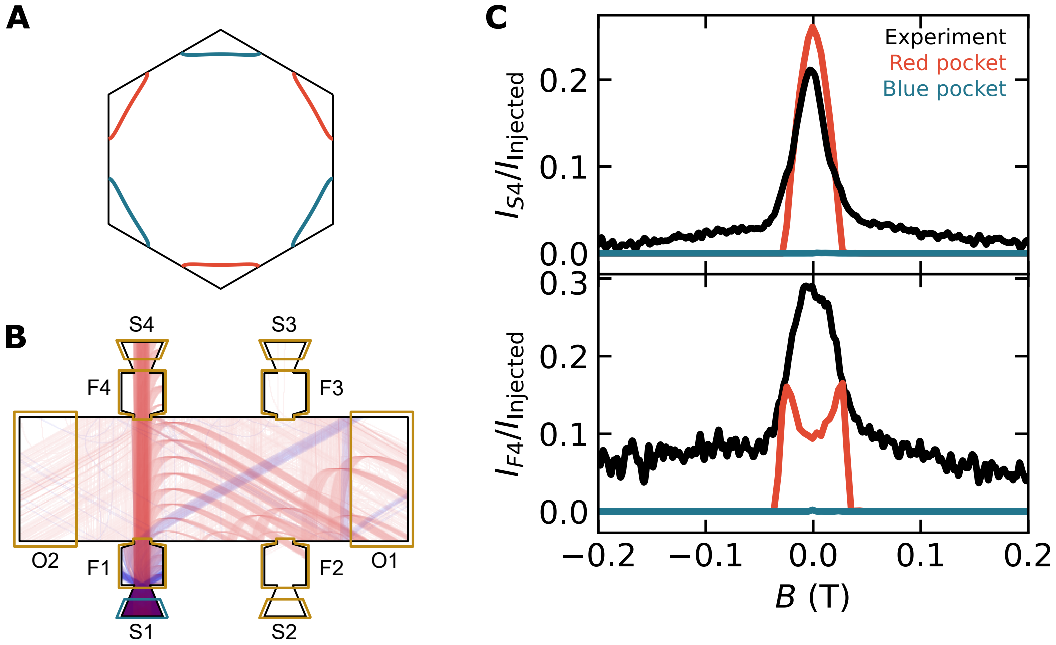

Figure 2.7: **Transport at $E_F = -135$ meV.** (**A**) Fermi surface at $E_F = -135$ meV in the K valley, which corresponds to a gate voltage of -7.05 V. The color coding corresponds to two different hole-like pockets in the Fermi surface. The Fermi surface of the K' valley is the time-reversed pair of the K valley. (**B**) Normalized heat map of the position of charge carriers, simulated using a ballistic Monte Carlo for the Fermi surface shown in (A) at a magnetic field of -0.011 T. Trajectories are color coded red or blue according to the different hole-like pockets in the Fermi surface shown in (A). A count for each plaquette is incremented when an electron's trajectory passes through that plaquette. This count is reflected in the intensity of either color, with higher intensity corresponding to a higher count (where the count has been cut off at a high number to provide contrast in the bulk of the device). Carriers are injected at the source (teal contact) and propagated until hitting a contact. Carriers hitting the source are absorbed and reinjected into the bulk of the device. All contacts colored gold are virtual grounds that perfectly absorb any incoming charge carrier. The device is oriented relative to the crystal axis such that the Fermi surface is oriented as shown in (A). (**C**) Fraction of injected current $I_{\mathrm{injected}} = I_{\mathrm{S1}} + I_{\mathrm{F1}}$ making it to S4 (upper panel) and F4 (lower panel) as a function of magnetic field. Simulation results, a frame of which are shown in (B), are color coded according red or blue according to which hole like-pocket of the Fermi surface was simulated. Experimental results are shown in black.

Similar analysis can be performed for a gate voltage $V_g = -7.05$ V, where the Fermi surface now consists of two distinct hole pockets in each valley (Fig. 2.7A). A snapshot of the simulation at a small field of -0.011 T shows that one of the pockets (blue) has a small number of states that are injected into the bulk at a large angle while the other pocket (red) forms an extremely well collimated beam. This extreme collimation comes from the strongly faceted nature of the Fermi surface at this gate voltage. This strongly collimated beam is shown in both the experimental and simulated dependence of the fractional current absorbed by S4 and F4 as a function of field. Surprisingly, there is a reasonable degree of quantitative agreement between experiment and theory for the fractional current reaching S4, which consists of an extremely sharp peak at zero field. The results are less consistent for the fractional current reaching F4: the simulation suggests that there should be two peaks at finite field while the experiment yields a single broad peak. The experimental peak does not appear to be well described by a single Gaussian or Lorentzian peak, so it may perhaps may be well described by two closely spaced peaks.

2.5 Temperature dependence

The temperature dependence of these low temperature features can yield information about carrier dynamics. The rate at which the peak in $I_{\mathrm{S4}}/I_{\mathrm{injected}}$ is suppressed with increasing temperature is much faster than expected for thermal broadening, so other scattering effects must be at play (Fig. 2.8A). We can use the area under the peak relative to the area at base temperature $A(T)/A(T_{\mathrm{base}})$ as an estimate of the fraction of electrons that propagate ballistically between S1 and S4. We can then estimate the scattering rate [6],

$$\tau(T)^{-1} = -\frac{2v_F}{\pi L}\log\left(\frac{A(T)}{A(T_{\mathrm{base}})}\right), \tag{2.2}$$

where v_F is the Fermi velocity (which I assumed to be that of pristine graphene, however this is likely not the best estimate near the miniband edge) and $L = 5.4\ \mu\mathrm{m}$ is the distance between S1 and S4. The extracted scattering rate is shown in Fig. 2.8 along with other extracted scattering rates at different Fermi energies from Ref. 6. The green trace corresponds to the expected scattering rate of a circular Fermi surface for low-angle scattering processes governed by Thomas-Fermi screened electron-electron interactions, which for temperatures below $T^* = 2v_F/k_B\sqrt{k_F/\pi L}$, can be described by

$$\tau_{e-e}^{-1} \approx \frac{(k_B T)^2}{2\hbar^2 v_F k_F}\log\left(\frac{3.6L}{w}\right), \tag{2.3}$$

where w is the width of the ohmic contacts [6]. The rate of scattering by phonons, inferred from the temperature dependence of the sheet resistance of encapsulated heterostructures, is much lower than either the measured values of τ^{-1} or the calculated values of τ_{e-e}^{-1} (2.8B). The results of Ref. 6 appear to be dominated by low-angle electron-electron scattering.

The scattering rate for the current device at $E_F = -135$ meV (orange trace in Fig. 2.8B) is initially larger at lower temperature but appears to rise less quickly with increasing temperature than any of the traces of Ref. 6. This does not mean electron-electron scattering is not dominant: the temperature dependence of electron-electron scattering dependents on the shape of the Fermi surface [58, 59]. In fact, at moderate temperatures (30 K $< T <$ 100 K), it appears that $\tau(T)^{-1} \propto T$, which is the expectation of a one dimensional Fermi surface [59]. This behavior is potentially due to the strongly faceted nature of the Fermi surface at

$E_F = -135$ meV.

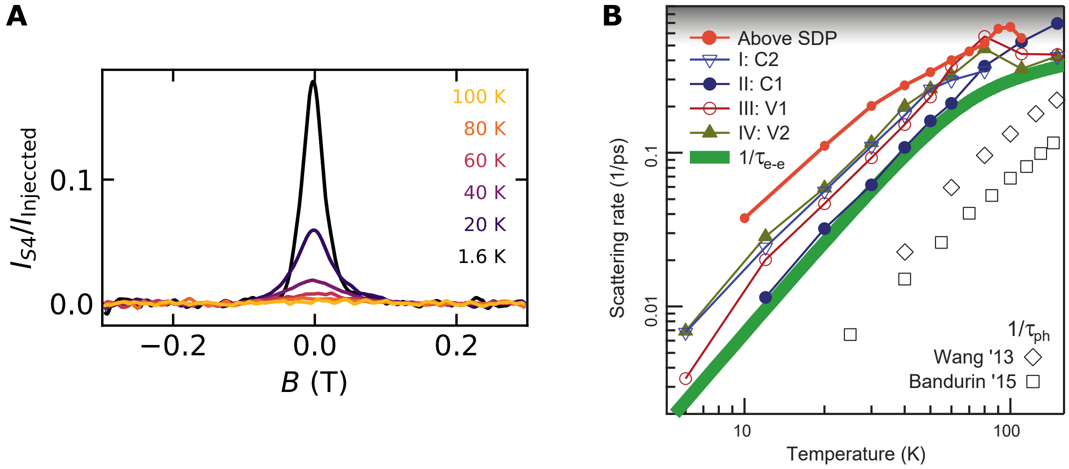

Figure 2.8: **Temperature dependence of collimatated beam.** (**A**) Temperature dependence of the fractional current to reach S4, $I_{\mathrm{S4}}/I_{\mathrm{injected}}$, as a function of field for $E_F = -135$ meV ($V_g = -7.05$ V). A smooth background has been subtracted from each curve, followed by Gaussian smoothing of each curve. (**B**) Orange filled circles correspond to scattering rates extracted from the amplitude of the zero-field peak shown in (A). Circles and triangles denote effective scattering rates $\tau(T)^{-1}$ extracted from the amplitude of TEF oscillations in Ref. 6. The heavy green curve shows the theoretical scattering rate τ_{e-e}^{-1} related to the electron-electron interaction. Square and diamond symbols denote the rate of scattering by phonons τ_{ph}^{-1} inferred from temperature-dependent sheet resistivity reported in Refs. 9 and 10. The detection limit set by noise is shaded. This panel is modified from Ref. 6.

2.6 Scanning gate microscopy measurements

Using a sharpened tungsten tip mounted on a tuning fork, we can apply a local scattering potential to the device. We will mount the sample on a stack of piezoelectric steppers so that it can be positioned relative to the tip. The tuning fork can be used to measure the height of the tip above the sample. We will first consider a circular Fermi surface (Fig. 2.9A). The magnetic field is tuned such that S1 and F2 are connected by a cyclotron orbit at the given magnetic field (Fig. 2.9B).

We have fabricated the device such that all contacts (except for the sources) have two separated traces that are connected at the device. For the following scanning measurements, one trace is used to measure the potential at each contact while the other measures the current. This allows us to perform a measurement of the potential of the contact at the device, ignoring the non-negligible trace resistance, even when the contact has a finite current flowing through it. We will actively feedback on the current drained by each contact such that each contact (except the source) functions as a virtual ground (held at zero potential relative to the source).

This allows for a simultaneous measurement of the current through each contact in the device.

The differential current of each contact (the change in current when the tip is used to apply a local scattering potential at a given location relative to no applied perturbation) as a function of the position of the scanning gate tip is measured at a constant tip height, applied potential, and magnetic field (Fig. 2.9C). As a sanity check, we see that the differential current between S1 and F1 is largely unaffected by the tip position; the vast majority of current that reaches F1 should come directly from S1. We can also see that the currents to contacts O2 and F4 are decreased when the tip is on the left side of the device and increased when the tip is on the right side of the device, which is consistent with the chosen sign of magnetic field. Finally, there is a roughly circular peak in the differential current corresponding to an increase (decrease) in the current drained by O1 (F2). This suggest that, for tip positions near the collimated beam, the tip is scattering current out of trajectories that are predominately reaching F2 into trajectories reaching O1.

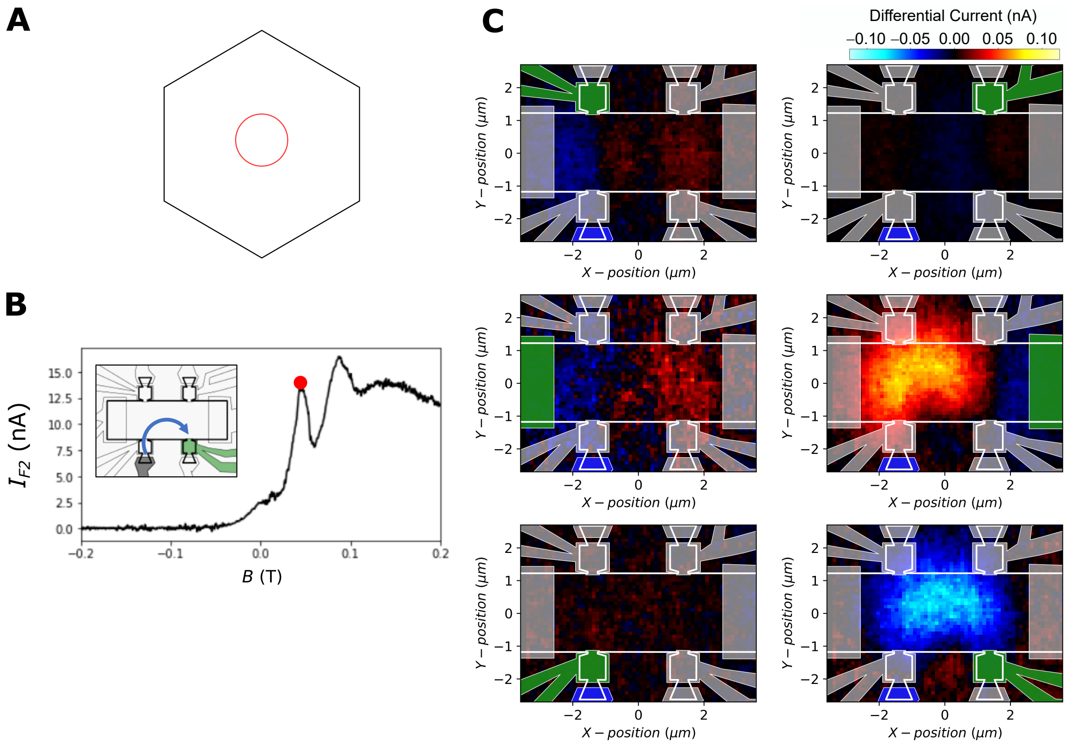

Figure 2.9: **Scanning gate microscopy measurements of a circular Fermi surface.** (**A**) Fermi surface at $E_F = 80$ meV which corresponds to a gate voltage of 1.20 V. (**B**) Current drained by F2 as a function of magnetic field. The red dot indicates the field at which S1 is connected to F2 via a single cyclotron orbit. Inset: Schematic of the device showing the trajectories of carriers that connect S1 and F2 when the field is tuned to the value of the red dot. (**C**) Differential current between the source (blue) and a virtual ground (green) measured as a function of the scanning gate tip position for a constant tip potential. All contacts besides the source function as virtual grounds, the currents through which are measured simultaneously and plotted individually. The field has been tuned to the value indicated by the red dot in (B).

Similar measurements can be performed for $E_F = -135$ meV ($V_g = -7.05$ V), where we expect, as discussed in the previous section, that the trajectories of carriers should be triangular. This triangular shape is clearly displayed in Fig. 2.11, where the differential current of $I_{\mathrm{F2}} + I_{\mathrm{S2}}$ is plotted. A rough guide of a potential dominant trajectory of the appropriate size is plotted in white. This colormap hints that the device may not be perfectly aligned to the crystal axis, as is assumed for the white guide and suggested by the asymmetry in Fig. 2.6. Rather, the colormap seems to suggest that the Fermi surface should be rotated a few degrees clockwise, however, more data would be needed to fit this rotation precisely. Additionally, the colormap for the current reaching O1 shows a broad scattering hot spot that appears near the corner of the approximated triangular trajectory (shown in Fig. 2.10). If electrons were merely being scattered away from

O2 and F4, there would most likely be a line of scattering (as seen for the circular Fermi surface in Fig. 2.9). The presence of a hotspot suggests that electrons scatter more strongly at the corners of the trajectories.

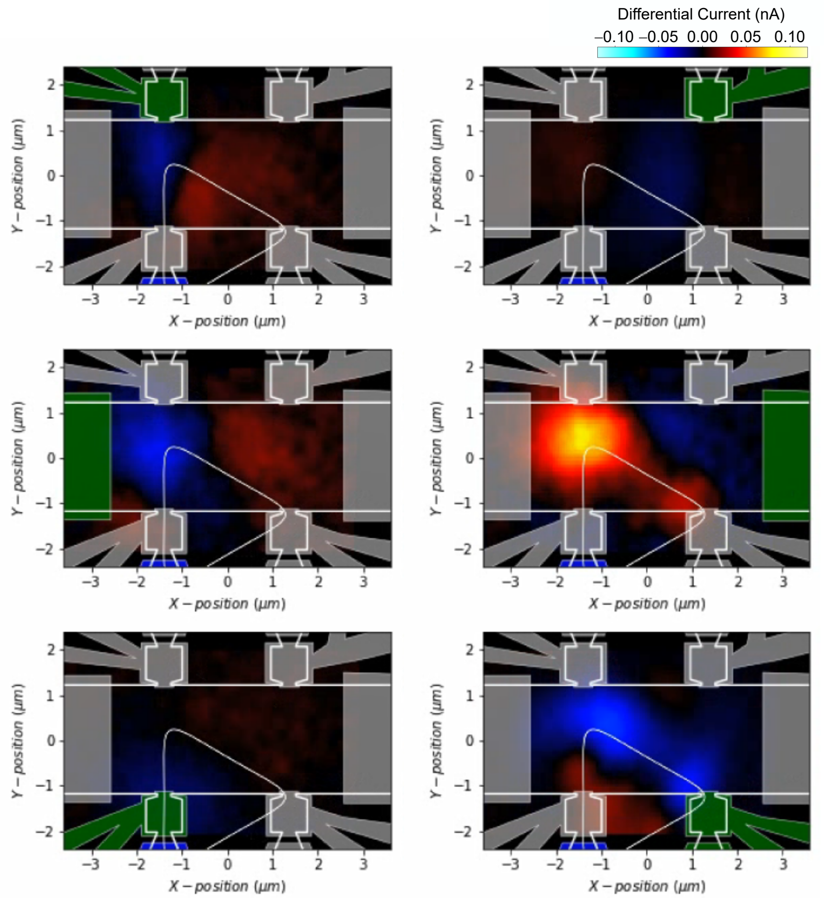

Figure 2.10: **Scanning gate microscopy of a triangular Fermi surface.** Differential current between the source (blue) and a virtual ground (green) measured as a function of the scanning gate tip position for a constant tip potential and $E_F = -135$ meV ($V_g = -7.05$ V). All contacts besides the source function as virtual grounds, the currents through which are measured simultaneously and plotted individually. The white trace is a guide showing a trajectory of the appropriate shape and size for the given E_F and B that would connect S1 to F2.

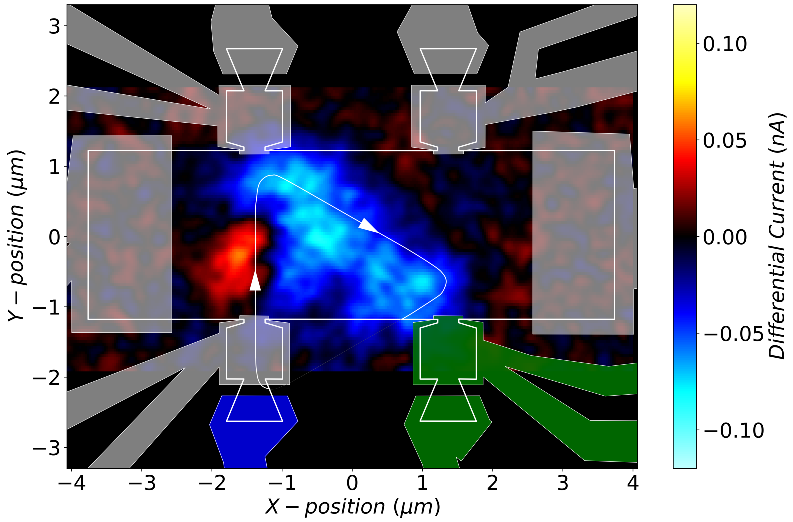

Figure 2.11: **High resolution scanning gate microscopy measurement of a triangular Fermi surface.** Differential current of $I_{\mathrm{F2}} + I_{\mathrm{S2}}$ (contacts colored green) when current is injected from the source (blue), measured as a function of the scanning gate tip position for a constant tip potential and $E_F = -135\ \mathrm{meV}$ ($V_g = -7.05\ \mathrm{V}$). All other contacts are also grounded. the white trace is a guide showing a trajectory of the appropriate shape and size for the given E_F and B.

Chapter 3

Flat bands in moiré systems

3.1 Magic-angle twisted bilayer graphene (tBLG)

3.1.1 Introduction

As we saw in the previous chapter, the electronic properties of monolayer graphene can be strongly affected by its surrounding environment (in that case, being aligned to a hBN crystal). We will now consider how the properties of few layer graphene are affected by how the layers are stacked.

First we will discuss how the stacking in a bilayer system affects its electronic properties. We are starting from two sheets of monolayer graphene that individually feature massless electrons [28,60] and a large kinetic energy, resulting in a system with negligible electronic correlations. The energetically preferred stacking of bilayer graphene is Bernal (AB), which already has drastically different electronic properties: featuring hyperbolic bands [50]. But what happens to the electronic properties of the composite system as we twist the layers away from Bernal stacking? We will first look at a theoretical model for an expectation of the band structure of such a twisted bilayer graphene system (tBLG). We will then look at the first major advances in exploring the most interesting region of twist angles.

3.1.2 Band Structure

This section will present the main results of a continuum model used to calculate the electronic properties of tBLG. For simplicity, we will restrict our calculations to the K valley, and drop any valley indices. An extended derivation of the continuum model can be found in Refs. 11 and 12.

The twisted bilayer system can be characterized by a twist angle θ (where we define zero twist angle as Bernal stacking) and a translation vector $\mathbf{d}$. Whether or not a particular twisted bilayer system forms a commensurate lattice is determined only by θ; sliding one layer with respect to the other in a commensurate structure modifies the unit cell of the structure but does not disturb the commensurately [11]. The bilayer only forms a two-dimensional crystal at a discrete set of angles, but for a generic twist angle, Bloch's theorem does not apply microscopically. Therefore, the electronic structure cannot be calculated directly. However, we can recover the periodicity for angles with strong interlayer coupling ($\theta < 10°$) and describe the electronic structure using Bloch bands for incommensurate twist angles by constructing a low-energy continuum model Hamiltonian [11].

The low-energy continuum model will consist of three terms: two single-layer Dirac-Hamiltonians that account for the isolated graphene sheets and a tunneling term to account for hopping between the layers. We can start by writing this as a block Hamiltonian in the basis of layer. Then the full Hamiltonian will be

$$H = \begin{pmatrix} h(\theta/2) & H_T \\ H_T^\dagger & h(-\theta/2) \end{pmatrix}, \tag{3.1}$$

where

$$h_{\mathbf{k}}(\theta) = -vk \begin{pmatrix} 0 & e^{i(\theta_k - \theta)} \\ e^{-i(\theta_k - \theta)} & 0 \end{pmatrix} \tag{3.2}$$

is the Dirac-Hamiltonian for a layer rotated by an angle θ, v is the Dirac velocity, $\mathbf{k}$ is the momentum measured from the layer's Dirac point, and θ_k is the momentum orientation relative to the x axis. This spinor Hamiltonian acts on the individual layer's A and B sublattice degrees of freedom.

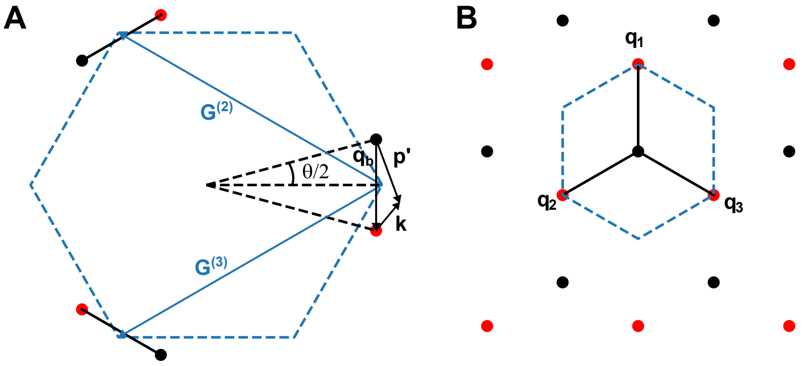

Figure 3.1: **Interlayer hopping parameters in tBLG.** (**A**) The blue dashed hexagon marks the Brillouin zone for an unrotated graphene sheet. The black (red) circles are the three equivalent K points for layer 1 (2) that are rotated by $(-)\theta/2$. Crystal momentum is conserved when $\mathbf{p}' - \mathbf{k} = \mathbf{q}_0$, $\mathbf{q}_1$, or $\mathbf{q}_2$. In the chosen reference frame, these momentum transfers have modulus $|\mathbf{q}_j| = 2|\mathbf{K}|\sin(\theta/2)$ and direction $(0,\, 1)$, $(-\sqrt{3}/2,\, -1/2)$, or $(\sqrt{3}/2,\, -1/2)$. Equivalent Dirac points are connected by the reciprocal lattice vectors $\mathbf{G}^{(2)}$ and $\mathbf{G}^{(3)}$, shown as solid blue lines. (**B**) A separate representation of the hopping parameters. When we account for repeated hopping, we generate this honeycomb lattice in reciprocal space. In a repeated zone scheme, the dots correspond to the Dirac points of the two layers. The dashed blue line marks the moiré band Wigner-Seitz cell. Figure adapted from Refs. 11 and 12.

To derive a continuum model for the tunneling term, we start with the core assumption that the interlayer tuneling amplitude between π-orbitals is a smooth function $t(r)$ of the spatial separation projected onto the graphene planes. We label the positions of the carbon atoms in the two layers by $\mathbf{R}$ and $\mathbf{R}'$. The two are related by $\mathbf{R}' = M(\theta)(\mathbf{R} - \tau) + \mathbf{d}$, where M is a rotation matrix and τ is a vector connecting the two atoms of a unit cell in a given plane. We can now find the matrix elements of H_T:

$$T^{\alpha,\beta}_{\mathbf{k},\mathbf{p}'} = \langle \Psi^{(1)}_{\mathbf{k},\alpha} | H_T | \Psi^{(2)}_{\mathbf{p}',\beta} \rangle \tag{3.3}$$

describes hopping for an electron with momentum $\mathbf{p}' = M\mathbf{p}$ on sublattice β of one layer hopping to a state with momentum $\mathbf{k}$ on sublattice α in the other layer. The projection of the wave function onto a given sublattice for either layer are

$$|\Psi^{(1)}_{\mathbf{k},\alpha}\rangle = \frac{1}{\sqrt{N}} \sum_{\mathbf{R}} e^{i\mathbf{k}(\mathbf{R}+\tau_\alpha)} |\mathbf{R} + \tau_\alpha\rangle \tag{3.4}$$

and

$$|\Psi^{(2)}_{\mathbf{p},\beta}\rangle = \frac{1}{\sqrt{N}} \sum_{\mathbf{R}'} e^{i\mathbf{p}(\mathbf{R}'+\tau'_\beta)} |\mathbf{R}' + \tau'_\beta\rangle, \tag{3.5}$$

where $\tau_A = 0$ and $\tau_B = \tau$. $\mathbf{R}$ is summed over the entire triangular Bravais lattice. We can now calculate the matrix elements. We can invoke the two-center approximation:

$$\langle \mathbf{R} + \tau_\alpha | H_T | \mathbf{R}' + \tau'_\beta \rangle = t(\mathbf{R} + \tau_\alpha - \mathbf{R}' - \tau'_\beta). \tag{3.6}$$

We then obtain

$$T^{\alpha,\beta}_{\mathbf{K}+\mathbf{k},\mathbf{P}'+\mathbf{p}'} = \sum_{\mathbf{G_1}\mathbf{G_2}} \frac{t_{\mathbf{K}+\mathbf{k}+\mathbf{G_1}}}{\Omega} e^{i\left[\mathbf{G_1}\tau_\alpha - \mathbf{G_2}(\tau_\beta - \tau) - \mathbf{G}'_\mathbf{2}\mathbf{d}\right]} \delta_{\mathbf{K}+\mathbf{k}+\mathbf{G_1},\mathbf{P}'+\mathbf{p}'+\mathbf{G}'_\mathbf{2}}, \tag{3.7}$$

where Ω is the area of the unit cell, $t_\mathbf{q}$ is the Fourier transform of the tunneling amplitude $t(\mathbf{r})$, K and P are the wave vectors to the Dirac points of the respective layers, and $\mathbf{G_1}$ and $\mathbf{G_2}$ are reciprocal lattice vectors. It should be noted that the total momenta we are now discussing are relative to the γ point of the Brillouin zone, not the Dirac point (which would be just the lower case momenta). The Kronecker delta is restricting our interlayer hopping to vectors within the union of $\mathbf{G_1}$ and $\mathbf{G_2}'$, i.e. it is restricting us to the moiré pattern.

We can now make some simplifications. It turns out that the spectrum is independent of $\mathbf{d}$ [11], so we can take $\mathbf{d} = 0$. The key reason that this model is useful is that, although t_q is not precisely known, it should rapidly fall to zero as a function of q on the reciprocal lattice vector scale. This comes from the fact that the separation between graphene layers $d_\perp$ is much larger than the separation between carbon atoms a. This is because the two-center integral $t(r)$ varies with $R = \sqrt{r^2 + d_\perp^2}$, therefore the dominant small r hopping processes vary with r on the scale of $d_\perp$. This causes t_q to fall precipitously with $qd_\perp > 1$ [11]. The terms that then contribute most strongly for tunneling near the Dirac point have $q = k_\mathrm{D}$ which corresponds to the

Brilloin zone corner wave vector magnitude. These correspond to the three reciprocal lattice vectors $\mathbf{0}$, $\mathbf{G}^{(2)}$, $\mathbf{G}^{(3)}$. The latter two vectors connect a Dirac point with its equivalent in the first Brillouin zone. When only these terms are retained,

$$T^{\alpha,\beta}(\mathbf{r}) = w\sum_{j=1}^{3}\exp(-i\mathbf{q}_j\cdot\mathbf{r})T_j^{\alpha,\beta}, \tag{3.8}$$

where

$$T_1 = \begin{pmatrix} 1 & 1 \\ 1 & 1 \end{pmatrix}, \quad T_2 = \begin{pmatrix} e^{i\phi} & 1 \\ e^{-i\phi} & e^{i\phi} \end{pmatrix}, \quad T_3 = \begin{pmatrix} e^{-i\phi} & 1 \\ e^{i\phi} & e^{-i\phi} \end{pmatrix}, \tag{3.9}$$

$w = t_{k_D}/\Omega \approx 110\ \mathrm{meV}$, and $\phi = 2\pi/3$. The $\mathbf{q}_j$'s are Dirac model momentum transfers that correspond to the three interlayer hopping processes:

$$\mathbf{q}_1 = \frac{8\pi}{3}\sin(\theta/2)\,(0,\ 1)\,, \quad \mathbf{q}_2 = \frac{8\pi}{3}\sin(\theta/2)\left(\frac{-\sqrt{3}}{2},\ \frac{-1}{2}\right), \quad \mathbf{q}_3 = \frac{8\pi}{3}\sin(\theta/2)\left(\frac{\sqrt{3}}{2},\ \frac{-1}{2}\right). \tag{3.10}$$

This tunneling term is periodic with the periodicity of the moiré pattern. To perform our numerical calculations, we will want to Fourier transform this back to reciprocal space:

$$T^{\alpha,\beta}_{\mathbf{K}+\mathbf{k},\mathbf{P}'+\mathbf{p}'} = w\sum_{j} T_j^{\alpha,\beta}\delta_{\mathbf{q}_j,\mathbf{k}-\mathbf{p}'}. \tag{3.11}$$

In real heterostructures, AA stacking is energetically unfavorable compared to Bernal stacking. This energy difference drives structural reconstruction, minimizing the area of the AA region [13]. A standard approach to simply model this reconstruction is to apply a weight factor to the different tunneling processes [61]. The above matrices then become

$$\begin{aligned} T_1 &= \begin{pmatrix} w_{AA}/w_{AB} & 1 \\ 1 & w_{AA}/w_{AB} \end{pmatrix}, \\ T_2 &= \begin{pmatrix} w_{AA}/w_{AB}e^{i\phi} & 1 \\ e^{-i\phi} & w_{AA}/w_{AB}e^{i\phi} \end{pmatrix}, \\ T_3 &= \begin{pmatrix} w_{AA}/w_{AB}e^{-i\phi} & 1 \\ e^{i\phi} & w_{AA}/w_{AB}e^{-i\phi} \end{pmatrix}, \end{aligned} \tag{3.12}$$

where we will take $w_{AA}/w_{AB} = 0.7$ [61].

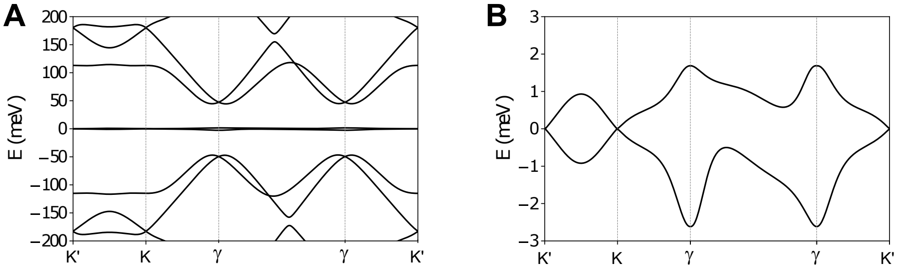

Figure 3.2: **Calculated band structure of tBLG.** (**A**) Band structure of tBLG in the K valley calculated using a continuum model Hamiltonian for $\theta = 1.05°$, $w = 117\ \mathrm{meV}$, and $w_{AA}/w_{AB} = 0.7$. The band structure for K' is the time reversed partner of the K band structure (**B**) Panel (A) replotted to more clearly show the dispersion of the nearly-flat valence and conduction bands.

Finally, we are now ready to numerically solve for the moiré bands. For a twist angle of $\theta = 1.05°$, the valence and conduction bands have become nearly-flat and well separated from higher minibands. In fact, their total bandwidth is $< 5\ \mathrm{meV}$. It should also be noted that the Dirac-like band touchings of the original single layer graphene dispersion are preserved at the K_M and K'_M points of the mini-Brillouin zone. As we will discuss, it seems likely the case that these Dirac-like touchings are symmetry protected [62–66] (but that may not be the case [67, 68]).

3.1.3 Fabrication

Somehow creating a bilayer system of two monolayer sheets of atoms with an arbitrary relative twist is a tall order experimentally. How are we going to move from this theoretical playground to a real experimental device? The previous section suggests that we should target a twist angle of $\sim 1.05°$ with an accuracy of perhaps a few hundred millidegrees.

Somewhat surprisingly, exfoliated graphene samples have been observed to sometimes retain a small interlayer twist [69]. Small twist angles can also be found when graphene is epitaxially grown on SiC [70]. However, neither of these methods allow for explicit targeting of a specific twist angle. It is possible to fold graphene sheets onto themselves [71–73]. Folding would likely produce large sheets of twisted graphene with different regions of different twists. One may be able to find a region near a targeted twist angle, but finding such a region would require a spatially resolved technique that can locally determine the twist angle, such as AFM or STM. With the development of the "tear-and-stack" dry-transfer method [46, 47] (Fig. 3.3), we now have a technique that can stack heterostructures while accurately targeting a specific angle with high angular accuracy.

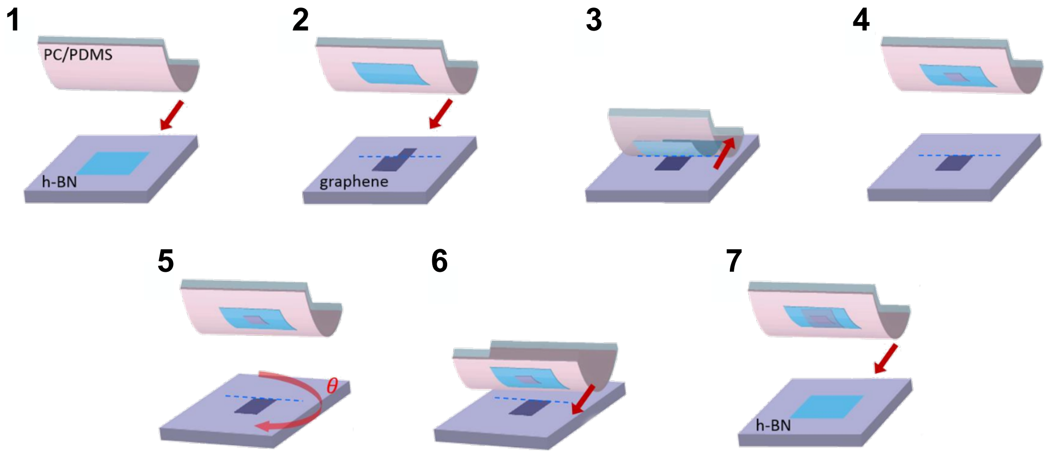

Figure 3.3: **Stacking tBLG heterostructures.** "Tear-and-stack" dry transfer technique used to create tBLG heterostructures. (1) We first pick up a hBN flake using a PC/PDMS stamp. (2) Position the hBN crystal over an exfoliated graphene flake and press the hBN down partially onto the graphene. (3) Once the hBN has been pressed down partially onto the graphene, retract the hBN, hopefully ripping the graphene cleanly in half. (4) Fully retract the stamp. (5) Rotate the remaining portion of the graphene flake to the desired twist angle. (6) Pick up the remaining portion of graphene using the ripped portion. (7) Finish the heterostructure. In this case, this includes fully encapsulating the heterostructure. Figure adapted from Ref. 13.

The devices we will consider consist of tBLG fully encapsulated in two hBN cladding layers (for the tBLG device considered in later chapters, each hBN layer is ~ 50 nm thick). To pick up the top hBN flake, we use a Poly(Bisphenol A carbonate) film/PDMS (Gel-Pak DGL-17-X8) stamp on a glass slide heated to 60 °C [46, 74]. Then, to stack two layers of graphene at a well defined twist angle, we use the van der Waals attraction between hBN and an exfoliated monolayer graphene flake while pressing down the hBN onto only a portion of the graphene to tear and pick up the contacted portion of monolayer graphene from the larger flake. The fact that we have controllably ripped the graphene sheet in half then allows us to rotate and pick up the remaining portion of the monolayer graphene [46, 47]. This process allows us to stack two layers of monolayer graphene to within $\pm 0.2°$, with the precision limited by motion of the flake during the tearing process. How cleanly the graphene sheet rips is a stochastic process that depends somewhat on how thick the graphene is, how well adhered it is to the hBN flake, and how well adhered the graphene flake is to the substrate. Ideally, the graphene flake should be stuck down well enough that it does not slide during the ripping, but not so much so that one cannot pull a portion of the flake off of the substrate. With a clean rip, one has a promising chance of achieving a heterostructure at the targeted angle. Because of the uncontrollability of this ripping process, people have begun moving away from "tear-and-stack" to graphene sheets that have been cut using AFM techniques [75, 76].

After picking up the remaining portion of graphene, a second hBN flake is picked up to fully encapsulate the tBLG. The completed stack is then transferred onto 300-nm-thick SiO_2 atop a degenerately doped Si substrate which is used as a back gate. These two remaining transfers do put a very nontrivial amount of strain on the heterostructure. Given that the tBLG is metastable (with the twist angle perhaps being pinned by disorder in the heterostruture), it may make sense to move to immediately dropping the completed tBLG onto an exfoliated hBN crystal instead of including this extra transfer step. Such precautions may help prevent relaxation of the twist angle in the heterostructure.

Now that we have a completed heterostructure, we can fabricate it into a measureable device. Specifically for the tBLG device discussed in Ch. 5 and Ch. 6, a Ti/Au top gate was deposited onto the completed heterostructure, and was subsequently used as a hard mask for a CHF_3/O_2 (50/5 sccm) etch to define a Hall bar region. During the mesa etch, the heterostructure was protected by resist extending outward from the hard mask near each of the leads of the Hall bar to provide space for making Cr/Au edge contacts [34] without risk of shorting to the top gate. Throughout all processing, the sample temperature was kept below $180\ ^\circ\mathrm{C}$ to prevent potential relaxation of the twist angle of the TBG. This dual gated architecture allows us to control both the carrier density in the channel and apply a perpendicular displacement field (see Appx. B).

3.1.4 Prior experimental work

With the advent of the "tear-and-stack" technique [46, 47], it became possible to fabricate tBLG with twist angles near those theoretically predicted to yield flat electronic bands. The first such sample [46] was fabricated with a twist angle of $1.08°$ (Fig. 3.4). One can first verify that the heterostructure retained a twist by the existence of superlattice gaps at carrier densities $n = \pm 4n_s = \pm 2.7 \times 10^{12}\ \mathrm{cm}^{-2}$ (the lighter shaded regions in Fig. 3.4), corresponding to full filling of the conductance and valence miniband, respectively. Following Sec. 1.2, such a density is consistent with the sample's ascribed twist angle.

The more surprising feature is the existence of strong conductance dips at half-filling of the conductance and valence minibands. Such features are not expected in the absence of electronic correlations; typically, metallic behavior is exhibit at finite filling of a band. When the Fermi level lies within flat bands, Coulomb interactions can greatly exceed the kinetic energy of the electrons and drive the system into strongly correlated phases [23–27].

Above $4\ \mathrm{K}$, the device behaves as a metal near half-filling. However, there is a metal-insulator transition at $4\ \mathrm{K}$. An Arrhenius activation fit to the temperature dependence of the conductivity yields a gap $\Delta \approx 0.31\ \mathrm{meV}$, two order of magnitude smaller than the superlattice gap [1].

Many of the features of this half-filled state are consistent with a Mott-like insulator. Such a state can arise from electrons being localized in the superlattice. Specifically, fits to Shubnikov-de Haas oscillations reveal a reduced value of the degeneracy and fits that extrapolate exactly to half-filling [1]. This is indicative of the half-filled state being a symmetry broken state, perhaps specifically a spin-charge separation in the prototypical Mott-like insulator. Additionally, the insulating state is suppressed by the application of a magnetic field. This suppression is insensitive to the orientation of the field, indicating that this suppression is due to a Zeeman effect [1].

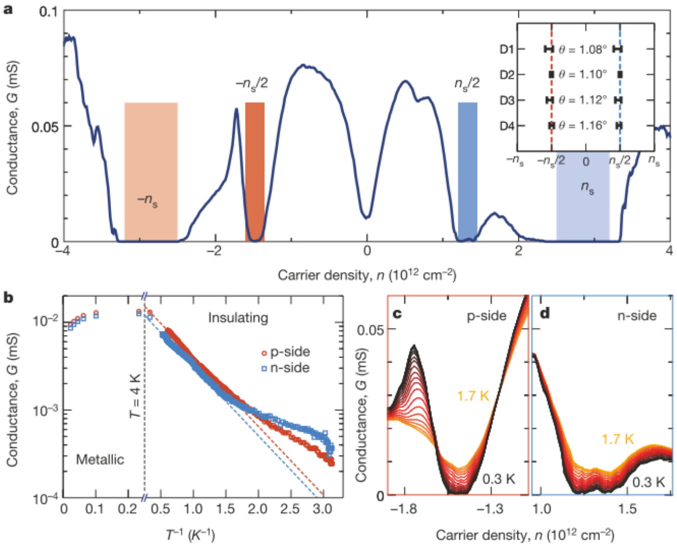

Figure 3.4: **Half-filling insulating states in tBLG.** (**A**) Measured conductance G of a tBLG device with twist angle $\theta = 1.08°$ and $T = 0.3$ K. The lighter-shaded regions are superlattice gaps at carrier density $n = \pm 4n_s = \pm 2.7 \times 10^{12}$ cm^{-2}. The darker-shaded regions denote half-filling states at $\pm 2n_s$. The inset shows the densities at which half-filling states in four different devices were measured in Ref. 1. (**B**) Minimum conductance values in the p-side (red) and n-side (blue) half-filling states in the $1.08°$ device. The dashed lines are fits of the form $\exp[-\Delta/(2kT)]$, where $\Delta \approx 0.31$ meV is the thermal activation gap. (**C, D**) Temperature-dependent conductance of the $1.08°$ device for temperatures from 0.3 K (black) to 1.7 K (orange) near the (C) p-side and (D) n-side half-filling states. Figure from Ref. 1. Note that Ref. 1 defines n_s as four carriers per moiré unit cell.

Shortly after the discovery of the insulating phase at half-filling, superconductivity was found nearby the half-filled state in the valence band of two tBLG devices with twist angles $\theta = 1.16°$ and $\theta = 1.05°$ and critical temperatures of approximately 1 K and 1.7 K, respectively (Fig. 3.5) [3].

The density phase diagram (Fig. 3.6) reveals two domes of superconductivity above and below the half-filled state and quantum oscillations near the half-filled state are consistent with a small Fermi surface. This behavior is similar to the underdoped cuprates. The carrier density at which tBLG superconducts is a record low for carrier density and an order of magnitude lower than typical two-dimensional superconductors [3]. The ratio of T_c to the size of the Fermi surface (density of about 10^{11} cm^{-2}) corresponds to one of the strongest pairing strengths between electrons in a superconductor.

As we will discuss in Ch. 4, zero resistance and non-linear $V - I$ characteristics (Fig. 3.5B) together are not sufficient evidence to prove a device is superconducting. For two-dimensional superconductors, the final piece of evidence is the existence of coherent transport. First looking at the magnetic field dependence, the superconducting state exhibits a maximum critical field of 70 mT (Fig. 3.7) that varies strongly with density.

Near the edges of the dome, there are oscillations in R_{xx} that may originate from phase-coherent transport. To view this more clearly, one can measure the critical current as a function of magnetic field (Fig. 3.8). Doing so, there are clear oscillations in the critical current with a period of $22.5\ \mathrm{mT}$ and $4\ \mathrm{mT}$ for devices M1 and M2 respectively. These periodicities correspond to junction ares of $0.09\ \mu\mathrm{m}$ and $0.5\ \mu\mathrm{m}$, both of which are smaller than the device area ($1\ \mu\mathrm{m}$). These devices do not have explicitly defined junctions. The oscillations likely arise from an array of junctions due to inhomogeneity within the sample, creating weak links in the superconductivity.

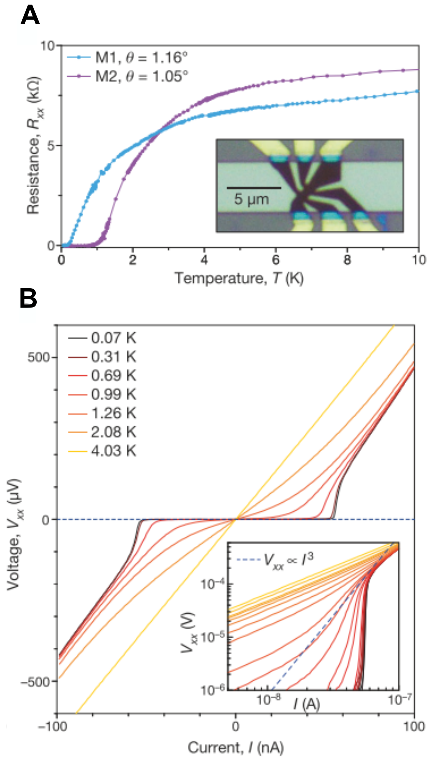

Figure 3.5: **Superconductivity in tBLG.** (**A**) Four-terminal resistance $R_{xx} = V_{xx}/I$ measured in two devices M1 and M2, that have twist angles of $\theta = 1.16°$ and $\theta = 1.05°$, respectively. The inset shows an optical image of device M1, including the main Hall bar (dark brown), electrical contacts (gold), back gate (light green), and $\mathrm{SiO_2/Si}$ substrate (dark grey). (**B**) Current-voltage ($V_{xx} - I$) curves for device M2 measured at $n = -1.44 \times 10^{12}\ \mathrm{cm}^{-2}$ and various temperatures. At the lowest temperature of $70\ \mathrm{mK}$, the curves indicate a critical current of approximately $50\ \mathrm{nA}$. The inset shows the same data on a logarithmic scale, which is typically used to extract the Berezinskii-Kosterlitz-Thouless transition temperature ($T_{\mathrm{BKT}} = 1.0\ \mathrm{K}$ in this case), by fitting to a $V_{xx} \propto I^3$ power law (blue dashed line). Figure adapted from Ref. 3.

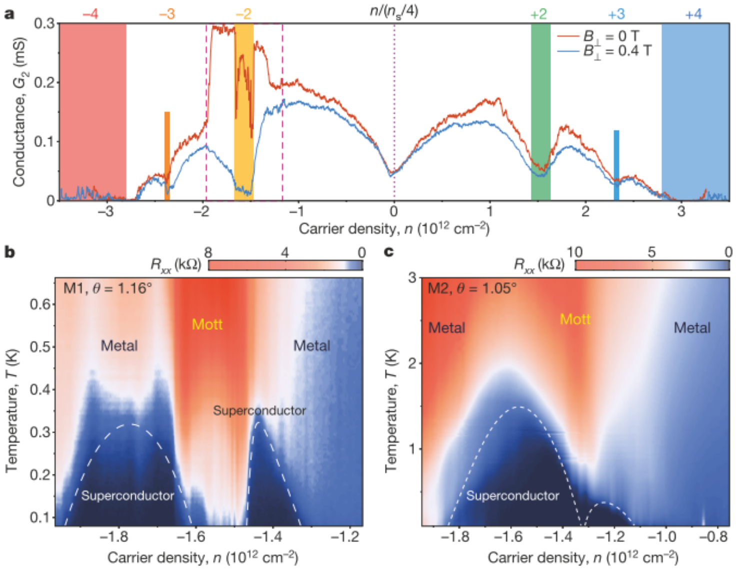

Figure 3.6: **Gate-tunability of superconductivity in tBLG.** (**A**) Two-terminal conductance $G_2 = I/V_{\text{bias}}$ of device M1 ($\theta = 1.16°$) measured in zero magnetic field (red) and with a perpendicular field of $B_\perp = 0.4$ T (blue). The curves exhibit the typical V-shaped conductance near charge neutrality ($n = 0$, vertical purple dotted line) and insulating states at the superlattice bandgaps ($n = \pm 4n_s$, the blue and red bars). They also exhibit reduced conductance at intermediate integer fillings of the superlattice owing to Coulomb interactions (other colored bars). Near a filling of -2 electrons per unit cell, there is considerable conductance enhancement at zero field that is suppressed with $B_\perp = 0.4$ T. This enhancement signals the onset of superconductivity. Measurements were performed at 70 mK with $V_{\text{bias}} = 10\ \mu$V. (**B**) Four-terminal resistance R_{xx}, measured at densities corresponding to the region bounded by the pink dashed lines in (A) as a function of temperature. Two superconducting domes are observed next to the half-filling state, which is labelled 'Mott' and centered around $-2n_s = -1.58 \times 10^{12}\ \text{cm}^{-2}$. The remaining regions in the diagram are labeled as 'metal' owing to the observed metallic temperature dependence. The highest critical temperature observed in device M1 is $T_c = 0.5$ K (as determined by 50% normal-state resistance). (**C**) Similar phase diagram for device M2, showing two asymmetric and overlapping superconducting domes. The highest critical temperature in device M2 is $T_c = 1.7$ K. Figure from Ref. 3. Note that Ref. 3 defines n_s as four carriers per moiré unit cell.

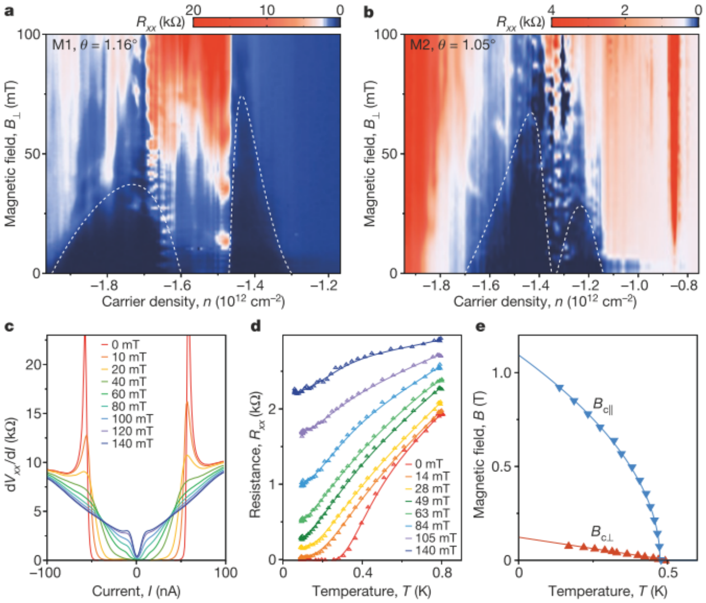

Figure 3.7: **Magnetic-field response of the superconducting state in tBLG.** (**A, B**) Four-terminal resistance as a function of density n and perpendicular magnetic field $B_\perp$ in devices (A) M1 and (B) M2. As well as the dome structures around half-filling, there are oscillatory features near the boundary between the superconducting phase and the correlated insulator phase. These oscillations are indicative of phase-coherent transport through inhomogeneous regions in the device. (**C**) Differential resistance dV_{xx}/dI as a function of DC bias current I for different $B_\perp$, measured for device M2. (**D**) $R_{xx} - T$ curves for different $B_\perp$, measured for device M1. (**E**) Perpendicular ($B_{c\perp}$) and parallel ($B_{c\parallel}$) critical magnetic field as a function of temperature for device M1. The fitting curves for $B_{c\perp}$ correspond to Ginzburg-Landau theory for a two-dimensional superconductor. $B_{c\parallel}$ is fitted to $B_{c\parallel}(0)(1 - T/T_c)^{1/2}$, where $B_{c\parallel}(0)$ is the parallel critical field at zero temperature. Measurements in (A-C) were conducted at 70 mK. Figure adapted from Ref. 3.

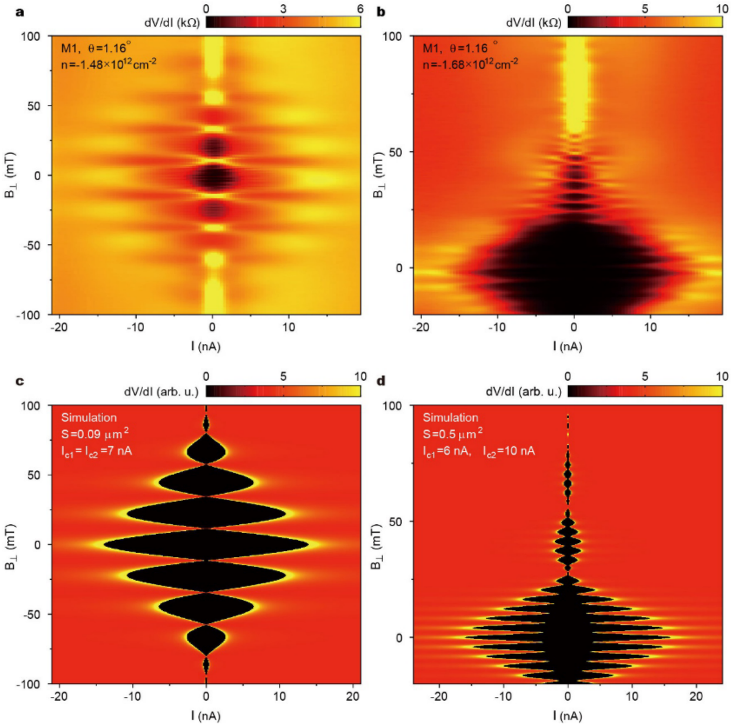

Figure 3.8: **Evidence of phase-coherent transport in superconducting tBLG.** (**A, B**) Differential resistance dV/dI versus bias current I and perpendicular field $B_\perp$, at two different charge densities n, corresponding to those in Fig. 3.7A. Periodic oscillations are observed in the critical current (identified approximately as the position of the bright peaks in dV/dI). (**C, D**) Simulations intended to reproduce qualitatively the behavior observed in A and B. Figure adapted from Ref. 3.

Each incremental improvement on device quality continues to yield new interesting areas of the phase diagram of tBLG. In these superconducting devices, in addition to the half-filled states, the devices exhibit signatures of an additional resistive state at three-quarters filling (Fig. 3.6). Given the extra two fold degeneracy of valley in the graphene, it is conceivable that one could observe additional Mott insulators at quarter fillings [77, 78]. This three-quarters-filled state is even more pronounced in a $1.14°$ device (in addition to another superconducting dome in the conduction band) (Fig. 3.9D) [14]. In Ch. 5, we will explore the nature of the correlated state at $n/n_s = 3$. In Ch. 6, we will explore evidence pointing to additional phenomena appearing at non-integer filling of the moiré superlattice.

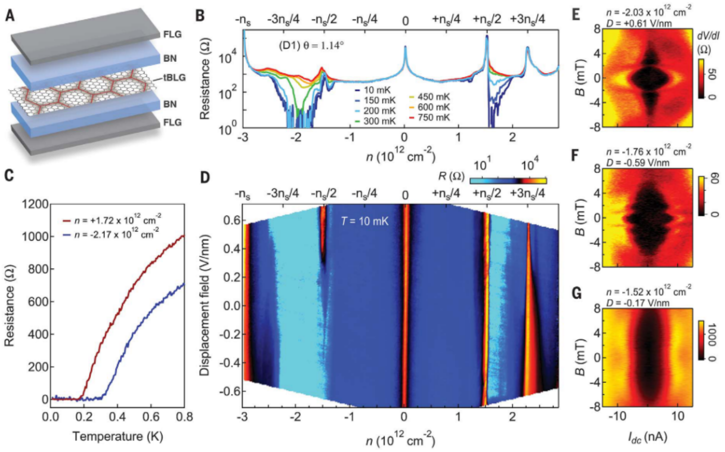

Figure 3.9: **Superconductivity in a $1.14°$ device.** (**A**) Schematic of an all-van der Waals tBLG heterostructure. tBLG is encapsulate between flakes of hBN, with encapsulating flakes of few-layer graphite acting as gates. (**B**) Temperature dependence of the resistance of device D1 over the density range necessary to fill the moiré unit cell, $n \in [-4n_s, 4n_s]$ at $D = 0$. The resistance drops to zero over a finite range of n for electron ($n > 2n_s$) and hole ($n < -2n_s$) doping. (**C**) Resistance as a function of temperature at optimal doping of the hole- and electron-doped superconductors in blue and red, respectively. (**D**) Resistance (R) of device D1 as a function of displacement field. At $-2n_s$, an insulating phase develops at positive D, whereas a superconducting phase develops at negative D. (**E** to **G**) Fraunhofer-like quantum interferences of the critical current, arising from one or more Josephson weak links within the sample, measured at (E) $n = -2.03 \times 10^{12}\ \mathrm{cm}^{-2}$ and $D = 0.61\ \mathrm{V/nm}$, (F) $n = -1.76 \times 10^{12}\ \mathrm{cm}^{-2}$ and $D = -0.59\ \mathrm{V/nm}$, and (G) $n = -1.52 \times 10^{12}\ \mathrm{cm}^{-2}$ and $D = -0.17\ \mathrm{V/nm}$. An anomalous quantum interference pattern with a minimum in I_c at zero field is observed in (G). The measured temperature is $T \approx 10\ \mathrm{mK}$ for all datasets unless otherwise noted. Figure adapted from Ref. 14. Note that Ref. 14 defines n_s as four carriers per moiré unit cell.

3.2 ABC-trilayer graphene/hexagonal boron nitride moiré superlattices

3.2.1 Introduction

In addition to tBLG, in the next few chapters we will also discuss ABC-stacked (rhombohedral) trilayer graphene that is rotationally aligned with hBN. As we will discuss in the remaining sections of this chapter, ABC-trilayer graphene/hBN (ABC-TLG/hBN) is another avenue for generating nearly flat electronic bands in a moiré superlattice. Pristine ABC-TLG, because of its cubic band and therefore a rather flat dispersion at low energy, can already exhibit strong correlations [45] and can potentially host spontaneous quantum Hall states [79]. The moiré superlattice in ABC-TLG/hBN heterostructure further creates isolated flat moiré minibands, that enhances the electron–electron correlation and topological effects in the system as we will discuss further in Sec. 3.2.3.

In a dual gated heterostructure (where we have gates both above and below the semiconducting layer), we can control both the carrier density n and the potential energy difference between the top and bottom graphene layers through an applied perpendicular displacement field D that we will discuss more thoroughly in Sec. 3.2.2. In tBLG, there is not typically a strong dependence on either the sign or magnitude of D [14] (with one notable exception being the tBLG device discussed in Ch. 5). We can at least anticipate the lack of dependence on the sign of D from the fact that (ignoring disorder in any real heterostructure), there is in principle nothing explicitly breaking the vertical symmetry of the heterostructure along the stacking direction in tBLG. The low energy flat minibands in tBLG are empirically isolated from higher order bands [46], that is expected when taking into account mutual relaxation of the two layers' lattices [80]. The low energy conduction and valence minibands have been variously predicted to meet at Dirac points at the CNP, which may [62,63] or may not [67,68] be symmetry protected. Therefore, at most, we may expect some effect of the displacement field on the bandwidth in tBLG in the case of symmetry protected Dirac-like band touchings. However, we will see that in ABC-TLG/hBN the bandwidth and topology of the moiré minibands can be conveniently controlled by the applied displacement field [2,4,20].

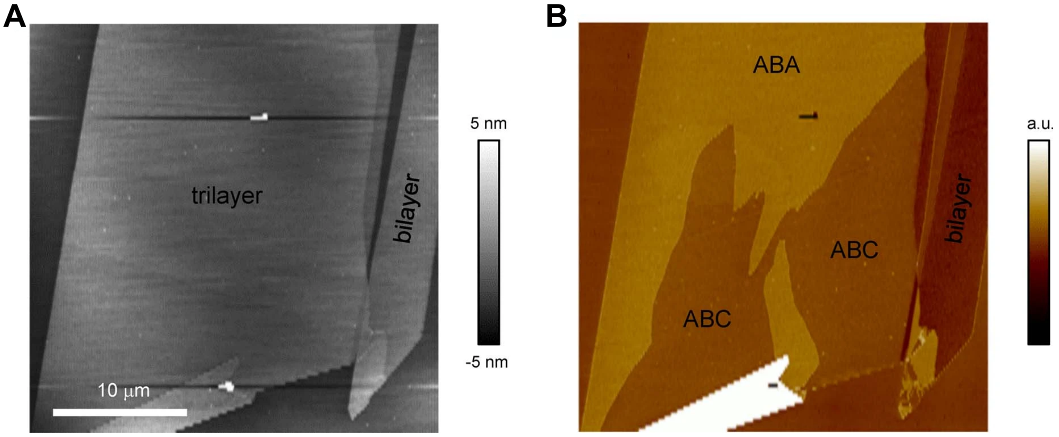

Figure 3.10: **Identifying ABC stacked domains in exfoliated TLG.** (**A**) Atomic force microscope topography image of an exfoliated TLG flake on $\mathrm{SiO_2/Si}$. (**B**) Near-field infrared image corresponding to (A) showing contrast between the ABA and ABC stacked regions.

3.2.2 Fabrication

We fabricated two ABC-TLG/hBN moiré superlattice devices following the method described in Ref. 2. There are two naturally occurring allotropes of trilayer graphene: energetically stable ABA-stacked TLG and metastable ABC-stacked TLG [81]. Near-field infrared nanoscopy is used to identify the ABC and ABA regions [82] (Fig. 3.10). In an effort to prevent potential relaxation of the ABC region in subsequent fabrication steps, the ABC region is isolated from adjacent ABA domains by atomic force microscope cutting [83]. The isolated ABC-TLG is then encapsulated in exfoliated hBN crystals using dry transfer methods, where we optically align apparent crystallographic edges of the hBN and ABC-TLG by eye to form the moiré superlattice [34, 84].

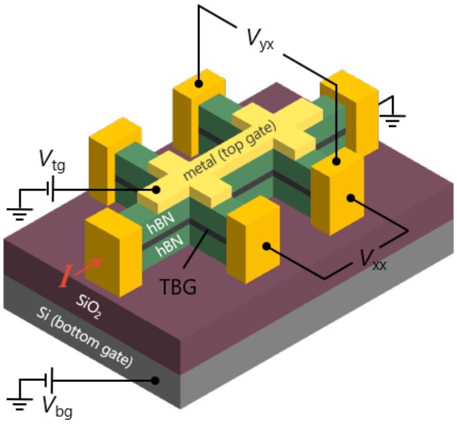

Figure 3.11: **Schematic of dual gated device.** Schematic of a dual-gated encapsulated graphene heterostructure Hall bar device and the typical measurement configuration.

The ABC-TLG/hBN heterostructures are fabricated into a dual-gated Hall bar geometry with one-dimensional edge contacts [34], a metal top gate, and a degenerately doped silicon bottom gate (Fig. 3.11) following standard nanofabrication procedures [34]. The dual-gate configuration allows us to control the carrier concentration and miniband bandwidth of the ABC-TLG/hBN heterostructure independently [17, 45, 85]: the doping relative to the charge neutrality point is set by $n = (D_{bg} - D_{tg})/e$, and the miniband bandwidth and topology are controlled by the applied vertical displacement field $D = (D_{bg}+D_{tg})/2$. Here, $D_{bg} = \epsilon_{bg}(V_{bg}-V_{bg}^0)/d_{bg}$ and $D_{tg} = -\epsilon_{tg}(V_{tg} - V_{tg}^0)/d_{tg}$ are the vertical displacement field below and above the ABC-TLG/hBN moiré superlattice, respectively, $\epsilon_{bg(tg)}$ and $d_{bg(tg)}$ are the dielectric constant and thickness of the back (top) dielectric layers, and $V_{bg(tg)}^0$ is the effective offset in the back (top) gate voltage caused by environment-induced carrier doping. e is the charge on the electron. See Appx. B for an extended discussion on mapping between gate voltages and (n, D). During fabrication, the ABC-TLG often relaxes to the lower energy ABA state during either stacking or device fabrication. However, if the ABC orientation survives fabrication, we find that the ABC stacking is stable over the course of many thermal cycles of the device.

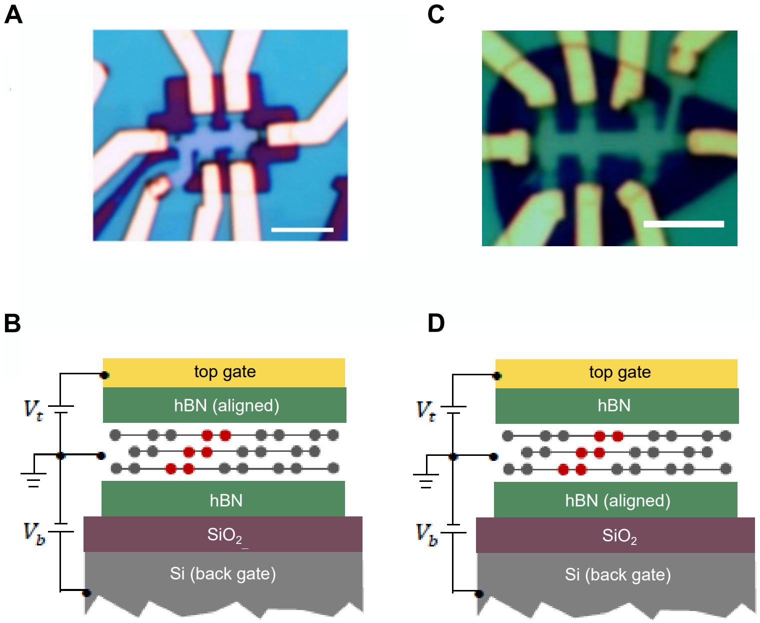

Figure 3.12: **ABC-TLG/hBN devices.** (**A**) Optical image of ABC-TLG/hBN device 1, the device that will be discussed in Ch. 4. Scale bar is 3 μm. (**B**) Schematic cross-sectional view of device 1 shown in (A). The red atoms represent on unit cell of ABC-TLG. Note that the top hBN is aligned in device 1. (**C**) Optical image of ABC-TLG/hBN device 2, the device that will be discussed in Ch. 5 and 6. Scale bar is 5 μm. (**D**) Schematic cross-sectional view of device 2 shown in (C). The red atoms represent on unit cell of ABC-TLG. Note that the bottom hBN is aligned in device 2.

It is important to note that we have defined the displacement field relative to the sign of the gate voltages. However, we really care about the energy difference between the graphene layer aligned to the hBN layer and the graphene layer that is not aligned. The two ABC-TLG/hBN devices have different cladding hBN layers aligned: device 1 (the main device discussed in Ch. 4) has its top hBN aligned with the TLG while device 2 (the main device discussed in Ch. 5 and Ch. 6) has its bottom hBN aligned with the TLG (Fig. 3.12). This difference leads to an overall sign difference between the two devices for the phenomena observed as a function of the displacement field as defined above. Because of this, it will always be explicitly stated whether the displacement field has tuned the bands to either be topologically trivial or non-trivial, which is the primary difference between the signs of the displacement field as we will discuss in the following section.

3.2.3 Band structure

Fig. 3.13 shows a schematic diagram of energetically stable ABA-stacked TLG and metastable ABC-stacked TLG. The low-energy bandstructure of ABA-stacked TLG consists of overlapping linear and quadratic dispersing bands. The transport properties are therefore governed by monolayer-like massless and bilayer-like massive quasiparticles (with a larger effective mass than in Bernal bilayer graphene) [79, 86–88]. Because of its associated mirror symmetry, an applied electric field to ABA-stacked TLG cannot open a gap, rather it leads to a tunable band overlap [17, 17, 79, 86, 89–100].

The ABC-stacking arrangement is the only arrangement in thicker N-layer graphene films (where $N > 2$) that maintains the features that make Bernal-stacked bilayer graphene's electronic structure interesting: (1) there are two low-energy sublattice sites so a two-band model provides a useful description of the physics; (2) these low-energy sublattice sites are localized in the outermost layers at sites A1 and BN; (3) these low-energy sites can be separated energetically by the application of a perpendicular electric field, leading to the formation of a gap [16,17,81,86,100]; (4) hopping between the low-energy sites is an N-step process through higher-energy states, resulting in a p^N dispersion for the conduction and valence bands, sublattice psuedospin chirality N, and a Berry phase of $N\pi$ [101]. Therefore, ABC-stacked TLG features an approximately cubic energy dispersion with the conduction and valence bands touching at a point close to the $K^{(')}$ points, and therefore a large effective mass at low energy [16, 81, 86, 89, 100–102], making ABC-stacked TLG already an interesting platform to explore strongly correlated physics. In fact, this cubic dispersion already yields relatively flat band, giving rise to strong electronic correlations and a spontaneously broken symmetry state in suspended ABC-TLG [45, 79, 81].

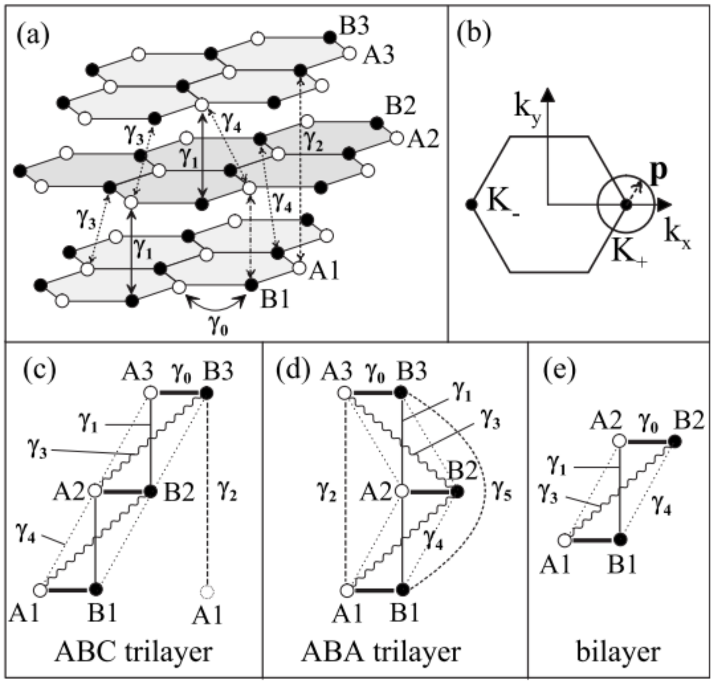
(a)
B3
A3
B2
A2
A1
B1
γ0
γ1
γ2
γ3
γ4
(b)
ky
kx
p
K-
K+
(c)
A3 γ0 B3
γ1
γ3
A2
B2
γ2
γ4
A1
B1
A1
ABC trilayer
(d)
A3 γ0 B3
γ1
γ3
B2
γ2
A2
γ5
γ4
A1
B1
ABA trilayer
(e)
A2 γ0 B2
γ1
γ3
γ4
A1
B1
bilayer

Figure 3.13: **ABC vs. ABA stacked TLG.** (**A**) Schematic of the ABC-stacked trilayer lattice containing sic sites in the unit cell, A (white circles) and B (black circles) on each layer, showing the Slonczewski-Weiss-McClure parameterization [15] of relevant couplings γ_0 to γ_4. (**B**) Schematic of the hexagonal Brillouin zone with two inequivalent valleys $\mathrm{K}^{(\prime)}$ shwoing the momentum $\mathbf{p}$ measured from the center of the valley K. (**C**) Schematic of the unit cell of ABC-stacked trilayer graphene, (**D**) ABA-stacked trilayer graphene, and (**E**) bernal stacked bilayer graphene. In (C), γ_2 describes a vertical coupling between sites B3 and A1 in different unit cells. Figure from Ref. 16.

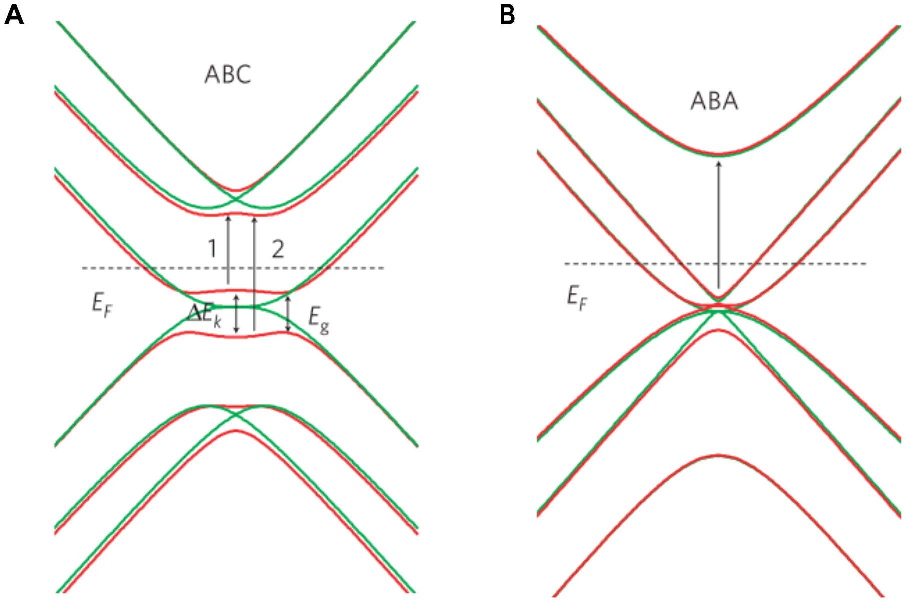

Figure 3.14: **Comparison of the bandstructure of ABA- and ABC-stacked TLG.** (**A**) The predicted bandstructure of ABC trilayer graphene with (red) and without (green) the presence of a perpendicular electric field, as calculated within the tight-binding model described in Ref. 17. Transitions 1 and 2 are the strongest optical transitions near the K-point for electron doping. (**B**) The predicted bandstructure of ABA trilayer graphene with (red) and without (green) a perpendicular electric field, as calculated within the tight-binding model described in Ref. 17. The arrow indicates the transition responsible for the main absorption peak at 0.5-0.6 eV observed in Ref. 17. Figure from Ref. 17.

With the advances made in dry-transfer techniques, we can take this one step further. In an ABC-TLG/hBN heterostructure in which the TLG is rotationally aligned to one of the hBN cladding layers, a moiré superlattice with a period of $15\ \mathrm{nm}$ folds the pristine TLG electronic band into a series of moiré minibands in the first moiré mini Brillouin zone [2, 35, 41–43, 52]. The single-particle bandstructure of ABC-TLG/hBN is described by the Hamiltonian $H = H_{\mathrm{ABC}} + V_{\mathrm{m}}$, where H_{ABC} is the Hamiltonian for ABC-TLG under a weak vertical electric field and V_{m} describes the effective potential acting on the ABC-TLG from the moiré superlattice. The ABC-TLG can be modeled using a six band model for the valley with index $+1$ [16,21,101],

$$H_{\mathrm{ABC}} = \begin{pmatrix} \Phi_V/2 & v_0\pi^\dagger & -v_4\pi^\dagger & v_3\pi & 0 & \gamma_2 \\ v_0\pi & \Phi_V/2 & \gamma_1 & -v_4\pi^\dagger & 0 & 0 \\ -v_4\pi & \gamma_1 & 0 & v_0\pi^\dagger & -v_4\pi^\dagger & v_3\pi \\ v_3\pi^\dagger & -v_4\pi & v_0\pi & 0 & \gamma_1 & 0 \\ 0 & 0 & -v_4\pi & \gamma_1 & -\Phi_V/2 & v_0\pi^\dagger \\ \gamma_2 & 0 & v_3\pi^\dagger & -v_4\pi & v_0\pi & -\Phi_V/2 \end{pmatrix}, \tag{3.13}$$

where $v_i = (\sqrt{3}/2)a\gamma_i/\hbar$, $a \sim 2.46$ angstrom is the lattice constant, $\pi = p_x + ip_y$, and Φ is the energy difference between the top and bottom layer of the ABC-TLG. We have the following tight-binding parameters shown in Fig. 3.13: nearest-neighbor intralayer hopping γ_0, nearest neighbor interlayer hopping γ_1, direct hopping between trilayer low-energy sites γ_2, hopping between lower-energy sites of the AB-stacked bilayer γ_3, and coupling between low- and high-energy sites located on different layers γ_4 [101]. We take $\mathbf{p} = (p_x, p_y)$ to be the momentum measured with respect to the center of the valley. The tight binding parameters can be obtained from a local density approximation *ab initio* calculation [103] to have values $(v_0, \gamma_1, \gamma_2, v_3, v_4) = (2676, 380, 8.3, 260, 104)$ meV.

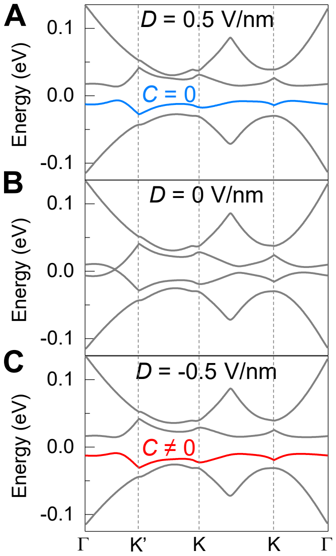

Figure 3.15: **Single-particle bandstructure of ABC-TLG/hBN.** (**A, B, and C**) Calculated single-particle bandstructure of ABC-TLG/hBN in the K valley for displacement fields $D/\epsilon_0 = 0.5$, 0, and -0.5 V/nm. At $D/\epsilon_0 = 0.5$ V/nm, a finite bandgap separates the conduction and valence minibands. The highest energy valence miniband is topologically trivial with $C = 0$. The bandgap closes at $D/\epsilon_0 = 0$ V/nm. At $D/\epsilon_0 = -0.5$ V/nm, the miniband invert to generate a new bandgap. The highest energy valence miniband becomes topologically nontrivial with a finite Chern number. The minibands of the K' are time-reversed pairs of the K valley minibands and have opposite Chern numbers.

Using the same model for the moiré hopping term as in Ref. 103, we can now calculate the single-particle bandstructure of ABC-TLG/hBN (Fig. 3.15). Figs. 3.15C, D, and E display the calculated single-particle bandstructure in ABC-TLG/hBN for the K valley at $D/\epsilon_0 = 0.5$ V/nm, 0 V/nm, -0.5 V/nm, respectively [21]. A displacement field of $D = \pm 0.5$ V/nm corresponds approximately to an energy difference between the layers of ABC-TLG of $\Phi = \pm 25$ meV. Without an applied displacement field, the low energy conduction and valence miniband overlap. However, with the application of a displacement field, the first hole miniband becomes well isolated from other bands. In fact, the bandwidth and topology of the moiré minibands in ABC-TLG/hBN can be controlled by the vertical displacement field D. At $D/\epsilon_0 = 0.5\ \mathrm{V/nm}$, a finite bandgap separates the conduction and valence miniband. The highest-energy valence miniband is flat with a bandwidth as narrow as $20\ \mathrm{meV}$, and it is topologically trivial with $C = 0$. At $D/\epsilon_0 = -0.5\ \mathrm{V/nm}$, a bandgap reopens, with band topology changed relative to positive D field. Specifically, the highest-energy valence miniband becomes topologically nontrivial with a finite Chern number and a narrow bandwidth of $20\ \mathrm{meV}$. This single-particle calculation will always predict that the valence miniband should have a Chern number $C = 3$ [4, 20, 21]. However, upon including interactions, this Chern number can become renormalized as we will discuss in Ch. 5. The electronic states in the K' valley are time reversed pairs of those in the K valley, and the topological minibands have opposite Chern numbers. The valence miniband, because it has a smaller bandwidth, should have stronger electron-electron interactions compared to the conduction miniband [4, 20, 104–106]. The on-site Coulomb repulsion energy, on the other hand, can be estimated by $U \approx e^2/(4\pi\epsilon_0\epsilon\lambda)$. For the moiré lattice constant $\lambda = 15\ \mathrm{nm}$ and an hBN dielectric constant $\epsilon = 4$, U is around $25\ \mathrm{meV}$, which is larger than the bandwidth of the valence miniband. This dominant on-site Coulomb repulsion can lead to Mott insulator states in the flat and isolated hole miniband as we will discuss in the following section [2, 104, 107]. Recent theories suggest that correlated topological phenomena could emerge in such graphene moiré superlattices, where a non-trivial band topology coexists with the nearly flat moiré miniband [4, 20, 104, 105].

3.2.4 Prior experimental work

Prior to the work that will be discussed in Ch. 4- 6, ABC-TLG/hBN had been shown to demonstrate strongly correlated physics in Ref. 2. A ABC-TLG/hBN Hall bar was fabricated following a similar procedure as that discussed in Sec. 3.2.2 (Fig. 3.16). Transport measurements can be used to check that the TLG retained its rhombohedral stacking through fabrication of the device. One can look at how the resistance at the CNP varies as the displacement field is changed. In an ABC-TLG device, the resistance increased from $\sim 3\ \mathrm{k\Omega}$ to $\sim 130\ \mathrm{k\Omega}$ as the displacement field was increased, indicating the formation of a bandgap. However, a ABA-TLG device displays very little dependence on the displacement field: the resistance increased from $500\ \Omega$ to $1\ \mathrm{k\Omega}$ with an applied displacement field of similar magnitude.

Another reliable indicator of the stacking is a Landau fan diagram (Fig. 3.18). The fan diagram for an ABC-TLG sample shows quantum Hall states of $\nu = 6$, 10, 14, 18..., indicating a twelve-fold zeroth Landau level, which is characteristic of ABC-TLG [102]. The Landau fan is more complicated for an ABA-TLG sample. Such a device shows Landau levels for both the bilayer-like and monolayer-like subbands, allowing for easy distinction from an ABC-TLG device.

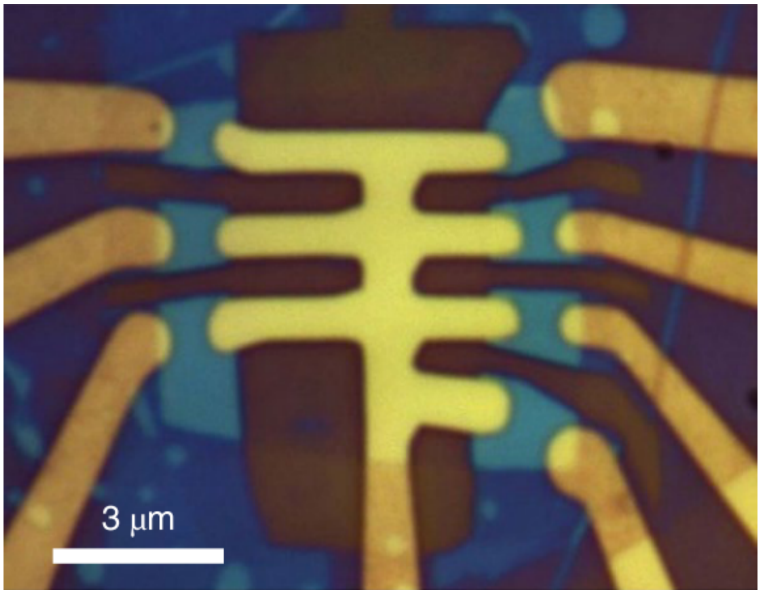

Figure 3.16: **Optical image of previously studied ABC-TLG/hBN moiré superlattice device.** Optical image of a dual-gated ABC-TLG/hBN moiré superlattice device. The bottom hBN crystal is aligned with the ABC-TLG in this device. Figure from Ref. 2.

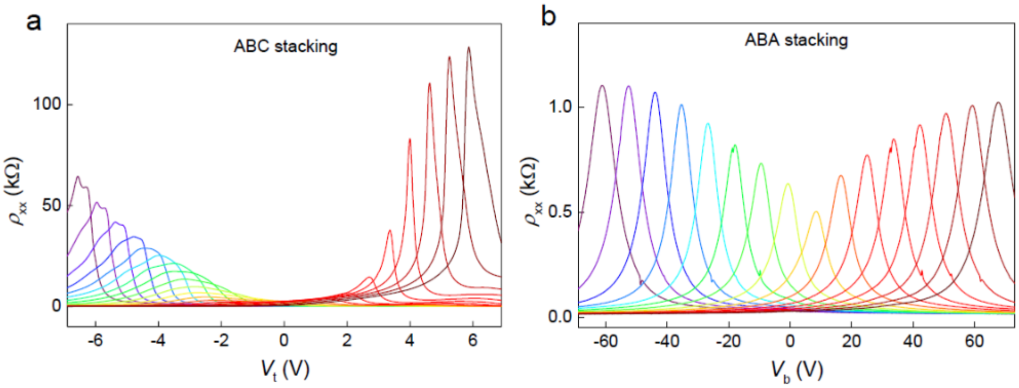

Figure 3.17: **Gate-dependent resistivity of ABC- and ABA-TLG.** (**A**) Resistivity of ABC-TLG as a function of V_{tg} varying V_{bg} from -50 V to 50 V. (**B**) Resistivity of ABA-TLG as a function of V_{bg} varying V_{tg} from -3 V to 3 V. Data were obtained at $T = 50$ K. Figure from Ref. 2.

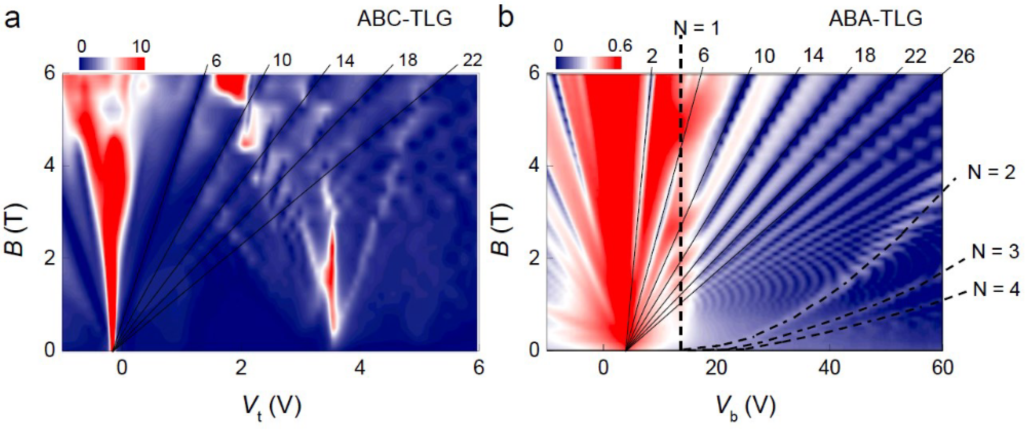

Figure 3.18: **Landau fan of ABC- and ABA-TLG/hBN moiré superlattices.** (**A**) Landau fan of ABC-TLG/hBN showing well-resolved quantum Hall states at filling factors $\nu = 6, 10, 14, 18...$, unambiguously confirming that the ABC-stacking has been retained in this device. (**B**) ABA-TLG is characterized by two sets of Landau levels, one from the bilayer-like subband and the other from the monolayer-like subband. The Landau levels of the bilayer-like and monolayer-like subbands are marked by solid and dashed lines, respectively. Figure from Ref. 2.

Although one can clearly see that the ABC-TLG/hBN device is indeed a superlattice from the Landua fan, let's take a step back and look at the simplest way one can typically diagnose this. By looking at the dependence of the longitudinal resistivity on carrier density, one can see if there are any additional peaks besides the CNP (Fig. 3.19A). In such a measurement, there are a number of additional resistance peaks. The resistance peaks that appear symmetrically about the CNP at -4.2 V and 3.6 V are the fully filled points (FFP), which corresponds to four carriers per moiré unit cell. Treating the gates with a parallel plate capacitance model, these peaks correspond to a density of $n_{\text{FFP}} = 2.1 \times 10^{12}$ cm^{-2}. As discussed in Sec. 1.2, this density corresponds to a moiré superlattice period of $\lambda = \sqrt{8/(\sqrt{3}n_{\text{FFP}})} = 15$ nm. One can fit the Landau levels for an independent and more accurate determination of n_{FFP} and λ [2].

There is a surprising additional resistance peak at half filling of the valence miniband that is in contrasts to a typical band insulator, where the resistance is close to a minimum at half filling. Such a resistance peak is indicative of a strongly correlated electronic state. In this measurement, the back gate gate voltage (V_{bg}) was set to 0 V.

One can strongly enhance these correlated states by suppressing the bandwidth of the valence miniband through the application of a displacement field. This can be achieved by tuning V_{bg} (Fig. 3.19B). At a much larger displacement field, there are two well defined resistance peaks at 1/2 and 1/4 filling. One can then measure ρ_{xx} as a function of V_{bg} and V_{tg} ((Fig. 3.19C), and then take line cuts at constant density to see how these resistance peaks depend on D (Fig. 3.19D). The resistivity at the CNP approximately monotonically increases with D, consistent with our expectation that D will open a bandgap at the CNP. For the two correlated resistance states, there is similar dependence with D: a sharp increase in resistance followed by a slight decrease with increasing magnitude of D. This behavior is consistent with theoretical calculations that show an initial decrease and subsequent increase in the bandwidth of the valence miniband with increasing D [2]. These calculations even predict a slight asymmetry with the sign of D, as is seen in the data.

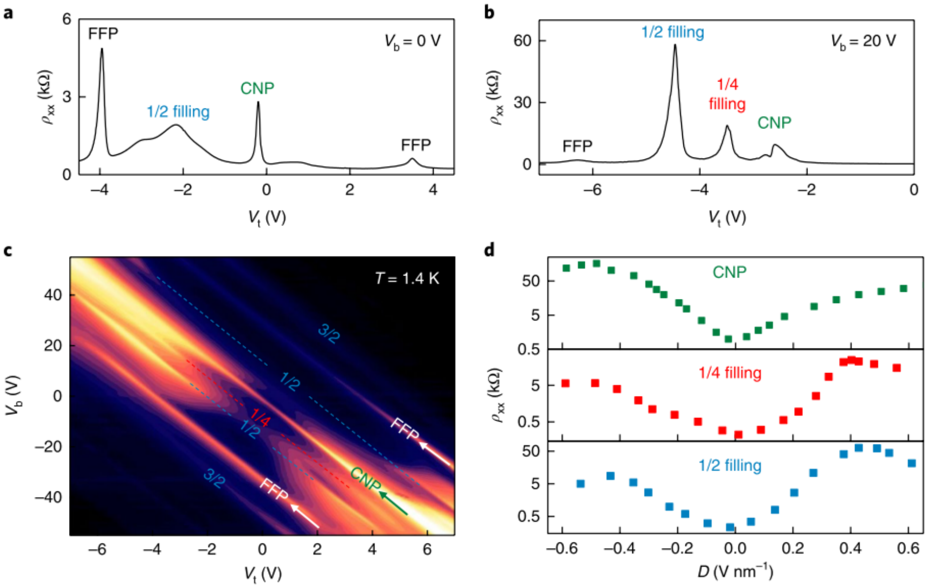

Figure 3.19: **Transport of gate-tunable Mott state.** (**A, B**) Top-gate-dependent resistivity of ABC-TLG/hBN moiré superlattice when (A) $V_{bg} = 0$ V and (B) 20 V. (**C**) Resistance as a function of V_{tg} and V_{bg}. The color scale is from 10 Ω to 100 kΩ in a logarithmic scale. The highlighted straight lines correspond to the charge-neutrality point (CNP), 1/4 filling, 1/2 filling, fully-filled point (FFP) and 3/2 filling resistance peaks. (**D**) Resistivity at the CNP (green), 1/4 filling on the hole side (red) and 1/2 filling on the hole side (blue) as a function of the displacement field D. The insulating behavior at 1/4 and 1/2 fillings, corresponding to one and two charges per lattice site, provide the defining signature of a Mott insulator. Figure from Ref. 2.

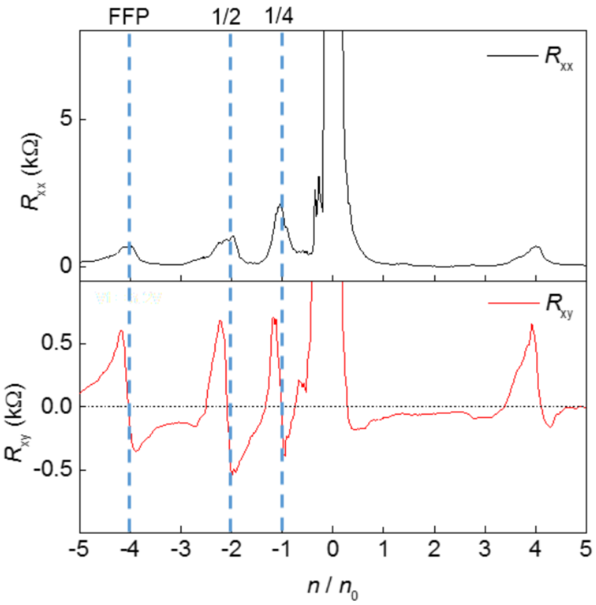

Figure 3.20: **Landau fan of ABC- and ABA-TLG/hBN moiré superlattices.** R_{xx} and R_{xy} as a function of n/n_s and fixed $D = 0.4\ \mathrm{V/nm}$ and $B = 1\ \mathrm{T}$. At fixed D, the band structure does not change while tuning the carrier density. There are resistance peaks at 1/4, 1/2, and full fillings in R_{xx} and zero R_{xy} corresponding to zero Hall density. n_s corresponds to one electron per unit cell. Figure from Ref. 2.

Ref. 2 has clearly demonstrated that, through the ability to tune the bandwidth of the low energy bands by applying a displacement field, one can tune ABC-TLG/hBN such that it exhibits strongly correlated electronic states. While it has shown that the correlated states at 1/2 and 1/4 filling are potentially gapped, it has not further explored the nature of the ground states at these fillings. We will explore the nature of these correlated states in Ch. 4 and 5. Additionally, in Ch. 6, we will explore a correlated state occurring at non-integer filling not seen in Ref. 2.

Chapter 4

Superconductivity in ABC-TLG/hBN

4.1 Introduction

It is often speculated that high-T_c superconductivity arises in a doped Mott insulator [77] as described by the Hubbard model [78, 108, 109]. An exact solution of the Hubbard model, however, is extremely challenging owing to the strong electron–electron correlations in Mott insulators. Therefore, it is highly desirable to study a tunable Hubbard system, in which systematic investigations of the unconventional superconductivity and its evolution with the Hubbard parameters can deepen our understanding of the Hubbard model.

As was discussed in the previous chapter, in addition to correlated insulating states, Ref. 3 found tBLG to exhibit clear superconductivity proximate in density to the candidate Mott insulator at half filling of the valence minibands. We have discussed the existence of similar correlated insulating states in the isolated conduction miniband of ABC-TLG/hBN in Sec. 3.2.4. Unlike in tBLG, theoretical calculations show ABC-TLG/hBN has the added benefit that the miniband bandwidth can be tuned by an applied displacement field (as discussed in Sec. 3.2.3), making it an attractive platform to explore correlated behavior emerging in a tunable triangular Hubbard model [2, 4]. In this chapter (which is adapted from Ref. 110), we will discuss signatures of tunable superconductivity in an ABC-TLG/hBN heterostructure around the $1/4$-filling correlated insulating state, corresponding to one hole per unit cell in the moiré superlattice, that emerge below 1 K. Two apparent superconducting domes are observed with electron and hole doping relative to the $1/4$-filling correlated insulating state. We will discuss transitions between superconducting, insulating, and metallic states in the ABC-TLG/hBN heterostructure which are readily controlled by the applied displacement field.

4.2 Basic characterization

Measurements were performed using ABC-TLG/hBN device 1 (shown in Fig. 3.12). The device was fabricated according to the procedure described in Sec. 3.2.2. A schematic of the triangular ABC-TLG/hBN moiré superlattice is shown in Fig. 4.1B. Fig. 4.1C displays the calculated energy dispersion of the lowest electron and hole minibands at the K point for an ABC-TLG/hBN heterostructure in which the moiré superlattice is formed with the top hBN flake and the potential energy difference between the bottom and top graphene layers is $2\Delta = -20\mathrm{meV}$ (corresponding to the vertical displacement field $D/\epsilon_0 = -0.4\ \mathrm{V/nm}$ [2]), where the negative sign denotes that the displacement field is pointing downward). In the ABC-TLG/hBN moiré superlattice, each miniband comprises a time-reversed pair of dispersions centred around the K and K' valleys in the original graphene Brillouin zone, where $E_{\mathrm{K}}(p) = E_{\mathrm{K}'}(-p)$, for a combined fourfold spin and valley degeneracy. According to our theoretical calculations, strong asymmetry between an electron and a hole exists in the ABC-TLG/hBN system. The first hole miniband (shown in red in Fig. 4.1C) is narrower and better separated from the other bands than the first electron miniband (shown in blue in Fig. 4.1C). At $2\Delta = -20\ \mathrm{meV}$, the first hole miniband has a bandwidth W of $11.7\ \mathrm{meV}$ and is separated from other bands by over $10\ \mathrm{meV}$. The on-site Coulomb repulsion energy can be estimated by $U \approx e^2/(4\pi\epsilon_0\epsilon\lambda)$. For the moiré lattice constant $\lambda = 15\ \mathrm{nm}$ and an hBN dielectric constant $\epsilon = 4$, $U \approx 25\ \mathrm{meV}$, which is larger than the value of W. This dominant on-site Coulomb repulsion can lead to Mott insulator states in the flat and isolated hole miniband [2, 104, 107].

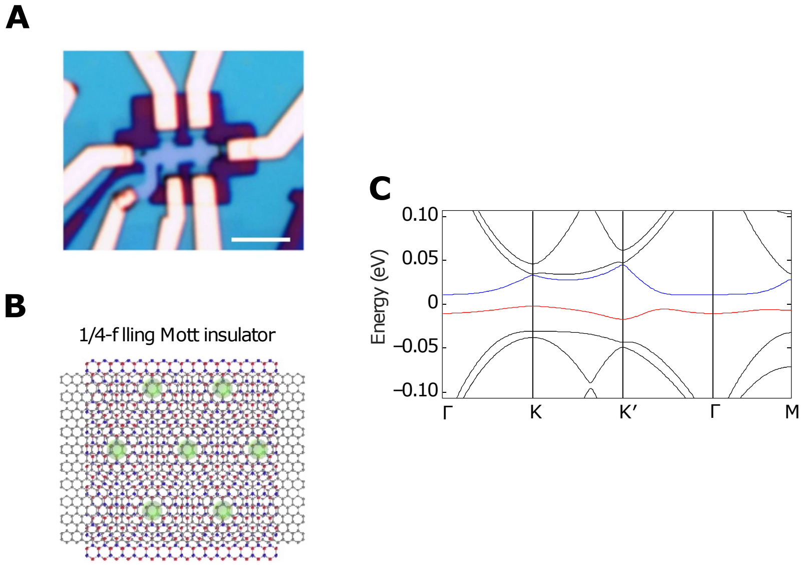

Figure 4.1: **Trilayer graphene/hBN moiré superlattice.** (**A**) Optical image of ABC-TLG/hBN device 1 with the top and bottom gates. Scale bar is 3 μm. (**B**) A schematic of the triangular ABC-TLG/hBN moiré superlattice and the 1/4-filling correlated insulating state, which corresponds to one hole per superlattice unit cell. (**C**) The single-particle energy dispersion of the lowest electron and hole minibands in the ABC-TLG/hBN superlattice with an effective potential energy difference between the bottom and top graphene layers of $2\Delta = -20\,\mathrm{meV}$, which can be generated by a vertical displacement field of $-0.4\,\mathrm{V/nm}$. It features a narrow and isolated hole miniband, shown highlighted in red. The first electron miniband is highlighted in blue.

The gate-dependent four-probe longitudinal resistance (R_{xx}) at a vertical displacement field of $-0.4\,\mathrm{V/nm}$ in ABC-TLG/hBN device 1 is shown in Fig. 4.2a for a temperature of 5 K. Prominent correlated insulating states are observed at $1/4$ and $1/2$ fillings of the hole miniband, corresponding to one hole and two holes per superlattice unit cell, respectively. R_{xx} as a function of V_{tg} and V_{bg} (Fig. 4.2e) shows the evolution of the charge neutral point (CNP), $1/4$ filling, $1/2$ filling, and full filling point (FFP) resistance peaks with the displacement field D. For relatively large D, resistance peaks can be clearly identified at $1/4$ and $1/2$ fillings of the valence miniband. As suggested above, the different behaviours of the positive and negative displacement fields arises from the fact that the moiré superlattice exists only at the top hBN/TLG interface in device 1.

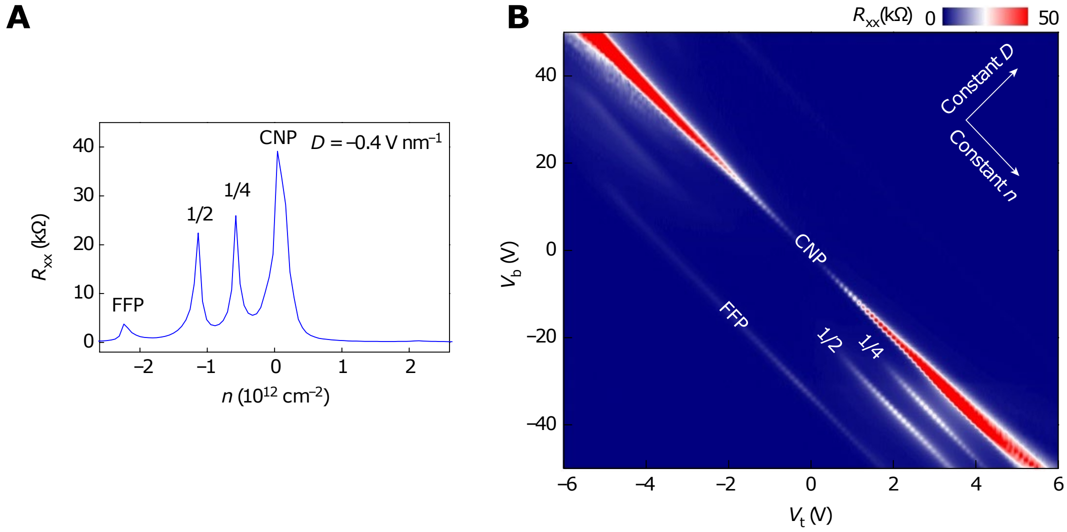

Figure 4.2: **Correlated insulators in trilayer graphene/hBN moiré superlattice.** (**A**) R_{xx} as a function of carrier density shows prominent correlated insulating states at 1/4 and 1/2 fillings with $D = -0.4\ \mathrm{V/nm}$ at $T = 5\ \mathrm{K}$. (**B**) R_{xx} as a function of V_{tg} and V_{bg} at $T = 5\ \mathrm{K}$. The resistance peaks at 1/4 and 1/2 fillings of the first hole miniband can be clearly identified for relatively large D.

4.3 Signatures of superconductivity.

We first focus on a state close to the well-developed $1/4$-filling correlated insulator with $D = -0.54\ \mathrm{V/nm}$ and $n = -5.4 \times 10^{11}\ \mathrm{cm}^{-2}$ (The carrier density at full filling is $4n_s = -2.24 \times 10^{12}\ \mathrm{cm}^{-2}$). The first signature of superconductivity is a sharp drop of R_{xx} from about $5\ \mathrm{k\Omega}$ to about $300\ \Omega$ within the narrow temperature range of $2\ \mathrm{K}$ to $0.2\ \mathrm{K}$. The resistance then remains nearly constant from $0.2\ \mathrm{K}$ down to $0.04\ \mathrm{K}$. An empirical fit to the Aslamazov–Larkin formula [111] of the $R_{xx} - T$ curve, shown as the solid line in Fig. 4.3A, yields an estimated superconducting T_c of $0.65\ \mathrm{K}$. Non-zero residual resistance can appear in measurements of microscopic superconducting samples with poor electrical contacts, as reported in some magic-angle twisted bilayer graphene samples [14] and other two-dimensional superconductors [112, 113]. The residual resistance may also have a contribution from non-equilibrium quasiparticles in microscopic devices [114].

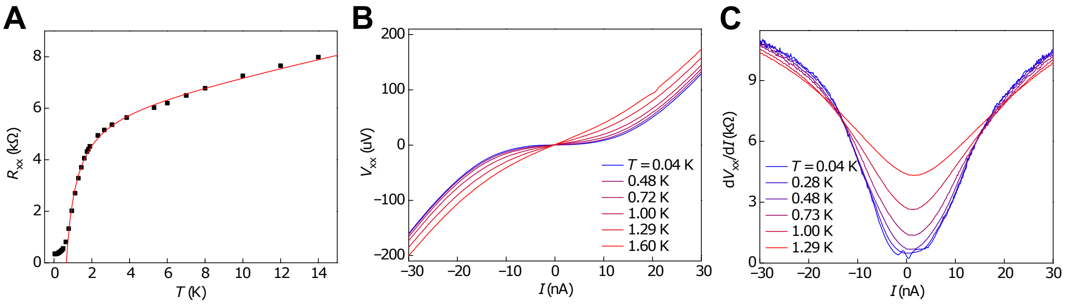

Figure 4.3: **Signatures of superconductivity in ABC-TLG/hBN.** (**A**) The $R_{xx} - T$ curve at $D = -0.54$ V/nm and $n = -5.4 \times 10^{11}$ cm^{-2} shows characteristic behavior of a superconducting transition. An empirical fit to the Aslamazov-Larkin formula (red line) yields an estimated superconducting transition temperature of 0.65 K. (**B**) $I - V$ curves at different temperatures show a plateau below the critical current at about 10 nA for temperatures below 0.3 K. This plateau region tilts and becomes close to linear at higher temperature, characteristic of a superconducting transition. (**C**) $dV_{xx}/dI - I$ curves at different temperatures. A critical current of about 10 nA is observed at the lowest temperatures.

A second signature of superconductivity comes from measurements of the current–voltage relationship ($I - V$ curves), as displayed in Fig.4.3b. At the lowest temperatures, the $I - V$ curves show a plateau below a critical current of about 10 nA. The plateau region tilts and exhibits nearly linear behaviour at higher temperature. Fig.4.3c shows the differential resistance dV/dI as a function of driving current, which provides a better visualization of the critical current of about 10 nA below 0.3 K and the evolution to a normal metal behaviour above about 1 K.

4.4 Searching for coherent oscillations

Zero resistance is not a sufficient criteria to label a material a superconductor. The material must additionally demonstrate either the Meissner effect or coherent transport. However, two-dimensional superconductors cannot generate sufficient screening field to exhibit a Meissner effect: we expect a screening field $B_{\text{screen}} \sim Bwt/\lambda^2$ where λ is the London penetration depth, w is the sample width, and t is the thickness of the material [115–117]. With the assumption of any reasonable London penetration depth, $B_{\text{screen}} \ll B$; any external magnetic field approximately uniformly penetrates the sample. However, this penetration does not prevent such a sample from exhibiting coherent oscillations when a Josephson junction is formed [115–117]. Given that we have not explicitly fabricated the sample in an explicit Josephson junction geometry, we will rely on inhomogeneity within the sample to provide a superconducting weak link. Coherent oscillations with periodicities of $\sim 5 - 10$ mT were observed in a tBLG sample under the same circumstances [3].

Fig. 4.4a displays the critical current behaviour in $dV/dI - I$ curves as a function of the perpendicular magnetic field $B_\perp$ at a base temperature of $40\ \mathrm{mK}$. There is a clear suppression of the apparent superconductivity by the magnetic field, where the superconductivity almost disappears at $B_\perp \approx 0.7$ T. Between 0.7 T and 2 T, the differential resistance at low bias is relatively small and it exhibits a weak nonlinear $I - V$ behaviour (Fig. 4.4b). This field scale is many times larger than that of the oscillations of tBLG and is unlikely resulting from phase coherent transport.

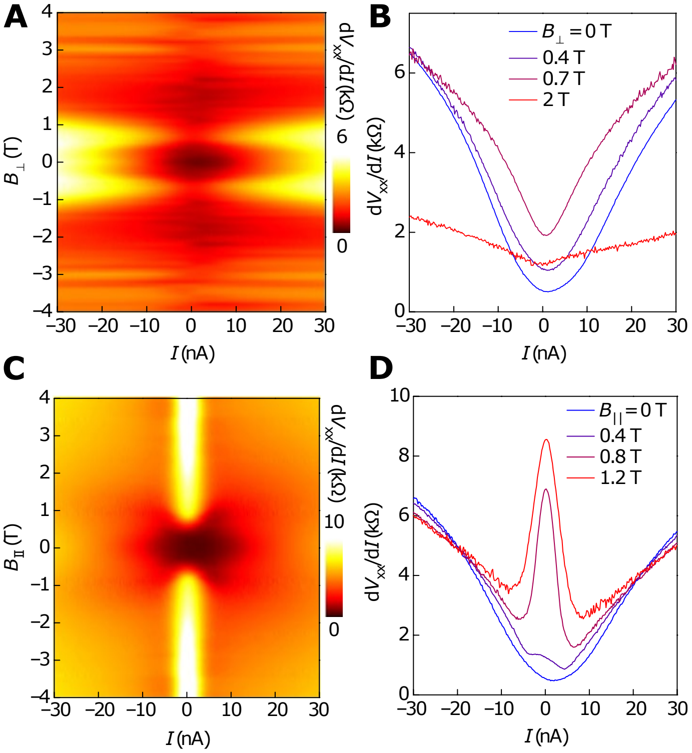

Figure 4.4: **Searching for coherent oscillations.** (**A**) The dV_{xx}/dI color plot as a function of direct current (DC) bias and perpendicular magnetic field at $T = 0.04$ K (**B**) Line cuts of (A) at $B_\perp = 0$ T, 0.4 T, 0.7 T, and 2 T. (**C**) The dV_{xx}/dI color plot as a function of direct current (DC) bias and in-plane magnetic field at $T = 0.04$ K (**D**) Line cuts of (C) at $B_{||} = 0$ T, 0.4 T, 0.8 T, and 1.2 T. A symmetrized $V_{xx}(B) = [V_{xx}(B) + V_{xx}(-B)]/2$ is presented to removed any possible V_{xy} component in all panels

Fig. 4.4c further displays the in-plane magnetic field dependence of the critical supercurrent behaviour at $40\ \mathrm{mK}$. Fig. 4.4c displays the $dV/dI - I$ curves as a function of the in-plane magnetic field, $B_{||}$, at $40\ \mathrm{mK}$. The apparent superconductivity in the device is suppressed by $B_{||}$, with the plateau vanishing above 0.7 T. At the same time, we observe an anomalous resistance peak close to zero current bias at large in-plane magnetic field. We do not know its origin and further experimental and theoretical studies will be needed to fully understand this in-plane magnetic field dependence.

4.5 Mapping the phase diagram

Next, we examine the superconductivity phase diagram as a function of T and n. We fix D at two different values: $D = -0.54\ \mathrm{V/nm}$, where both the $1/2$- and $1/4$-filling Mott states appear (Fig. 4.5a); and $D/\epsilon_0 = -0.17\ \mathrm{V/nm}$, where only the $1/2$-filling Mott state appears (Fig. 4.5b).

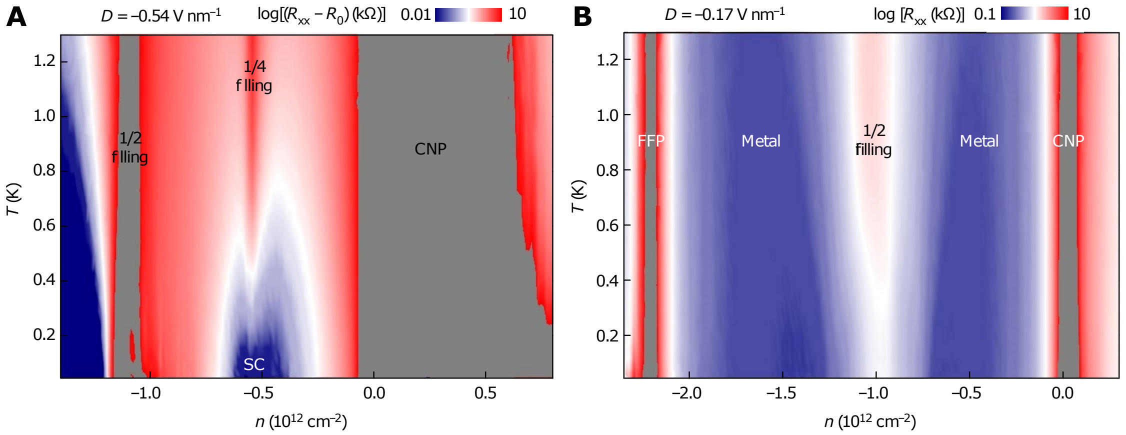

Figure 4.5: **Carrier-density-dependent phase diagram.** R_{xx} as a function of carrier density and temperature at (**A**) $D = -0.54\ \mathrm{V/nm}$ and (**B**) $D = -0.17\ \mathrm{V/nm}$. The superconducting phase emerges at low temperature near the 1/4-filling Mott state for $D = -0.54\ \mathrm{V/nm}$. Only the 1/2-filling Mott state exists for $D = -0.17\ \mathrm{V/nm}$, and no superconductivity exits at base temperature. Both the superconducting phase and the metallic phase show very small resistance values at base temperature, but they can be distinguished by the supercurent behaviour in the $I - V$ and $dI - dV$ curves and by the $R - T$ dependence (Fig. 4.6b vs. Fig. 4.6d). $R_0 = 380\ \Omega$.

At $D/\epsilon_0 = -0.54\ \mathrm{V/nm}$, two apparent superconducting domes emerge at low temperature near the $1/4$-filling Mott state: superconductivity appears to exist for both electron and hole doping relative to the $1/4$-filling Mott state, analogous to the behaviour seen in high-T_c copper oxides [109]. This also resembles the behaviour observed in magic-angle twisted bilayer graphene around $1/2$ hole filling [3], although more recent work suggests that lower disorder produces only one dome, at slight hole doping relative to the Mott insulator [14]. The presence of superconductivity even at $1/4$-filling in our measurements may be attributed to the charge inhomogeneity in the trilayer graphene devices, that can lead to patches of superconductivity when the average filling corresponds to a Mott insulator, as seen at higher temperatures [110] .

The behaviour around the $1/2$-filling Mott state is less clear, perhaps reflecting a weaker superconducting state. The resistance remains rather high on the electron-doping side of the $1/2$-filling point. The $R - T$ curve for hole doping relative to the $1/2$-filling Mott state is consistent with a phase transition, but the $I - V$ and $dI/dV - V$ are not consistent with a superconducting state [110]. Further studies will be required to establish the nature of this state.

At $D/\epsilon_0 = -0.17$ V/nm, where only the $1/2$-filling Mott state exists, the phase diagram shows no superconductivity even at base temperature. The metal phases show very small resistance values at base temperature, but they can be distinguished from superconducting phases by their $R - T$ dependencies and the lack of nonlinear behaviour in the $I - V$ and dV/dI curves.

The ABC-TLG/hBN system offers a platform with which to investigate the evolution of superconductivity where the bandstructure of the miniband can be continuously tuned by D. We fix the carrier concentration at a constant $n = -5.2 \times 10^{11}\ \mathrm{cm}^{-2}$, which corresponds to a small electron doping relative to the $1/4$-filling Mott states, and examine the electronic phases at different D. The four-probe resistance R_{xx} as a function of D and T is displayed as a two-dimensional color plot in Fig. 4.6a. At small D where the miniband bandwidth is relatively broad, the system exhibits a metallic phase. Fig. 4.6b shows the $R_{xx} - T$ plot at $D/\epsilon_0 = 0$ V/nm, where the resistance is low and constant, suggesting that impurity scattering dominates at very low temperature. When D is increased to a positive value, we observe a phase transition from the metallic state to a correlated insulating state caused by the field-induced narrowing of the hole miniband [2]. A line cut at $D/\epsilon_0 = 0.45$ V/nm of Fig. 4.6a shows the insulating $R_{xx} - T$ behaviour of such a correlated insulating state (Fig. 4.6c). Superconductivity, however, never appears for positive D at this n. As D is decreased, we observe an evolution from the metallic phase ($D/\epsilon_0 > -0.28$ V/nm) to a candidate superconducting phase ($D/\epsilon_0 < -0.53$ V/nm) (we limited $|D|$ to 0.6 V/nm to avoid possible damage to the gate dielectrics). The transition region between $D/\epsilon_0 = -0.28$ V/nm and -0.53 V/nm exhibits complex behaviour, and we refer to it as a “correlated resistive state” because the overall resistance is relatively high compared with the metallic region. Fig. 4.6e shows several $R - T$ curves with different behaviours in this transition region.

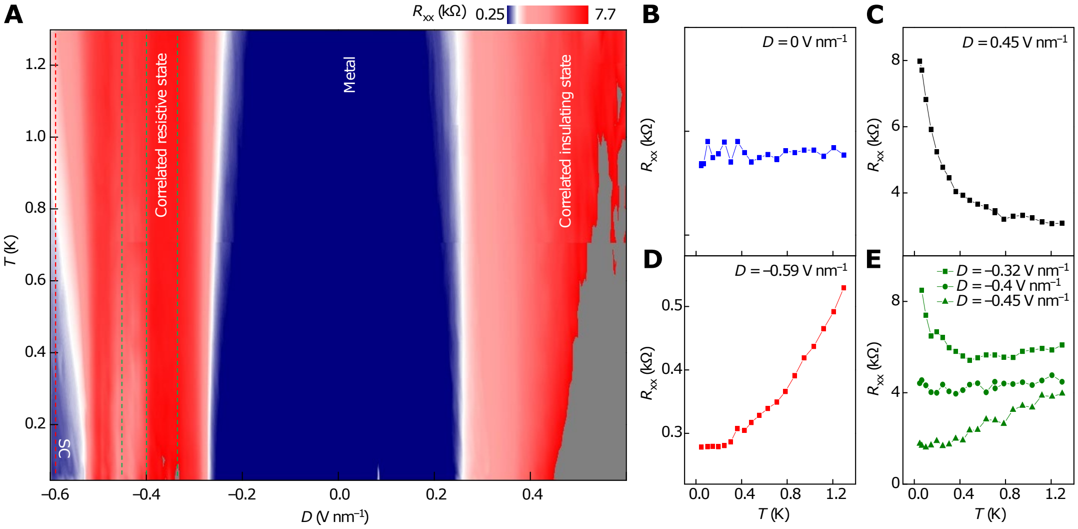

Figure 4.6: **Tunable electronic phases with the displacement field.** (**A**) R_{xx} as a function of D and T at fixed doping $n = -5.2 \times 10^{12}\ \mathrm{cm}^{-2}$ relative to the CNP, corresponding to slight electron doping relative to 1/4-hole filling. D modifies the band structure of the minibands in ABC-TLG/hBN, and therefore the charge correlations. As a function of D, the system can be tuned across four different electronic states from left to right: superconducting, correlated resistive state, metal, and correlated insulating state. (**B-E**) Vertical line cuts of (A) at selected D values to illustrate the $R_{xx} - T$ behavior of different electronic states. (B) The metallic state at $D = 0\ \mathrm{V/nm}$ shows a low and constant resistance owing to the dominating impurity scattering. (C) The correlated insulating state at $D = 0.45\ \mathrm{V/nm}$ shows an increased resistance at lower temperature. (D) The superconducting state at $D = -0.59\ \mathrm{V/nm}$ shows a rapidly decreasing resistance to a constant residual value at lower temperature. (E) The transition region between $D = -0.28\ \mathrm{V/nm}$ and $D = -0.53\ \mathrm{V/nm}$ exhibits rather complex behavior, and we refer to it as a "correlated resistive state" because the overall resistance is relatively high compared with the metallic region. The state at $D = -0.32\ \mathrm{V/nm}$ shows a weak insulator-like behavior with increased reistance at the lowest temperatures, the state at $D = -0.4\ \mathrm{V/nm}$ show an almost constant but relatively large resistance value, and the state at $D = -0.45\ \mathrm{V/nm}$ displace a strange-metal-like behavior with an almost linear decrease of resistance at low temperature.

4.6 Discussion

The ABC-TLG/hBN superlattice thus provides a unique model system with which to study the triangular Hubbard model with fourfold onsite degeneracy, associated with an isolated and electrically controllable nearly flat fourfold-degenerate miniband. In this system, we experimentally find tunable Mott insulator states and signatures of tunable superconductivity. Further studies of such a tunable quantum system may shed light on the longstanding question of high-T_c superconductivity's relationship to the Hubbard model. ABC-TLG/hBN systems may also reveal new types of electronic states—such as spin liquid phases [104], electrically tunable Chern bands [4, 20], and topological triplet superconductivity [107, 118]—all of which have been recently predicted for a triangular Hubbard model based on ABC-TLG/hBN superlattices.

We have used the term superconductivity somewhat liberally in this chapter while the sample has not quite been rigorously demonstrated to be a superconductor. In Ch. 7, we will revisit the results of this chapter and possible explanations for the observed behavior. The main points of concern are that: (1) while R_{xx} fell precipitously with decreasing temperature (Fig.4.3A), the resistance never fell to zero, (2) non-linear behavior was observed in both $V-I$ and $dV/dI-I$ (Fig.4.3B and C) but neither clearly show a superconducting gap with a well defined critical current, and (3) the field scale of the oscillations observed (Fig.4.4).

Chapter 5

Magnetism at integer filling in moiré systems

5.1 Ferromagnetism in Twisted Bilayer Graphene

5.1.1 Introduction

This section is adapted from Ref. 18.

In weakly dispersing bands, electron-electron interactions dominate over kinetic energy, often leading to interesting correlated phases. Graphene has emerged as a preeminent platform for investigating such flat bands because of the control of the band structure enabled by stacking multiple layers and the tunability of the band filling via electrostatic gating. In particular, the moiré superlattice of so-called "magic-angle" twisted bilayer graphene (tBLG), in which one monolayer graphene sheet is stacked on top of another with a relative angle of rotation between the two crystal lattices of near one degree, is predicted to host nearly flat bands of $\sim 10\ \mathrm{meV}$ width [11, 80, 119].

In the single-particle picture, the flat bands are four-fold degenerate because of spin and valley symmetries [46]. However, magic-angle tBLG has recently been shown to exhibit high-resistance states at half $(1/2)$ and three-quarter $(3/4)$ filling of the conduction and valence bands [1, 14] and at one-quarter $(1/4)$ filling of the conduction band [14], all cases where metallic behavior would be expected in the absence of interactions. Surprisingly, magic-angle tBLG can become superconducting when doping slightly away from $1/2$ filling of either the conduction or valence band [3, 14].

Theoretical calculations have raised the possibility of magnetic order as a result of interactions lifting spin and valley degeneracies [66, 120–126]. Here, we present unambiguous experimental evidence of emergent ferromagnetism at $3/4$ filling of the conduction band in tBLG: a giant anomalous Hall (AH) effect that displays hysteresis in magnetic field. We also find evidence of chiral edge conduction. Our results suggest that the $3/4$-filling state is a correlated Chern insulator.

5.1.2 Fabrication and basic device characterization

The device we will discuss was fabricated from a heterostructure assembled using a "tear-and-stack" dry-transfer method [46, 47] with a target twist angle $\theta = 1.17°$, as discussed in Sec. 3.1.3. The graphene is encapsulated in two $50\ \mathrm{nm}$ thick hBN cladding layers that both protect the channel from disorder and serve as a dielectric for electrostatic gating. The completed heterostructure was transferred onto a 300-nm-thick $\mathrm{SiO_2}$ atop a degenerately doped Si substrate that serves as a back gate. The heterostructure was then fabricated into a Hall bar geometry using standard lithographic techniques (Fig. 5.1, inset). During fabrication, a $\mathrm{Ti/Au}$ top gate was deposited onto the completed heterostructure. In such a dual gated geometry, we can independently tune both the charge carrier density n in the tBLG and an applied perpendicular displacement field D [18,127] (see Appx. B for details on mapping between voltages applied to the gates and these parameters).

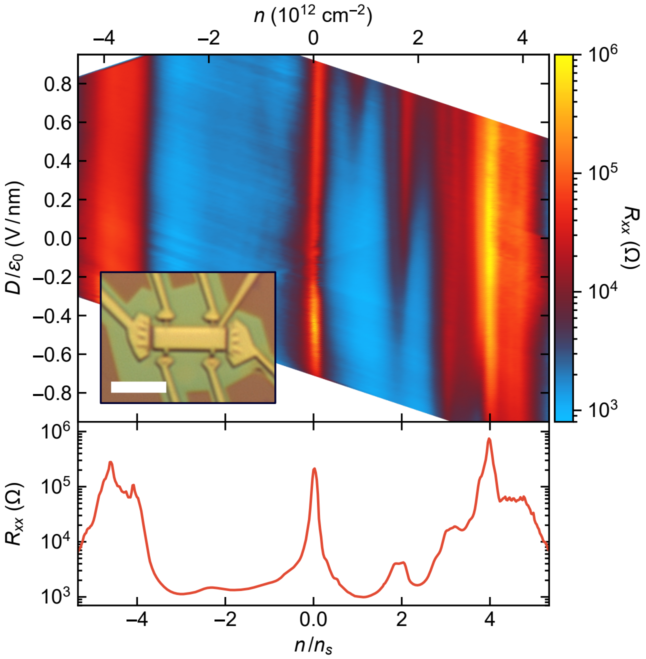

Figure 5.1: **Correlated states in near-magic-angle tBLG.** (Upper panel) Longitudinal resistance R_{xx} of the tBLG device (measured between contacts separated by 2.15 squares) as a function of carrier density n (shown on the top axis) and perpendicular displacement field D (left axis), which are tuned by the top- and back-gate voltages, at $2.1\ \mathrm{K}$. n is mapped to a filling factor relative to the superlattice density n_s, corresponding to one electrons per moiré unit cell, shown on the bottom axis. (Inset) Optical micrograph of the completed device. The scale bar is $5\ \mu\mathrm{m}$. (Lower panel) Line cut of R_{xx} with respect to n taken at $D/\epsilon_0 = -0.22\ \mathrm{V/nm}$ showing the resistance peaks at full filling of the superlattice, and additional peaks likely corresponding to correlated states emerging at intermediate fillings. Figure replicated from Ref. 18.

As an initial search for signatures of correlated effects in the device, we measured the dependence of the longitudinal resistance on n and D using standard lock-in techniques with a $5\ \mathrm{nA}$ RMS AC bias current (Fig. 5.1, upper panel). We observe a number of resistance peaks at different carrier densities. Namely, we observe a strong resistance peaks at the charge neutrality point (CNP) and at densities $\pm 4n_s = 3.37 \times 10^{12}\ \mathrm{cm}^{-2}$ corresponding to full filling of the mini-Brillouin zone (mBZ) of the tBLG superlattice (four electrons or holes per superlattice unit cell). As discussed in Sec. 1.2, this value of n_s corresponds to a twist angle $\theta = 1.20^\circ \pm 0.01^\circ$ in the tBLG heterostructure [35], very near the target angle of 1.17°.

In addition to these peaks that are expected from a single-particle picture of the tBLG band structure, there are additional high resistance states at $1/4$, $1/2$, and $3/4$ fillings of the conduction mini-band. Such fillings correspond to one, two, and three electrons per superlattice unit cell. At the time of this study, such features had previously been attributed to correlated insulating states [3, 14].

We observe another unexpected peak at $n/n_s = -4.6$ and a corresponding shoulder on the full filling peak of the electron side (seen in Fig. 5.1, lower panel). These features do not obviously correspond to some integer number of charge carriers per superlattice unit cell. It was claimed in Ref. 18, that such a feature likely results from the lattice alignment of the top graphene sheet with the top hexagonal boron nitride layer. The density $4.6n_s$ corresponding to an angle $\theta = 0.81^\circ \pm 0.02^\circ$ [35]. It is the case that for this heterostructure, such near-alignment with the top hBN layer is borne out by optical images of the heterostructure (Fig. 5.2); the bottom hBN is far from aligned with the bottom graphene sheet. However, it may be the case that such features are common in tBLG devices; this behavior is present in other tBLG samples where it is not reported whether or not the hBN is well aligned with the graphene [14, 128]. Despite this, alignment of one of the hBN cladding layers seems plausible in this device and is one obvious explanation to the phenomena seen within this device, as we will discuss shortly. Vertical asymmetry in the heterostructure from the alignment of the hBN may play a role in the strong dependence of the peak structure on the sign and magnitude of the displacement field.

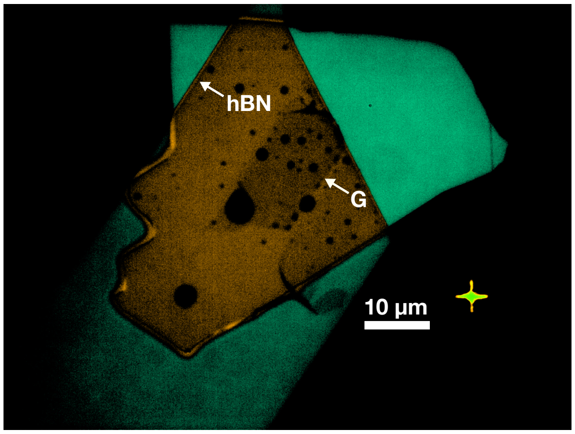

Figure 5.2: **Micrograph of the tBLG heterostructure.** A false color optical micrograph of the completed heterostructure (before lithography) demonstrates the rotational alignment of the top hBN layer and graphene. The arrow labeled ‘G’ indicates a crystallographic edge of the top graphene layer of the tBLG while the arrow labeled ‘hBN’ indicates a crystallographic edge of the top encapsulating hBN crystal. Based on this micrograph, the alignment of the crystallographic edge of the top hBN to that of top graphene of the tBLG is consistent with the experimentally measured angle of $\theta_{\mathrm{hBN}} = 0.83° \pm 0.02°$ (calculated based on the density corresponding to the peak we associate with the hBN moiré pattern; see Fig. 5.1). The bottom hBN is far from rotational alignment with the bottom graphene layer of the tBLG.

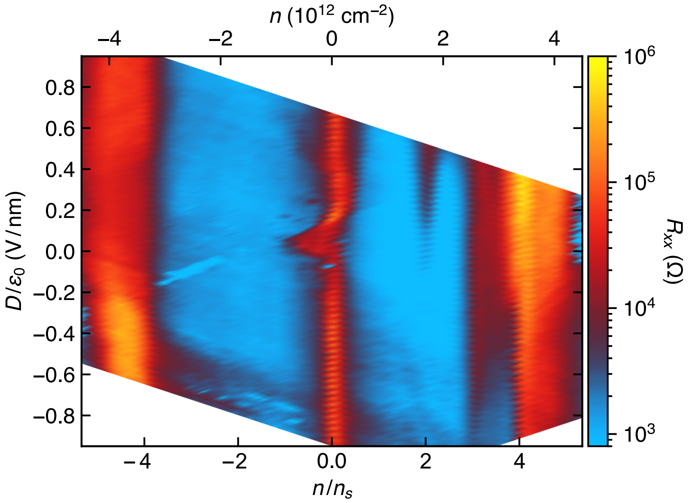

Figure 5.3: **Displacement field dependence from separate cooldown.** Longitudinal resistance R_{xx} of the tBLG device (measured between contacts separated by 2.15 squares at 40 mK) as a function of carrier density n (shown on the top axis), filling factor relative to the superlattice density n_s (bottom axis), and the applied perpendicular displacement field D (left axis).

The dependence of the longitudinal resistance R_{xx} on displacement field is not perfectly reproducible between cooldowns. Fig. 5.3 shows a map of R_{xx} as a function n and D at $T = 40\ \mathrm{mK}$ for a separate cooldown of the device. When compared with Fig. 5.1, Fig. 5.3 appears to have an overall shift in D. In addition to this shift, there is an offset in the gate voltages corresponding to the resistance peak at the CNP that varies between cooldowns. We have accounted for this in calculating n and D. Comparing to Fig. 5.1, this cooldown exhibits a shift of the CNP resistance peak centered near $0.05\ \mathrm{V/nm}$. Additionally, the position of the CNP resistance peak in the calculated density n does not appear to exhibit a significant change with D, aside from asymmetric broadening near $D = 0$ that disappears at larger $|D|$ (cf. Fig. 5.1 where the line traced by the peak in the 2D map appears to have a small kink). The differences between cooldowns are likely caused by variations in the disorder landscape seen by the tBLG, which can be changed by thermal cycling the device. This variability between cooldowns did not impact our ability to observe the basic phenomena we will shortly discuss.

5.1.3 Comparison to a superconducting tBLG device with misaligned hBN

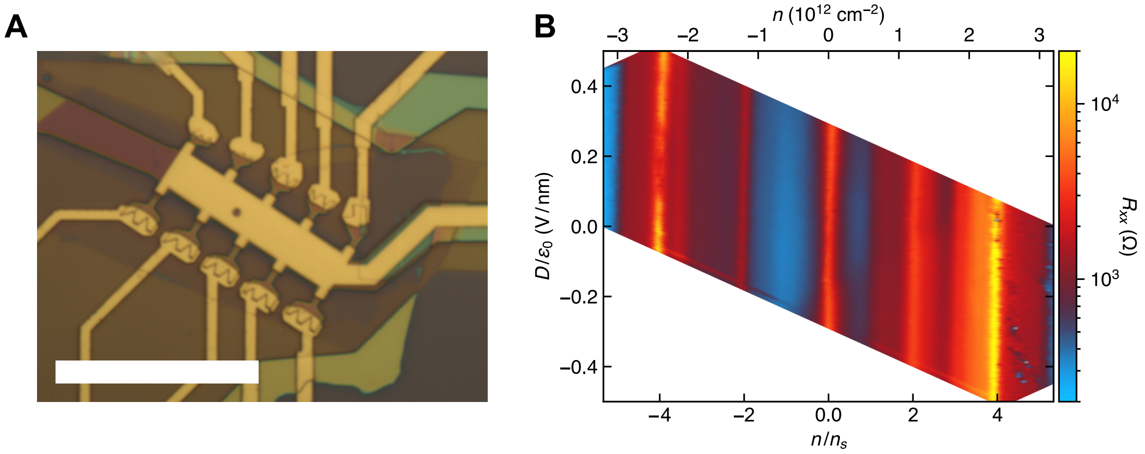

Figure 5.4: **Displacement field dependence of superconducting tBLG device with misaligned hBN.** (**A**) An optical micrograph of the completed device. The scale bar is $20\ \mu\mathrm{m}$. (**B**) Longitudinal resistance R_{xx} of the misaligned tBLG device (measured between contacts separated by 1.25 squares at $1.5\ \mathrm{K}$) as a function of carrier density n (shown on the top axis, or as a filling factor relative to the superlattice density shown on the bottom axis) and perpendicular displacement field D. We do not observe zero resistance as we are above the superconducting transition temperature, for a better comparison with Fig. 5.1.

To explain the dependence of transport on the sign of the displacement field in the main device of this section, we can compare it to the dependence in a second tBLG device (with a $1.05° \pm 0.02°$ twist angle) where the graphene has been intentionally misaligned with each of the hBN cladding layers. This second device has an additional graphite back gate that should help to drastically reduce disorder of the potential landscape within the tBLG by screening the effect of charges in the SiO_2 [35]. Also replacing the top metal gate with a second graphite gate could lead to further improvement [14, 129].

When the longitudinal resistance is measured as a function of the applied gate voltages, this device shows drastically different dependence on the applied displacement field than the main device. With the graphene misaligned with both hBN layers, the device is in an approximately symmetric dielectric environment (up to differences in disorder, hBN thicknesses, and gate materials). As a result, the longitudinal resistance has no features that strongly depend on the sign of the displacement field.

The stark contrast between the displacement field dependence of this misaligned device and the main device suggests that the vertical symmetry of the heterostructure is broken in the latter. This could result from disorder, but as previously, it appears that the symmetry could be broken by the alignment of one of the two hBN cladding layers with the tBLG. While the device with misaligned hBN did not show any of the phenomena discussed in the following sections, it did superconduct with cooled to lower temperatures.

5.1.4 Magnetic field response

Magnetotransport in graphene-based heterostructures typically does not depend on the history of the applied field. Surprisingly, we find in our main device that in a narrow range of n near $n/n_s = 3$, transport is hysteretic with respect to an applied out-of-plane magnetic field B (Fig. 5.5A). When the applied field is swept to zero from a large negative value, a large AH resistance $R_{yx} \approx \pm 6$ kΩ remains, with the sign depending on the direction of the field sweep, indicating that the sample has a remnant magnetization. This large AH signal is especially striking given the absence of both transition metals (typically associated with magnetism) and heavy elements (to give spin-orbit coupling) in tBLG. If the field is left at zero, the magnetization is very stable, with no significant change in the Hall resistance observed over the course of six hours (Fig. 5.6). As the field is increased beyond a coercive field of order $100\ \mathrm{mT}$ opposite to the direction of the training field, the Hall signal changes sign, pointing to a reversal of the magnetization.

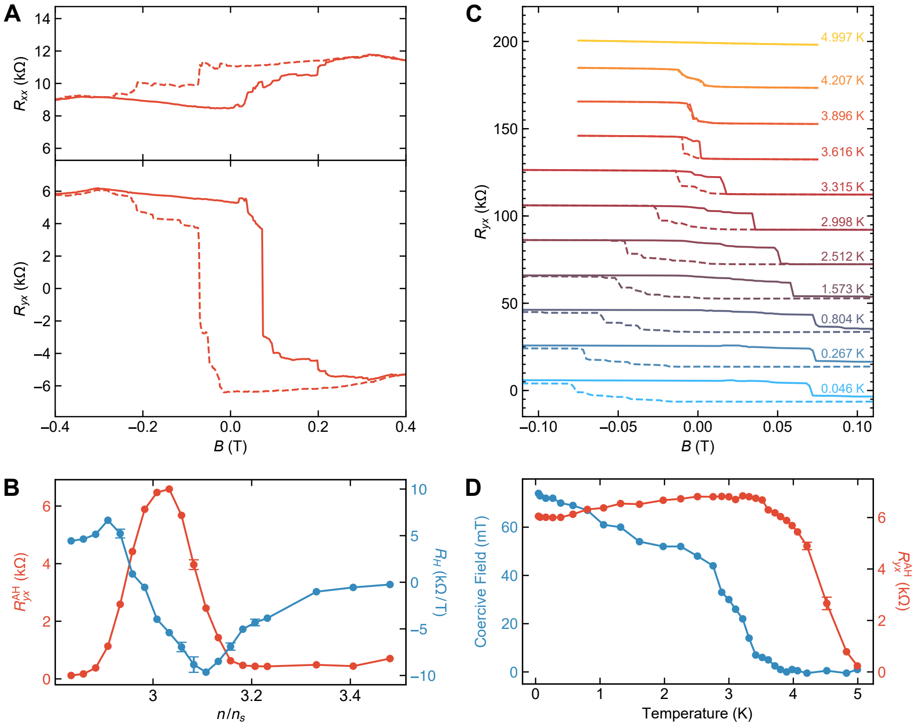

Figure 5.5: **Emergent ferromagnetism near three-quarters filling.** (**A**) Magnetic field dependence of the longitudinal resistance R_{xx} (upper panel) and Hall resistance R_{yx} (lower panel) with $n/n_s = 2.984$ and $D/\epsilon_0 = -0.62\ \mathrm{V/nm}$ at $30\ \mathrm{mK}$, demonstrating a hysteretic anomalous Hall effect resulting from emergent magnetic order. The solid and dashed lines correspond to measurements taken while sweeping the magnetic field B up and down, respectively. (**B**) Zero-field anomalous Hall resistance R_{yx}^{AH} (red) and ordinary Hall slope R_{H} (blue) as a function of n/n_s for $D/\epsilon_0 \approx -0.6\ \mathrm{V/nm}$. R_{yx}^{AH} is peaked sharply with a maximum around $n/n_s = 3.032$, coincident with R_{H} changing sign. These parameters are extracted from line fits of R_{yx} versus B on the upward and downward sweeping traces in a region where the B-dependence appears dominated by the ordinary Hall effect. The error bars reflect fitting parameter uncertainty along with the effect of varying the fitting window, and are omitted when smaller than the marker. (**C**) Temperature dependence of R_{yx} versus B at $D/\epsilon_0 = -0.62\ \mathrm{V/nm}$ and $n/n_s = 2.984$ between $46\ \mathrm{mK}$ and $5.0\ \mathrm{K}$, showing the hysteresis loop closing with increasing temperature. Successive curves are offset vertically by $20\ \mathrm{k\Omega}$ for clarity. (**D**) Coercive field and anomalous Hall resistance (extracted using the same fitting procedure as above) plotted as a function of temperature from the same data partially shown in (C). Data in Fig. 5.5 were taken during a separate cooldown from that of the data in the rest of the figures, but show representative behavior [18]

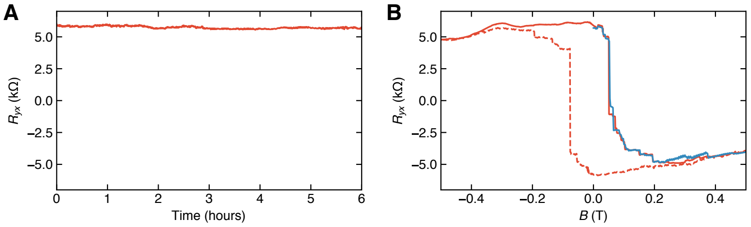

Figure 5.6: **Temporal stability of the magnetization.** (**A**) Hall resistance R_{yx} at $n/n_s = 2.984$ and $D/\epsilon_0 = -0.52\ \mathrm{V/nm}$ as a function of time over the course of 6 hours in zero field, after first magnetizing the sample by applying $-500\ \mathrm{mT}$ and then returning the field to $0\ \mathrm{T}$. (**B**) A full hysteresis loop taken prior to the measurement shown in (A) is displayed in red. The blue trace shows the behavior of R_{yx} as the field is swept from 0 to $500\ \mathrm{mT}$ following the measurement in (A). A clear anomalous Hall jump in the blue trace is comparable to those in the continuous red loop, indicating that the magnetization was stable through the 6 hour pause.

Multiple intermediate jumps appear near the coercive field. To check the repeatability of the hysteresis loop structure, we swept the applied magnetic field between $\pm 250\ \mathrm{mT}$ twelve times while maintaining a constant density and displacement field (Fig. 5.7). The structure of the hysteresis loop is very consistent between sweeps with many of the intermediate jumps appearing highly repeatable. These jumps likely correspond to some magnetic domain structure with domains of varying coercivities, or to a repeatable pattern of domain wall motion and pinning. This behavior may result from inhomogeneity caused by local variations in the twist angle between the graphene sheets, which has recently been directly imaged using transmission electron microscopy [13], or by local variations in electrostatic potential [130]. Additionally, we see a dip (of unknown origin) in the Hall resistance on the advanced side of zero field for both directions of the hysteresis loop.

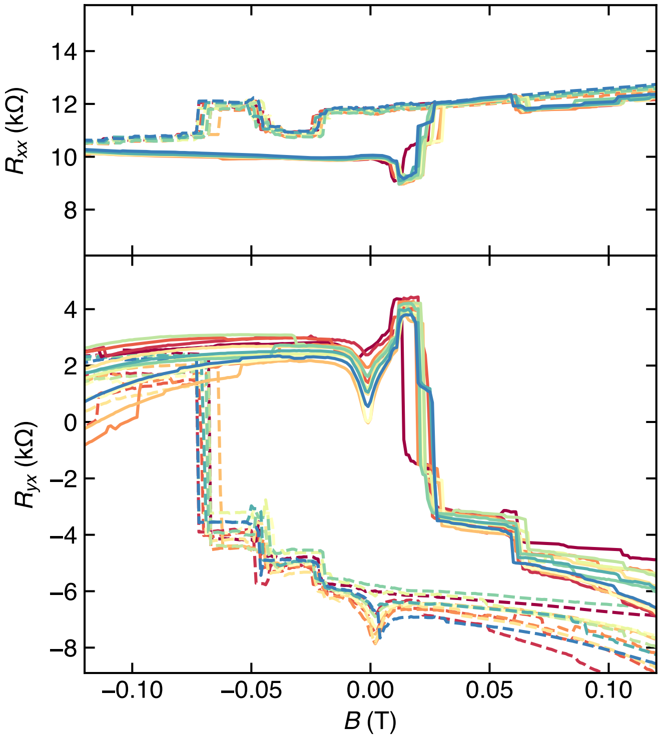

Figure 5.7: **Repeated hysteresis loops.** Longitudinal resistance R_{xx} (top panel) and Hall resistance R_{yx} (bottom panel) are shown as a function of magnetic field for twelve consecutive loops of the field between $\pm 250\ \mathrm{mT}$ for $n/n_s = 3.032$ and $D/\epsilon_0 = 0\ \mathrm{V/nm}$ (in the same cooldown as that of Fig. 5.3). The solid and dashed lines correspond to measurements taken while sweeping the magnetic field B up and down, respectively.

Hysteresis loops of R_{yx} and R_{xx} would ideally be antisymmetric and symmetric, respectively (in the sense that $R_{ij}(B) = \pm\widetilde{R}_{ij}(-B)$, where R_{ij} and $\widetilde{R}_{ij}$ are measured with the field sweeping in opposite directions). We find that R_{yx} hysteresis loops are roughly antisymmetric but offset vertically by $-1\ \mathrm{k\Omega}$. R_{xx} is nearly flat with field, but has an antisymmetric component, presumably because of mixing in of the large changes in R_{yx}.

We define the coercive field as half the difference between the fields where the largest jumps in R_{yx} occur on the upward and downward sweeps. With increasing temperature T, the coercive field steadily decreases before vanishing at $3.9\ \mathrm{K}$ (Fig. 5.5, C and D). This monotonic dependence could be expected, since flipping individual domains or moving domain walls in a magnet is usually thermally activated [131].

The Hall signal appears to be the sum of two parts: an anomalous component that reflects the sample magnetization [132], and a conventional component linear in field with a Hall slope R_{H} (Fig. 5.5B). To clearly separate the two components of the Hall effect, we define the anomalous component as half the difference between $B = 0$ Hall signals on the up and down sweeps of applied field: $R_{yx}^{\mathrm{AH}} = \left|R_{yx}^{\uparrow} - R_{yx}^{\downarrow}\right|/2$, where $R_{yx}^{\uparrow(\downarrow)}$ is the Hall resistance remaining at zero field after the sample has been magnetized by an upward (downward) applied field. If we took $R_{yx}^{\uparrow(\downarrow)}$ to equal the raw values of $R_{yx}(B = 0)$ under the two sweep directions, our reported parameters would be affected by small jumps in the resistance close to zero field. Instead, in analyzing the data, we examine a sweep toward zero field from a positive (negative) field higher than the coercive field; starting at a chosen high field cutoff, we include data until the first significant jump in R_{yx}. We fit a line to this subset and extrapolate or interpolate the value at $B = 0$ to estimate $R_{yx}^{\uparrow(\downarrow)}$. By varying the high field cutoff, we can estimate the uncertainty in the fitting parameters. We use the slope of these same linear fits as a measure of the conventional component of the Hall signal, R_{H}. Unlike the coercive field, the magnitude of the residual anomalous Hall resistance at zero field, R_{yx}^{AH}, does not vary monotonically with temperature: R_{yx}^{AH} rises slightly with increasing T up to 2.8 K, before rapidly falling to zero by 5 K (Fig. 5.5, C and D).

Although the hysteresis is observable over a wide range of displacement fields (Fig. 5.8), it only emerges in a narrow range of densities near $3/4$ filling of the mBZ. R_{yx}^{AH} displays a sharp peak as a function of n/n_s, reaching 6.6 kΩ for $n/n_s = 3.032$ with a full width at half maximum of $0.16n_s$ (Fig. 5.5B). It is interesting to note the asymmetry R_{yx}^{AH} as a function of n: namely there is a very sharp onset from zero as n/n_s increases towards 3 but as n/n_s is increased further, R_{yx}^{AH} falls rapidly but then remains above zero at the measured densities. It appears that the system remains magnetic at higher densities (this will be discussed further in Ch.6). These measurements were made along a trajectory for which D changes by approximately 10% coincident with the primary intended change in n [18]. In a separate measurement, we observed hysteresis loops with R_{yx}^{AH} up to 10.4 kΩ (Fig. 5.9).

The gate-voltage dependence of the conventional linear Hall slope R_{H} [18] appears typical for a transition from p-type- to n-type-dominated conduction in a semimetal or small-gap semiconductor, with $|R_{\mathrm{H}}|$ rising when approaching the transition from either side, then turning over and crossing through zero (Fig. 5.5B). Recent studies of near-magic-angle tBLG have reported high resistance at $3/4$ filling [3,14] (cf. our Fig. 5.1), suggesting that spin and valley symmetries are spontaneously broken, resulting in a low density of states (or a gap) at this filling. Our results similarly indicate a possible correlated insulating state, here with an AH effect in a narrow range of densities around this same filling.

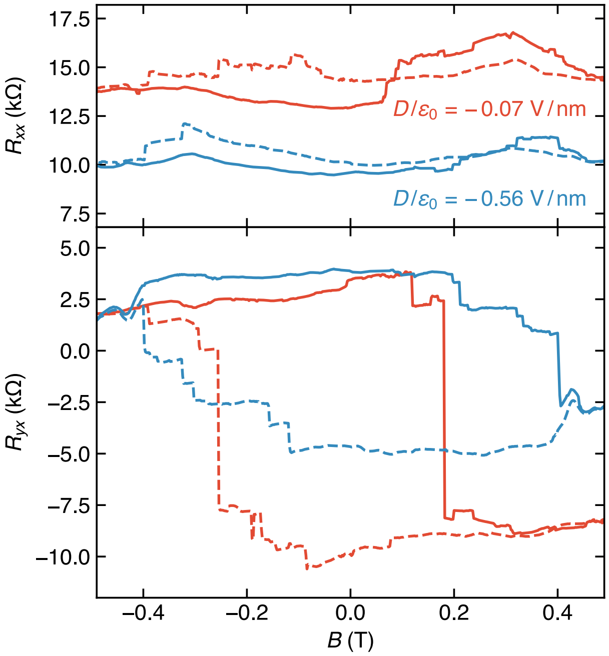

Figure 5.8: **Displacement field dependence of hysteresis loops.** Longitudinal resistance R_{xx} (upper panel) and Hall resistance R_{yx} (lower panel) at $n/n_s = 2.996$ for two different displacement fields as labeled in the figure. Although tuning the displacement field from a large negative field to near zero causes a slight change in the longitudinal resistance and the hysteresis loop structure, the tBLG magnetic field dependence remains hysteretic.

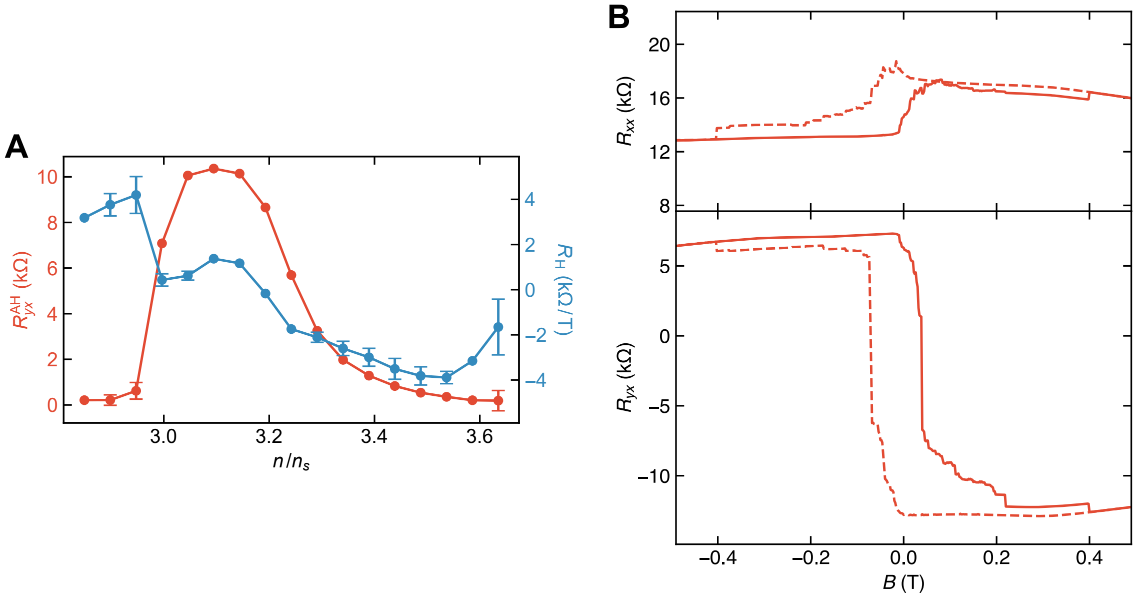

Figure 5.9: **Density dependence near $3/4$ with fixed displacement field at 2.1 K.** (**A**) Zero-field anomalous Hall resistance R_{yx}^{AH} (red) and ordinary Hall slope R_{H} (blue) as a function of n/n_s while maintaining a constant displacement field $D/\epsilon_0 = -0.22$ V/nm. R_{yx}^{AH} is peaked at $n/n_s = 3.096$, close to the position of the peak at 0.758 in Fig. 5.5B and again coincident with a sign change in R_{H}. The full width at half maximum is slightly increased, at 0.07 instead of 0.04. (**B**) Magnetic field dependence of the longitudinal resistance R_{xx} (upper panel) and Hall resistance R_{yx} (lower panel) at $n/n_s = 3.096$, the largest hysteresis loop of the series shown in (A), with $R_{yx}^{\mathrm{AH}} = 10.4$ kΩ.

The state at $1/4$ filling might be expected to behave similarly to the $3/4$ state due to the possible breaking of spin and valley degeneracies. Although we see signatures of a correlated state at $1/4$ filling (Fig. 5.1), we were unable to observe an AH effect near the $1/4$ state. Theoretical calculations [66] indicate that interactions modify the band dispersion differently at different commensurate fillings. Empirically, it is clear that the prominence of the resistance peaks and the displacement field dependence differs significantly between $1/4$ and $3/4$, suggesting that the correlated states at the two fillings are not equivalent.

5.1.5 Nonlocal transport

The presence of a giant AH effect in an apparent insulator is reminiscent of a ferromagnetic topological insulator approaching a Chern insulator state [19, 133, 134], where it would exhibit a quantum anomalous Hall (QAH) effect. An ideal QAH state is characterized by an insulating 2D bulk and chiral edge state, which conduct without dissipation. This implies ρ_{xx} approaches zero and Hall resistivity ρ_{yx} is quantized to h/Ce^2 [135, 136], where h is Planck's constant, e is the electron charge, and C is the Chern number arising from the Berry curvature of the filled bands ($C = \pm 1$ in presently available QAH materials). Chiral edge modes associated with a quantized Hall system manifest in nonlocal transport measurements [137, 138]. In an ideal QAH system described by the Büttiker edge state model [139], floating metallic contacts equilibrate with the chiral edge states that propagate into them, and therefore take on the potential of either the source or the drain contact (in the absence of non-ideal contact resistances), depending on the chirality of the edge states. In a ferromagnetic QAH insulator, this chirality is determined by the direction of the magnetization, leading to hysteresis in the Hall resistance as a function of applied magnetic field. The number of edge modes, each contributing e^2/h to the source-drain conductance, is given by C, leading to a source-drain resistance of h/Ce^2. As a result, when a current I flows from source to drain, floating terminals will have a voltage of either hI/Ce^2 or 0, referenced to the drain, if the contact is forward along the edge state direction of flow from the source or drain, respectively. Clearly our results are not those of an ideal QAH system. Dissipation can cause deviations from the ideal behavior, while still giving results differing from classical diffusive transport. Below we present and analyze our experimental evidence for nonlocal transport in the magnetic state.

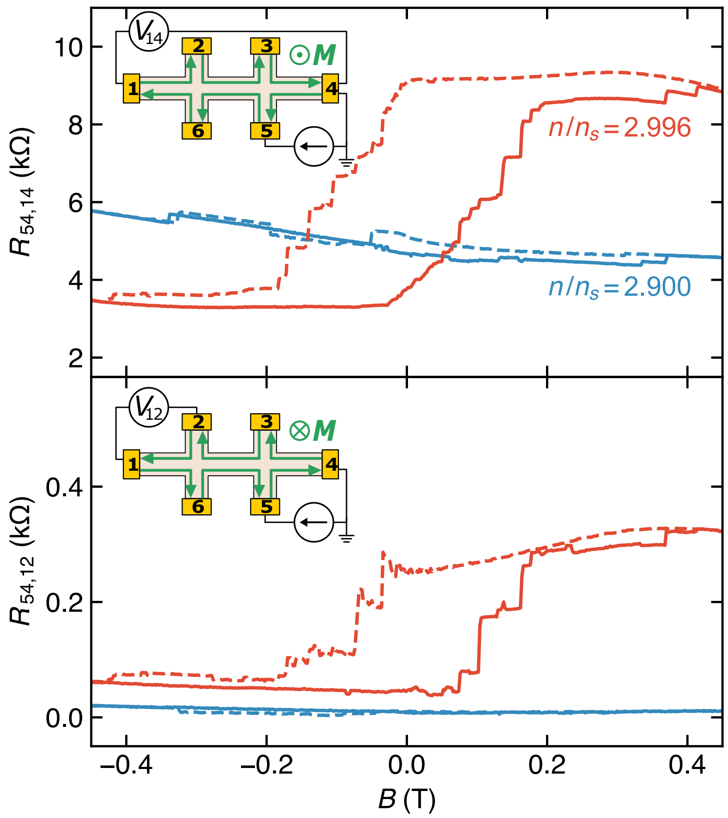

Figure 5.10: **Nonlocal resistances providing evidence of chiral edge states.** Three- and four- terminal nonlocal resistances $R_{54,14}$ and $R_{54,12}$, measured at 2.1 K with $D/\epsilon_0 = -0.22$ V/nm, are shown in the upper and lower panels, respectively. For $n/n_s = 2.9$ (blue) away from the peak in AH resistance R_{yx}^{AH}, the nonlocal resistances are consistent with diffusive bulk transport. However, with $n/n_s = 2.996$ (red) in the magnetic regime where R_{yx}^{AH} is maximal, large, hysteretic nonlocal resistances suggest chiral edge states are present. The inset schematics display the respective measurement configurations. Green arrows in the upper inset represent the apparent edge state chirality for positive magnetization, while in the lower inset they reflect negative magnetization.

The three-terminal resistance $R_{54,14}$, where $R_{ij,k\ell} = V_{k\ell}/I_{ij}$ with $V_{k\ell}$ the voltage between terminals k and ℓ when a current I_{ij} flows from terminal i to j, is shown in Fig. 5.10 (upper panel) for two values of n/n_s. When the density is tuned away from the center of the magnetic regime, $R_{54,14}$ is $\sim$5 kΩ and nearly independent of applied field. We ascribe this behavior to diffusive bulk transport and a finite contact resistance to ground. By contrast, at the center of the magnetic regime we observe a hysteresis loop with $R^{\downarrow}_{54,14} = 3.3$ kΩ and $R^{\uparrow}_{54,14} = 9.1$ kΩ, where $R^{\uparrow(\downarrow)}_{ij,k\ell}$ are the remnant resistances at zero field after the sample has been magnetized by an upward (downward) applied field. The difference $|R^{\uparrow}_{54,14} - R^{\downarrow}_{54,14}|$ is largest near the peak in R_{yx}^{AH} shown in Fig. 5.5B. For an ideal QAH effect, we would expect $R_{54,14}$ to be either 0 or h/Ce^2 (25.813 kΩ for $C = 1$) and will alternate between the two if the chirality is reversed. With non-ideal contacts, three-terminal resistances will also be offset by an additional contact resistance from the drain. While the difference $|R^{\uparrow}_{54,14} - R^{\downarrow}_{54,14}| = 5.8\ \mathrm{k}\Omega$ is smaller than the ideal $C = 1$ QAH case by a factor of 4, it could be consistent with a QAH state in combination with other dissipative transport mechanisms or a complex network of domain walls (in addition to contact resistance). These three-terminal measurements alone cannot rule out diffusive bulk transport with a very large (anomalous) Hall coefficient, but, as we will see, four-terminal measurements suggest this is unlikely.

In contrast to the three-terminal case, four-terminal nonlocal resistances where the voltage is measured far from the current path are exponentially small in the case of homogeneous diffusive conduction [140]. For an ideal QAH system, four-terminal resistances should always be 0 if measured between two voltage contacts on the same side of the perimeter relative to the source and drain, which is the case for the measurements we will present here. For $n/n_s = 2.9$, away from the peak in R_{yx}^{AH}, the measured $R_{45,12} = 10\ \Omega$ (Fig. 5.10, lower panel) is indeed small. In the magnetic regime at $n/n_s = 3.0$, however, the four-terminal resistance is two orders of magnitude larger than the 3 Ω expected from homogeneous bulk conduction, with a hysteresis loop yielding $R^{\downarrow}_{54,12} = 42\ \Omega$ and $R^{\uparrow}_{54,12} = 240\ \Omega$. Although, in an ideal QAH state with pure chiral edge conduction this four-terminal resistance would be zero, the presence of additional conduction paths, such as extra non-chiral edge states [9], parallel bulk conduction, or transport along magnetic domain walls [141,142], can result in large, hysteretic nonlocal resistances.

The case of transport via the 2D bulk in the absence of edge states is different in large part because of the nonzero longitudinal resistivity ρ_{xx}. The voltage of floating contacts will depend not only on the Hall resistivity ρ_{yx}, but will also pick up a contribution from ρ_{xx} times a geometrical factor (in addition to an offset from the drain contact resistance) that may be a significant fraction of the two-terminal source-drain resistance. For bulk transport with a relatively small Hall angle (the common case for an anomalous Hall effect, where typically $\rho_{yx}/\rho_{xx} \sim 0.1$ or less [143]), three-terminal resistances in a geometry like that of our nonlocal measurement configuration should differ between opposite magnetizations by a relatively small amount compared to their average value since the contribution from ρ_{xx} dominates, though this difference could be significant if the Hall angle is instead large. As in the QAH case, four-terminal resistances between contacts on the same side of the perimeter should not depend on the sign of the magnetization [140]. Although nonzero, the four-terminal resistance in a nonlocal configuration similar to ours will be exponentially small: if current is passed between two contacts on one end of a long, thin strip while the voltage difference is measured between two contacts on the opposite end, the resulting nonlocal resistance from bulk conduction alone is $R_{\mathrm{NL}}^{\mathrm{4T}} \approx (\rho_{xx}/\pi)\exp(-\pi l/w)$, where l and w are the length and width of strip, respectively [140].

An additional possibility is that chiral edge states are present along with some other dissipative conduction channels. While carriers are only transmitted in one direction between adjacent pairs of contacts in an ideal QAH state, in this case backscattering between contacts in the opposite direction becomes possible through the additional channel, leading to nonzero four-terminal resistances. One such scenario, analyzed in Ref. 9, is a QAH state with additional, non-chiral edge states. Compared to the ideal QAH case, the presence of this channel allowing transmission of carriers in the opposite direction of the chiral edge states leads to a reduced difference in the three-terminal resistances between opposite chiralities. Four-terminal nonlocal resistances are also expected to be relatively large in comparison to those in either a pure QAH effect or the case of bulk conduction without edge states, and can differ between opposite magnetizations; this phenomenon results from the combination of nonlocal transport from the chiral edge states along with dissipation due to backscattering. Similar effects can occur from the combination of chiral edge states and any conduction mechanism allowing such backscattering, including others that could be present in the tBLG system: nonzero bulk conductivity due to a small or spatially varying gap, or additional one-dimensional conduction paths through the bulk along a network of magnetic domain walls [141, 142] (due to the Chern number changing sign between domains of opposite magnetization).

Our measurements appear to be best explained by this latter situation, with both chiral edge channels and some other conduction mechanism like those described above. The three-terminal resistance $R_{54,14}$ shown in Fig. 5.10 exhibits significant hysteresis and differs by a large but non-quantized value between the two magnetizations for the density where the AH effect is strongest. This measurement rules out an ideal QAH effect but is still suggestive of nonlocal transport along edge channels. The behavior of the four-terminal resistance $R_{54,12}$ at this density, with a hysteresis loop saturating at approximately 42 Ω and 240 Ω for upward and downward magnetization, respectively, is likewise inconsistent with a homogeneous Chern insulator state. However, it also excludes the possibility of homogeneous bulk transport, which would yield $R_{54,12} \approx 3\ \Omega$. Both of these nonlocal measurements are instead consistent with chiral edge transport in combination with another conduction path giving rise to dissipation, which is also likely the explanation for the large but non-quantized AH effect we observed in transport in a typical Hall measurement configuration (Fig. 5.5).

5.1.6 Response to DC bias current

Surprisingly, we find that the $n/n_s = 3$ state is extremely sensitive to an applied DC current. All of the measurements described above were performed with a 5 nA RMS AC bias current, but we observed curious behavior when we added a DC bias I_{DC} to this small AC signal. Sweeping I_{DC} between ±50 nA with $B = 0$ (Fig. 5.11), we found that the differential Hall resistance dV_{yx}/dI follows a hysteresis loop reminiscent of its magnetic field dependence. This loop was very repeatable after a slight deviation from the first trace (black trace, Fig. 5.11), for which I_{DC} was ramped from 0 to -50 nA after first magnetizing the sample in a -500 mT field.

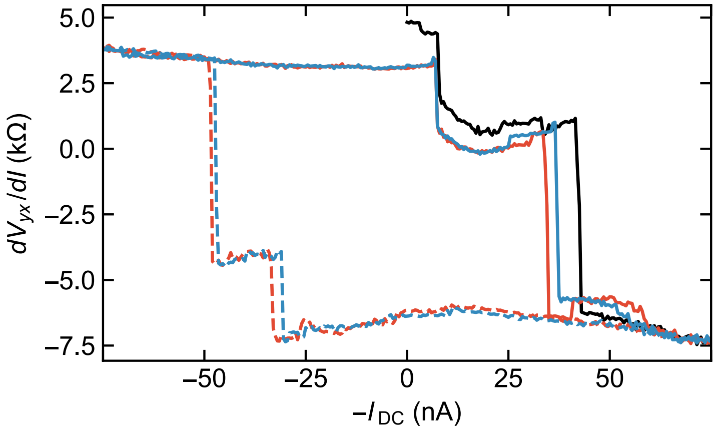

Figure 5.11: **Current-driven switching of the magnetization.** Differential Hall resistance dV_{yx}/dI measured with a 5 nA AC bias as a function of an applied DC current $I_{\rm DC}$ at 2.1 K with $D/\epsilon_0 = -0.22$ V/nm and $n/n_s = 2.996$. Note that dV_{yx}/dI is plotted against $-I_{\rm DC}$ for better comparison with magnetic field hysteresis loops. After magnetizing the sample in a -500 mT field and returning to $B = 0$, $I_{\rm DC}$ was swept from 0 to -50 nA (black trace), resulting in dV_{yx}/dI changing sign. Successive loops in $I_{\rm DC}$ between ±50 nA demonstrate reversible and repeatable switching of the differential Hall resistance (red and blue, with solid and dashed traces corresponding to opposite sweep directions).

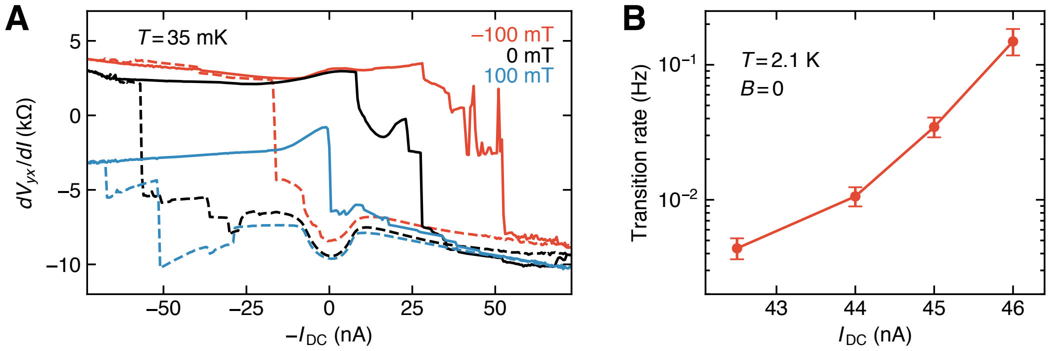

Figure 5.12: **Current-driven switching in nonzero magnetic field, and characterization of the transition.** (**A**) Hysteresis loops of the differential Hall resistance dV_{yx}/dI with respect to DC current (plotted as $-I_{\rm DC}$ as in Fig. 5.11) at three different static magnetic fields after the sample was magnetized at 500 mT. These data were taken at 35 mK with $n/n_s = 2.996$ and $D/\epsilon_0 = -0.22$ V/nm during the same cooldown as for the data of Fig. 4. (**B**) Transition rate of the apparent magnetization switching at a fixed current $I_{\rm DC}$ after magnetizing the sample with a -75 nA current (at $T = 2.1$ K and zero field). The transition appears to be a memoryless process.

The dependence of the DC current hysteresis loop on applied field at $T = 35\ \mathrm{mK}$ is shown in Fig. 5.12A. For each loop, the magnetic field was first increased to $500\ \mathrm{mT}$ and then decreased to the target field before cycling the DC current I_{DC}. Evidently, the applied field shifts the critical current required to switch the differential Hall resistance dV_{yx}/dI. Consistent with our expectation, when a nonzero field is applied, the magnitude of the current required to switch the apparent magnetization to the direction opposite (aligned) to the field is increased (decreased). It also appears from the loop at $100\ \mathrm{mT}$ that with sufficient field in the direction in which the sample has been magnetized, the DC current cannot completely reverse the magnetization, since dV_{yx}/dI remains significantly lower after switching than it does in the loops at 0 or $-100\ \mathrm{mT}$.

We further attempted to study the dynamics of the switching transition by measuring the time dependence of the differential Hall signal when I_{DC} was close to a value at which we observe large jumps in the loop shown in Fig. 5.11. With the current fixed near the jump at $\sim$45 nA, dV_{yx}/dI appears stable for a short time before rapidly switching (we did not measure the switching time itself since our lock-in measurements could not resolve changes on a time scale faster than $\sim$1 s). By repeatedly bringing I_{DC} to $-75\ \mathrm{nA}$ and back to a target current near the jump (at a rate of $0.7\ \mathrm{nA/s}$), then measuring dV_{yx}/dI as a function of time, we were able to investigate the statistics of this time lapse before the transition occurred. We find that the delay time before the switch appears to be exponentially distributed, indicating that the transition is a memoryless process that does not depend on the total charge transported. The corresponding transition rate (Fig. 5.12B) rapidly increases with I_{DC} near the currents at which we observe jumps in the full hysteresis loops, which were obtained by sweeping I_{DC} slowly at an average rate of $0.15\ \mathrm{nA/s}$.

The switching of dV_{yx}/dI is clear evidence that, like the external magnetic field, the applied DC current bias modifies the magnetization. This phenomenon might be similar to switching in other ferromagnetic materials, in which spin-transfer or spin-orbit torques can influence the magnetization. However, the current necessary to flip the moment appears to be very small [144]. It may be the case that the bulk current can either redistribute electrons [145] or directly generate a net orbital magnetization [146] due to the reduced lattice symmetry of tBLG aligned to hBN. It has also been proposed that a current could efficiently drive domain wall motion in a QAH system due to quantum interference effects from the edge states [147].

5.1.7 Evidence for orbital Chern insulator

At large positive displacement fields, a dip in longitudinal resistance forms near $n = 3n_s$ (Fig. 5.13). Characterizing the anomalous Hall across this dip in R_{xx} at a displacement field of $D/\epsilon_0 = 0.59\ \mathrm{V/nm}$, we see that the anomalous Hall resistance changes sign as the density crosses $3.12n_s$ (Fig. 5.14). This change in the sign of the anomalous Hall perhaps indicates the existence of two different ferromagnetic states that can be stabilized in different regions of parameter space (as we will also discuss in Ch. 6). The sign of the magnetic field controls the preferred magnetization direction, as the magnetic moment wants to align with the field. However, the magnetization of an orbital Chern insulator reverses sign as the chemical potential passes through the gap [148]. Therefore, the magnetization of each valley, and hence the magnetization for a

Chern insulator of each Chern number, reverses as a function of carrier density for an orbital Chern insulator.

This reversal of the sign of the anomalous Hall at a large displacement field is perhaps indicating that the $3/4$ state is an orbital Chern insulator. It is unclear, however, why this behavior is only observed at large displacement fields. Displacement field appears to enhance the gap at $3/4$ filling, given that the resistance peak at $3/4$ filling increases with increasing D. If this reversal of the sign of the anomalous Hall is due to an orbital Chern insulator, then the chemical potential has to be more homogeneously residing within the gap despite the inhomogeneity of the sample.

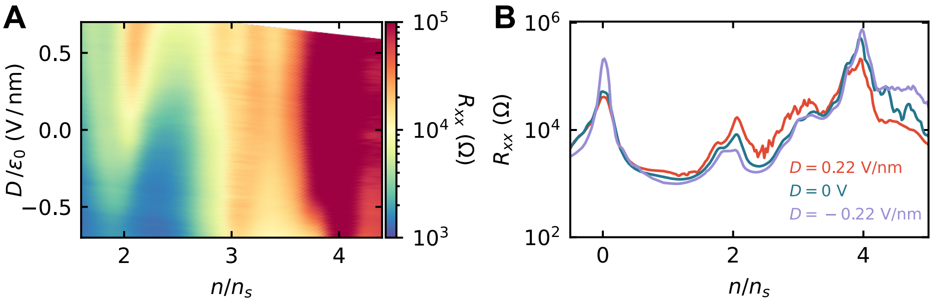

Figure 5.13: **Displacement field dependence near $n = 3n_s$.** (**A**) Longitudinal resistance R_{xx} as a function of both n and D. Panel is a zoomed in portion of Fig. 5.1 centered near $n = 3n_s$. (**B**) Line cuts of (A) showing R_{xx} as a function of n at three different displacement fields.

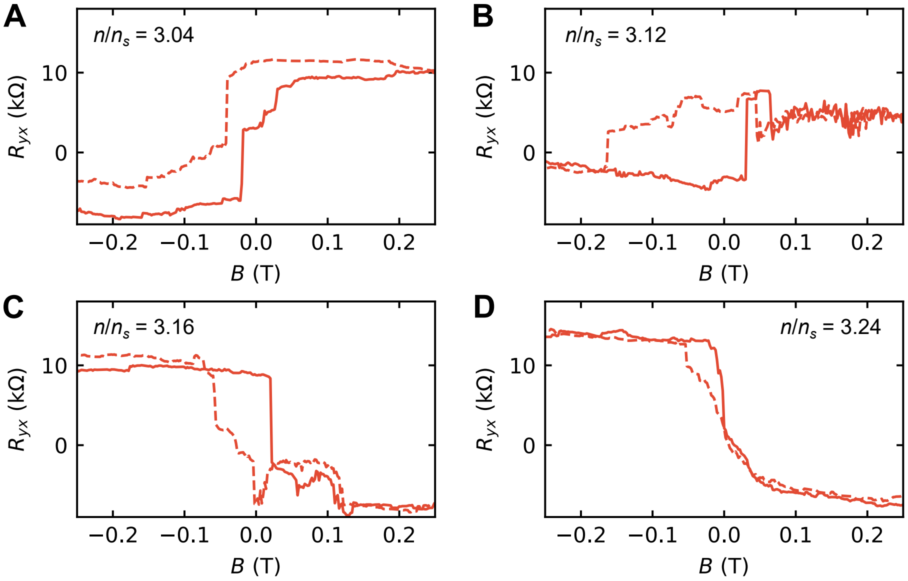

Figure 5.14: **Hysteresis loops at large a positive displacement field.** Magnetic field dependence of R_{yx} for a displacement field of $D/\epsilon_0 = 0.59$ V/nm and charge densities of (**A**) $3.04n_s$, (**B**) $3.12n_s$, (**C**) $3.16n_s$, and (**D**) $3.24n_s$. Measurements are performed at 2.16 K.

5.1.8 Discussion

Our observation of a large hysteretic AH effect establishes a ferromagnetic moment associated with the apparent $3/4$ correlated insulating state. Specifically, we suggest that this state is a Chern insulator, with the AH effect arising intrinsically from Berry curvature in the band structure. Extrinsic mechanisms for AH, based on scattering rather than band topology, cannot contribute to the Hall resistance of an insulator [132], yet the measured R_{yx}^{AH} is largest at an apparent insulating state. Furthermore, our measurements yield a ratio of resistivities ρ_{yx}/ρ_{xx} up to 1.4, almost an order of magnitude larger than any other reported AH [143] apart from magnetic topological insulators exhibiting a QAH effect (here we convert our measured resistances to resistivities which we approximate as spatially homogeneous). With $\rho_{yx} \lesssim 0.4h/e^2$ and $\rho_{xx} \approx 0.3h/e^2$ the present device is clearly not an ideal Chern insulator. Yet after early magnetically doped topological insulators showed comparable values [149–151], growth improvements in those materials soon yielded QAH [19, 133, 134]. If the present device is a nascent Chern insulator, the largest measured $R_{yx}^{\mathrm{AH}} \approx h/2.5e^2$ limits the possible Chern number to $C = 1$ or 2.

In combination with nonlocal transport that appears incompatible with homogeneous bulk conduction, the sheer magnitudes of the Hall and longitudinal resistances suggest a picture of chiral edge modes in combination with a poorly conducting bulk or a network of magnetic domain walls resulting from inhomogeneity. These possibilities can be directly explored in future experiments using spatially resolved magnetometry to search for domains and transport in a Corbino geometry to measure bulk conduction independent of chiral edge modes if domain walls can be removed.

Achieving a Chern insulator state by definition requires opening a topologically nontrivial gap. The low energy flat minibands in magic-angle tBLG are empirically isolated from higher order bands [46], which is expected when taking into account mutual relaxation of the two layers' lattices [80]. The low energy conduction and valence minibands have been variously predicted to meet at Dirac points at the CNP, which may [62, 63] or may not [67, 68] be symmetry protected. The rotational alignment of the tBLG to one of the hBN cladding layers in our device could thus be key to the observed AH effect: the associated periodic moiré potential should on average break A-B sublattice symmetry, opening or enhancing a gap at the mini-Dirac points. A gap associated with such symmetry breaking has been seen [35, 152, 153] and explained [51, 154, 155] in heterostructures of monolayer or Bernal-stacked bilayer graphene aligned with hBN. At $3/4$ filling of the conduction band of thus-gapped magic angle tBLG, spin and valley symmetry may be spontaneously broken, and 3 of the 4 flavors filled with the other empty. This scenario could account for our observation of an apparent Chern insulator. Indeed, Ref. 66 predicts a QAH effect arising in tBLG (without aligned hBN) at $3/4$ filling from such a mechanism (see Ref. 20 for a prediction of a similar situation in graphene-based moiré systems).

Aside from the topological aspect, the appearance of magnetism in this system is striking. Unlike previous studies of graphitic carbon exhibiting magnetism due to adsorbed impurities [156] or defects [157, 158] (including Ref. 159, where the magnetism observed in bulk graphite has since been attributed to defects [160, 161]), the order in the present device appears to emerge because of interactions in a clean graphene-based system; the anomalous Hall signal appears only in a narrow range of densities around a state that may be spin and valley polarized. Such intrinsic magnetism also stands in contrast to the magnetic topological insulators, where exchange coupling is induced through doping with transition metals [133, 136, 138]. Further experiment and theory will be needed to elucidate the order parameter, which may have both spin and orbital components or break spatial symmetry (cf. Ref. 162 for a model in which an antiferromagnet is a Chern insulator).

The discovery of a possible new platform for QAH physics, less disordered than the familiar magnetic chalcogenide alloys, may offer hope for more robust quantization, with applications in metrology [135], quantum computation [163–165], or low-power-consumption electronics. The ability to switch the magnetization in tBLG with an applied DC current might have practical applications in extremely low-power magnetic memory architectures, given the orders-of-magnitude smaller critical current density required for flipping the magnetization compared to prior devices [144]. More broadly, understanding the magnetic order and topological character of the correlated insulating states will be crucial to unraveling the rich phase diagram of tBLG.

An AH effect can either be intrinsic, arising from Berry curvature of the filled bands, or extrinsic, resulting from scattering mechanisms. One cause of an extrinsic AH effect, skew scattering, is associated with a linear relationship $\sigma_{xy} \propto \sigma_{xx}$ (where σ_{xy} and σ_{xx} are the Hall and longitudinal conductivities, respectively), which is clearly inconsistent with our data: for datasets parameterized by either n/n_s or temperature, shown in Fig. 5.15 A and C, this relationship is highly nonlinear. However, distinguishing between intrinsic Berry curvature and the other extrinsic mechanism, side jump scattering, is more challenging. Generally, the observed AH effect is compared with the theoretical expectation for the intrinsic contribution [132], but a clear theoretical consensus does not yet exist in the literature in this case.

Instead, we have argued that the size of ρ_{yx}^{AH} compared to that in other AH materials is evidence that its source is intrinsic. We reiterate and expand on this comparison here. As mentioned, the largest ratio of resistivities measured in our device is $\rho_{xy}/\rho_{xx} = 1.4$, whereas previously reported (extrinsic or intrinsic) AH materials yield $\rho_{xy}/\rho_{xx} \lesssim 0.2$ [143], except for the magnetic topological insulators exhibiting near-vanishing ρ_{xx} in the QAH effect. Further, we found ρ_{yx}^{AH} as large as $0.4h/e^2$, greater than in early magnetic topological insulators [133, 149, 151]. The corresponding longitudinal resistivity of $0.3h/e^2$ is also comparable to that of the first samples of those same materials to display near-quantization of ρ_{yx} in zero field ($\rho_{yx} \geq 0.98h/e^2$) [19, 150].

We have also argued that the origin is topological based on the appearance of the AH effect in an apparent insulating state. When the Fermi level is in a gap at zero temperature, the extrinsic mechanisms cannot contribute to σ_{xy} [132]. In these conditions, the system is in a Chern insulating state if the occupied bands carry a net Chern number, or in a trivial insulating state with $\sigma_{xy} = 0$ otherwise. As we have discussed, the state at three-quarters filling is evidently not a single-domain, ideal Chern insulator given that ρ_{xx} does not vanish. However, we believe that our data could be consistent with the presence of a small, topologically nontrivial gap. One piece of evidence for this is that the ordinary Hall slope passes through zero and changes sign near the value of n at which ρ_{yx}^{AH} is maximized (see Fig. 5.5B). A corresponding dip is seen in σ_{xx} as a function of n/n_s, shown in Fig. 5.15D.

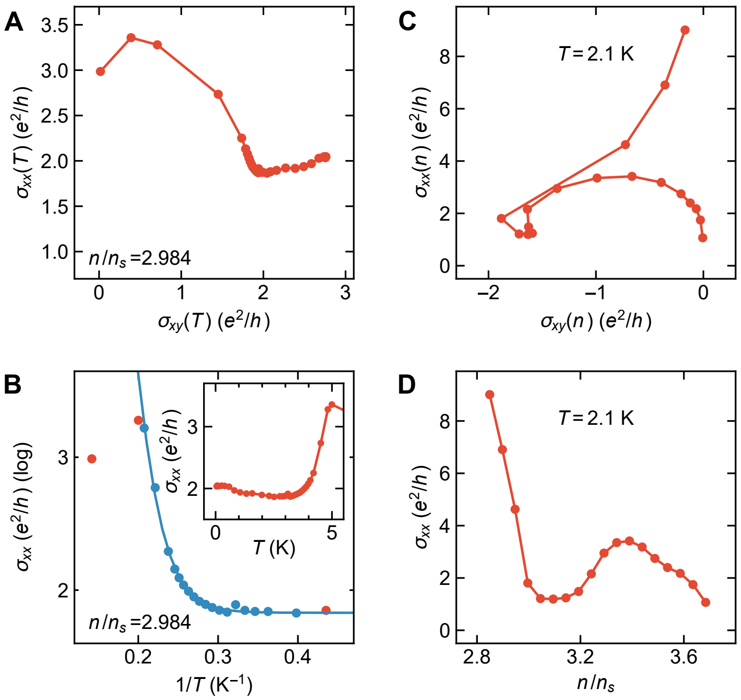

Figure 5.15: **Behavior of the conductivity tensor.** (**A**) The longitudinal conductivity σ_{xx} is plotted parametrically against the Hall conductivity σ_{yx} for a series of measurements at different temperatures with the density fixed at $n/n_s = 2.984$ and $D/\epsilon_0 = -0.62$ V/nm (shown in Fig. 5.5C). All conductivity values in this figure have been extracted from resistance measurements taken at 50 mT when sweeping the applied field downward from a value larger than the coercive field (so the sample has been magnetized by an upward field). The resistivity is derived from the measurements by assuming a homogeneous sample, and the conductivities are given by $\sigma_{xx} = \rho_{xx}/\left(\rho_{xx}^2 + \rho_{yx}^2\right)$ and $\sigma_{xy} = \rho_{yx}/\left(\rho_{xx}^2 + \rho_{yx}^2\right)$. The relationship between σ_{xy} and σ_{xx} is not consistent with an extrinsic AH effect resulting from skew scattering. (**B**). Arrhenius plot of σ_{xx} on a log scale versus $1/T$, with the same data shown in (A). The blue curve shows a fit of the data for $4.9 \text{ K} > T \geq 2.5$ K (the points shown in blue) to a model of activated conductivity with an additional, temperature-independent conduction channel (data points shown in red are excluded from the fit), yielding an estimated activation scale of $T_0 = 43$ K. (Inset) σ_{xx} is plotted on a linear scale against temperature. (**C**) σ_{xx} is plotted parametrically against σ_{xy} for a series of measurements at different densities at $T = 2.1$ K, with $D/\epsilon_0 = -0.22$ V/nm. These data were obtained during the same cooldown as that of the data shown in Figs. 5.1, 5.10, and 5.11. Again, the behavior appears inconsistent with skew scattering. Moreover, it is qualitatively similar to the density dependence of the conductivity in a magnetic topological insulator approaching a QAH effect shown in Ref. 19. (**D**) σ_{xx} as a function of n/n_s, from the same data as in (C), showing the emergence of a dip in σ_{xx} around $n/n_s = 3$ consistent with the approach to a Chern insulator state.

In other studies of near-magic-angle tBLG samples, a high-resistance state has also been observed at $n/n_s = 3/4$ [3, 14]. They did not report large AH effect. The difference may be due to the alignment of the tBLG with hBN in our experiment.

With nonlocal measurements also suggestive of edge state transport, we believe our collection of evidence suggests the system is approaching a Chern insulating state, but it remains to explain why it is non-ideal. There could be several reasons ρ_{yx} is not quantized and ρ_{xx} is nonzero, contrary to the expectation for a QAH effect. For one, the 2D bulk may not be strongly insulating, leading to both a nonzero ρ_{xx} and a reduction in the measured value of ρ_{yx} [133, 149].

Exploring the possibility of bulk conduction via the temperature dependence of σ_{xx}, we find that below 3 K some conduction mechanism persists, relatively insensitive to temperature (Fig. 5.15B). Between 3 K and 5 K, conductivity rises with increasing temperature, but this is not a large enough range to allow us to conclusively identify possible activated behavior in parallel with the temperature-insensitive conduction. Above 5 K, where the AH signal vanishes (see Fig. 5.5), the conductance stops rising. We speculate that a substantial gap may only exist at lower temperatures in the magnetic phase. For the purpose of estimating a possible gap size, we can fit these data for $T < 4.9$ K to a model of activated conductivity with a parallel, temperature-independent conduction channel: $\sigma_{xx} = \sigma_0 e^{-T_0/T} + \sigma_1$, where T_0 is the thermal activation temperature scale, and σ_0 and σ_1 are constants. (In fact, σ_{xx} reaches a minimum and then increases slightly as the temperature decreases, as can be seen in the inset to Fig. 5.15B; we do not know the origin of this minimum, but we speculate that it could result from increasing mobility in a parallel channel at low temperature. To best estimate the possible gap size while avoiding complications from this behavior at the lowest temperatures, we also limit the fit range to exclude data at temperatures lower than 2.5 K, where σ_{xx} is minimized.) This fit yields an activation scale $T_0 = 43$ K, corresponding to an estimated gap of $\Delta = 2k_BT_0 = 7.5\ \mathrm{meV}$ (including data at temperatures below 2.5 K makes the fit substantially worse but only modestly changes the fitted T_0 to 51 K). Although with a gap of this size, we might expect a well-quantized AH effect in our measurements at low temperature, the presence of an apparent additional conduction mechanism prevents this.

The low temperature residual conduction may be explained by inhomogeneity, which may result from local variations in twist angle or density, as we have noted elsewhere. Because of spatial variations in the density or gap size, it may be impossible to achieve a state in this sample with the Fermi level uniformly in the gap. Additionally, if such inhomogeneity results in a mixed domain state, edge states at domain walls could form a complex network resulting in nonzero ρ_{xx} and non-quantized ρ_{yx} even at zero temperature, and even if the magnitude of the gap were uniform (see Refs. 141 and 142 for examples of very simple mixed domain configurations yielding significant ρ_{xx}). Given the signs of inhomogeneity we have observed, we suspect at least one of these scenarios may be realized in our sample. Even though such effects prevent the observation of a clear QAH effect, our results nonetheless point to the existence of a topologically nontrivial gap opened by interactions.

The mechanism for opening such a topological gap remains to be determined. Interactions could spontaneously break the spin and valley symmetries, leaving 3 of the 4 flavors in the conduction miniband filled with the other empty [66]. With a topological gap opened between the conduction and valence minibands, perhaps resulting from sublattice symmetry breaking due to the aligned hBN cladding layer, a Chern insulator state could thus exist at $3/4$ filling. Alternatively, it could instead be the case that the $3/4$ state is not both spin and valley polarized. For example, it is predicted that noncoplanar chiral magnetic order can give rise to a $C = 1$ Chern insulator state at $3/4$ filling of a single (spinful) band in a Hubbard model on a triangular lattice [166]. If the valley degeneracy is unbroken, a similar insulating state in tBLG at $3/4$ filling might have Chern number $C = 2$ from the contribution of each valley. Further study will be needed to clarify the exact nature of the apparent insulating state we have observed.

To be clear: the experimental data we present do not unambiguously demonstrate that the three-quarters state is a Chern insulator. A non-quantized AH effect could result from Berry curvature even if the Fermi level is not in a gap, though, as discussed above, the magnitude of the Hall angle observed here far exceeds that of any reported AH system not known to host a Chern insulator state.

Another possibility is an AH analogue to the Hall insulator [167, 168]. In such a state, as $T \to 0$, $\rho_{xx} \to \infty$ while ρ_{xy} remains finite and nonzero, corresponding to $\sigma_{yx} \propto \sigma_{xx}^2 \to 0$. This alternative might be plausible given that the peak in R_{yx}^{AH} (Fig. 5.5) occurs at a peak in R_{xx} (Fig. 5.1) rather than at a minimum of R_{xx} as would be expected for a Chern insulating state. However, when we attempt to extract conductivities from our resistivity measurements, their temperature dependence appears inconsistent with a Hall insulator: with decreasing temperature, σ_{xx} initially falls but then saturates (Fig. 5.15B), and σ_{yx} increases (Fig. 5.15A). Furthermore, the Hall insulator state is not known to host topologically protected edge states, the presence of which is suggested by our nonlocal transport measurements.

5.2 Angular dependence of magnetisation in tBLG

5.2.1 Introduction

The previous section, tBLG was shown to be ferromagnetic in a narrow range of carrier densities strongly peaked near $3/4$ filling of the flat conduction band, [18] where full filling corresponds to four electrons per moiré unit cell accounting for spin and valley degeneracies [46]. The magnetism was revealed by a large hysteretic anomalous Hall effect as large as $10.4\ \mathrm{k}\Omega$ [18]. Evidence of chiral edge states from nonlocal transport [18] has indicated that the magnetic state may be an incipient Chern insulator.

However, the precise nature of the ferromagnetic ground state is an open question. In ferromagnetic materials, exchange interactions break time reversal symmetry favoring long-range order of electron spins. Though the motion of electrons can generate an orbital magnetic dipole moment, we are unaware of any magnetic material where the magnetism is dominated by the orbital magnetic moment independent of spin. This is precisely the prediction for tBLG of Refs. 64, 65, 148, 169–172. Despite these predictions, there are competing theories in which spin plays a role in the magnetism [66, 120, 121, 126, 162, 172]. The response of the magnetic state to out-of-plane or in-plane magnetic fields will directly elucidate any anisotropy of the magnetism. In this section, I will show that the magnetism in tBLG is highly anisotropic, and therefore dominated by the orbital magnetic moment, given that spin-orbit coupling in graphene is weak [5].

5.2.2 Measuring magnetic anisotropy

To control the orientation of the device relative to the field from the solenoid, we mounted the sample's chip carrier in an attocube atto3DR two-axis piezoelectric rotator. The atto3DR combines two rotators: one to control the tilt angle θ of the sample relative to the field to tune the relative magnitudes of the out-of-plane and in-plane components of the field (see Fig. 5.16A inset) and one to rotate about the normal of the stage to control the direction of the in-plane component of the field relative to the sample. Rotation is eucentric: the sample location in the solenoid is fixed as its orientation is changed. The rotator is equipped with a resistive readout for each axis for determining the angular position of the stage. We calibrated this readout using the Hall resistance R_{yx} of the device in a regime where the (ordinary) Hall effect is a measure of the out-of-plane field ($n = 0.04n_s$, where no anomalous Hall is present). All the data we present are accompanied by estimates of the angular position and error bounds based on this calibration. A precise calibration is particularly important when the field is nearly in-plane to avoid a significant unintended out-of-plane component when the magnitude of the total field is large. For all our nominally in-plane field measurements, the out-of-plane component remained smaller than the out-of-plane coercivity of the sample. We define the tilt angle θ such that 90° corresponds to a nominally out-of-plane field while 0° corresponds to a nominally in-plane field as seen by the device. The in-plane component and out-of-plane component of the field are then $B_{||} = B\cos(\theta)$ and $B_\perp = B\sin(\theta)$, respectively, where B is the magnitude of the applied field and θ is the tilt angle.

We have measured hysteresis loops of R_{yx} for different tilt angles of the device with the device tuned to be ferromagnetic ($n/n_s = 2.984$ and $D/\epsilon_0 = -0.30\ \mathrm{V/nm}$). The coercive field, identified by the dominant jump in the Hall signal, increases as the sample is rotated so that the field is in the plane of the sample (Fig. 5.16A). When the hysteresis loops at the various angles are plotted as a function of the out-of-plane component of the magnetic field, $B_\perp$, the most prominent jump in R_{yx} consistently occurs at $122 \pm 1\ \mathrm{mT}$ for each tilt angle down to a tilt angle of $4.71^\circ \pm 0.10^\circ$ (Fig. 5.16B), indicating that the magnetization is indeed highly anisotropic and likely dominated by the orbital magnetic moment.

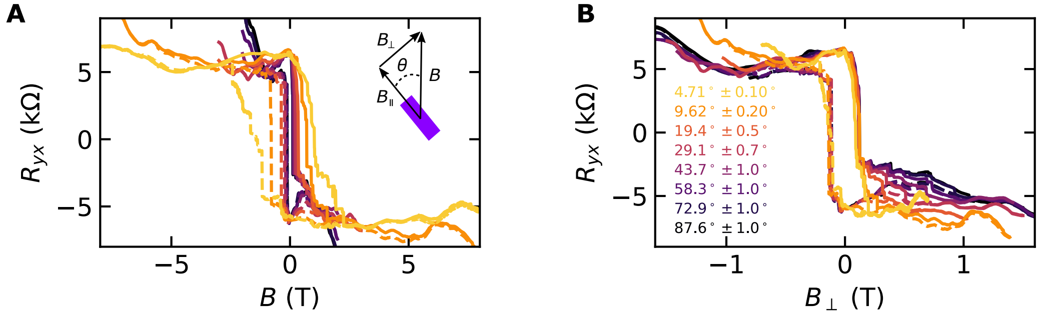

Figure 5.16: **Angular dependence of magnetic hysteresis loops.** Magnetic field dependence of the Hall resistance R_{yx} with $n/n_s = 2.984$ and $D/\epsilon_0 = -0.30$ V/nm at 29 mK as a function of the angle of the device relative to the field direction; $0°$ corresponds to field in the plane of the sample. The hysteresis loops are plotted as a function of (a) the applied field and (b) the component of the field perpendicular to the plane of the sample. The solid and dashed lines correspond to sweeping the magnetic field B up and down, respectively.

5.2.3 Affects of large in-plane field

The increased magnitude of the in-plane field as we lower the tilt angle does not significantly affect the hysteresis loops down to a tilt angle of $4.71° \pm 0.10°$ (plotted vs. $B_\perp$ in Fig. 5.16B and B in Fig. 5.17A), where the in-plane field reaches $B_\parallel = 0.69$ T. However, as the sample is tilted closer to perfectly in-plane, this uniaxial behavior begins to break down. At $1.82° \pm 0.10°$, the measured Hall resistance is significantly reduced compared to the hysteresis loops with a nearly out-of-plane field (Fig. 5.17B). As the tilt angle is further reduced, any semblance of the initial hysteresis loops for angles closer to a nearly out-of-plane field is lost (Fig. 5.17C and D).

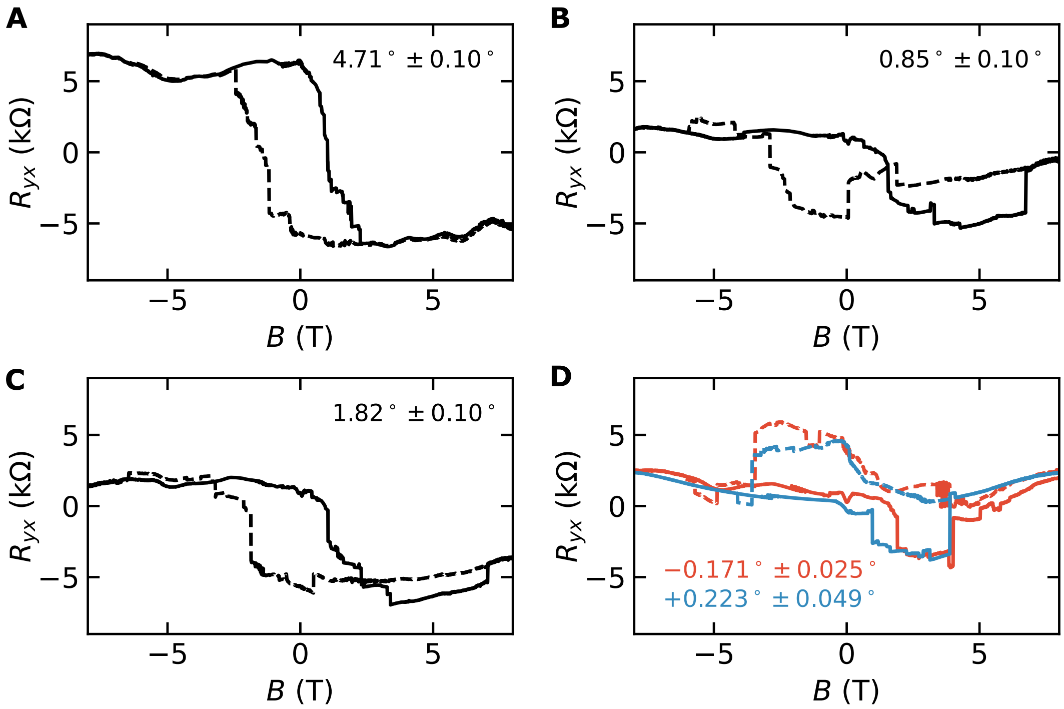

Figure 5.17: **Hysteresis loops for nearly in-plane fields.** Angular dependence of R_{yx} vs B with $n/n_s = 2.984$ and $D/\epsilon_0 = -30\ \mathrm{V/nm}$ for angles of the field relative to the plane of the sample: (a) $4.71° \pm 0.10°$, (b) $1.82° \pm 0.10°$, (c) $0.85° \pm 0.10°$, (d) $+0.223° \pm 0.049°$, and $-0.171° \pm 0.025°$. All traces were taken at $27\ \mathrm{mK}$ except for the trace with tilt angle $+0.223° \pm 0.049°$, which was taken at $1.35\ \mathrm{K}$.

To explore whether the effects seen when the field is nearly in-plane are the results of a small residual out-of-plane field, we compare hysteresis loops performed at small angles of similar magnitude but opposite sign (Fig. 5.17D). The two R_{yx} vs. B curves are very similar despite magnetic field angle deviating from in-plane in opposite directions, so the out-of-plane components are opposite for the two curves (see Fig D.3D in Appx. D for corresponding R_{xx} curves.) It is unlikely that this behavior results from a significant $B_\perp$: a tilt angle of more than $700\ \mathrm{mdeg}$ would be needed to exceed the nominal coercive field of $100\ \mathrm{mT}$ at $8\ \mathrm{T}$. Such misalignment is well outside our expected experimental error so that for the data presented in Fig. 5.17, the coercive field is exceeded in every hysteresis loop except the traces in Fig. 5.17D. Furthermore, were significant misalignment the source of the residual Hall signal, we would expect R_{yx} to be antisymmetric in field and the device would likely recover some portion of its initial magnetization upon cycling the field, as is the case for larger tilt angles. While the $1.82°$ and $0.85°$ hysteresis loops differ significantly from the out-of-plane field hysteresis loop, both recover a large proportion of their initial polarization (depending on the sign of the field). These results strongly suggest that the hysteresis loop seen at very small angles results from the in-plane field. It should be noted that these hysteresis loops are not performed with the sample initially in a maximally polarized state. Additionally, the two traces in Fig. 5.17D were performed at different temperatures. (A similar comparison shown in Fig. D.7 of Appx. D is performed at a constant temperature with the sample at a different in-plane angle, yielding similar results.)

To further explore this change in behavior when the field is nearly in the plane, we start with the sample initially magnetized by a primarily out-of-plane magnetic field. The applied field is returned to zero, and the sample is then rotated to as close to in-plane as possible in zero magnetic field (for this measurement, the resultant tilt angle is -57 ± 21 mdeg). Once rotated, a magnetic field is applied at this very small angle to the sample (red trace in Fig. 5.18). When $B_{\|}$ exceeds 5 T, we observe no hysteresis or jumps in the Hall resistance indicating an apparent transition from the Chern insulating state to a different state: above 5 T, both R_{xx} and R_{yx} show repeatable oscillations of order 2 KΩ in size that appear to depend only on the magnitude of $B_{\|}$ (see Appx. D). The accessible range of field is insufficient to say whether or not these oscillations are periodic in $B_{\|}$ or $1/B_{\|}$. The high field state may or may not be polarized in spin and/or orbit. If it does have an orbital polarization, it is no longer set by the out-of-plane field component. The high-in-plane-field state also does not show a strong anomalous Hall signal. Were the Hall signal arising primarily from coupling to the magnetization, one would expect $R_{yx}(M) = -R_{yx}(-M)$, where M is the magnetization of the sample. If high field were indeed fixing the orbital polarization, its direction and thus the Hall component of the signal should reverse with field direction. Any such signal is swamped by a large longitudinal signal mixed in (which is symmetric in B, see Appx. D), so either this high-in-plane-field state lacks orbital polarization or the large in-plane field changes the topological character of bands so there's no net Chern number.

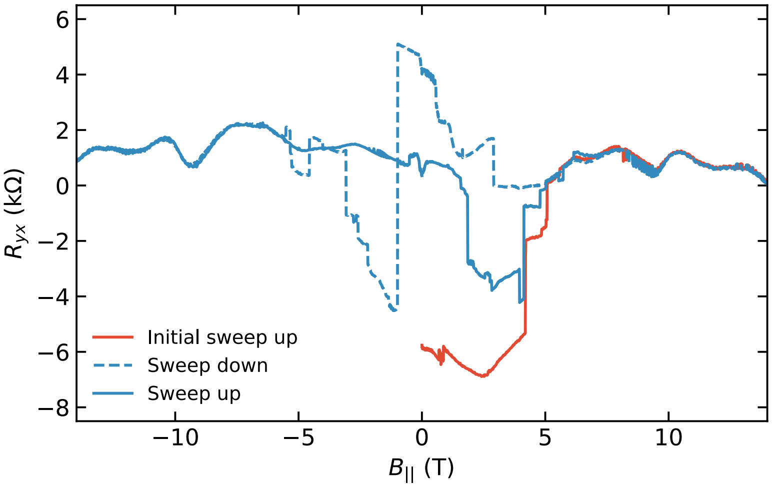

Figure 5.18: **Erasing the initial magnetic state.** In-plane hysteresis loops of R_{yx} with $n/n_s = 2.984$ and $D/\epsilon_0 = -30$ V/nm at 26 mK. The sample is initially polarized with an out-of-plane field. The sample is then rotated to -57 ± 21 mdeg in zero magnetic field. The field $B_{\|}$ is then increased from zero (red trace) before completing a hysteresis loop (blue traces).

Under $5\ \mathrm{T}$, orbital polarization is being modified by in-plane field somehow, not by the small out of plane component. Upon decreasing $B_{||}$, R_{yx} shows evidence of recovered magnetic behavior in R_{yx}, but never recovers its initial value which nominally corresponds to a maximally polarized state (blue traces in Fig. 5.18). This behavior below $5\ \mathrm{T}$ may result from a repeatable pattern of out-of-plane orbital domains that is set by an in-plane field: Fig. 5.17D and Fig. 5.18 share the same direction of in-plane field and bear similar structure in their hysteresis loops despite slight differences in tilt angles. Fig. D.7 is similar to Fig. 5.17D but with the sample having been rotated in-the-plane by 20° so that the direction of the in-plane field relative to the device is different. Again, Fig. D.7 displays a somewhat repeatable hysteresis loop as a function of a predominately in-plane field, albeit of different structure presumably due to the different direction of the in-plane field.

5.2.4 Discussion

While this device does not exhibit quantized Hall resistance or zero longitudinal resistance, it does exhibit what appears to be incipient Chern insulating behavior [18], which would suggest the ground state at low in-plane fields is spin and valley polarized [64,65]. Given that spin-orbit coupling is extremely weak in graphene, there should not be significant anisotropy in the direction spins prefer unless higher order bands are mixed in. In fact, there might be no relation between the direction of spin polarization and valley polarization. Starting in the out-of-plane orbitally polarized state, R_{yx} rises with an applied in-plane field (red trace in Fig. 5.18, up to 2T), possibly indicating that the spin is oriented by the external field, widening the gap to charge-carrying spin excitations. Alternatively, if the low-field QAH state results from a state that is valley-polarized and spin-unpolarized, then polarizing spin could destroy any QAH through the removal of valley-polarization or mixing with higher-order bands [64, 120]; the lack of quantization in our measurements does open the door for the low-field ground state being metallic with strong anomalous Hall rather than a Chern insulator. On the other hand, because of the finite thickness of tBLG, it is also possible that an in-plane field directly couples to the orbital moments [173]. A sufficiently large in-plane field could then drive the sample into a valley unpolarized state.

Regardless of the dominant mechanism of how in-plane field couples to the device, it seems that either the bands are losing their topological character by the mixing in of higher bands [174], or the in-plane field is driving a repopulation of the bands. Thus far, no evidence of magnetism has been observed at $n/n_s = 1$ [18, 175], which should nominally be similar to $n/n_s = 3$. Therefore there may be a competing ground state which does not have a net Chern number and would not exhibit a QAHE.

We have observed that the magnetization of tBLG is sensitive primarily to the out-of-plane component of the field, requiring a threshold coercive field to flip the magnetization. A single value of $B_\perp$ required to switch the measured anomalous Hall resistance is consistent with an uniaxial nature of the magnetization. It is unlikely that this uniaxial behavior is related to the electron spin because of the extremely low spin-orbit coupling in graphene. Rather, it is likely that the $3/4$ state is an orbital ferromagnet. Because the electrons are effectively confined to the plane, this would provide the high degree of anisotropy observed.

5.3 Chern insulating state in ABC-TLG/hBN moiré superlattice

5.3.1 Introduction

This section is adapted from Ref. 21.

The ABC-trilayer graphene/hBN (ABC-TLG/hBN) moiré superlattice provides an attractive platform with which to explore Chern insulators because it features nearly flat moiré minibands with a valley-dependent, electrically tunable Chern number [4, 20]. Here we report the experimental observation of a correlated Chern insulator in an ABC-TLG/hBN moiré superlattice. We show that reversing the direction of the applied vertical electric field switches the moiré minibands of ABC-TLG/hBN between zero and finite Chern numbers, as revealed by large changes in magneto-transport behaviour. For topological hole minibands tuned to have a finite Chern number, we focus on quarter filling, corresponding to one hole per moiré unit cell. A correlated Chern insulator with $C = 2$ quantum anomalous Hall effect [133] emerges around $1/4$ filling of the topological hole miniband when the bandwidth is sufficiently narrowed by applying a displacement field in one direction. The correlated Chern insulator spontaneously breaks time-reversal symmetry, exhibiting strong ferromagnetic hysteresis and a zero-field anomalous Hall resistance over $8\ \mathrm{k}\Omega$. For magnetic fields exceeding $0.4\ \mathrm{T}$, the Hall resistance is well quantized at $h/2e^2$ (where h is Planck's constant and e is the charge on the electron), which implies $C = 2$. Our discovery of a $C = 2$ Chern insulator at zero magnetic field should open up opportunities for discovering correlated topological states, possibly with topological excitations [176], in nearly flat and topologically nontrivial moiré minibands

5.3.2 Basic characterization

This section focuses on a device separate from the device discussed in Chapter 4, but both device exhibit similar phenomenology.

As the voltages applied to the gates are tuned, measurements of ρ_{xx} reveal several resistance peaks (Fig. 5.19) in the ABC-TLG/hBN device across the parameter space controlled by V_t and V_b. In addition to the peaks corresponding to band insulating states at the charge neutrality point and fully filled point, tunable correlated insulator states emerge at $1/4$ filling and $1/2$ filling of the hole miniband (that is, one and two holes per moiré unit cell) when a finite displacement field $|D|$ narrows the moiré minibands. There are two apparent asymmetries of the correlated insulator states in ABC-TLG/hBN at $1/4$ and $1/2$ charge fillings: between the electron and hole minibands, and between positive and negative D. Prominent correlated insulator states are observed in the hole minibands but not in the electron minibands because the hole miniband has a much smaller bandwidth for finite $|D|$ (Ref. 2). The asymmetry between the positive and negative D fields arises from the fact that the moiré superlattice exists only between the ABC-TLG and the bottom hBN in this device (this is opposite to the case of the device discussed in Ch. 4). Interestingly, the direction of the displacement field has been predicted to determine not only the relative bandwidth but also the topology of the hole miniband. For a device with moiré superlattice between ABC-TLG and the bottom (top) hBN, a positive (negative) D leads to a trivial hole miniband with $C = 0$ and smaller bandwidth, while a negative (positive) D leads to a topological hole miniband with $C \neq 0$ and larger bandwidth [4,20]. The difference in bandwidth and topology is reflected in the electrical transport behaviour: in the device with the moiré superlattice at the bottom hBN, we observe stronger correlated insulators in the trivial hole miniband with positive D, because holes are easier to localize in the narrower trivial band than in the broader topological band with negative D (Ref. 104). Our previous studies have shown that superconductivity can emerge when we dope the $1/4$ filling correlated insulator state in selected parameter spaces of the trivial hole miniband [110].

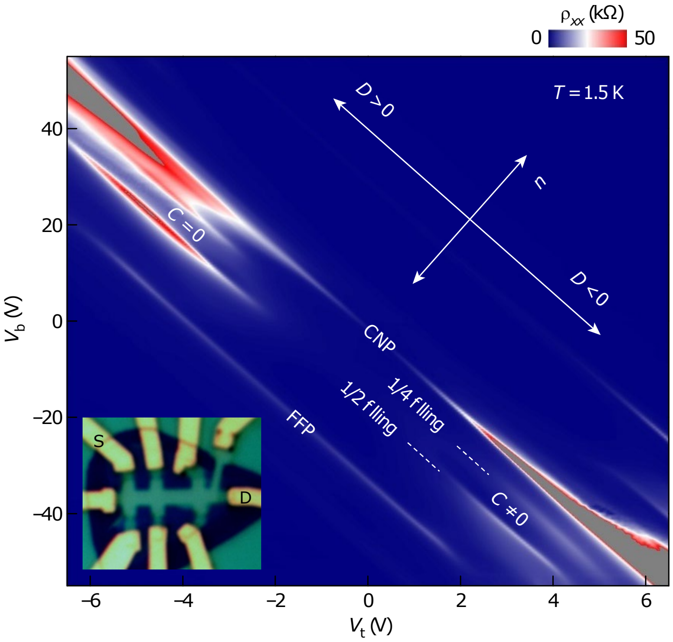

Figure 5.19: **Tunable Chern bands in ABC-TLG/hBN moiré superlattice.** Color plot of the longitudinal resistivity ρ_{xx} as a function of V_t and V_b at $T = 1.5$ K. The arrows show the direction of changing doping n and displacement field D, respectively. In addition to the band insulating states (characterized by the resistance peaks) at the charge neutral point (CNP) and fully filled point (FFP), tunable correlated insulator states also emerge at 1/4 and 1/2 filling of the hole minibands at large displacement field $|D|$. It has been predicted theoretically [4,20] that the hole miniband is topical (that is, Chern number $C \neq 0$) for $D < 0$ and trivial ($C = 0$) for $D > 0$. The inset shows the optical image of the device. In this device, the graphene is aligned with the bottom hBN (this is opposite to the device discussed in Ch. 4, which leads to an overall flipping of the gate map with respect to the sign of D). The Hall bar is 1 μm wide.

5.3.3 Magnetic field response

To better probe the topological aspects of the moiré minibands, we turn to magneto-transport studies. At $D = 0$, the correlation effect in the system is relatively weak, and the magneto-transport data exhibit well defined quantum Hall states and a Landau fan diagram at low magnetic fields (see Fig. 5.20), demonstrating the very high quality of our sample. With large displacement field, the moiré miniband bandwidth becomes narrower, and the dominant electron–electron interaction dramatically changes the magneto-transport behaviour. Fig. 5.21A, B displays the color plot of ρ_{xx} as a function of the hole doping and the vertical magnetic field B for $D/\epsilon_0 = -0.5\ \mathrm{V/nm}$ (at $T = 0.06$ K) and $D/\epsilon_0 = 0.4\ \mathrm{V/nm}$ (at $T = 1.5$ K), respectively. Fig. 5.21C, shows the corresponding Hall resistivity ρ_{yx} data. Experimental data for $D/\epsilon_0 = -0.5\ \mathrm{V/nm}$ at 1.5 K exhibit qualitatively similar behaviour to those at 0.06 K [21]. We have used $n_s = 5.25 \times 10^{11}\ \mathrm{cm}^{-2}$ as the unit of carrier density, which corresponds to one hole per moiré lattice site (that is, $1/4$ filling). The magneto-transport data exhibit distinct behaviours for the topological moiré miniband at negative D and the trivial miniband at positive D (Refs. 4 and 20). Specifically, a strong quantum Hall state emerges from the $1/4$ filling point for $D/\epsilon_0 = -0.5\ \mathrm{V/nm}$ but not for $D/\epsilon_0 = 0.4\ \mathrm{V/nm}$. The dashed line in Fig. 5.21A traces the minimum in ρ_{xx} following the relation $n = \nu eB/h$ for $\nu = 2$. This quantum Hall state is well developed at very low magnetic fields, and originates from the $1/4$ filling resistive state at zero magnetic field (Fig. 5.21A). At the same time, ρ_{yx} is very large at weak magnetic fields and exhibits a jump in value when the magnetic field switches sign across $B = 0$ T (Fig. 5.21C). By contrast, stronger correlated insulator states are observed for $D/\epsilon_0 = 0.4\ \mathrm{V/nm}$, but no signatures of quantum oscillations or quantum Hall effects are present (Fig. 5.21B). In addition, Fig. 5.21D shows that the Hall resistivity signal tends to be rather small for all hole doping at $D/\epsilon_0 = 0.4\ \mathrm{V/nm}$. (The relatively large ρ_{yx} signals at $1/4$ and $1/2$ fillings are artifacts caused by crosstalk from the large ρ_{xx} of the correlated insulator states, and they do not change sign when the magnetic field is reversed.)

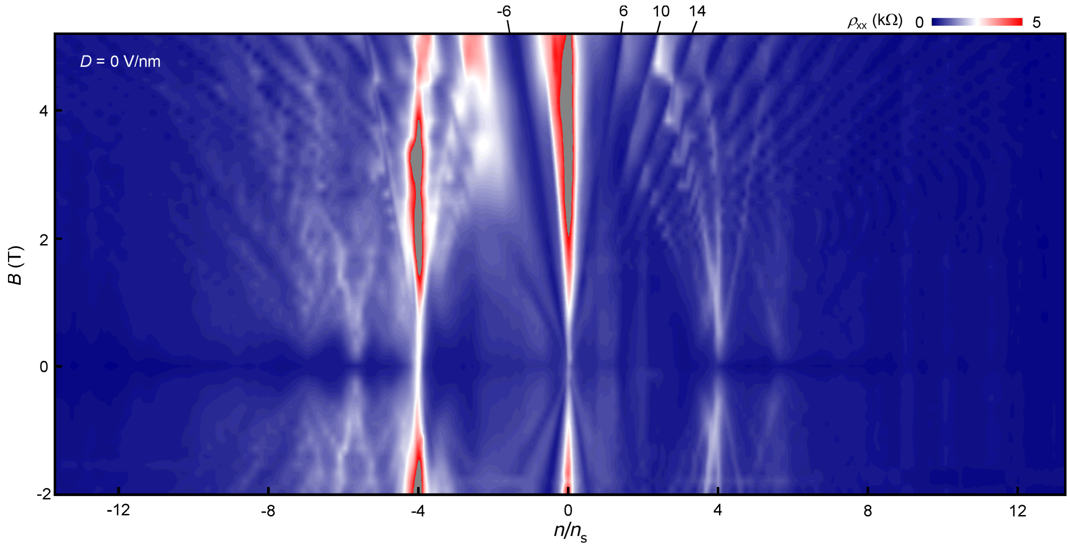

Figure 5.20: **Landau fan at $D = 0$ V/nm.** Longitudinal resistivity ρ_{yx} as a function of carrier density and magnetic field at displacement field $D = 0$ V/nm. Clear Landau levels develop from the charge neutrality point and fully filled points, which is direct evidence of the high quality of the encapsulated ABC-TLG device. The first resolved quantum Hall state of the charge neutrality point is $\nu = 6$. This Landau fan diagram establishes conclusively that we have ABC trilayer graphene in the hBN encapsulated device; it is completely different from the Landau fan diagram of ABA trilayer graphene (see Ref. 2).

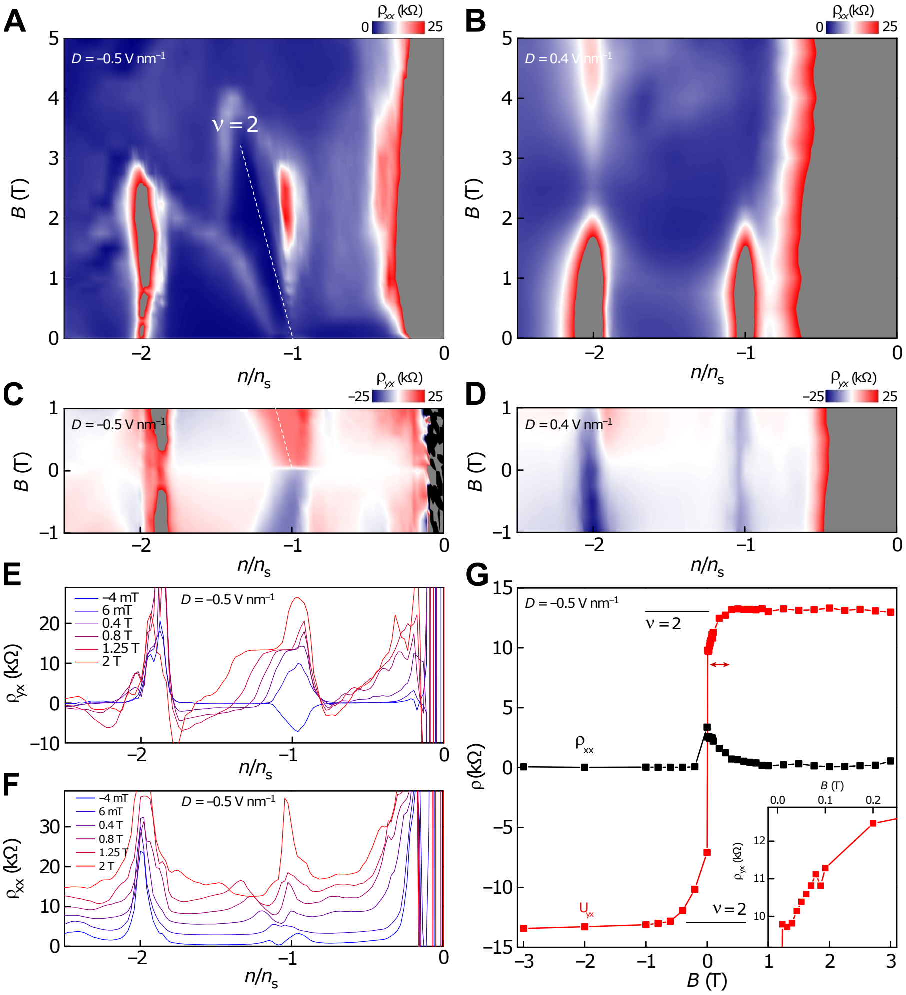

Figure 5.21: **Quantum Hall effect from the correlated $C = 2$ Chern insulator.** (**A, C**) Color plot of (A) ρ_{xx} and (C) ρ_{yx} as a function of carrier density and magnetic field for the topological hole miniband at $D = -0.5$ V/nm and $T = 0.06$ K. The experimental data at $T = 1.5$ K are qualitatively similar. (**B, D**) Corresponding (B) ρ_{xx} and (D) ρ_{yx} plots for the trivial hole miniband at $D = 0.4$ V/nm and $T = 1.5$ K. n_s corresponds to the carrier density of the 1/4 filling of the first miniband. No quantum Hall signatures are present in the trivial hole miniband, whereas a $\nu = 2$ quantum Hall effect characterized by a minimum of ρ_{xx} and a quantized ρ_{yx} emerges from 1/4 filling of the topological hole miniband. (**E, F**) Horizontal line cuts of (A) and (C), respectively. (E) shows that ρ_{yx} is well quantized beyond $B = 0.4$ T. An offset of 2.5 kΩ is applied for each trace in (F) (**G**) Line cut of ρ_{xx} and ρ_{yx} along the quantum Hall state (denoted by the dashed lines in (A) and (E)) shows that ρ_{yx} reaches a quantized value of $\nu = 2$ at 0.4 T, and a large ρ_{yx} persists down to zero magnetic field. It represents a quantum anomalous Hall state for the $C = 2$ correlated Chern insulator at $1/4$ filling. The inset shows a zoomed-in plot of ρ_{yx} at small magnetic field.

Fig. 5.21E, F shows ρ_{yx} and ρ_{xx} as a function of density for a few representative magnetic field values, corresponding to horizontal line cuts in Fig. 5.21C and A, respectively. ρ_{yx} is well quantized for magnetic field larger than 0.4 T at the value of 13.0 ± 0.2 kΩ, that is, the expected quantized value of $h/2e^2 = 12.9$ kΩ is within the empirical uncertainty. ρ_{xx} exhibits a corresponding minimum in the quantum Hall state, with a minimum resistivity less than 60 Ω at 2 T. Fig. 5.21G further displays ρ_{yx} and ρ_{xx} as a function of the magnetic field along the quantum Hall state following the dashed line in Fig. 5.21C, with the inset showing a zoomed-in plot of ρ_{yx} between 0 to 0.2 T. ρ_{yx} smoothly reaches the quantized value at 0.4 T. ρ_{yx} maintains a large though not quantized value all the way to zero magnetic field, and a large jump of ρ_{yx} is observed when the magnetic field changes sign.

The $\nu = 2$ quantum Hall state at $1/4$ filling at $D/\epsilon_0 = -0.5$ V/nm cannot be explained by a conventional integer quantum Hall effect from single-particle Landau levels. Instead, we argue that it represents a quantum anomalous Hall state from a correlated Chern insulator. First, this quantum Hall state only exists at negative D, where the miniband is predicted to have a non-trivial Chern number, and is absent at the positive D, where the band is predicted to be trivial. Second, it is well established that the lowest single-particle Landau level in ABC-TLG should be a $\nu = 3$ state owing to a winding number of 3 close to the valence band maximum [102]. Third, only one quantum Hall state is observed anywhere, and the quantized Hall resistivity appears to start at very low magnetic field. If the observed quantum Hall state of $1/4$ filling at $D/\epsilon_0 = -0.5$ V/nm is from the lowest single-particle Landau level, similar Landau levels should also exist close to the charge neutrality point and the $1/2$ filling correlated insulators, and higher Landau levels should be observable. (See Fig. 5.20 for a single-particle Landau fan diagram in the same device, where $D = 0$ and the electron correlation is weak.) Finally, an apparent non-zero quantum Hall-like gap was observed for the $1/4$ filling Chern insulator state down to $B = 0$ T; the size of the gap continuously increases with increasing B (Fig. 5.22). All our data can be naturally explained by a $\nu = 2$ Chern insulator state at $1/4$ filling. Such a $C = 2$ correlated Chern insulator should feature quantized Hall resistivity ρ_{yx} and a corresponding magnetic field dependent carrier density based on the Streda formula [177]. This Chern insulator at $1/4$ filling is a strongly correlated state that breaks the valley degeneracy and fills only the $C = 2$ electronic band in one valley. The nearly flat and tunable moiré minibands in the ABC-TLG/hBN moiré heterostructure are critical for the realization of such a correlated topological state.

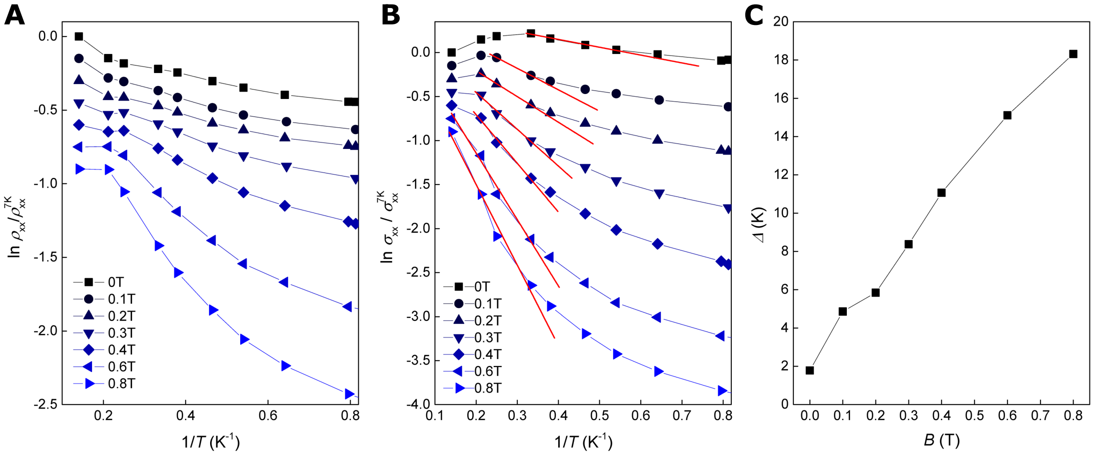

Figure 5.22: **Anomalous Hall effect and ferromagnetism.** (**A-C**) Arrhenius plot of the (A) longitudinal resistivity ρ_{xx}, (B) longitudinal conductivity σ_{xx}, and (C) the estimated gap at different magnetic field Δ. A manual offset of -0.15 is applied between each curve in (A) and (B). The gap size in (C) is extracted from the linear fit of $\sigma_{xx} \propto e^{-\Delta/2k_BT}$ (red line) in (B). We note that the Arrhenius plot is only valid for a limited temperature range, suggesting deviation from the thermal activated behavior at low temperatures. Therefore, the estimated gaps have relatively large uncertainty. However, the qualitative behavior is robust: insulating behavior is observed at all magnetic fields, and the quantized Hall insulator at finite magnetic field connects smoothly with the anomalous Hall insulator at zero magnetic field, supporting the identification of the state as a Chern insulator.

The correlated Chern insulator, persisting to zero magnetic field, spontaneously breaks the time-reversal symmetry and can generate valley-flavor ferromagnetism at $1/4$ filling. Indeed, ferromagnetism and strong anomalous Hall signals emerge from the Chern insulator state at zero magnetic field. Fig. 5.23A shows the temperature-dependent Hall resistivity when a small perpendicular B is swept between -0.1 T and 0.1 T. The Hall resistivity displays a clear anomalous Hall signal with strong ferromagnetic hysteresis. At $B = 0$ T, ρ_{yx} is non-zero and depends on the magnetic field sweep direction, a defining ferromagnetic feature. At the base temperature of $T = 0.06$ K, the anomalous Hall signal reaches a maximum of $\rho_{yx}^{\mathrm{AH}} = 8$ kΩ and a coercive field as large as $B_c = 30$ mT. The inset in Fig. 5.23A shows the temperature dependence of ρ_{yx}^{AH} and B_c: both signals decrease monotonically with increasing temperature, reaching zero at $T = 3.5$ K. The zero magnetic field ρ_{yx}^{AH} is already close to 12.9 kΩ. An almost perfect quantization of the $C = 2$ quantum anomalous Hall [105] Chern insulator appears at a magnetic field as low as 0.4 T.

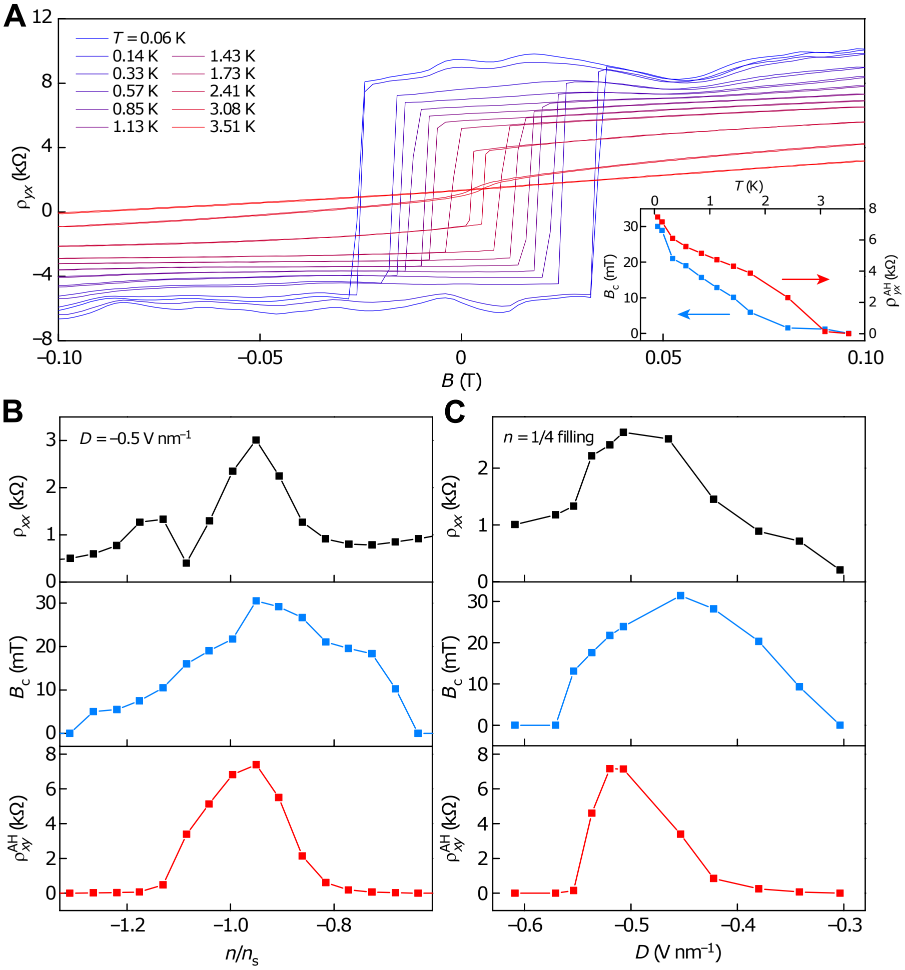

Figure 5.23: **Anomalous Hall effect and ferromagnetism.** (**A**) Magnetic-field-dependent ρ_{yx} at $1/4$ filling and $D = -0.5$ V/nm at different temperatures. The Hall resistivity displace a clear anomalous Hall signal with strong ferromagnetic hysteresis. At the base temperature of $T = 0.06$ K, the anomalous Hall signal can be as large as $\rho_{yx}^{\mathrm{AH}} = 8$ kΩ and the coercive field is $B_c = 30$ mT. The inset shows the extracted coercive field B_c and anomalous Hall signal ρ_{yx}^{AH} as a function of temperature. (**B**) The evolution of ρ_{xx}, B_c, and ρ_{yx}^{AH} as a function of hole doping at $D = -0.5$ V/nm and $T = 0.06$ K. The strongest anomalous Hall signal is observed close to $n = n_s$. (**C**) The evolution of ρ_{xx}, B_c, and ρ_{yx}^{AH} as a function of the displacement field D at $n = n_s$ and $T = 0.06$ K. The strongest anomalous Hall signal is observed when the device is most insulating (that is, largest ρ_{xx}).

The ferromagnetism is tunable by n and D and appears only in a limited parameter space of n and D. In Fig. 5.21E, ρ_{yx} near $n = n_s$ presents different signs at $B = -4$ mT and 6 mT, which is much smaller than B_c. For this measurement, the magnetic field is fixed and carrier density is swept from a non-ferromagnetic state to a ferromagnetic state, which leads to ρ_{yx} with different signs even in small positive and negative magnetic fields. A clearer n-dependence of ρ_{xx}, B_c and ρ_{yx}^{AH} at $D/\epsilon_0 = -0.5\ \mathrm{V/nm}$ at the base temperature is shown in Fig. 5.23B by sweeping the magnetic field at different fixed n. B_c and ρ_{yx}^{AH} both have maximum values close to $n = n_s$. However, ρ_{yx}^{AH} shows a stronger carrier doping dependence and decreases to almost zero at $n = n_s \pm 0.2n_s$, while B_c decreases to zero at $n = n_s \pm 0.35n_s$. ρ_{xx} displays an unusual behaviour with both a resistance peak and a resistance dip close to $n = n_s$, the origin of which requires further experimental and theoretical study. Fig. 5.23C shows the D-dependence of ρ_{xx}, B_c and ρ_{yx}^{AH} at $n = n_s$. ρ_{xx} shows a maximum at $D/\epsilon_0 = -0.5\ \mathrm{V/nm}$, which might be due to the narrowest bandwidth and strongest correlation effects at this displacement field [2]. ρ_{yx}^{AH} also shows a maximum at $D/\epsilon_0 = -0.5\ \mathrm{V/nm}$, suggesting the importance of electron–electron correlations to the observed anomalous Hall signal. A finite ρ_{yx}^{AH} can be observed with D/ϵ_0 between $-0.3\ \mathrm{V/nm}$ and $-0.57\ \mathrm{V/nm}$. A non-zero B_c is present in the same D range, although the maximum B_c appears at $D/\epsilon_0 = -0.45\ \mathrm{V/nm}$.

5.3.4 Hartree-Fock calculations

The observed $C = 2$ correlated Chern insulator can be understood theoretically from the topological moiré minibands when the electron–electron interactions are considered. Previous theoretical calculations predict a valley Chern number $C = 3$ for the single-particle hole miniband for negative D (Refs. 4 and 20), but our results suggest that interaction effects can renormalize the valley Chern number. Fig. 5.24A, B shows the single-particle band structures of the lowest few moiré minibands in ABC-TLG/hBN moiré superlattices for positive and negative displacement fields. For the negative D values (supporting a non-zero valley Chern number), the valence band overlaps with the remote lower band (see Fig. 5.24A). We incorporate the interaction effects in Hartree–Fock theory. When the valence band is close to the band below (at large $|D|$) or when the interaction strength is sufficiently strong (with small dielectric constant), the self-energy corrections mix the valence band and the lower band, leading to reduction of the Chern number to $C = 2$. As shown in Fig. 5.24C, when the dielectric constant is around 4 (effective screening from the dielectric constant of hBN), the valley Chern number is expected to be 2 for a large range of displacement field values.

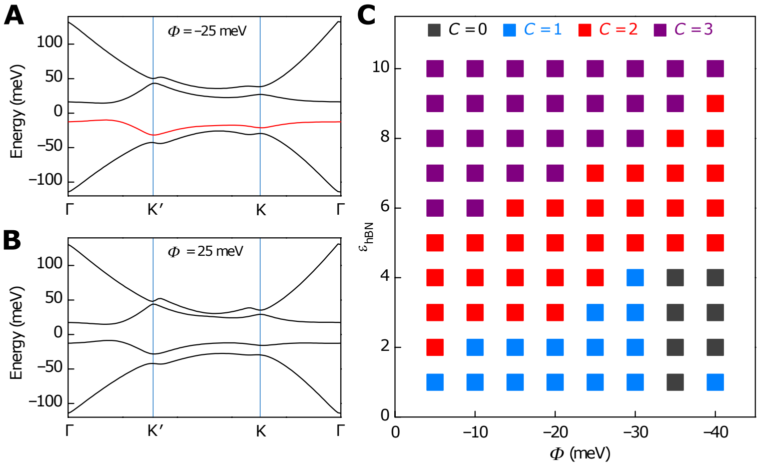

Figure 5.24: **Calculated Chern number including the electron-electron interaction effects.** (**A, B**) Calculated single-particle band structure of the ABC-TLG/hBN moiré superlattice for $\Phi = -25$ meV and 25 meV, respectively. Here Φ is the energy difference between the top and bottom layers of the ABC-TLG, and $\Phi = -25$ meV corresponds to the vertical displacement field around $D = -0.5$ V/nm. The red line highlights the topological hole miniband for $\Phi = -25$ meV. (**C**) Calculated Chern number of the hole miniband as a function of the energy difference Φ and the effective dielectric constant ϵ_{hBN} after including the electron-electron interaction effects using the Hartree-Fock approximation. The resulting band Chern number can be 2 for parameters close to the experimental device where $\Phi \approx -25$ meV and $\epsilon_{\mathrm{hBN}} \approx 4$.

5.3.5 Discussion

Our observation of a tunable $C = 2$ Chern insulator in ABC-TLG/hBN moiré superlattice provides an opportunity to explore correlated topological states in van der Waals moiré heterostructures. For example, fractional Chern insulators and non-Abelian states could emerge from strong correlations in nearly flat topological minibands once the quality of moiré heterostructures is further improved. In particular, the flat $C = 2$ Chern band has the potential to host novel fractional Chern insulator states beyond the fractional quantum Hall paradigm [178, 179], that we will discuss in the following chapter.

Chapter 6

Magnetism at non-integer filling in moiré systems

6.1 Magnetism at non-integer filling in ABC-TLG/hBN

6.1.1 Introduction

The flat bands resulting from moiré superlattices in magic-angle twisted bilayer graphene (MATBG) and ABC-trilayer graphene aligned with hexagonal boron nitride (ABC-TLG/hBN) have been shown to give rise to orbital magnetism associated with correlated Chern insulators centered at integer multiples of n_s, the density corresponding to one electron per moiré superlattice unit cell [18, 21, 175]. In this section we will discuss the experimental observation of ferromagnetism at fractional filling of the moiré superlattice in ABC-TLG/hBN. We perform magneto-transport measurements to map out the phase diagram of an ABC-TLG/hBN heterostructure as a function of the carrier density n, the vertical displacement field D, and the vertical magnetic field B. The ferromagnetic state exhibits prominent ferromagnetic hysteresis behavior with large anomalous Hall resistivity in the region when the topological Chern band is partially filled between $n = -2.1n_s$ and $-2.7n_s$ and D/ϵ_0 ranges from $-0.45\ \mathrm{V/nm}$ to $-0.55\ \mathrm{V/nm}$. The ferromagnetic state exhibits hysteresis and shows a zero-field anomalous Hall (AH) signal as large as $-4.8\ \mathrm{k\Omega}$ at $n = -2.3n_s$ and $D/\epsilon_0 = -0.48\ \mathrm{V/nm}$. The large AH signal is accompanied by a peak in the longitudinal resistivity as a function of n. In addition, the longitudinal resistivity of the magnetic states increase slightly when reducing temperature, suggesting that the states showing ferromagnetism are insulating.

We will also see that this ferromagnetism depends very sensitively on the control parameters in the moiré system: not only the magnitude of the anomalous Hall signal, but also the sign of the hysteretic ferromagnetic response can be modulated by tuning the carrier density and displacement field. Our discovery of electrically tunable ferromagnetism in a moiré Chern band at non-integer filling highlights the opportunities for exploring new correlated ferromagnetic states in moiré heterostructures.

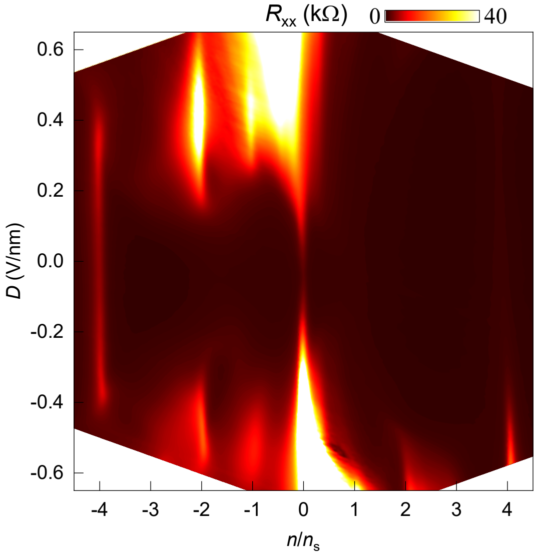

Figure 6.1: **Longitudinal resistance of ABC-TLG/hBN.** Longitudinal resistance $R_{xx} = V_{xx}/I$ as a function of band filling factor n/n_s and vertical displacement field D at $T = 1.5$ K. In addition to the band insulating states at the charge neutrality point ($n = 0$) and the fulling filled point ($n = -4n_s$), correlated insulator states emerge at $1/4$ filling ($n = -n_s$) and $1/2$ filling ($n = -2n_s$) at finite $|D|$.

6.1.2 Basic and magneto-transport characterization

This electronic bandstructure of the moiré minibands can be conveniently tuned by the D field in ABC-TLG/hBN heterostructure. Fig. 6.1 displays the longitudinal resistance R_{xx} as a function of band filling n/n_s and displacement field D in the device. In addition to the band insulating states (characterized by resistance peaks) at the charge neutral point ($n = 0$) and the fully filled point ($n = -4n_s$), correlated insulator states also emerge at $1/4$ filling ($n = -n_s$) and $1/2$ filling ($n = -2n_s$) of the hole minibands (i.e. one and two holes per moiré unit cell, respectively) [2]. These correlated states appear at finite displacement field $|D|$, presumably because they require narrowing of the moiré minibands. All measurements in this section are performed at 0.07 K and with an AC excitation current $I = 0.5$ nA RMS unless otherwise noted.

To explore ferromagnetism and evidence for band topology, we turn to magneto-transport measurements. Fig. 6.2A and B show the longitudinal resistance at $B = 0$ T as a function of the band filling of topologically trivial and non-trivial valence minibands at $D/\epsilon_0 = 0.4$ V/nm and -0.47 V/nm, respectively. In the trivial flat band (at $D/\epsilon_0 = 0.4$ V/nm), strong Mott insulator states are present at $n = -n_s$ and $n = -2n_s$. In the topological flat band (at $D/\epsilon_0 = -0.47$ V/nm), weaker resistance peaks are observed at $n = -n_s$, $n = -2n_s$, and $n = -2.3n_s$. Fig. 6.2C and D display the corresponding two-dimensional plots of the Hall resistance R_{yx} as a function of the hole doping and the perpendicular magnetic field B (normal to ABC-TLG/hBN layers). In the trivial flat band (at $D/\epsilon_0 = 0.4\ \mathrm{V/nm}$), the Hall resistance signal tends to be rather small for all hole doping (Fig. 6.2C) and no ferromagnetic signature is observed. (The large signals at $n = -n_s$ and $n = -2n_s$ fillings are artifacts coming from crosstalk from the large R_{xx} of the correlated insulator states; they do not change sign when the magnetic field is reversed.) With the displacement field reversed $D/\epsilon_0 = -0.47\ \mathrm{V/nm}$, the behavior is strikingly different: at carrier densities around $n = -n_s$ and $n = -2.3n_s$, the Hall resistance R_{yx} is very large at weak magnetic fields and persists down to zero magnetic field. R_{yx} switches sign abruptly at a magnetic field close to, but away from, zero (Fig. 6.2D; field is swept from positive to negative). Such behavior is characteristic of a ferromagnetic state. Indeed, the state at $n = -n_s$ has been previously [21] shown to be a $C = 2$ Chern insulator state. The Chern insulating state at $n = n_s$ is characterized by orbital ferromagnetism with a quantized AH signal of $h/2e^2$ at $0.5\ \mathrm{T}$. We note that the magnetic field required to quantize the AH effect is larger here than in [21] because $D/\epsilon_0 = -0.47\ \mathrm{V/nm}$ is different from $D = -0.5\ \mathrm{V/nm}$, which produced the strongest Chern insulator The Chern insulator at $n = -n_s$ can be understood as arising from a single fully-filled valley-polarized Chern band [106]. The state around $n = -2.3n_s$, in contrast, is a completely new magnetic state that has not been predicted and emerges, surprisingly, at non-integer filling of the moiré miniband.

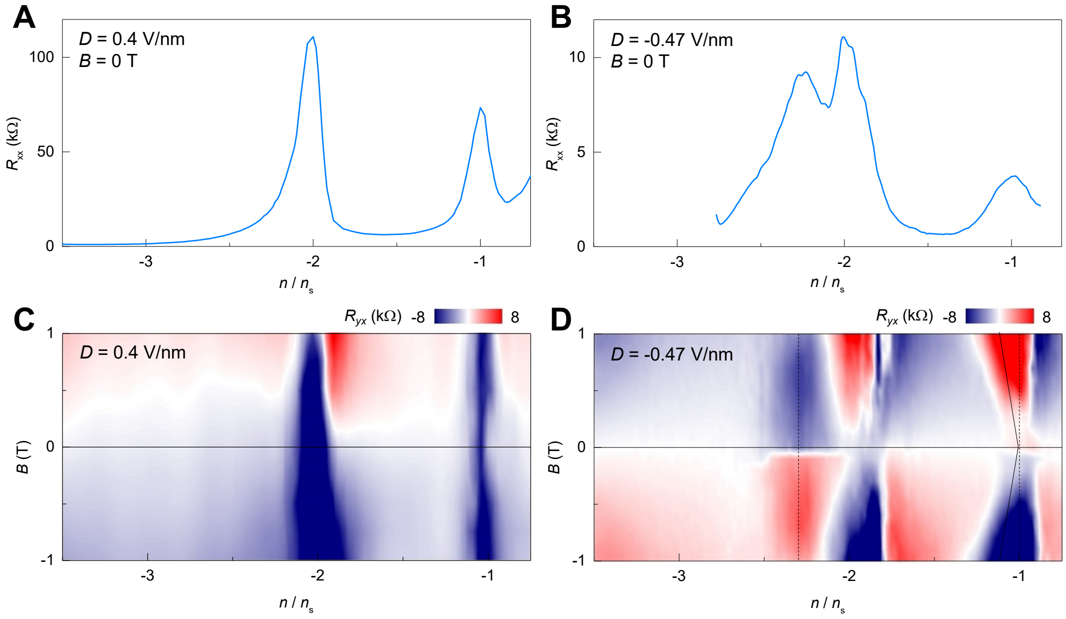

Figure 6.2: **Longitudinal and Hall resistances at selected values of D.** (**A and B**) Longitudinal resistance R_{xx} as a function of band filling at $D = 0.4\ \mathrm{V/nm}$ and $-0.47\ \mathrm{V/nm}$, respectively. (**C and D**) Corresponding color plots of the Hall resistance as a function of band filling and perpendicular magnetic field. For (C) $D = 0.4\ \mathrm{V/nm}$, the Hall resistance tends to be small for all doping and no ferromagnetic signature is observed (the relatively large signals at $n = -n_s$ and $n = -2n_s$ in (C) are artifacts coming from crosstalk from the large R_{xx}, evinced by the observation that they do not change sign when the magnetic field is reversed). For (D) $D = -0.47\ \mathrm{V/nm}$, the Hall resistance is very large at weak magnetic fields and can persist down to zero magnetic field at $n = -n_s$ and $n = -2.3n_s$ (denoted by the two dashed vertical lines). The non-zero values of R_{yx} at $B = 0$ represents AH signals from ferromagnetic states at $n = -n_s$ and $n = -2.3n_s$. The state at $n = -n_s$ has been identified as a $C = 2$ Chern insulator state (two oblique solid lines) with orbital ferromagnetism [21]. The AH at $n = -2.3n_s$ results from a new magnetic state that emerges at non-integer filling of the topological hole miniband.

To establish the region of parameter space where the new magnetic state exists, we applied $B = 0.2\ \mathrm{T}$ to favor polarization, and track R_{yx} as a function of n and D (Fig. 6.3A). In an oval region of parameter space centered around $n = -2.3n_s$ and $D/\epsilon_0 = -0.48\ \mathrm{V/nm}$ (outlined by the dashed line in Fig. 6.3A, which is discussed in more detail below), R_{yx} is large and negative. Fig. 6.3B shows the corresponding two-dimensional plots of R_{xx} as a function of n/n_s and D at a weak magnetic field $B = 0.2\ \mathrm{T}$. This oval region also shows enhanced R_{xx} compared with the surrounding region, as shown in Fig. 6.3B. This suggests that the ferromagnetic phase in this range of parameters is always insulating.

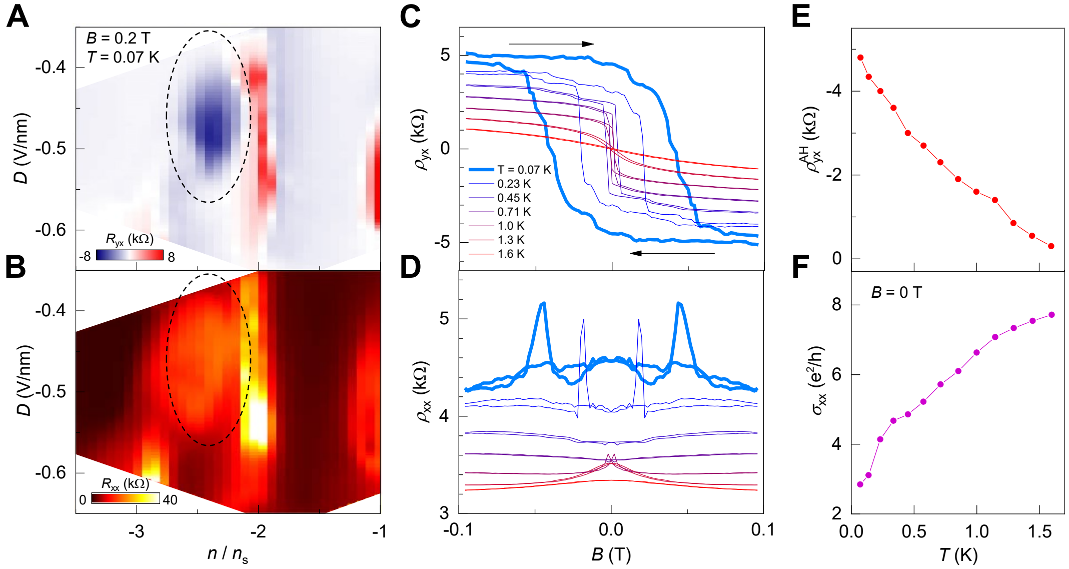

Figure 6.3: **Anomalous Hall effect at non-integer filling.** (**A and B**) R_{yx} and R_{xx} as functions of band filling and displacement field, respectively, for the valence miniband at $B = 0.2$ T and $T = 0.07$ K. The dashed oval outlines a region with large R_{yx} signals at very small field between $n = -2.1n_s$ and $2.6n_s$ and between $D = -0.4$ and -0.53 V/nm (more detail is given in Fig. 6.4). The oval region also shows enhanced R_{xx} in (B), suggesting that the ferromagnetic phase is insulating (**C and D**) Magnetic-field dependent anti-symmetrized ρ_{yx} and symmetrized ρ_{xx} ad different temperatures for the ferromagnetic state with largest AH at the center of the oval region ($n = -2.3n_s$ and $D = -0.48$ V/nm). The AH signal shows clear ferromagnetic hysteresis in (C), reaching $\rho_{yx}^{\mathrm{AH}} = -4.8$ kΩand a coercive field of $B_c = 0.04$ T at $T = 0.07$ K. (**E and F**) The evolution of ρ_{yx}^{AH} and σ_{xx} as a function of temperature at $n = -2.3n_s$ and $D = -0.48$ V/nm. The amplitude of ρ_{yx}^{AH} decreases with increasing T, vanishing around 1.6 K, while σ_{xx} increases with increasing T.

6.1.3 Characterizing the magnetic state

Next we examine in detail the B field and temperature dependence of the new magnetic state at which the AH has the largest magnitude ($n = -2.3n_s$ and $D/\epsilon_0 = -0.48$ V/nm). We measure the anti-symmetrized Hall resistivity $\rho_{yx}(B, \mathrm{up}) = (R_{yx}(B, \mathrm{up}) - R_{yx}(-B, \mathrm{down}))/2$, $\rho_{yx}(B, \mathrm{down}) = (R_{yx}(B, \mathrm{down}) - R_{yx}(-B, \mathrm{up}))/2$ and symmetrized longitudinal resistivity $\rho_{xx}(B, \mathrm{up}) = (R_{xx}(B, \mathrm{up}) + R_{xx}(-B, \mathrm{down}))/2 \cdot W/L$, $\rho_{xx}(B, \mathrm{down}) = (R_{xx}(B, \mathrm{down}) + R_{xx}(-B, \mathrm{up}))/2 \cdot W/L$, where up/down indicates the direction in which the magnetic field was being swept, the channel width $W = 1\ \mu$m, and the channel length $L = 4\ \mu$m (we use ρ_{yx} when presenting AH signals as functions of the magnetic field to eliminate longitudinal resistance contributions, but we use the directly measured R_{yx} when presenting color maps of the dependence of

Hall resistance on n and D). When B is swept over the narrow range between -0.1 to 0.1 T, the Hall resistivity ρ_{yx} shows a clear AH signal with strong ferromagnetic hysteresis (Fig. 6.3C). The AH signal reaches $\rho_{yx}^{\mathrm{AH}} = -4.8\ \mathrm{k}\Omega$ with a coercive field of $B_c = 0.04$ T at the base temperature of $T = 0.07$ K. ρ_{yx}^{AH} decreases monotonically with increasing temperature, reaching almost zero at $T = 1.6$ K (Fig. 6.3E). We note that ρ_{yx}^{AH} at $n = -2.3n_s$ exhibits the opposite sign compared to that of the Chern insulator at $n = -n_s$ (see Ch.5).

Fig. 6.3D shows that the overall longitudinal resistivity of the magnetic state increases as temperature is lowered. Fig. 6.3E and F display the AH signal ρ_{yx}^{AH} and longitudinal conductivity σ_{xx} (derived from the measured resistivities) as functions of the temperature at $B = 0$ T. As the temperature is lowered, the ferromagnetic state strengthens, as evinced by increasing ρ_{yx}^{AH} and the conductivity σ_{xx} decreases. The temperature dependencies of ρ_{xx} and σ_{xx} suggest that the ferromagnetic state is insulating. However, we do not observe well-defined Arrhenius behavior (see plot of $\log\,\sigma_{xx}$ versus $1/T$ in Fig. 6.6C).

Next we examine the evolution of the AH signal as a function of D and n. We sweep the field up and down over a small range of magnetic fields and measure ρ_{yx}. Fig 6.4A shows the D-dependence at fixed doping of $n = -2.5n_s$. Beginning at $D/\epsilon_0 = -0.49\ \mathrm{V/nm}$, where there is no nonlinearity, the hallmark of AH, the AH grows with less negative D as one approaches the center of the oval. Upon tuning away from the center of the oval, the AH signal decreases quickly and becomes zero at $D/\epsilon_0 = -0.38\ \mathrm{V/nm}$. Surprisingly, the AH reappears at $D = -0.37\ \mathrm{V/nm}$, accompanied by a switch in sign of the hysteresis loop. It then decreases and becomes very small again for $D \lesssim -0.35\ \mathrm{V/nm}$.

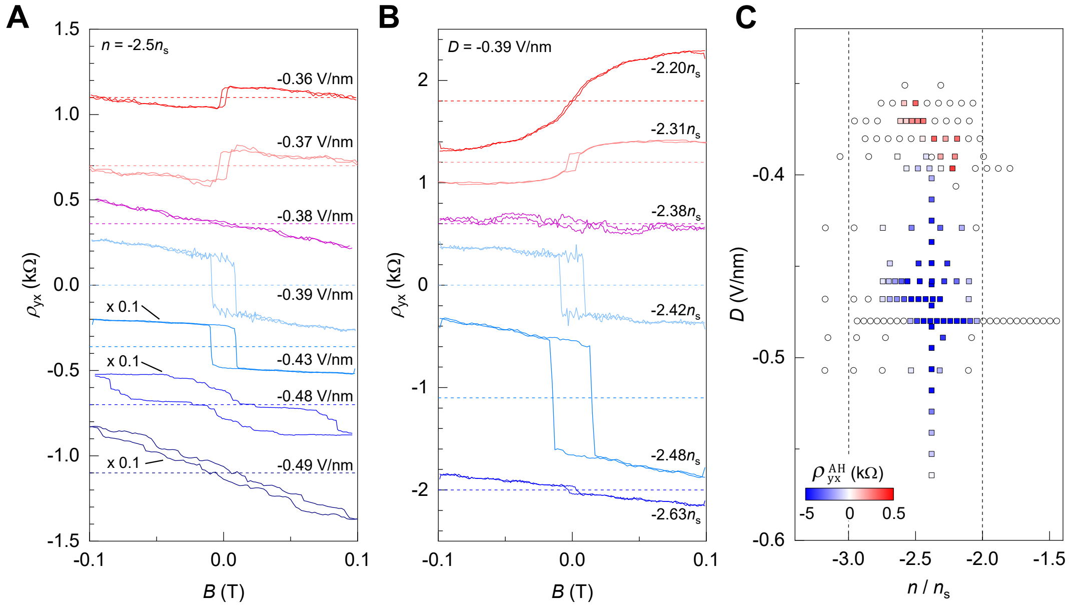

Figure 6.4: **Tunable anomalous Hall effect at non-integer filling.** (**A**) The D-dependent ferromagnetism at $n = -2.5n_s$. The AH resistance is maximal at $D = -0.48\ \mathrm{V/nm}$, becomes zero at $D = -0.38\ \mathrm{V/nm}$, and then reappears with a sign change at $D = -0.37\ \mathrm{V/nm}$. The ρ_{yx} signals at $D = -0.49$, -0.48, and $-0.43\ \mathrm{V/nm}$ are manually multiplied by a factor of 0.1 for clarity. (**B**) The n-dependent ferromagnetism at fixed $D = -0.39\ \mathrm{V/nm}$. The AH signal reaches a maximum at $n = -2.48n_s$, becomes nearly zero at $n = -2.38n_s$, and reappears with a sign change at $n = -2.31n_s$. Although the hysteresis is gone at $n = -2.2n_s$, the strongly nonlinear dependence indicates a large AH; AH vanishes at less negative n. Each curve in (A and B) is offset for clarity, and the dashed lines denote zero ρ_{yx}. (**C**) The individual squares represent measured AH resistance, with color scale shown in the lower left corner. The circles represent data with no measurable AH.

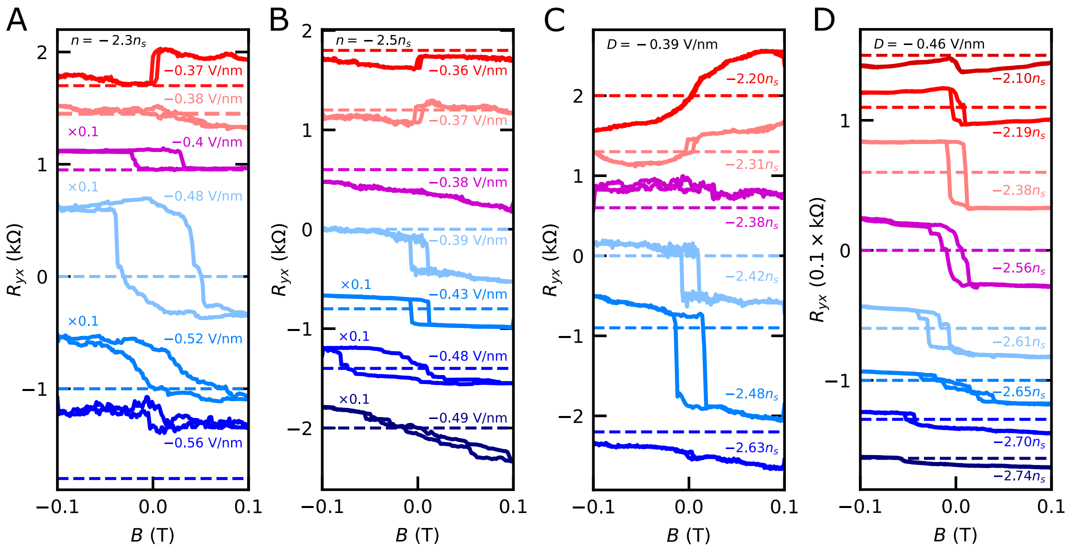

Figure 6.5: **Additional hysteresis loops.** R_{yx} as a function of magnetic field at (**A**) fixed $n = -2.3n_s$ for various D, (**B**) at fixed $n = -2.5n_s$ for various D, (**C**) at fixed $D = -0.39$ V/nm for various n, and (**D**) at fixed $D = -0.46$ V/nm for various n. Each curve is offset for clarity, with the dashed line of the same color denoting $R_{yx} = 0$ for that data set. The dashed line is often not located at the center of the corresponding AH loop due to cross-talk of R_{xx} because of inhomogeneity. The traces annotated with an adjacent 'x0.1' are manually multiplied by a factor of 0.1.

The magnitude and sign of the ferromagnetic hysteresis also depends sensitively on the carrier density n for a fixed $D/\epsilon_0 = -0.39$ V/nm (Fig. 6.4B). At this displacement field, the AH signal reaches a first maximum at $n = -2.48n_s$. With less negative n, the AH signal decreases quickly. Then the AH signal changes sign, and although the hysteresis disappears near $n = -2.31n_s$, the non-linear component, which is the best measure of the AH signal, continues to grow as n is made less negative.

To visualize the dramatic change of the ferromagnetic state with n and D, we indicate the parameter space with negative and positive ρ_{yx}^{AH} in Fig. 6.4C with blue and red squares, respectively, where the intensity of the color indicates the magnitude of the anomalous Hall signal. Values of $(n,\, D)$ where AH is zero are indicated by circles. A variety of additional magnetic field sweeps for various values of n and D are shown in Fig. 6.5 for the same sample studied in Fig. 6.4. We note that the hysteresis loops of the magnetic state can be rather complicated close to the oval boundaries, at which the AH vanishes. Some hysteresis loops show multiple intermediate jumps in ρ_{yx} (R_{yx}), and some hysteresis loops appear at non-zero magnetic fields (Fig. 6.4 and Fig. 6.5).

6.1.4 Behavior of the conductivity tensor

The behavior of the conductivity tensors σ_{xx} and σ_{xy} can yield insights into the mechanism of the observed AH at non-integer filling. The AH effect can either be intrinsic, arising from Berry curvature of the filled bands, or extrinsic, resulting from a scattering mechanism. We suggest AH at the non-integer filling is intrinsic. First, the AH is only observed for the sign of the D field which leads to the Chern band according to our band structure calculation, and not at the other sign which is predicted to lead to a topological trivial band. Second, skew scattering, one of the extrinsic mechanisms leading to AH in magnetic metals, gives rise to a linear relationship between σ_{xy} and σ_{xx}. Fig 6.6A and B clearly show nonlinear relationships between σ_{xy} and σ_{xx} when either density or temperature are varied [132]. It is more challenging to rule out side jump scattering, another extrinsic mechanism. Both of these mechanisms, however, can be effective only in metallic materials and, as shown in Fig. 6.2B, the AH occurs where the longitudinal resistance is quite high, perhaps indicating that the device is insulating. Furthermore the longitudinal conductivity demonstrates insulating temperature dependence, increases with increasing temperature, as shown in Fig. 6.6C. Third, the largest anomalous Hall angle σ_{xy}/σ_{xx} is close to unity, which is much larger than previously reported extrinsic or intrinsic AH materials (≤ 0.2) [132, 143] except for Chern insulators [18, 19, 21, 133, 134, 175], which also suggests the intrinsic mechanism.

Fig. 6.6D shows σ_{xy} and σ_{xx} as functions of n at $D = -0.48$ V/nm at $B = 0$ T. The large σ_{xy} is accompanied with a drop of σ_{xx} which is one would expect for a Chern insulator. We believe that the absence of quantization of the former and non-zero value of the latter probably results from the presence of domains.

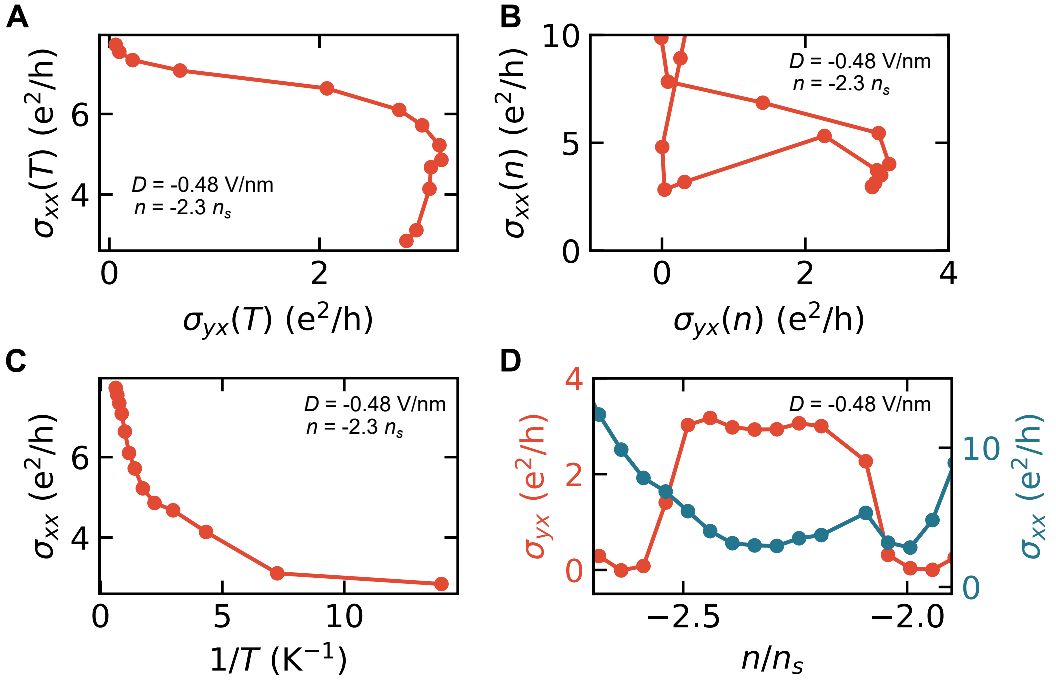

Figure 6.6: **Behavior of the conductivity tensor at $B = 0$ T.** (**A**) The longitudinal conductivity σ_{xx} is plotted parametrically against the Hall conductivity σ_{xy} for a series of measurements at different temperatures with the density and displacement field fixed at $n = -2.3n_s$ and $D = -0.48$ V/nm. (**B**) σ_{xx} is plotted parametrically against σ_{xy} for a series of measurements at different densities for fixed temperature $T = 0.07$ K and displacement field $D = -0.48$ V/nm. (**C**) Arrhenius plot of σ_{xx} on a log scale versus $1/T$. (**D**) σ_{xx} and σ_{xy} as functions of carrier density, from the same data as in (B), showing the emergence of a dip in σ_{xx} accompanied by the σ_{xy} maximum around $n = -2.3n_s$.

6.1.5 Discussion

We have shown that ferromagnetism can emerge not only at integer filling of a miniband in an ABC-TLG/hBN moiré superlattice [21] but also in a region centered about non-integer filling, behavior which is currently unique among the reported magnetic states in moiré systems. As with AH in other moiré systems, the system appears to be insulating at zero field and the magnitude of the AH is large, indicating that it is unlikely that the AH arises from some scattering mechanism as in ferromagnetic metals. We therefore assume that, while the ferromagnetic state at non-integer filling in ABC-TLG/hBN as yet exhibits significant longitudinal resistance and no quantization of AH, the large AH arises, as it does in the other systems, from a combination of band topology and electron-electron interactions. Interactions break valley/spin degeneracy, and give a gap between the bands with opposite Chern numbers. The observed magnetic state appears only when the valence miniband has been tuned by the applied displacement field to be topologically non-trivial, suggesting the importance of band topology for realizing the magnetic state.

The ferromagnetic hysteresis in Hall resistance at non-integer filling can change sign with field effect control of D and n, perhaps indicating that different ferromagnetic states can be stabilized in different regions of parameter space [148]. This reversal of the sign of AH as a function of carrier density is similar to that recently reported for ferromagnetism centered at $n = 3n_s$ in twisted monolayer-bilayer graphene [180]. These authors report that the Hall resistance saturates near $h/2e^2$ on both sides of the sign reversal, while the longitudinal resistance $R_{xx} \leq 1$ kΩ, suggesting that on the two sides of the sign reversal there are Chern insulators with Chern numbers $C = \pm 2$. The sign reversal of the AH with carrier density reported here can then be explained as follows: with an applied external magnetic field, we control the preferred magnetization direction, as the magnetic moment wants to align with the field. But Chern number is not simply related to magnetization: the magnetization of an orbital Chern insulator reverses as the chemical potential passes through the gap [148]. Therefore, the magnetization of each valley, and hence the magnetization for a Chern insulator of each Chern number, reverses as a function of carrier density, yielding the measured reversal of AH resistance. The sign of the AH is not reported to be sensitive to D in twisted monolayer-bilayer graphene [180] as it is for the non-integer filling ferromagnetic state in the present work. However, it is predicted that the sign of the magnetization of an orbital Chern insulator of a given Chern number also depends on gap size, the bandwidth of the bands, and the valley splitting [148]. Tuning D strongly affects these parameters in ABC-TLG/hBN, therefore it is perhaps not surprising that, for fixed chemical potential, we see a sign flip in the measured AH resistance as a function of D, as well. Twisted monolayer-bilayer graphene has also been found to be magnetic in a region centered near $n = n_s$ but this state does not exhibit a sign change of AH as a function of carrier density [76, 180].

Thus both the large AH and its sign reversal likely arise from a correlation-induced gap between bands with opposite Chern numbers. Whereas it is straightforward to understand such a gap in twisted monolayer-bilayer graphene at integer filling as caused by electron-electron interactions simply by symmetry breaking of the spin/valley degrees of freedom [76, 148, 180], a gap at non-integer filling as in the ABC-trilayer graphene/hBN moiré system suggests a more complicated ground state.

6.2 Evidence for magnetism at non-integer filling in tBLG

While we were able to clearly observe signatures of magnetism at non-integer filling repeatably across multiple ABC-TLG/hBN devices, here we will discuss more sporadic signatures of a similar state in tBLG. In all cooldowns of the device discussed in Sec. 5.1, we observed that the anomalous Hall, although small, remains non-zero in approximately the region $n \sim 0.72n_s$ to $\sim 0.9n_s$ (as shown previously in Fig. 5.5). However, on several cooldowns of the same device, we see strikingly different behavior: in addition to the appearance of small non-zero anomalous Hall far above $n = 3n_s$, we see an isolated secondary peak centered near $n = 3.5n_s$ (Fig. 6.7). This peak exhibits a maximum value of slightly more than $1/3$ that of the main peak; $R_{yx}^{\mathrm{AH}} = 3.10$ kΩ at $n = 3.5n_s$ and $R_{yx}^{\mathrm{AH}} = 9.04$ kΩ at $n = 3.08n_s$.

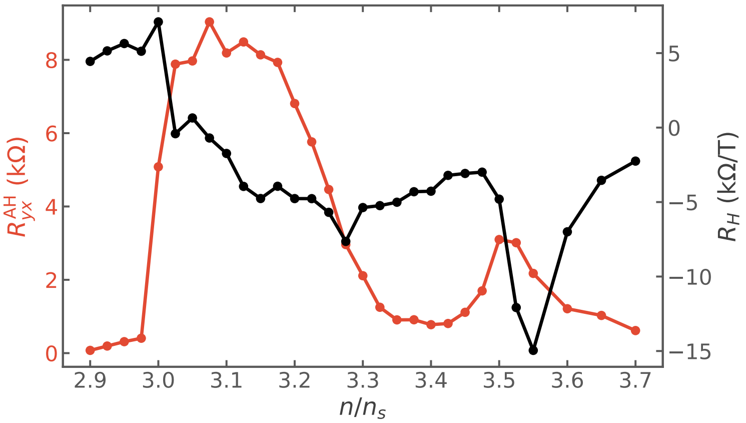

Figure 6.7: **Peak in anomalous Hall at non-integer filling.** Zero-field anomalous Hall resistance R_{yx}^{AH} (red) and ordinary Hall slope R_{H} (black) as a function of n/n_s for $D/\epsilon_0 = -0.22$ V/nm. R_{yx}^{AH} is peaked with a maximum around $n/n_s = 3.08$, coincident with R_{H} changing sign. Additionally, we observe a second peak in R_{yx}^{AH} at $n/n_s = 3.5$ that is approximately $1/3$ the height of the main peak. This secondary peak is coincident with a strong dip in R_{H}.

It is somewhat surprising that a feature that is so prominent on one cooldown is totally absent on others. However, as we discussed in Sec. 5.1, there was significant variation between cooldowns for the zero field R_{xx} gate maps shown in Figs. 5.1 and 5.3; there appears to be a significant shift in the intrinsic displacement field between cooldowns (there was no clear feature to ascribe to zero displacement field so the gate maps are really plotted against the additional applied displacement field). Perhaps the state is simply more fragile than the state at $n = 3n_s$ and only exists in a particular range of D. It could also be the case that the state is particularly sensitive to the frozen background disorder potential seen by the device during a given cooldown, which is a potential explanation for the shift in D between cooldowns. Without the ability to assign a particular feature to a known displacement field, we cannot orient ourselves absolutely and say definitively where this feature exists in the parameter space.

This secondary peak in anomalous Hall at $n = 3.5n_s$ could be consistent with a fractional Chern insulating state at half-filling of a single spin-valley flavor band [171]. The main piece of evidence in favor of this explanation at this point is that the Hall resistance is centered at and exists only in a narrow region near $n = 3.5n_s$. Evidence of a well quantized Hall signal will be needed before we can definitively declare this as the explanation. An alternative explanation, given that the device has been shown to be quite inhomogeneous as previously discussed, is that this secondary peak corresponds to doping some island that is heavily doped relative to the rest of the device to $n = 3n_s$. This would neatly explain why the state is sporadically observed but seems somewhat unlikely; most forms of disorder would simply blur a feature, not create a separated, well isolated domain in the device. For example, twist angle disorder, which is potentially the dominant disorder in the device, has been directly observed to vary smoothly [13].

Chapter 7

Outlook

7.1 Superconductivity in ABC-TLG/hBN

At this point, superconductivity in tBLG has been clearly demonstrated and replicated by many groups (see Refs. 75 and 181 for a characterization of transition temperature as a function of twist angle). However, the phase diagram is far from clear, and many devices behave quite differently. It is possible to achieve superconductivity in devices with either weak or no signatures of correlated insulating states [75, 182, 183], likely indicating that the superconducting phase competes with the proximate correlated insulating states. An even stranger tBLG device displayed multiple pockets of superconductivity [128], showing that it is perhaps possible to achieve superconductivity at any filling within the flat bands.

Beyond ABC-TLG/hBN, there are many other moiré based systems that show signatures of superconductivity but fall short in some way [180, 184–187]. Recent measurements in tBLG may provide a potential explanation for the phenomena observed in these systems. A number of different Chern insulating states can be induced with the application of a small magnetic field in tBLG [188–191], indicating that there are competing phases that are not far apart in energy. Subsequently, it was found that such a transition could be driven by either the application of an in-plane magnetic field or by increasing temperature [192, 193]. As the new phase is favored by a magnetic field, it is likely spin/valley polarized in some way. Therefore, we are likely seeing a Pomeranchuk like phase transition: a transition from a disordered state at low temperature to a entropically favored ordered state at high temperature. For this to be an entropically favored ordered state, it needs to have a very small stiffness in its order parameter, allowing for strong fluctuations. These fluctuations manifest as a large change in the resistivity across the phase transition.

A similar effect could explain the phenomena that have been previously ascribed to superconductivity in these other flat band moiré systems. In a flat band system, symmetry broken states are likely going to be competitive if the bandwidth is small enough. If the order parameter also has a small stiffness, it could drive such a Pomeranchuk like phase transition, leading to the precipitous drop in resistivity as a function of temperature that was ascribed to a superconducting phase transition.

7.2 Ferromagnetism at integer filling

While the tBLG device discussed in Ch. 5 does not exhibit quantized Hall resistance or zero longitudinal resistance, it does exhibit what appears to be incipient Chern insulating behavior, that would suggest the ground state at low in-plane fields is spin and valley polarized [64, 65]. In fact, subsequent measurements of tBLG have revealed precise quantization of the Hall resistivity coincident with small longitudinal resistivity [175], conclusively demonstrating that the $3/4$ state is a Chern insulator with Chern number $C = 1$. The highly anisotropic response of the magnetic state to the direction of applied field demonstrated by the rotator measurements shown in Ch. 5 suggests that because spin-orbit coupling in graphene is weak [5], the ferromagnetic state is dominated by a orbital magnetic moment. These measurements are consistent with recent measurements using a superconducting quantum interference device that found the magnetization to be approximately 2-4 Bohr magneton per moiré unit cell [194]. The measurements were performed near the $3/4$-filling state, which corresponds to a single hole per moiré unit cell. As the measured magnetization significantly exceeds the expected 1 Bohr magneton per moiré unit cell for a single spin, these measurements also suggest that the magnetism is dominated by the orbital component. Though the motion of electrons can generate an orbital magnetic dipole moment, we are unaware of any magnetic material where the magnetism is dominated by the orbital magnetic moment independent of spin. However for tBLG, this is precisely the prediction of Refs. 64, 65, 148, 169–172. Despite these predictions, there are competing theories in which spin plays a role in the magnetism [66, 120, 121, 126, 162, 172].

In such an orbital magnetic state, the role of electron spin is an open question. Given that spin-orbit coupling is extremely weak in graphene, there should not be significant anisotropy in the direction spins prefer unless higher order bands are mixed in. Alternatively, if the low-field QAH state results from a state that is valley-polarized and spin-unpolarized, then polarizing spin could destroy any QAH through the removal of valley-polarization or mixing with higher-order bands [64, 120]; the lack of quantization in our measurements does open the door for the low-field ground state being metallic with strong anomalous Hall rather than a Chern insulator. On the other hand, because of the finite thickness of tBLG, it is also possible that an in-plane field directly couples to the orbital moments [173]. A sufficiently large in-plane field could then drive the sample into a valley unpolarized state.

We have observed a phase transition into a different state when the in-plane field exceeds 5 T. Regardless of the dominant mechanism of how in-plane field couples to the device, it seems that either the bands are losing their topological character by higher order bands mixing in [174], or the in-plane field is driving a repopulation of the bands. Thus far, no evidence of magnetism has been observed at $n/n_s = 1$ [18, 175], that should nominally be similar to $n/n_s = 3$. Therefore, there may be a competing ground state that does not have a net Chern number and would not exhibit a QAHE.

The lack of magnetic tBLG samples is of particular note. A Chern insulator requires nontrivial band topology and a gap between bands of different Chern numbers. The Dirac-like band touchings of the flat bands may [63, 195] or may not [67, 68] be symmetry protected. The tBLG samples are encapsulated in hexagonal boron nitride (hBN) flakes to protect the device from disorder and serve as a dielectric for electrostatic gating.

Such a gap could be opened by the apparent alignment of the tBLG crystal axis to that of one of the cladding hBN layers, which breaks the in-plane two-fold rotation symmetry [64, 65, 148, 196], thus gapping the bands. Both tBLG samples that exhibit ferromagnetism appear to have this alignment [18, 175], while this alignment has been typically intentionally avoided when fabricating other samples. Alternatively, self-consistent Hartree-Fock calculations show that in-plane two-fold rotation symmetry may be broken spontaneously [66]. More devices are required to determine if alignment with hBN is required for tBLG to become magnetic.

Finally, we have reported in Ch. 5 that the magnetization of the sample can be manipulated by applying an extremely small DC current of order $10\ \mathrm{nA}$, demonstrating that this magnetic state may be potentially useful for extremely low-power magnetic memory. This sensitivity to DC current is also reported in Ref. 175. The current required is, to our knowledge, the lowest of any memory system capable of in-situ readout and manipulation [144, 197, 198]. However, the precise mechanism behind this sensitivity in tBLG is not known. It may be possible that current in the bulk, while not present in the QAHE limit, may either redistribute electrons [145] or directly generate a net orbital magnetization due to the reduced lattice symmetry of tBLG aligned to hBN [146] allowing for switching of the valley polarization. While finite longitudinal resistance indicates the existence of dissipitive transport, in the QAHE limit, current flows only along the edge of the device. It has been proposed that charge current could efficiently drive reciprocal domain wall motion in a QAH system owing to quantum interference effects from the chiral edge states [147]. An interplay of edge-state physics and antisymmetric between the edges of the device may lead to a given current direction favoring a specific sign of the magnetization [175]. The orbital nature of the magnetism may prove to be key in understanding the sensitivity to an applied current.

7.3 Ferromagnetism at non-integer filling

The observed evidence of potential fractional quantum anomalous Hall (FQAH) is quite exciting. Previously, FQAH states at zero magnetic field have not been clearly observed in experiment. In Ch. 6, we discussed evidence of such a FQAH state in two ABC-TLG/hBN devices. While the state seems to arise from a combination of band topology and electron-electron interactions, we cannot conclusively say the state is a FQAH insulator without quantized Hall resistance and zero longitudinal resistance. This may be a matter of increasing the strength of electron-electron interactions. The simplest approach that might yield a modest improvement would be to use graphite gates at a larger distance away from the ABC-TLG. The use of graphite would hopefully yield improved device quality. Using a thicker dielectric would hopefully reduce any residual screening effects of the gates that were previously making the state weaker [75]. Another route would be to increase interlayer coupling by applying hydrostatic pressure [14, 199].

The path forward is less clear for the search of FQAH in tBLG. Both of the tBLG devices that have exhibited ferromagnetism at $3/4$ filling exhibit non-zero anomalous Hall in the approximate density range $3n_s < n < 3.7n_s$ (Ch. 5 and Ref. 175). However, a secondary peak in the AH was only observed in a single cooldown near $n = 3.5n_s$ (Ch. 6). This inconsistency may be due to the sensitivity of the state to charge disorder or displacement field. Unfortunately the only magnetic tBLG device clean enough to display quantization [175] is singly-gated. While the role of displacement field is less clear in tBLG than in ABC-TLG/hBN, it does appear important in magnetic tBLG: while non-zero hysteresis does exist in a large range of displacement fields, displacement field does tune the anomalous Hall in a non-trivial way. It may be the case that the state at $3.5n_s$ only exists in a narrow range of displacement field which we were able to achieve on one particular cooldown (there is significant evidence that the displacement field in the device changed significantly between cooldowns, see Ch. 5). Hopefully a dual-gated heterostructure which is clean enough to display quantization will elucidate what may be happening at $3.5n_s$.

Appendix A

Designing a vdWs transfer station

In this appendix, we will discuss a transfer station I designed with fabricating twisted vdWs heterostructures in mind. Thanks to Yuan Cao and Pablo Jarillo-Herrero for showing me their setup and teaching me their procedure for fabricating tBLG heterostructures. From their advice, I was able to build a transfer setup that has worked very well for fabricating twisted vdWs heterostructures.

The transfer station consists of two micromanipulator assembly: a sample assembly and a stamp assemblies. The sample assembly is based on an XY-translation stage (Newport 462-XY-M) with manual actuators (DM-25L). These actuators provide $25\ \mathrm{mm}$ of travel with an additional ultra-fine positioner that allows $0.2\ \mathrm{mm}$ of travel with $0.1\ \mu\mathrm{m}$ of sensitivity. This level of sensitivity is nice to have in one pair of the two XY-translation stages in the system, but one could get away with slightly less sensitivity. On top of this stage is a very precise rotation stage (Newport CONEX-URS50BCC) which has an absolute guaranteed accuracy of $\pm 20\ \mathrm{mdeg}$ but can do much better if one accounts for backlash. Finally, we mount the sample stage on top of the rotation stage. The sample stage comes with a vacuum feed-through for holding down samples, a slot for a heater cartridge (Omega HDC00001), and a mount for a thermocouple (Omega WTK-8-60). The thermoetry is controlled using a PID controller (Omega 16DPT-225-C24). The sample stage is separated from the rotation stage by glass to hopefully help prevent excessive heating of the rotation stage. The screws holding down the sample stage are stainless steel, but could be replaced with a less thermally conductive material.

The stamp assembly is based on an XYZ-translation stage (Newport 562-XYZ-LH). The X and Y axes are equipped with manual actuators (Newport HR-13) that have $0.5\ \mu\mathrm{m}$ sensitivity. The Z axis is equipped with a motorized actuator (Newport CONEX-TRB12CC). Newport offers motorized actuators based on both servo motors and piezoelectric steppers. I opted to use the servo motor option. The servo motors do not seem to have any issues with overshooting that impact transfers. The piezoelectric steppers are based on using microsteps which may cause a small amount of jitter. This motorized actuator has a minimum incremental step size of $100\ \mathrm{nm}$ which is small enough for successful transfers. A dual-axis goniometer (Thorlabs GNL20) is mounted on the XYZ-translation stage, allowing to control the tilt of the stamp relative to the sample stage.

Finally, the stamp stage is mounted on the goniometer. The stamp stage has a vacuum feed-through for holding the stamp.

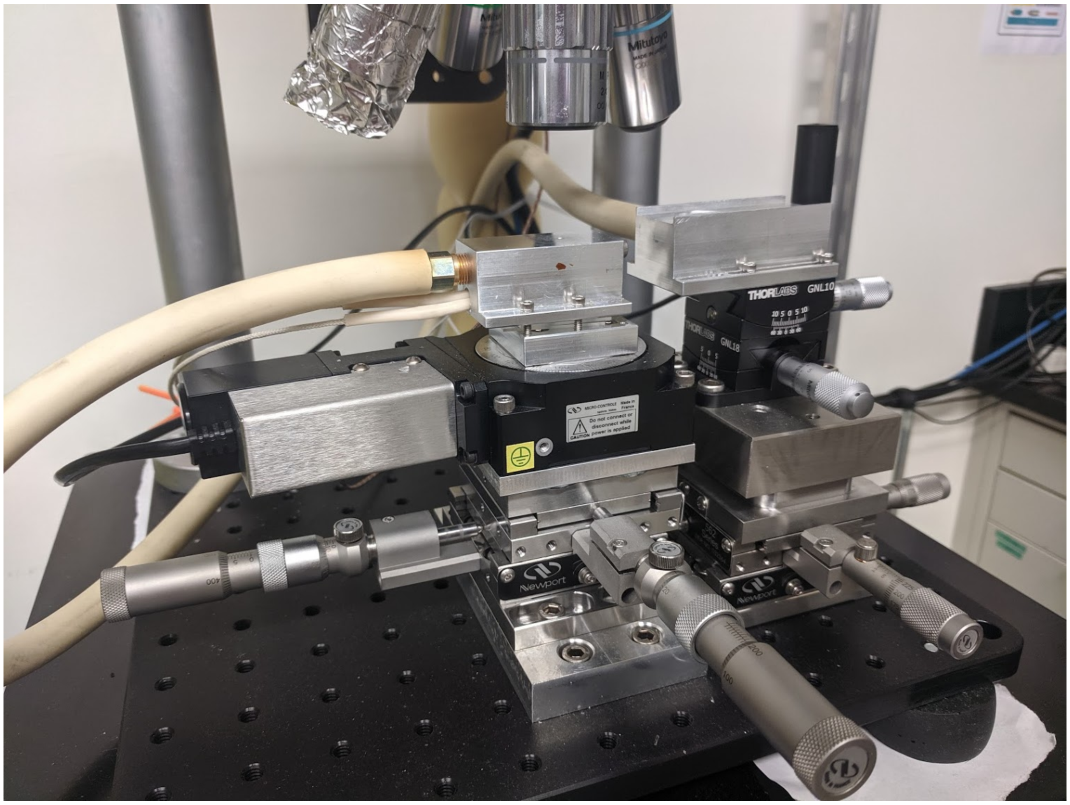

Figure A.1: **vdWs transfer station.** Sample side (left) and stamp side (right) micromanipulator assembly that comprise the vdWs transfer station. The base is a 1 in optical breadboard.

The vacuum system is built with a small diaphragm pump (Gast DOA-P701-AA). Vibrations from the pump can couple to the transfer stage via the vacuum lines. This can be alleviated by running the vacuum line through some sort of vibration reduction system. For the current setup, I run the line through a 5 gallon bucket filled with sand (Fig. A.2). For additional isolation, the transfer station is placed on a bench top vibration isolation platform (Minus K 50BM-4).

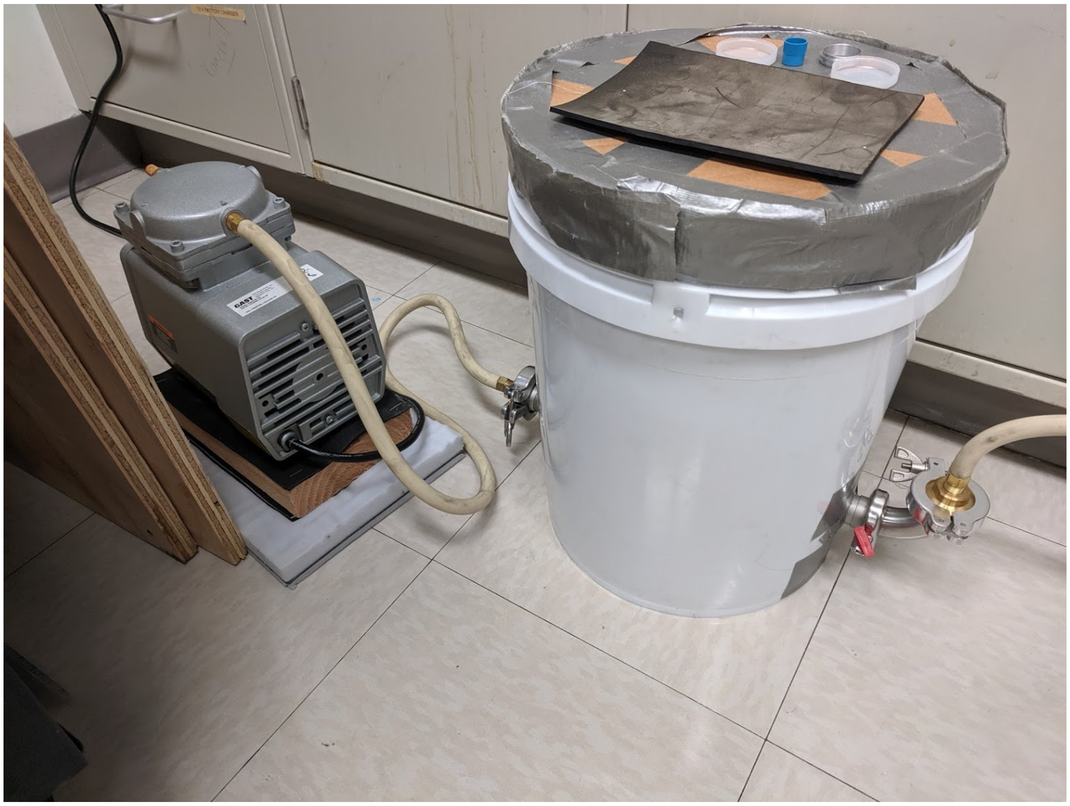

Figure A.2: **Isolating transfer station from pump vibrations.** Without any isolation, the vibrations of the diaphragm pump (shown on the left) would couple through the vacuum line to the transfer station, negatively impacting transfer quality. To mitigate this, the vacuum line is run through a 5 gallon bucket filled with sand (shown on the right).

Finally, the optics are built around a Mitutoyo FS70 turret with Periplan eye pieces (GW 10x/26). In such a setup, it is crucial to have long working distance objectives. The transfer station is equiped with three Mitutoyo M Plan Apo objectives (2X/0.055, 10X/0.28, 50X/0.55). The 10X is the workhorse objective most often used during transfers. Finally, the turret is equipped with a Flea3 color camera (FL3-U3-20E4C-C) for computer monitoring of the transfer.

Appendix B

Gate voltages to charge density and displacement field

In a dual gated heterostructure with a back and top gate, the gates control both the charge density n in and apply a displacement field D to the gated heterostructure. We will model both gates are parallel plate capacitors with capacitance per unit area $c_i = C_i/A_i = \epsilon_i/d_i$, where ϵ_i and d_i are the dielectric constant and thickness of the dielectric layer separating the gate from the semiconducting layer. Then the carrier density in the gated layer is simply the sum of the two carrier densities accrued by both gates

$$n = \frac{c_{bg}}{e}\left(V_{bg} - V_{bg}^0\right) + \frac{c_{tg}}{e}\left(V_{tg} - V_{tg}^0\right), \tag{B.1}$$

where $V_{bt(tg)}$ is the voltage applied to the back (top) gate, (V_{bg}^0, V_{tg}^0) is the charge neutrality point, and e is the charge of an electron. The displacement field D is related to the net electric field crossing the semiconducting layer. This is somewhat complicated as there should be screening effects at play but it is standard practice in the field to take the following definition:

$$D = \frac{1}{2}(\epsilon_{bg}E_{bg} + \epsilon_{tg}E_{tg}) = \frac{1}{2}\left(\frac{\epsilon_{bg}(V_{bg} - V_{bg}^0)}{d_{bg}} - \frac{\epsilon_{tg}(V_{tg} - V_{tg}^0)}{d_{tg}}\right) = \frac{1}{2}(c_{bg}(V_{bg} - V_{bg}^0) - c_{tg}(V_{tg} - V_{tg}^0)). \tag{B.2}$$

We will typically consider the quantity D/ϵ_0, such that we are working in units of V/nm. Given that the gates are working in tandem, we can fit a line to particular features. We will do so for the charge neutrality point. We then get

$$V_{tg} = -mV_{bg} + b, \tag{B.3}$$

where $m = c_{bg}/c_{tg}$ is the ratio of the gate capacitances. We will assume that $D = 0$ when $(V_{bg}, V_{tg}) = (0, 0)$. In the case of a Si back gate and a metallic top gate, one can check that the expected displacement field due to the work function difference between the gates is small (~ -0.01 V/nm). Any non-zero displacement field at zero gate voltages due to other effects will then yield a constant offset in the calculated displacement field. Under this assumption, we obtain the relation that

$$0 = -c_{bg}V_{bg}^0 + c_{tg}V_{tg}^0. \tag{B.4}$$

Plugging this into the linear relation, we obtain

$$V_{tg}^0 = mV_{bg}^0. \tag{B.5}$$

We now want to find the point on our line fit to the charge neutrality point where $D = 0$. We can substitute this relation into equation B.1:

$$\begin{aligned} 0 &= c_{bg}(V_{bg} - V_{bg}^0) + c_{tg}(V_{tg} - V_{tg}^0) && \text{(B.6)} \\ &= m(V_{bg} - V_{bg}^0) - mV_{bg} + b - mV_{bg}^0 && \text{(B.7)} \\ &= b - 2mV_{bg}^0. && \text{(B.8)} \end{aligned}$$

Solving for the offsets:

$$V_{bg}^0 = \frac{b}{2m}, \quad V_{tg}^0 = \frac{b}{2}. \tag{B.9}$$

We can now transform to this new coordinate space based on our fit to the charge neutrality point following the prescription that

$$\begin{aligned} n &= \frac{c_{tg}}{e}\left(mV_{bg} + V_{tg} - b\right), && \text{(B.10)} \\ \frac{D}{\epsilon_0} &= \frac{c_{tg}}{2\epsilon_0}\left(mV_{bg} - V_{tg}\right). && \text{(B.11)} \end{aligned}$$

We can also invert this transformation:

$$\begin{aligned} V_{bg} &= \frac{1}{2}\left(b + \frac{en}{c_{tg}} - \frac{2\epsilon_0 D}{c_{tg}}\right), && \text{(B.12)} \\ V_{tg} &= \frac{1}{2m}\left(b + \frac{en}{c_{tg}} + \frac{2\epsilon_0 D}{c_{tg}}\right). && \text{(B.13)} \end{aligned}$$

Appendix C

Simulating ballistic electrons

This section is adapted from Ref. 200. A maintained repository of the code used to perform simulations like those of Ref. 200 and Ch. 2 can be found at Ref. 201

As we have previously discussed in Ch. 2, in ultra-clean 2D materials, transport is ballistic over large length scales at sufficiently low temperatures. We aim to semi-classically model ballistic transport for a generic Fermi surface in a given 2D geometry. By modeling the ballistic trajectories in a magnetic field, on can gain an effective map of the current density within the device. Additionally, by monitoring the interactions of the charge carriers with the edges of the device, one can gain qualitative predictions for the field-dependence of the voltage at a given ohmic contact. We model the electrons trajectories according to their semiclassical equations of motion for an out-of-plane magnetic field $\boldsymbol{B} = B\hat{\boldsymbol{z}}$:

$$\hbar v_F = \frac{\partial \varepsilon}{\partial k}, \quad \hbar \dot{\boldsymbol{k}} = -e\boldsymbol{E} + eB\hat{\boldsymbol{z}} \times \boldsymbol{v} \tag{C.1}$$

where $\hbar$ is the reduced Planck's constant, e is the charge of an electron, v_F is the Fermi velocity, and $\boldsymbol{E}$ is the electric field experienced by the electron. In the ballistic regime, there is negligible electric field in the bulk, therefore we assume that $\boldsymbol{E} = 0$. Because we are not concerned with transit times of the electrons, we can ignore the Fermi velocity v_F.

We need either a numerical or analytical model for the Fermi surface (FS) we want to simulate that we will discretize into a series of state labeled by an index n. For an electron propagating in a magnetic field, the equations of motion yield that the real space trajectory is a 90° rotation of the FS scaled by a factor of $\hbar/eB$ [6]. By following their calculated real space trajectory, we can model the electron transport in the bulk of the device.

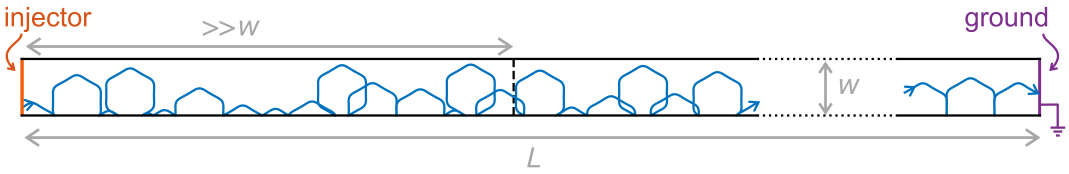

Figure C.1: **Simulating a two-terminal bar.** Electrons propagate along a bar of length L and width w. The injector (left) and ground (right) are assumed to be perfect ohmic contacts. A virtual line placed a distance several times thew width of the bar away from the injection point is used to calculate backward scattered electrons.

One of the simplest devices we can simulate is a two terminal bar, where carriers are injected into a two-dimensional bar of width w and length L. Ohmic contacts are created at two ends of the bar which will serve as an injector and a ground. When injecting an electron into the system or scattering from an edge of the device, the probability of injecting into a state n of the discretized Fermi surface is

$$p\left(n\right) = cos\left(\theta\left(n\right) - \phi\right), \tag{C.2}$$

where $\theta\left(n\right) = tan(v_y/v_x)$ is the direction of propagation of the state n and ϕ is the angle of the normal to the edge. The Fermi surface is numerically discretized into states separated by constant arc length to remove the probability distribution's dependence on Fermi velocity [8]. Carriers follow their semi-classical path, ignoring bulk scattering, until interacting with either an edge or ohmic contact of the device. In the case of a non-ohmic edge, a carrier is either specularly reflected into the appropriate momentum conserving state or scattered into a new randomly state chosen according to the probability distribution for that edge. For ohmic contacts, one has the additional parameter of the probability a carrier is absorbed by the contact. To ensure detailed-balance, if a floating contact or the injecting contact absorbs an incident carrier, the carrier is reemitted at a random position along the lead in a randomly chosen allowed state for that edge.

The magnetic field is not modeled in the injecting ohmic contact; electrons are injected uniformly across the edge of the contact into states chosen according to the probability distribution for the contact. At high magnetic fields (cyclotron diameter smaller than the width of the bar), there is a significant chance than an injected carrier will not interact with the side walls of the device before returning to the injector. We can estimate the two-terminal resistance of the bar in this regime by calculating the number of backward-propagating carriers through a line perpendicular to the channel several times the bars width from the injecting contact. By measuring the transport properties far from the injector, we are not susceptible to the issue of carriers that do not interact with the side walls of the device.

Appendix D

Additional tBLG data

D.1 Quantum oscillations

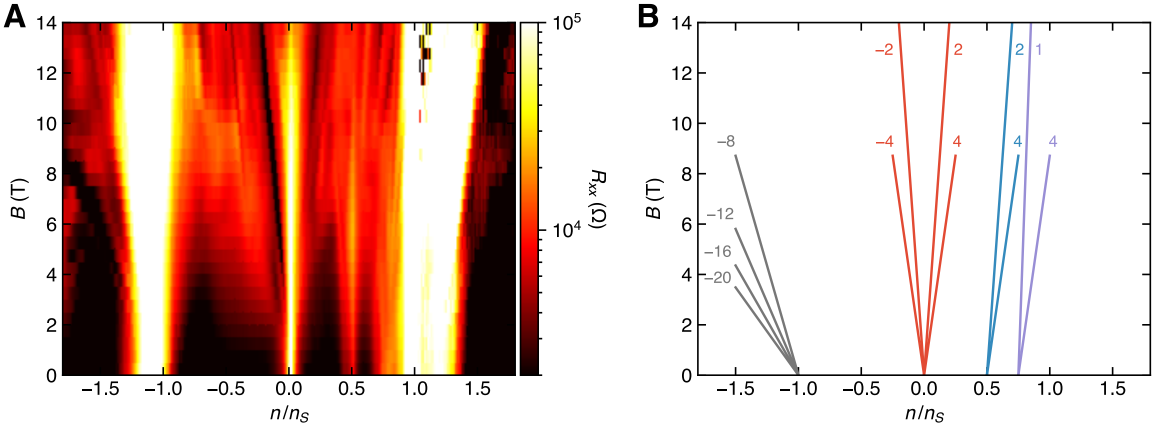

Figure D.1: **Quantum oscillations of tBLG at fixed displacement field.** (**A**) Landau fan diagram of the longitudinal resistance R_{xx} taken at 2.1 K for a fixed displacement field $D/\epsilon_0 = 0$ V/nm. Emerging from the CNP, we observe the Landau levels $\nu = \pm 2, \pm 4$. We further observe Landau levels from $n/n_s = 1/2$ of $\nu = 2, 4$, from $n/n_s = 3/4$ of $\nu = 1, 4$, and the sequence from $n/n_s = -1$ of $\nu = -8, -12, -16, -20$. (**B**) Schematic of the Landau levels observed in (A).

We observe several sets of Landau fans emerging from the high resistance states of the tBLG (Fig. D.1A). The discernible quantum oscillations are represented schematically in Fig. D.1B. The degeneracy of Landau levels is representative of the symmetries of the electronic band structure and may yield information about where spin, valley, or layer symmetry may be broken.

Emerging from the CNP, the $\nu = \pm 2$ and ± 4 Landau levels are clearly visible. This is slightly surprising as one might expect the level sequence to reflect spin and valley degeneracies, and hence four-fold degenerate Landau levels, as has been seen previously in magic angle tBLG samples [3, 14]. In the fan emerging from $n/n_s = 2$, we see similar periodicity with signs of $\nu = 2$ and 4. Additionally, there is a strong enhancement of the resistance at $n/n_s = 2$ with the applied out-of-plane magnetic field, peaking at roughly 6 T, in contrast to the behavior of the apparent correlated insulating state observed by Cao *et al.* [1]. The $n/n_s = 3$ fan exhibits a further reduction of the periodicity such that we only observe clear signatures of $\nu = 4$ and 4. This reduction in symmetry at $n/n_s = 3$ could reflect interaction-driven lifting of the degeneracies: if the conduction bands for three spin-valley flavors are fully filled, we may be observing the quantum oscillations of a single flavor. No clear quantum oscillations emerge from $n/n_s = 4$, but the presence of $\nu = -8, -12, -16$, and -20 levels originating from $n/n_s = -4$ is consistent with what has been seen in other tBLG samples [3, 14].

D.2 Longitudinal resistance data

In this section, we provide the corresponding longitudinal resistance data for the figures of Sec. 5.2. Fig. D.2 shows the longitudinal resistance R_{xx} corresponding to the Hall resistance data of Fig. 5.16. As was seen previously with this device [18], R_{xx} displays visible hysteresis, presumably due to mixing in of the Hall signal from inhomogeneity in the device. When plotted as a function of the perpendicular field component (Fig. D.2B), we see that the longitudinal resistance depends mostly on the perpendicular field component with some small variations from angle to angle, perhaps due to an effect of the in-plane magnetic field.

Fig. D.3 shows the longitudinal resistance R_{xx} corresponding to the Hall resistance data of Fig. 5.17. As the angle of the sample is tuned closer and closer to a purely in-plane magnetic field, the variations in the longitudinal resistance become smaller. As the field becomes perfectly in-plane, the hysteresis loop seen at larger tile angles is diminished. We see jumps in the longitudinal resistance that likely correspond to the flipping of magnetic domains.

Finally, Fig. D.4 shows the (A) longitudinal and (B) Hall response of a state magnetized out-of-plane to a purely in-plane field. Panel B is reproduced from Fig. 5.18. As was previously discussed, applying an in-plane magnetic field erases the initial magnetic state and goes through a phase transition to a different state above 5 T in-plane field. Below this critical field, the magnetic state is recovered but the full polarization of the system is not. This leads to a reduction in the longitudinal and magnitude of the Hall resistance.

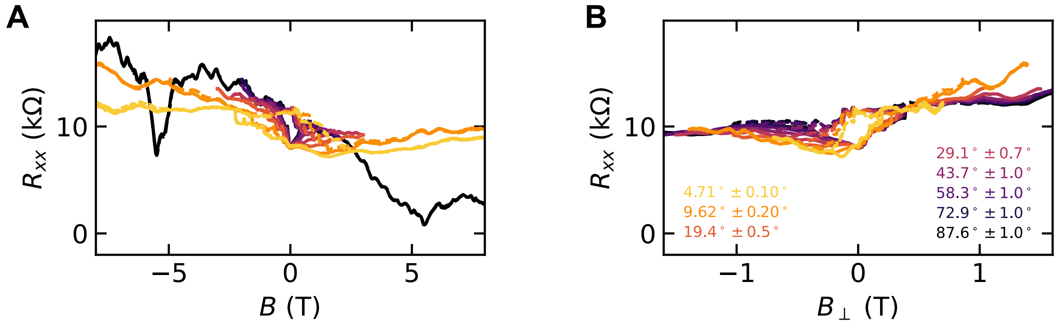

Figure D.2: **Angular dependence of longitudinal Resistance in magnetic hysteresis loops.** Magnetic field dependence of the longitudinal resistance R_{xx} corresponding to the data shown in Fig. 5.16, with $n/n_s = 2.984$ and $D/\epsilon_0 = -0.30$ V/nm at 29 mK as a function of the angle of the device relative to the field direction; 0° corresponds to field in the plane of the sample. The hysteresis loops are plotted as a function of (a) the applied field and (b) the component of the field perpendicular to the plane of the sample. The solid and dashed lines correspond to sweeping the magnetic field B up and down, respectively.

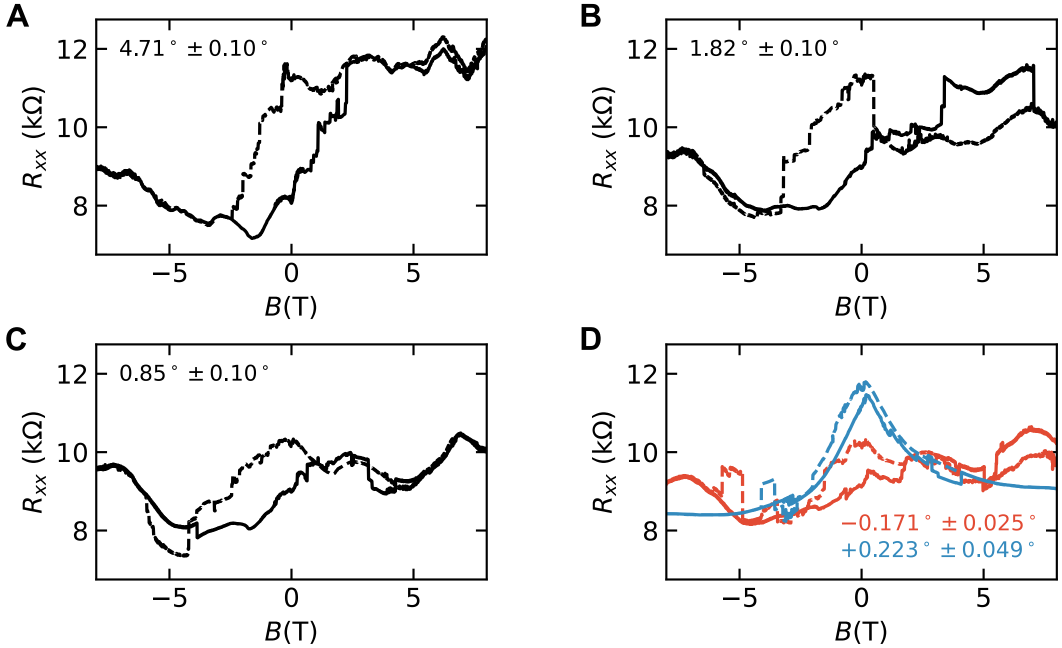

Figure D.3: **Hysteresis loops for nearly in-plane fields.** Angular dependence of the longitudinal resistance R_{xx} vs B corresponding to the data shown in Fig. 5.17 with $n/n_s = 2.984$ and $D/\epsilon_0 = -30$ V/nm for angles of the field relative to the plane of the sample: (a) $4.71° \pm 0.10°$, (b) $1.82° \pm 0.10°$, (c) $0.85° \pm 0.10°$, (d) $+0.223° \pm 0.049°$, and $-0.171° \pm 0.025°$. All traces were taken at 27 mK except for the trace with tilt angle $+0.223° \pm 0.049°$, which was taken at 1.35 K.

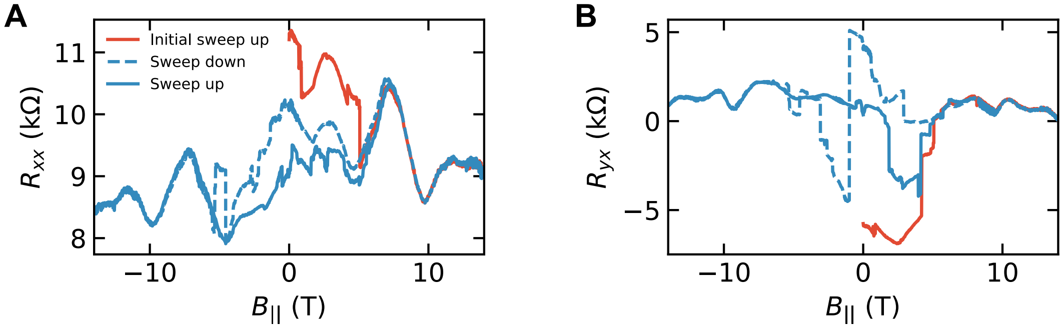

Figure D.4: **Erasing the initial magnetic state.** In-plane hysteresis loops of the longitudinal resistance R_{xx} corresponding to the data shown in Fig. 5.18 with $n/n_s = 2.984$ and $D/\epsilon_0 = -30\ \mathrm{V/nm}$ at $26\ \mathrm{mK}$. The sample is initially polarized with an out-of-plane field. The sample is then rotated to $-57 \pm 21\mathrm{mdeg}$ in zero magnetic field. The field $B_{||}$ is then increased from zero (red trace) before completing a hysteresis loop (blue traces).

D.3 Antisymmetric components and dependence on magnitude of in-plane field

When the antisymmetric component of the data presented in Fig. 5.18 is extracted (shown in Fig. D.5), we see that for small in-plane fields, the system is strongly hysteretic. Although a typical ferromagnetic hysteretic loop is not observed as a function of in-plane field, we do see that there is a large discrepancy between the up and down sweeps. Above an in-plane field of $5\ \mathrm{T}$, the two traces are largely similar, with much smaller deviations between the two. Additionally, the antisymmetric component of the Hall remains quite small, staying below $\sim 0.5\ \mathrm{k\Omega}$.

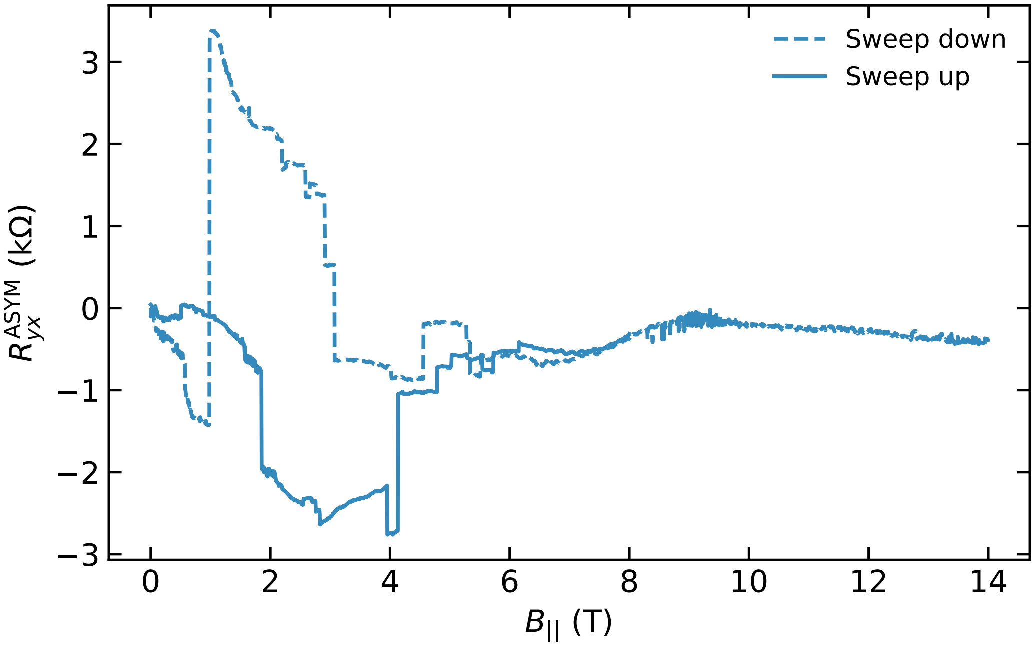

Figure D.5: **Antisymmetric component of in-plane hysteresis loop.** Antisymmetric component of the Hall resistance R_{yx}^{ASYM} corresponding to the Hall data shown in Fig. 5.18 with $n/n_s = 2.984$ and $D/\epsilon_0 = -30\ \mathrm{V/nm}$ at $26\ \mathrm{mK}$. The initial up sweep has been omitted in this figure.

When the data from Fig. D.4 is plotted against the magnitude of the field (shown in Fig. D.6 for fields above 6 T), we again see that those parts of the data outside of $\pm 6\ \mathrm{T}$ are remarkably similar. For large in-plane fields, the longitudinal and Hall resistances are qualitatively similar with an offset of $0.5\ \mathrm{k\Omega}$ between the respective signs of field. This likely indicates that the sample is no longer orbitally polarized. The similarity of the longitudinal and Hall resistance suggests that the Hall signal results from mixing in of the longitudinal signal.

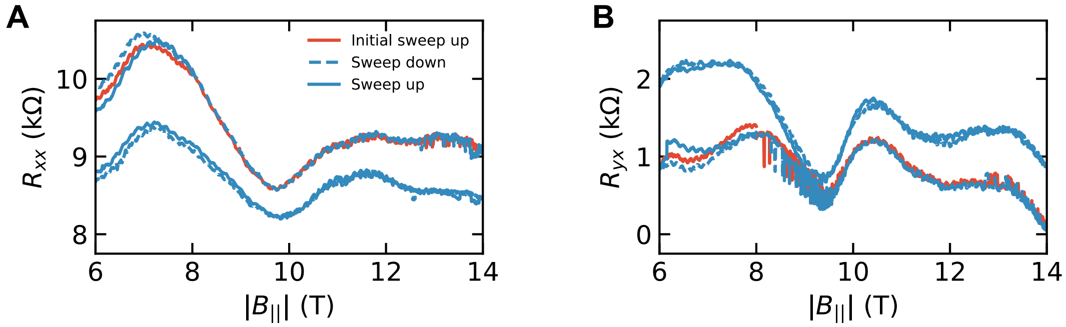

Figure D.6: **Dependence on the magnitude of the in-plane field.** In-plane hysteresis loops of corresponding longitudinal resistance R_{xx} to the data shown in Fig. 5.18 with $n/n_s = 2.984$ and $D/\epsilon_0 = -30$ V/nm at 26 mK. The sample is initially polarized with an out-of-plane field. The sample is then rotated to -57 ± 21mdeg in zero magnetic field. The field $B_{||}$ is then increased from zero (red trace) before completing a hysteresis loop (blue traces). The range of resistance shown in both panels is the same.

D.4 Effect of out-of-plane at small tilt angles

In this section we present additional data similar to those in Fig. 5.17D where we investigate the effect of the sign of a small out-of-plane field in the background of a large in-plane field at small tilt angles (Fig. D.7). Note that for the presented data, the sample has been rotated in the plane by 20° relative to the traces performed in Fig. 5.17D so that the sample is oriented in a different direction relative to the in-plane component of the field. Between the two traces, there are numerous jumps in R_{yx}, some which occur at similar values of B and some which are slightly shifted between the two traces. However, these shifts are not consistent with the change in out of plane field component, as there is an order of magnitude difference in the magnitude of the out-of-plane field between the two traces. This suggests that the features in Fig. 5.17D and Fig. D.7 are primarily a response to the in-plane field.

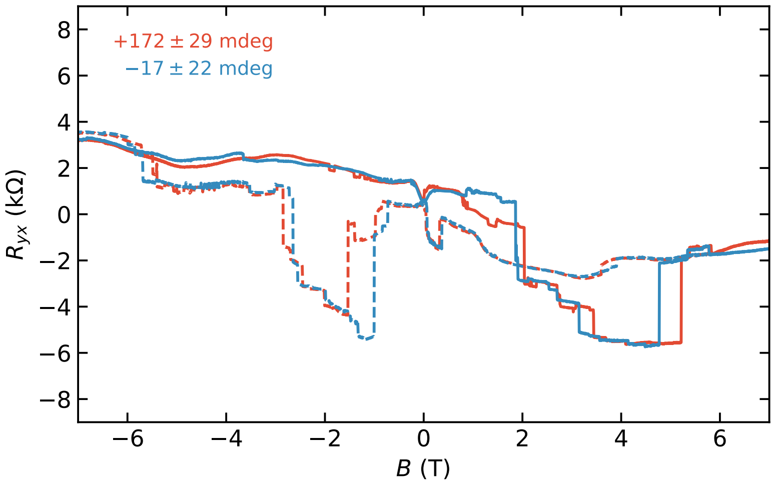

Figure D.7: **Flipping a small out-of-plane field at small angles.** Magnetic field hysteresis loops where R_{yx} is measured at two small angles of opposite sign: $+172 \pm 29$ mdeg in red and -17 ± 22 mdeg in blue. Both traces were taken at 28 mK with $n/n_s = 2.984$ and $D/\epsilon_0 = -30$ V/nm. The sample has been rotated in the plane by an angle of 20° relative the measurements performed in Fig. 5.17.

D.5 Effect of in-plane field on longitudinal resistivity

For completeness, we have examined the effect of an in-plane field at other carrier densities. The longitudinal resistivity ρ_{xx} does not depended significantly on $B_{\parallel}$ except in the range of densities $n/n_s = 0.1$ to 0.65, where ρ_{xx} increases with increasing $B_{\parallel}$ (Fig. D.8). This behavior is counter to the superconducting device presented in Ref. 14.

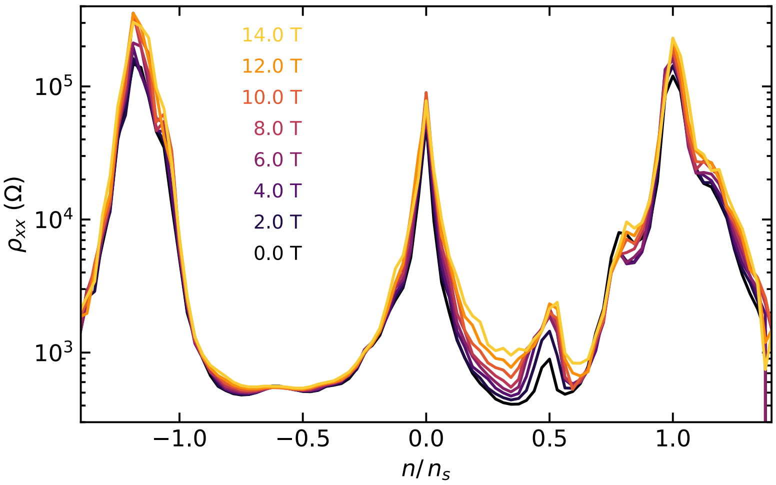

Figure D.8: **In-plane field dependence of longitudinal resistivity.** Longitudinal resistivity ρ_{xx} as a function of carrier density n for several different in-plane magnetic fields at a fixed displacement field of $D/\epsilon_0 = -0.30\ \mathrm{V/nm}$ and 1.2 K for a tilt angle of $-62 \pm 23\mathrm{mdeg}$.

Bibliography

[1] Cao, Y. *et al.* Correlated insulator behaviour at half-filling in magic-angle graphene superlattices. *Nature* **556**, 80–84 (2018).

[2] Chen, G. *et al.* Evidence of a gate-tunable Mott insulator in a trilayer graphene moiré superlattice. *Nature Physics* **15**, 237–241 (2019).

[3] Cao, Y. *et al.* Unconventional superconductivity in magic-angle graphene superlattices. *Nature* **556**, 43–50 (2018).

[4] Chittari, B. L., Chen, G., Zhang, Y., Wang, F. & Jung, J. Gate-Tunable Topological Flat Bands in Trilayer Graphene Boron-Nitride Moiré Superlattices. *Physical Review Letters* **122**, 16401 (2019).

[5] Sichau, J. *et al.* Resonance Microwave Measurements of an Intrinsic Spin-Orbit Coupling Gap in Graphene: A Possible Indication of a Topological State. *Physical Review Letters* **122**, 46403 (2019).

[6] Lee, M. *et al.* Ballistic miniband conduction in a graphene superlattice. *Science* **353**, 1526–1529 (2016).

[7] Wallbank, J. R., Patel, A. A., Mucha-Kruczyński, M., Geim, A. K. & Fal'ko, V. I. Generic miniband structure of graphene on a hexagonal substrate. *Physical Review B* **87**, 245408 (2013).

[8] Barnard, A. W. *et al.* Absorptive pinhole collimators for ballistic Dirac fermions in graphene. *Nature Communications* **8**, 15418 (2017).

[9] Wang, J., Lian, B., Zhang, H. & Zhang, S.-C. Anomalous Edge Transport in the Quantum Anomalous Hall State. *Physical Review Letters* **111**, 086803 (2013).

[10] Bandurin, D. A. *et al.* Negative local resistance caused by viscous electron backflow in graphene. *Science* **351**, 1055–1058 (2016).

[11] Bistritzer, R. & MacDonald, A. H. Moiré bands in twisted double-layer graphene. *Proceedings of the National Academy of Sciences* **108**, 12233–12237 (2011).

[12] Filipe, G. & Catarina, S. Twisted bilayer graphene — electronic and optical properties (Doctoral dissertation). *Técnico Lisboa* (2017).

[13] Yoo, H. *et al.* Atomic and electronic reconstruction at the van der Waals interface in twisted bilayer graphene. *Nature Materials* **18**, 448–453 (2019).

[14] Yankowitz, M. *et al.* Tuning superconductivity in twisted bilayer graphene. *Science* **363**, 1059–1064 (2019).

[15] Dresselhaus, M. S. & Dresselhaus, G. Intercalation compounds of graphite. *Advances in Physics* **51**, 1–186 (2002).

[16] Koshino, M. & McCann, E. Trigonal warping and Berry's phase $N\pi$ in ABC-stacked multilayer graphene. *Physical Review B* **80**, 165409 (2009).

[17] Lui, C. H., Li, Z., Mak, K. F., Cappelluti, E. & Heinz, T. F. Observation of an electrically tunable band gap in trilayer graphene. *Nature Physics* **7**, 944–947 (2011).

[18] Sharpe, A. L. *et al.* Emergent ferromagnetism near three-quarters filling in twisted bilayer graphene. *Science* **365**, 605–608 (2019).

[19] Checkelsky, J. G. *et al.* Trajectory of the anomalous Hall effect towards the quantized state in a ferromagnetic topological insulator. *Nature Physics* **10**, 731–736 (2014).

[20] Zhang, Y.-H. H., Mao, D., Cao, Y., Jarillo-Herrero, P. & Senthil, T. Nearly flat Chern bands in moiré superlattices. *Physical Review B* **99**, 075127 (2019).

[21] Chen, G. *et al.* Tunable correlated Chern insulator and ferromagnetism in a moiré superlattice. *Nature* **579**, 56–61 (2020).

[22] Si, Q. & Steglich, F. Heavy Fermions and Quantum Phase Transitions. *Science* **329**, 1161–1166 (2010).

[23] Wu, C., Bergman, D., Balents, L. & Das Sarma, S. Flat Bands and Wigner Crystallization in the Honeycomb Optical Lattice. *Physical Review Letters* **99**, 70401 (2007).

[24] Mielke, A. Exact ground states for the Hubbard model on the Kagome lattice. *Journal of Physics A: Mathematical and General* **25**, 4335–4345 (1992).

[25] Lieb, E. H. Two theorems on the Hubbard model. *Physical Review Letters* **62**, 1201–1204 (1989).

[26] Iglovikov, V. I., Hébert, F., Grémaud, B., Batrouni, G. G. & Scalettar, R. T. Superconducting transitions in flat-band systems. *Physical Review B* **90**, 94506 (2014).

[27] Tsai, W.-F., Fang, C., Yao, H. & Hu, J. Interaction-driven topological and nematic phases on the Lieb lattice. *New Journal of Physics* **17**, 55016 (2015).

[28] Novoselov, K. S. *et al.* Two-dimensional gas of massless Dirac fermions in graphene. *Nature* **438**, 197–200 (2005).

[29] Burson, K. M. *et al.* Direct Imaging of Charged Impurity Density in Common Graphene Substrates. *Nano Letters* **13**, 3576–3580 (2013).

[30] Tan, Y.-W. *et al.* Measurement of Scattering Rate and Minimum Conductivity in Graphene. *Physical Review Letters* **99**, 246803 (2007).

[31] Cho, S. & Fuhrer, M. S. Charge transport and inhomogeneity near the minimum conductivity point in graphene. *Physical Review B* **77**, 81402 (2008).

[32] Yan, J. & Fuhrer, M. S. Correlated Charged Impurity Scattering in Graphene. *Physical Review Letters* **107**, 206601 (2011).

[33] Dean, C. R. *et al.* Boron nitride substrates for high-quality graphene electronics. *Nature Nanotechnology* **5**, 722–726 (2010).

[34] Wang, L. *et al.* One-Dimensional Electrical Contact to a Two-Dimensional Material. *Science* **342**, 614–617 (2013).

[35] Hunt, B. *et al.* Massive Dirac Fermions and Hofstadter Butterfly in a van der Waals Heterostructure. *Science* **340**, 1427–1430 (2013).

[36] Weiss, D., Klitzing, K. V., Ploog, K. & Weimann, G. Magnetoresistance Oscillations in a Two-Dimensional Electron Gas Induced by a Submicrometer Periodic Potential. *Europhysics Letters (EPL)* **8**, 179–184 (1989).

[37] Carmona, H. A. *et al.* Two Dimensional Electrons in a Lateral Magnetic Superlattice. *Physical Review Letters* **74**, 3009–3012 (1995).

[38] Albrecht, C. *et al.* Fermiology of Two-Dimensional Lateral Superlattices. *Physical Review Letters* **83**, 2234–2237 (1999).

[39] Sandner, A. *et al.* Ballistic Transport in Graphene Antidot Lattices. *Nano Letters* **15**, 8402–8406 (2015).

[40] Forsythe, C. *et al.* Band structure engineering of 2D materials using patterned dielectric superlattices. *Nature Nanotechnology* **13**, 566–571 (2018).

[41] Dean, C. R. *et al.* Hofstadter's butterfly and the fractal quantum Hall effect in moiré superlattices. *Nature* **497**, 598–602 (2013).

[42] Ponomarenko, L. A. *et al.* Cloning of Dirac fermions in graphene superlattices. *Nature* **497**, 594–597 (2013).

[43] Yang, W. *et al.* Epitaxial growth of single-domain graphene on hexagonal boron nitride. *Nature Materials* **12**, 792–797 (2013).

[44] Shi, Z. *et al.* Gate-dependent pseudospin mixing in graphene/boron nitride moiré superlattices. *Nature Physics* **10**, 743–747 (2014).

[45] Lee, Y. *et al.* Competition between spontaneous symmetry breaking and single-particle gaps in trilayer graphene. *Nature Communications* **5**, 5656 (2014).

[46] Cao, Y. *et al.* Superlattice-Induced Insulating States and Valley-Protected Orbits in Twisted Bilayer Graphene. *Physical Review Letters* **117**, 116804 (2016).

[47] Kim, K. *et al.* van der Waals Heterostructures with High Accuracy Rotational Alignment. *Nano Letters* **16**, 1989–1995 (2016).

[48] Balents, L., Dean, C. R., Efetov, D. K. & Young, A. F. Superconductivity and strong correlations in moiré flat bands. *Nature Physics* **16**, 725–733 (2020).

[49] Giovannetti, G., Khomyakov, P. A., Brocks, G., Kelly, P. J. & Van Den Brink, J. Substrate-induced band gap in graphene on hexagonal boron nitride: Ab initio density functional calculations. *Physical Review B - Condensed Matter and Materials Physics* **76** (2007).

[50] Castro Neto, A. H., Guinea, F., Peres, N. M. R., Novoselov, K. S. & Geim, A. K. The electronic properties of graphene. *Reviews of Modern Physics* **81**, 109–162 (2009).

[51] Moon, P. & Koshino, M. Electronic properties of graphene/hexagonal-boron-nitride moiré superlattice. *Physical Review B* **90**, 155406 (2014).

[52] Yankowitz, M. *et al.* Emergence of superlattice Dirac points in graphene on hexagonal boron nitride. *Nature Physics* **8**, 382–386 (2012).

[53] Tsoi, V. Focusing of electrons in a metal by a transverse magnetic field. *Soviet Journal of Experimental and Theoretical Physics Letters* **19**, 70 (1974).

[54] van Son, P. C., van Kempen, H. & Wyder, P. New method to study the electron-phonon interaction in metals. *Physical Review Letters* **58**, 1567–1570 (1987).

[55] Beenakker, C. W. J., van Houten, H. & van Wees, B. J. Mode Interference Effect in Coherent Electron Focusing. *Europhysics Letters (EPL)* **7**, 359–364 (1988).

[56] Taychatanapat, T., Watanabe, K., Taniguchi, T. & Jarillo-Herrero, P. Electrically tunable transverse magnetic focusing in graphene. *Nature Physics* **9**, 225–229 (2013).

[57] Markiewicz, R. S. The topological significance of saddle point van Hove singularities: a comparison of orbital switching and magnetic breakdown. *Journal of Physics: Condensed Matter* **6**, 3059–3072 (1994).

[58] Hodges, C., Smith, H. & Wilkins, J. W. Effect of fermi surface geometry on electron-electron scattering. *Physical Review B* **4**, 302–311 (1971).

[59] Kaveh, M. & Wiser, N. Electron-electron scattering in conducting materials. *Advances in Physics* **33**, 257–372 (1984).

[60] Zhang, Y., Tan, Y.-W., Stormer, H. L. & Kim, P. Experimental observation of the quantum Hall effect and Berry's phase in graphene. *Nature* **438**, 201–204 (2005).

[61] Koshino, M. & Nam, N. N. T. Effective continuum model for relaxed twisted bilayer graphene and moiré electron-phonon interaction. *Physical Review B* **101**, 195425 (2020).

[62] Po, H. C., Zou, L., Vishwanath, A. & Senthil, T. Origin of Mott Insulating Behavior and Superconductivity in Twisted Bilayer Graphene. *Physical Review X* **8**, 031089 (2018).

[63] Zou, L., Po, H. C., Vishwanath, A. & Senthil, T. Band structure of twisted bilayer graphene: Emergent symmetries, commensurate approximants, and Wannier obstructions. *Physical Review B* **98**, 085435 (2018).

[64] Zhang, Y.-H., Mao, D. & Senthil, T. Twisted bilayer graphene aligned with hexagonal boron nitride: Anomalous Hall effect and a lattice model. *Physical Review Research* **1**, 033126 (2019).

[65] Bultinck, N., Chatterjee, S. & Zaletel, M. P. Mechanism for Anomalous Hall Ferromagnetism in Twisted Bilayer Graphene. *Physical Review Letters* **124**, 166601 (2020).

[66] Xie, M. & MacDonald, A. H. Nature of the Correlated Insulator States in Twisted Bilayer Graphene. *Physical Review Letters* **124**, 097601 (2020).

[67] Kang, J. & Vafek, O. Symmetry, Maximally Localized Wannier States, and a Low-Energy Model for Twisted Bilayer Graphene Narrow Bands. *Physical Review X* **8**, 031088 (2018).

[68] Koshino, M. *et al.* Maximally Localized Wannier Orbitals and the Extended Hubbard Model for Twisted Bilayer Graphene. *Physical Review X* **8**, 031087 (2018).

[69] Rong, Z. Y. & Kuiper, P. Electronic effects in scanning tunneling microscopy: Moiré pattern on a graphite surface. *Physical Review B* **48**, 17427–17431 (1993).

[70] Hass, J. *et al.* Why Multilayer Graphene on $4H-\mathrm{SiC}(000\bar{1})$ Behaves Like a Single Sheet of Graphene. *Physical Review Letters* **100**, 125504 (2008).

[71] Schmidt, H., Lüdtke, T., Barthold, P. & Haug, R. J. Mobilities and scattering times in decoupled graphene monolayers. *Physical Review B* **81**, 121403 (2010).

[72] Dobrik, G., Tapasztó, L., Nemes-Incze, P., Lambin, P. & Biró, L. P. Crystallographically oriented high resolution lithography of graphene nanoribbons by STM lithography. *physica status solidi (b)* **247**, 896–902 (2010).

[73] Wang, B. *et al.* Controlled Folding of Single Crystal Graphene. *Nano letters* **17**, 1467–1473 (2017).

[74] Bhandari, S. *et al.* Imaging Cyclotron Orbits of Electrons in Graphene. *Nano Letters* **16**, 1690–1694 (2016).

[75] Saito, Y., Ge, J., Watanabe, K., Taniguchi, T. & Young, A. F. Independent superconductors and correlated insulators in twisted bilayer graphene. *Nature Physics* **16**, 926–930 (2020).

[76] Chen, S. *et al.* Electrically tunable correlated and topological states in twisted monolayer–bilayer graphene. *Nature Physics* 2004.11340 (2020).

[77] Mott, N. F. The Basis of the Electron Theory of Metals, with Special Reference to the Transition Metals. *Proceedings of the Physical Society. Section A* **62**, 416–422 (1949).

[78] Imada, M., Fujimori, A. & Tokura, Y. Metal-insulator transitions. *Reviews of Modern Physics* **70**, 1039–1263 (1998).

[79] Zhang, F., Jung, J., Fiete, G. A., Niu, Q. & MacDonald, A. H. Spontaneous Quantum Hall States in Chirally Stacked Few-Layer Graphene Systems. *Physical Review Letters* **106**, 156801 (2011).

[80] Nam, N. N. T. & Koshino, M. Lattice relaxation and energy band modulation in twisted bilayer graphene. *Physical Review B* **96**, 075311 (2017).

[81] Bao, W. *et al.* Stacking-dependent band gap and quantum transport in trilayer graphene. *Nature Physics* **7**, 948–952 (2011).

[82] Ju, L. *et al.* Topological valley transport at bilayer graphene domain walls. *Nature* **520**, 650–655 (2015).

[83] Li, H. *et al.* Electrode-Free Anodic Oxidation Nanolithography of Low-Dimensional Materials. *Nano Letters* **18**, 8011–8015 (2018).

[84] Chen, G. *et al.* Emergence of Tertiary Dirac Points in Graphene Moiré Superlattices. *Nano Letters* **17**, 3576–3581 (2017).

[85] Zou, K., Zhang, F., Clapp, C., MacDonald, A. H. & Zhu, J. Transport Studies of Dual-Gated ABC and ABA Trilayer Graphene: Band Gap Opening and Band Structure Tuning in Very Large Perpendicular Electric Fields. *Nano Letters* **13**, 369–373 (2013).

[86] Guinea, F., Castro Neto, A. H. & Peres, N. M. R. Electronic states and Landau levels in graphene stacks. *Physical Review B* **73**, 245426 (2006).

[87] Guinea, F., Castro Neto, A. H. & Peres, N. M. R. Electronic properties of stacks of graphene layers. *Solid State Communications* **143**, 116–122 (2007).

[88] Koshino, M. & Ando, T. Orbital diamagnetism in multilayer graphenes: Systematic study with the effective mass approximation. *Physical Review B* **76**, 85425 (2007).

[89] Craciun, M. F. *et al.* Trilayer graphene is a semimetal with a gate-tunable band overlap. *Nature Nanotechnology* **4**, 383–388 (2009).

[90] Zhu, W., Perebeinos, V., Freitag, M. & Avouris, P. Carrier scattering, mobilities, and electrostatic potential in monolayer, bilayer, and trilayer graphene. *Physical Review B* **80**, 235402 (2009).

[91] Zhu, W., Neumayer, D., Perebeinos, V. & Avouris, P. Silicon Nitride Gate Dielectrics and Band Gap Engineering in Graphene Layers. *Nano Letters* **10**, 3572–3576 (2010).

[92] Liu, Y., Goolaup, S., Murapaka, C., Lew, W. S. & Wong, S. K. Effect of Magnetic Field on the Electronic Transport in Trilayer Graphene. *ACS Nano* **4**, 7087–7092 (2010).

[93] Bao, W. *et al.* Magnetoconductance Oscillations and Evidence for Fractional Quantum Hall States in Suspended Bilayer and Trilayer Graphene. *Physical Review Letters* **105**, 246601 (2010).

[94] Koshino, M. & McCann, E. Gate-induced interlayer asymmetry in ABA-stacked trilayer graphene. *Physical Review B* **79**, 125443 (2009).

[95] Mak, K. F., Shan, J. & Heinz, T. F. Electronic Structure of Few-Layer Graphene: Experimental Demonstration of Strong Dependence on Stacking Sequence. *Physical Review Letters* **104**, 176404 (2010).

[96] Wu, B.-R. R. Field modulation of the electronic structure of trilayer graphene. *Applied Physics Letters* **98**, 263107 (2011).

[97] Avetisyan, A. A., Partoens, B. & Peeters, F. M. Electric field tuning of the band gap in graphene multilayers. *Physical Review B* **79**, 35421 (2009).

[98] Avetisyan, A. A., Partoens, B. & Peeters, F. M. Electric-field control of the band gap and Fermi energy in graphene multilayers by top and back gates. *Physical Review B* **80**, 195401 (2009).

[99] Kumar, S. B. & Guo, J. Multilayer graphene under vertical electric field. *Applied Physics Letters* **98**, 222101 (2011).

[100] Aoki, M. & Amawashi, H. Dependence of band structures on stacking and field in layered graphene. *Solid State Communications* **142**, 123–127 (2007).

[101] Zhang, F., Sahu, B., Min, H. & MacDonald, A. H. Band structure of ABC-stacked graphene trilayers. *Physical Review B* **82**, 035409 (2010).

[102] Zhang, L., Zhang, Y., Camacho, J., Khodas, M. & Zaliznyak, I. The experimental observation of quantum Hall effect of l=3 chiral quasiparticles in trilayer graphene. *Nature Physics* **7**, 953–957 (2011).

[103] Jung, J., Raoux, A., Qiao, Z. & MacDonald, A. H. Ab initio theory of moiré superlattice bands in layered two-dimensional materials. *Physical Review B* **89**, 205414 (2014).

[104] Zhang, Y.-H. & Senthil, T. Bridging hubbard model physics and quantum hall physics in trilayer graphene/h-bn moiré superlattice. *Physical Review B* **99**, 205150 (2019).

[105] Liu, J., Ma, Z., Gao, J. & Dai, X. Quantum Valley Hall Effect, Orbital Magnetism, and Anomalous Hall Effect in Twisted Multilayer Graphene Systems. *Physical Review X* **9**, 1–12 (2019).

[106] Repellin, C., Dong, Z., Zhang, Y.-h. & Senthil, T. Ferromagnetism in Narrow Bands of Moiré Superlattices. *Physical Review Letters* **124**, 187601 (2020).

[107] Zhu, G.-Y., Xiang, T. & Zhang, G.-M. Spin-valley antiferromagnetism and topological superconductivity in the trilayer graphene Moire super-lattice. *arXiv* 1806.07535 (2018).

[108] Hubbard, J. Electron correlations in narrow energy bands. II. The degenerate band case. *Proceedings of the Royal Society of London. Series A. Mathematical and Physical Sciences* **277**, 237–259 (1964).

[109] Lee, P. A., Nagaosa, N. & Wen, X.-G. Doping a Mott insulator: Physics of high-temperature superconductivity. *Reviews of Modern Physics* **78**, 17–85 (2006).

[110] Chen, G. *et al.* Signatures of tunable superconductivity in a trilayer graphene moiré superlattice. *Nature* **572**, 215–219 (2019).

[111] Aslamasov, L. G. & Larkin, A. I. The influence of fluctuation pairing of electrons on the conductivity of normal metal. *Physics Letters A* **26**, 238–239 (1968).

[112] Xi, X. *et al.* Ising pairing in superconducting NbSe2 atomic layers. *Nature Physics* **12**, 139–143 (2016).

[113] Fatemi, V. *et al.* Electrically tunable low-density superconductivity in a monolayer topological insulator. *Science* **362**, 926–929 (2018).

[114] Yagi, R. Charge imbalance observed in voltage-biased superconductor–normal tunnel junctions. *Physical Review B* **73**, 134507 (2006).

[115] Clem, J. R. Josephson junctions in thin and narrow rectangular superconducting strips. *Physical Review B* **81**, 144515 (2010).

[116] Kogan, V. G., Dobrovitski, V. V., Clem, J. R., Mawatari, Y. & Mints, R. G. Josephson junction in a thin film. *Physical Review B* **63**, 144501 (2001).

[117] Moshe, M., Kogan, V. G. & Mints, R. G. Edge-type Josephson junctions in narrow thin-film strips. *Physical Review B* **78**, 20510 (2008).

[118] Xu, C. & Balents, L. Topological Superconductivity in Twisted Multilayer Graphene. *Physical Review Letters* **121**, 087001 (2018).

[119] Fang, S. & Kaxiras, E. Electronic structure theory of weakly interacting bilayers. *Physical Review B* **93**, 235153 (2016).

[120] Kang, J. & Vafek, O. Strong Coupling Phases of Partially Filled Twisted Bilayer Graphene Narrow Bands. *Physical Review Letters* **122**, 246401 (2019).

[121] Ochi, M., Koshino, M. & Kuroki, K. Possible correlated insulating states in magic-angle twisted bilayer graphene under strongly competing interactions. *Physical Review B* **98**, 081102 (2018).

[122] Dodaro, J. F., Kivelson, S. A., Schattner, Y., Sun, X. Q. & Wang, C. Phases of a phenomenological model of twisted bilayer graphene. *Physical Review B* **98**, 1–8 (2018).

[123] Thomson, A., Chatterjee, S., Sachdev, S. & Scheurer, M. S. Triangular antiferromagnetism on the honeycomb lattice of twisted bilayer graphene. *Physical Review B* **98**, 075109 (2018).

[124] Venderbos, J. W. F. & Fernandes, R. M. Correlations and electronic order in a two-orbital honeycomb lattice model for twisted bilayer graphene. *Physical Review B* **98**, 245103 (2018).

[125] Seo, K., Kotov, V. N. & Uchoa, B. Ferromagnetic Mott state in Twisted Graphene Bilayers at the Magic Angle. *Physical Review Letters* **122**, 246402 (2019).

[126] Padhi, B. & Phillips, P. W. Pressure-induced metal-insulator transition in twisted bilayer graphene. *Physical Review B* **99**, 205141 (2019).

[127] Oostinga, J. B., Heersche, H. B., Liu, X., Morpurgo, A. F. & Vandersypen, L. M. K. Gate-induced insulating state in bilayer graphene devices. *Nature Materials* **7**, 151–157 (2008).

[128] Lu, X. *et al.* Superconductors, orbital magnets and correlated states in magic-angle bilayer graphene. *Nature* **574**, 653–657 (2019).

[129] Zibrov, A. A. *et al.* Tunable interacting composite fermion phases in a half-filled bilayer-graphene Landau level. *Nature* **549**, 360–364 (2017).

[130] Xue, J. *et al.* Scanning tunnelling microscopy and spectroscopy of ultra-flat graphene on hexagonal boron nitride. *Nature Materials* **10**, 282–285 (2011).

[131] Emori, S., Umachi, C. K., Bono, D. C. & Beach, G. S. D. Generalized analysis of thermally activated domain-wall motion in Co/Pt multilayers. *Journal of Magnetism and Magnetic Materials* **378**, 98–106 (2015).

[132] Nagaosa, N., Sinova, J., Onoda, S., MacDonald, A. H. & Ong, N. P. Anomalous Hall effect. *Reviews of Modern Physics* **82**, 1539–1592 (2010).

[133] Chang, C.-Z. *et al.* Experimental Observation of the Quantum Anomalous Hall Effect in a Magnetic Topological Insulator. *Science* **340**, 167–170 (2013).

[134] Kou, X. *et al.* Scale-Invariant Quantum Anomalous Hall Effect in Magnetic Topological Insulators beyond the Two-Dimensional Limit. *Physical Review Letters* **113**, 137201 (2014).

[135] Fox, E. J. *et al.* Part-per-million quantization and current-induced breakdown of the quantum anomalous Hall effect. *Physical Review B* **98**, 75145 (2018).

[136] Yu, R. *et al.* Quantized Anomalous Hall Effect in Magnetic Topological Insulators. *Science* **329**, 61–64 (2010).

[137] Bestwick, A. J. *et al.* Precise Quantization of the Anomalous Hall Effect near Zero Magnetic Field. *Physical Review Letters* **114**, 187201 (2015).

[138] Chang, C.-Z. *et al.* Zero-Field Dissipationless Chiral Edge Transport and the Nature of Dissipation in the Quantum Anomalous Hall State. *Physical Review Letters* **115**, 57206 (2015).

[139] Büttiker, M. Absence of backscattering in the quantum Hall effect in multiprobe conductors. *Physical Review B* **38**, 9375–9389 (1988).

[140] van der Pauw, L. J. & van der Pauw, L. A Method of Measuring Specific Resitivity and Hall Effect of Discs of Arbitrary Shape. *Philips Research Reports* **13**, 1–9 (1958).

[141] Rosen, I. T. *et al.* Chiral transport along magnetic domain walls in the quantum anomalous Hall effect. *npj Quantum Materials* **2**, 69 (2017).

[142] Yasuda, K. *et al.* Quantized chiral edge conduction on domain walls of a magnetic topological insulator. *Science* **358**, 1311–1314 (2017).

[143] Liu, E. *et al.* Giant anomalous Hall effect in a ferromagnetic kagome-lattice semimetal. *Nature Physics* **14**, 1125–1131 (2018).

[144] Apalkov, D., Dieny, B. & Slaughter, J. M. Magnetoresistive Random Access Memory. *Proceedings of the IEEE* **104**, 1796–1830 (2016).

[145] Su, Y. & Lin, S.-Z. Switching of valley polarization and topology in twisted bilayer graphene by electric currents. *arXiv* 1806.07535 (2020).

[146] He, W.-Y., Goldhaber-Gordon, D. & Law, K. T. Giant orbital magnetoelectric effect and current-induced magnetization switching in twisted bilayer graphene. *Nature Communications* **11**, 1650 (2020).

[147] Upadhyaya, P. & Tserkovnyak, Y. Domain wall in a quantum anomalous Hall insulator as a magneto-electric piston. *Physical Review B* **94**, 020411 (2016).

[148] Zhu, J., Su, J.-J. & MacDonald, A. H. The Curious Magnetic Properties of Orbital Chern Insulators. *arXiv* 2001.05084 (2020).

[149] Checkelsky, J. G., Ye, J., Onose, Y., Iwasa, Y. & Tokura, Y. Dirac-fermion-mediated ferromagnetism in a topological insulator. *Nature Physics* **8**, 729–733 (2012).

[150] Chang, C.-Z. *et al.* Thin Films of Magnetically Doped Topological Insulator with Carrier-Independent Long-Range Ferromagnetic Order. *Advanced Materials* **25**, 1065–1070 (2013).

[151] Kou, X. *et al.* Interplay between Different Magnetisms in Cr-Doped Topological Insulators. *ACS Nano* **7**, 9205–9212 (2013).

[152] Amet, F., Williams, J. R., Watanabe, K., Taniguchi, T. & Goldhaber-Gordon, D. Insulating behavior at the neutrality point in single-layer graphene. *Physical Review Letters* **110**, 216601 (2013).

[153] Amet, F. Novel phenomena driven by interactions and symmetry breaking in graphene (Doctoral dissertation). *Stanford University* (2014).

[154] Mucha-Kruczyński, M., Wallbank, J. R. & Fal'ko, V. I. Heterostructures of bilayer graphene and h-BN: Interplay between misalignment, interlayer asymmetry, and trigonal warping. *Physical Review B* **88**, 205418 (2013).

[155] Jung, J., Dasilva, A. M., MacDonald, A. H. & Adam, S. Origin of band gaps in graphene on hexagonal boron nitride. *Nature Communications* **6**, 6308 (2015).

[156] Yeh, N.-C., Sugihara, K., Dresselhaus, M. S. & Dresselhaus, G. Transport properties and magnetic interactions in acceptor-type magnetic graphite intercalation compounds. *Physical Review B* **40**, 622–635 (1989).

[157] Esquinazi, P. *et al.* Induced Magnetic Ordering by Proton Irradiation in Graphite. *Physical Review Letters* **91**, 227201 (2003).

[158] Mombrú, A. W. *et al.* Multilevel ferromagnetic behavior of room-temperature bulk magnetic graphite. *Physical Review B* **71**, 100404 (2005).

[159] Kopelevich, Y., Medina Pantoja, J. C., da Silva, R. R., Mrowka, F. & Esquinazi, P. Anomalous Hall effect in graphite. *Physics Letters A* **355**, 233–236 (2006).

[160] Červenka, J., Katsnelson, M. I. & Flipse, C. F. J. Room-temperature ferromagnetism in graphite driven by two-dimensional networks of point defects. *Nature Physics* **5**, 840–844 (2009).

[161] Esquinazi, P. *et al.* On the low-field Hall coefficient of graphite. *AIP Advances* **4**, 117121 (2014).

[162] Zhou, P., Sun, C. Q. & Sun, L. Z. Two Dimensional Antiferromagnetic Chern Insulator: NiRuCl 6. *Nano Letters* **16**, 6325–6330 (2016).

[163] Lian, B., Sun, X.-Q., Vaezi, A., Qi, X.-L. & Zhang, S.-C. Topological quantum computation based on chiral Majorana fermions. *Proceedings of the National Academy of Sciences* **115**, 10938–10942 (2018).

[164] He, Q. L. *et al.* Chiral Majorana fermion modes in a quantum anomalous Hall insulator–superconductor structure. *Science* **357**, 294–299 (2017).

[165] Mahoney, A. C. *et al.* Zero-field edge plasmons in a magnetic topological insulator. *Nature Communications* **8**, 1836 (2017).

[166] Martin, I. & Batista, C. D. Itinerant Electron-Driven Chiral Magnetic Ordering and Spontaneous Quantum Hall Effect in Triangular Lattice Models. *Physical Review Letters* **101**, 156402 (2008).

[167] Kivelson, S., Lee, D.-H. & Zhang, S.-C. Global phase diagram in the quantum Hall effect. *Physical Review B* **46**, 2223–2238 (1992).

[168] Hilke, M. *et al.* Experimental evidence for a two-dimensional quantized Hall insulator. *Nature* **395**, 675–677 (1998).

[169] Wu, F., Das Sarma, S., Sarma, S. D. & Das Sarma, S. Collective Excitations of Quantum Anomalous Hall Ferromagnets in Twisted Bilayer Graphene. *Physical Review Letters* **124**, 046403 (2020).

[170] Alavirad, Y. & Sau, J. D. Ferromagnetism and its stability from the one-magnon spectrum in twisted bilayer graphene. *arXiv* 1907.13633 (2019).

[171] Repellin, C. & Senthil, T. Chern bands of twisted bilayer graphene: fractional Chern insulators and spin phase transition. *arXiv* 1912.11469 (2019).

[172] Zhang, Y.-H. & Senthil, T. Quantum Hall spin liquids and their possible realization in moiré systems. *Physical Review B* **102**, 115127 (2020).

[173] Lee, J. Y. *et al.* Theory of correlated insulating behaviour and spin-triplet superconductivity in twisted double bilayer graphene. *Nature Communications* **10**, 1–28 (2019).

[174] Kwan, Y. H., Parameswaran, S. A. & Sondhi, S. L. Twisted bilayer graphene in a parallel magnetic field. *Physical Review B* **101**, 205116 (2020).

[175] Serlin, M. *et al.* Intrinsic quantized anomalous Hall effect in a moiré heterostructure. *Science* **367**, 900–903 (2020).

[176] Bergholtz, E. J. & Liu, Z. Topological Flat Band Models and Fractional Chern Insulators. *International Journal of Modern Physics B* **27**, 1330017 (2013).

[177] Macdonald, A. H. *The Quantum Hall Effects. In Quantum Coherence inMesoscopic Systems(ed. Kramer, B.)* (Springer, 1991).

[178] Liu, Z., Bergholtz, E. J., Fan, H. & Läuchli, A. M. Fractional Chern Insulators in Topological Flat Bands with Higher Chern Number. *Physical Review Letters* **109**, 186805 (2012).

[179] Wang, Y.-F., Yao, H., Gong, C.-D. & Sheng, D. N. Fractional quantum Hall effect in topological flat bands with Chern number two. *Physical Review B* **86**, 201101 (2012).

[180] Polshyn, H. *et al.* Nonvolatile switching of magnetic order by electric fields in an orbital Chern insulator. *arXiv* 2004.11353 (2020).

[181] Cao, Y. *et al.* Nematicity and Competing Orders in Superconducting Magic-Angle Graphene. *arXiv* 2004.04148 (2020).

[182] Stepanov, P. *et al.* Untying the insulating and superconducting orders in magic-angle graphene. *Nature* **583**, 375–378 (2020).

[183] Arora, H. S. *et al.* Superconductivity in metallic twisted bilayer graphene stabilized by WSe2. *Nature* **583**, 379–384 (2020).

[184] Liu, X. *et al.* Tunable spin-polarized correlated states in twisted double bilayer graphene. *Nature* **583**, 221–225 (2020).

[185] He, M. *et al.* Symmetry breaking in twisted double bilayer graphene. *Nature Physics* (2020).

[186] Shi, Y. *et al.* Tunable van Hove Singularities and Correlated States in Twisted Trilayer Graphene. *arXiv* 2004.12414 (2020).

[187] Wang, L. *et al.* Correlated electronic phases in twisted bilayer transition metal dichalcogenides. *Nature Materials* **19**, 861–866 (2020).

[188] Wu, S., Zhang, Z., Watanabe, K., Taniguchi, T. & Andrei, E. Y. Chern Insulators and Topological Flat-bands in Magic-angle Twisted Bilayer Graphene. *arXiv* 2007.03735 (2020).

[189] Das, I. *et al.* Symmetry broken Chern insulators and magic series of Rashba-like Landau level crossings in magic angle bilayer graphene. *arXiv* 2007.13390 (2020).

[190] Nuckolls, K. P. *et al.* Strongly Correlated Chern Insulators in Magic-Angle Twisted Bilayer Graphene. *arXiv* 2007.03810 (2020).

[191] Choi, Y. *et al.* Tracing out Correlated Chern Insulators in Magic Angle Twisted Bilayer Graphene. *arXiv* 2008.11746 (2020).

[192] Saito, Y. *et al.* Isospin Pomeranchuk effect and the entropy of collective excitations in twisted bilayer graphene. *arXiv* 2008.10830 (2020).

[193] Rozen, A. *et al.* Entropic evidence for a Pomeranchuk effect in magic angle graphene. *arXiv* 2009.01836 (2020).

[194] Tschirhart, C. L. *et al.* Imaging orbital ferromagnetism in a moiré Chern insulator. *arXiv* 2006.08053 (2020).

[195] Po, H. C., Zou, L., Senthil, T. & Vishwanath, A. Faithful tight-binding models and fragile topology of magic-angle bilayer graphene. *Physical Review B* **99**, 195455 (2019).

[196] Song, J. C. W., Samutpraphoot, P. & Levitov, L. S. Topological Bloch bands in graphene superlattices. *Proceedings of the National Academy of Sciences* **112**, 10879–10883 (2015).

[197] Jonietz, F. *et al.* Spin Transfer Torques in MnSi at Ultralow Current Densities. *Science* **330**, 1648–1651 (2010).

[198] Fan, Y. *et al.* Magnetization switching through giant spin–orbit torque in a magnetically doped topological insulator heterostructure. *Nature Materials* **13**, 699–704 (2014).

[199] Yankowitz, M. *et al.* Dynamic band-structure tuning of graphene moiré superlattices with pressure. *Nature* **557**, 404–408 (2018).

[200] Bachmann, M. D. *et al.* Super-geometric electron focusing on the hexagonal Fermi surface of PdCoO2. *Nature Communications* **10**, 1–8 (2019). URL `http://dx.doi.org/10.1038/s41467-019-13020-9`.

[201] Sharpe, A. L. & Barnard, A. W. Monte carlo code for propagating electrons within an arbitrary geometry for a given fermi surface: `https://github.com/dgglab/ballistic_montecarlo`.